Annual reports on NMR Spectroscopy

Volume 60

List of Contributors

C. Ader, *Institut für Biophysik und, Physikalische Biochemie, Universität Regensburg, D-93040 Regensburg, Germany*

E. Brunner, *Institut für Biophysik und Physikalische Biochemie, Universität Regensburg, D-93040 Regensburg, Germany*

Paul D. Ellis, *Environmental Molecular Sciences Laboratory, K8–98, Pacific Northwest National Laboratory, Richland, WA 99352, USA*

Ludger Ernst, *Department of Chemistry, Technical University of Braunschweig, 38106 Braunschweig, Germany*

Stephan L. Grage, *Institut für Biologische Grenzflächen, Forchungszentrum Karlsruhe, Hermann-von-Helmholtz-platz 1, 76344 Eggenstein-Leopoldshafen, Germany*

C. Gröger, *Institut für Biophysik und,Physikalische Biochemie, Universität Regensburg, D-93040 Regensburg, Germany*

A. Iuga, *Institut für Biophysik und Physikalische Biochemie, Universität Regensburg, D-93040 Regensburg, Germany*

Andrew S. Lipton, *Environmental Molecular Sciences Laboratory, K8–98, Pacific Northwest National, Laboratory, Richland, WA 99352, USA*

David A. Middleton, *Faculty of Life Sciences, University of Manchester, Sackville Street, Manchester M601QD, UK*

Anthony Watts, *Department of Biochemistry, University of Oxford, South Parks Road, Oxford OX1 3QU, UK*

Preface

Volume 60 of Annual Reports on NMR consists of chapters representing the very broad scope of NMR applications to five areas of science. The first contribution is on Low Temperature Solid-State NMR Spectroscopy. A Strategy for the Direct Observation of Quadrupolar Nuclides of Biological Interest by P. D. Ellis and A. S. Lipton; this is followed by an account on NMR Methods for Characterising Ligand–Receptor and Drug–Membrane Interactions in Pharmaceutical Research by D. A. Middleton; L. Ernst reports on Recent Advances in NMR Studies of Cyclophanes; Applications of Solid State ^{31}P NMR Spectroscopy are covered by A. Iuga, C. Ader, C. Groeger and E. Brunner; finally, S. L. Grage and A. Watts report Applications of REDOR for Distance Measurements in Biological Solids. My sincere thanks go to all of these reporters for their interesting and timely accounts.

Royal Society of Chemistry
Burlington House
Piccadilly
London, UK

G. A. WEBB
May 2006

Low-Temperature Solid-State NMR Spectroscopy. A Strategy for the Direct Observation of Quadrupolar Nuclides of Biological Interest

PAUL D. ELLIS AND ANDREW S. LIPTON

Biological Sciences Division; K8-98, Environmental Molecular Sciences Laboratory, Pacific Northwest National Laboratory, 902 Battelle Boulevard, Richland, WA 99352, USA

This review presents a self-contained summary of the experimental methods necessary to perform a low-temperature solid-state nuclear magnetic resonance (NMR) experiment. Specific references are made for Zn^{2+} and Mg^{2+}. However, this is not a comprehensive review of the NMR literature of these nuclides. As the review is concerned with solid-state NMR spectroscopy of quadrupolar nuclides, we limit the discussions to odd-half-integral spin systems, i.e. $\frac{3}{2}$, $\frac{5}{2}$, $\frac{7}{2}$, and $\frac{9}{2}$ spins. The reason for the limitation is due to the "relative ease" of observing the central transition, which is common to all of these nuclides. The review is divided into two major sections; the first dealing with experimental methods, e.g. use of low-temperature, magnetization-transfer, spin echo methods, and questions dealing with nonspecific binding. Following those discussions we turn to the introduction of structure into the experiment, i.e. the use of triple resonance experiments to selectively introduce dipolar interactions and the use of molecular theory.

ANNUAL REPORTS ON NMR SPECTROSCOPY
VOLUME 60 ISSN 0066 4103
DOI 10.1016/S0066-4103(06)60001-X

1. INTRODUCTION

Our group has been interested in the applications of nuclear magnetic resonance (NMR) spectroscopy of diamagnetic metal ions as a means to understand the role of these metals in metalloproteins. For the present discussion, the native metals of interest are Zn^{2+} and Mg^{2+}. In the past these investigations have utilized surrogate metals, e.g. Cd^{2+} for Zn^{2+}, as a means to circumvent the undesirable NMR properties of the native metals.[1–3] The scope of this review is to describe in some detail the strategy we employ to observe and analyze the results of NMR experiments directed toward the native metals in metalloproteins.

It is important to ask at this point as to why such experiments are important. Central to addressing this question is the chemistry of these two ions. Foremost, Zn^{2+} and Mg^{2+} are strong Lewis acids that are stable with respect to their oxidation states of $+2$. In both cases, the ions have closed shells: Zn^{2+} has a $3d^{10}$ configuration whereas Mg^{2+} has a $2s^22p^6$ configuration. These electron configurations significantly restrict the type of spectroscopy that can be used to follow their respective chemistries. Their closed shells preclude electron paramagnetic resonance (EPR) as suitable choice, and likewise, UV/Vis is similarly eliminated. As a result, these metals belong to a group with similar electron configurations that have been termed spectroscopically silent metal ions. At first glance these ions appear to be boring and colorless. Yet, it is the Lewis acid properties with a stable oxidation states that makes these metals central to the chemistry of a large class of metal-dependent proteins.

In the case of Zn^{2+}, enzymatic reactions are catalyzed by coordinating a nucleophilic water to lower its pK_a, coordinating and polarizing a ligand (such as a carbonyl oxygen or a thiolate), and/or stabilizing the developing negative charge in a transition state.[4,5] Second, Zn^{2+} is able to adopt a range of coordination numbers from 4 to 6 and geometric configurations that allow the metal to accommodate structural rearrangements that can occur during the course of chemical reactions.[6–8] Finally, although zinc is generally tightly bound to proteins, its pendant ligands can undergo rapid exchange necessary for efficient catalysis.

The hydrolytic chemistry of Mg^{2+} is central to DNA repair biology.[9] This chemistry is accomplished by the ability of Mg^{2+} to lower the pK_a of a bound water or as a polarizing agent for a bound ligand. As in the case of Zn^{2+}, Mg^{2+} can stabilize an incipient negative charge developed during a reaction. However, in contrast to Zn^{2+}, the coordination number for Mg^{2+} is typically six and usually with oxygen-donating ligands. Further, rather than being tightly bound to the protein of interest like Zn^{2+}, Mg^{2+} is often weakly bound to the protein and as a result its catalytic chemistry is affected during its transient residence in the proteins of interest. As we will demonstrate subsequently, this latter difference between Zn^{2+} and Mg^{2+} has a profound effect on the strategy for performing spectroscopy on these two ions.

The central paradigm of hydrolytic metalloproteins is that a metal ion such as Zn^{2+} or Mg^{2+} significantly lowers the pK_a of the metal-bound water from a value of nominally 14 to one more appropriate of a physiological environment, while

avoiding undesired redox chemistry. In contrast to this hydrolytic chemistry there have been recent examples of a new class of Zn^{2+} sites: those involved in catalysis of alkyl group transfer.[10–12] These Zn^{2+} sites are typically thiolate rich, and in some cases the Zn^{2+} is coordinated exclusively to thiolates. Although these resemble "structural" Zn^{2+} sites, they are nevertheless reactive, promoting the alkylation of a substrate thiolate that is, at least transiently, bound to the Zn^{2+}.

The following are some questions that are driving ongoing research with these metals:

For Zn^{2+}

- Can a determination of the pK_a be made on Zn^{2+}-bound water in a resting enzyme?
- Can "activated" Zn^{2+}-bound water be treated as a simple weak acid?
- How are thiolate-rich sites such as those involved in alkyl transfer reactions different from those in structural thiolate sites?

For Mg^{2+}

- Is Mg^{2+} always in an octahedral coordination environment, with its open coordination sites filled with water?
- Can the ratio of OH^-/H_2O bound to Mg^{2+} be determined?

As the reader may notice these are basically simple questions and yet they have remained unanswered. However, the answers have profound mechanistic implications as to how the metal functions in metal-dependent proteins. If, in an ideal world, you had perfect bond distances and/or a complete understanding of the electrostatics around the metal center, these questions could be answered. However, in a real world it is going to take a combination of methods to infer bond distances and electrostatics. The bond distances arise from X-ray experiments and the electrostatic arise from solid-state NMR spectroscopy of quadrupolar nuclides. However, each of these methods has their shortcomings and we discuss them below.

Until very recently the only method that could address these questions has been X-ray scattering methods (either X-ray scattering/diffraction, electron scattering/diffraction, or absorption-detected electron scattering – i.e., EXAFS). In the case of X-ray diffraction addressing these questions offers significant challenges. The most important of these challenges revolve around the overall resolution of the structure. Typical X-ray resolution of proteins is on the order of 2 Å. As a result of this resolution the uncertainty in a given bond distance is on the order of ± 0.1 Å. Unfortunately that uncertainty is also on the order of the difference in bond lengths between $X_3Zn\text{-}OH$ and $X_3Zn\text{-}OH_2$. Hence, unless the structure has a remarkable overall resolution, X-ray scattering/diffraction methods cannot tell the difference between OH^- and OH_2 bound Zn^{2+}. Even with exceptional resolution the crystallographer must deal with the apparent disorder around the metal site, i.e. water vs. hydroxide bound to the metal. The problem associated with the uncertainty in a given bond distance is problematic to *all* of the questions we have asked relative to Zn^{2+}. The problems facing X-ray methods as applied to Mg^{2+}-dependent proteins

are more challenging. In addition to issues associated with the uncertainty in a given bond distance is the nature of the basic physics of the X-ray scattering experiment, i.e. the electron count. Mg^{2+}, O^{2-}, and Na^{+} are isoelectronic and as a result they scatter X-rays nearly identically. Further, positional disorder and incomplete site occupancy can lead to confusion between disordered water and the presence of Mg^{2+}. Hence, unless the crystallographer is looking for Mg^{2+} it is easily missed. In fact it is common to use a surrogate ion such as Mn^{2+} as a means to find Mg^{2+}-binding sites in Mg^{2+}-dependent proteins. In summary, many of the important issues with respect to the metallobiochemistry of Zn^{2+} and Mg^{2+} are challenging to address by X-ray methods. Having said that, much of what is currently known about these metal ions in biology comes from X-ray scattering and/or EXAFS experiments.

The only other form of spectroscopy that can be used to address the questions posed above is NMR spectroscopy. As we shall shortly demonstrate, there are numerous challenges with respect to this experiment as well. Both Zn^{2+} and Mg^{2+} are examples of a quadrupolar nuclide with a spin of $\frac{5}{2}$. The nature of the quadrupole is such that their resonances are broad and this further exacerbates the central problem with these so-called low-gamma nuclei, namely their inherent low sensitivity.[13] If that was not enough of a challenge, these spins are diluted by virtue of their functional environment, i.e. in the DNA repair protein Polymerase β (Pol β)[14–16] there are two unique Mg^{2+} sites (25 Da each) within the total mass of the (~39 kDa) protein. Add to that the additional dilution brought about by the damaged DNA, and we have created a significant challenge. In order to quantify this dilution factor consider the following example. In magnesium acetate dihydrate the percent Mg^{2+} is ~17%. In Pol β the percent Mg^{2+} is on the order of 0.13%. The dilution factor in this case is ~132. Adding damaged DNA and including buffers/salts only makes this dilution greater. The focus of this review is to delineate what is needed to overcome these challenges.

This review presents a self-contained summary of the experimental methods necessary to perform a low-temperature solid-state NMR experiment. Specific references are made for Zn^{2+} and Mg^{2+}. However, this is not a comprehensive review of the NMR literature of these nuclides. In the writing of this review we made a couple of assumptions about the NMR expertise of the reader. The first is that the reader is familiar with the basics of NMR spectroscopy. Second, the reader has some interest in solid-state NMR methods and their application to the novel solution of important problems. Additionally, as the review is concerned with solid-state NMR spectroscopy of quadrupolar nuclides, we limit the discussions to odd-half-integral spin systems, i.e. $\frac{3}{2}$, $\frac{5}{2}$, $\frac{7}{2}$, and $\frac{9}{2}$ spins. The reason for the limitation is due to the "relative ease" of observing the central transition, which is common to all of these nuclides. The review is divided into two major sections: the first dealing with experimental methods, e.g. use of low-temperature, magnetization-transfer, spin echo methods, and questions dealing with nonspecific binding. Following those discussions we turn to the introduction of structure into the experiment, i.e. the use of triple-resonance experiments to selectively introduce dipolar interactions and the use of molecular theory. Finally, we summarize these methods and come back to some of the questions we raised above.

2. EXPERIMENTAL METHODS

2.1. Preliminary comments

The principal observable in a solid-state NMR experiment on a quadrupolar nuclide is the quadrupole coupling constant, C_q.[17] This coupling constant is directly proportional to the electric field gradient (EFG) at the nuclide of interest and is given by

$$C_q = q_{zz}\left[\frac{e^2}{a_0^3 h}\right]Q.$$

$$= q_{zz} \cdot 46.852 \text{ MHz (for } ^{25}\text{Mg)} \tag{1a}$$

$$= q_{zz} \cdot 35.245 \text{ MHz (for } ^{67}\text{Zn)} \tag{1b}$$

Here Q is the quadrupole moment of the nucleus in question, and q_{zz} the zz element of the field-gradient tensor. The atomic constants (e, a_0, and h) have their usual meanings. We can experimentally determine C_q and contrast that value against that predicted with *ab initio* calculations. The important point is that the quadrupole coupling constant is directly proportional to the electrostatics around the nucleus in question. Hence, the coupling constant will be sensitive to charge differences of various ligands and/or the ability of the ligand to polarize various orbitals associated with the Zn^{2+} (or Mg^{2+}). This is why an NMR experiment on a quadrupolar nuclide is essential to address the questions posed in Section 1. To second order (approximately), the lineshape for the central transition for a quadrupolar nuclide is proportional to

$$\omega \propto \frac{C_q^2}{\omega_0[I(2I-1)]^2}. \tag{2}$$

That is, the breadth of the lineshape is proportional to the square of C_q and inversely proportional to the Larmor frequency of the nucleus in question. This field dependence becomes an essential tool in the disentanglement of quadrupolar lineshapes. Another factor that can be important is the factor $[I(2I-1)]^2$. Basically, as the value of the nuclear spin increases, the breadth of the lineshape decreases. For I values of $\frac{9}{2}$, $\frac{7}{2}$, $\frac{5}{2}$, and $\frac{3}{2}$ the value of $[I(2I-1)]^2$ decreases dramatically: 1296, 441, 100, and 9, respectively. The I value dependence given above is approximate but reflects the strong dependence of the lineshape on the value of I. For example, all other factors being equal, the lineshape for a spin $\frac{3}{2}$ nuclide is about 10 times broader than the lineshape for a $\frac{5}{2}$ spin.

Before discussing the various experimental methods, it is important to discuss the overall applicability of the approach summarized here. While we utilize Zn^{2+} and Mg^{2+} as our examples, the methods discussed are not limited in their applicability to these ions specifically. In Table 1, we summarize the NMR properties of some representative quadrupolar nuclei that can be exploited by the methods discussed here.

Table 1. NMR properties of select quadrupolar nuclides of biological and/or environmental interest at 9.4 T

Atom	Spin	Gamma	Natural abundance	NMR frequency	Relative quadrupole moment[a]	Relative sensitivity equal number of spins
^{9}Be	1.50	−3.7594	100	56.2427	0.353	11.3548
^{17}O	2.50	−3.6266	0.037	54.2560	0.171	10.1935
^{23}Na	1.50	7.0760	100	105.8610	0.693	75.7159
^{25}Mg	2.50	−1.6370	10.13	24.4904	1.329	0.9375
^{33}S	1.50	2.0517	0.76	30.6946	0.452	1.8457
^{39}K	1.50	1.2484	93.1	18.6768	0.390	0.1782
^{43}Ca	3.50	−1.7999	0.145	26.9275	0.272	1.2461
^{51}V	3.50	7.032	99.76	105.2027	0.347	74.3122
^{59}Co	3.50	6.3171	100	94.5074	2.800	53.8737
^{63}Cu	1.50	7.0904	69.09	106.0764	1.467	76.1791
^{65}Cu	1.50	7.5958	30.910	113.6375	1.360	93.6579
^{67}Zn	2.50	1.6726	4.11	25.0230	1.000	1.0000
^{73}Ge	4.50	−0.9332	7.760	13.9612	1.307	0.1737
^{87}Sr	4.50	−1.1594	7.020	17.3453	2.233	0.3331
^{95}Mo	2.50	−1.743	15.72	26.0763	0.147	1.1317

[a]The quadrupole moments came from the reviews of Pyykkö.[113,114] The reader should consult these references for the sign of any given quadrupole moment.

If two nuclides have the same nuclear spin, comparable quadrupole moments, and their remaining NMR parameters are similar, then the relative sensitivities should give the reader an approximate idea of the relative difficulty of experiments on the two nuclei, e.g. ^{67}Zn and ^{25}Mg. From Table 1, we estimate that ^{67}Zn and ^{25}Mg are of comparable difficulty. If, however, the nuclear spins are different, e.g. ^{67}Zn and ^{65}Cu, then approximating the difficulty of a given experiment on a given nuclide relative to another is slightly more complicated. For example, if we have extensive experience with ^{67}Zn proteins and would like to explore an analogous series of experiments on a Cu^{+} protein, using enriched ^{65}Cu, the table can be useful. If we assume for a moment that we can excite and measure *only* the $\pm\frac{1}{2}$ transition for a quadrupolar nuclide, then the relative sensitivity of two nuclides (as in the case of ^{65}Cu and ^{67}Zn) loses its dependence on the nuclear spin so that the relative sensitivity for an equal number of nuclei, $S_{\text{Cu to Zn}}$, simply becomes the ratio of the cube of their respective γ's, i.e.

$$S_{\text{Cu to Zn}} = \left(\frac{\gamma_{\text{Cu}}}{\gamma_{\text{Zn}}}\right)^{3}. \tag{3}$$

The numbers reported in Table 1 for relative sensitivity are for an equal number of nuclei. The proposed selective excitations may be difficult to accomplish experimentally, but the tabulated relative sensitivity should serve as a reasonable

approximation for the relative ease when comparing one experiment to another. However, from the relationship depicted in Eq. (2) there are two other factors that must be included: the value of C_q and the dependence of the lineshape on nuclear spin. If we assume the quadrupole coupling constants are comparable, the ^{65}Cu lineshape is going to about an order of magnitude broader than the corresponding ^{67}Zn lineshape. Hence, the factor of 90 greater sensitivity of ^{65}Cu over ^{67}Zn (obtained from Table 1) reduces to about an order of magnitude of greater sensitivity but still making experiments feasible.

2.2. Cryogenic methods

As mentioned in Section 1, one of the biggest problems the NMR experiment must overcome is its low sensitivity. Recall that this includes the intrinsic sensitivity of the nuclide and the consequences of the dilution of the nucleus of interest in the protein matrix. Significant gain can be made in sensitivity by cooling both the sample and coil to cryogenic temperatures. When both the sample and coil are cooled there is a corresponding increase in the signal to noise ratio (S/N),[18–20] i.e.

$$S/N \propto T^{-3/2}. \tag{4}$$

this relation assumes the coil is the dominate noise source at this temperature. Hence, a reduction in temperature from nominally 293 to 10 K could lead to an increase in the S/N by a factor of roughly 159 or a time-savings on the order of 25,000. We say ''could'' in the previous sentence because there are factors, such as the noise temperature of the preamplifier, which can act to reduce this factor. To avoid this issue in particular, a cryogenic preamplifier should be employed in these experiments.[18] Other factors include placement of capacitors, utilization of shields, length and temperature of the connecting cables, etc. These practical issues are outside the scope of the present discussions. As we shall discuss in subsequent sections, there are still impressive gains to be made, however, it is prudent to discuss some details of how we accomplish the low temperatures.

2.2.1. *Cryostats*

The experiments summarized in this review have been performed using an Oxford Instruments continuous flow cryostat.[21] Such a system offers stable control of the operating temperature over an extended range as well as protection of the magnet bore from potentially devastating consequences such as freezing the magnet seals. The constraint on the inside working diameter of the cryostat is dictated by both the cryostat and magnet bore. For a typical ''wide bore'' magnet with an 89 mm bore (nominally 70 mm with room temperature shims) the inside working diameter for the cryostat is 50 mm. For a medium bore magnet with a diameter of 63 mm room temperature bore (nominally 50 mm with shims), such a cryostat leaves a working diameter of ~30 mm. Using magnets with a bore significantly smaller than 63 mm is, in all probability, impractical for the type of experiments we will describe here.

The room temperature shims can, of course, be removed providing a larger working diameter inside the cryostat or leaving the working diameter the same; allowing the cryostat to be more efficient. Under the heat load of the probe and radio frequency (RF) heating we employ a flow rate between 1.5 and 2.0 L/h at a pressure between 600 and 800 mbar. Under these conditions and using a 250 L dewar, we can run for about 7 days.

At a cost of about $4/L, the weekly operating cost of cryogens is $1,000 or an annual cost of at least $50,000/yr. However, there is an alternative to this annual expense that can eventually save precious research funds. The alternative is to employ a "cryogen-free" cryostat. Such devices are common in the physics literature and can now be made to have sufficient cooling power to handle typical NMR heat/power loads on the order of 1 W at 5 K. This type of heat dissipation is more than enough to handle a solid-state NMR experiment of the type discussed here. The interested reader can search the Internet for the term "cryogen-free cryostats" to learn more about such cryostats and to identify potential vendors to build one.

2.2.2. *Probe considerations*

The next point to consider is the nature of the probe used for these experiments. There are several variations on probe designs that simply depend on the nature of a given experiment and the needs of the user. However, we have made a fundamental decision with respect to all of our probes, i.e. they are *not* capable of magic angle spinning (MAS) experiments. Rather, all of the probes are static in nature. The reasons for this decision are easy and basically revolve around two points: the inherent difficulty of spinning a sample at cryogenic temperatures and the consequences of sample dilution discussed above. Recently, efforts have been made to spin at these temperatures[22] and these experiments have overcome many of the difficulties with low-temperature spinning. However, to do so, they had to employ small diameter spinners and thus have had to sacrifice sample size for spinning stability. The rationale for such a decision is clear, they could gain back the lost signal due to the smaller sample by the reduced temperature. For our application, we cannot afford to give away anything due to the dilution of the metal ion in the samples that are of interest to us. There are other technical issues associated with how fast you have to spin for quadrupole couplings in the range 10–30 MHz, but those details are secondary to losses in sensitivity.

All of our experiments to date have either been double- or triple-resonance experiments and the cryogenic probe designs have been published.[23,24] To optimize the NMR sensitivity of low-gamma nuclides, we have chosen to employ a cross-coil design for our probes where the inner coil is tuned to protons. The inside diameter of this coil is 5 mm. An engineering drawing of the coil deck we use is shown in Fig. 1. For simplicity we have omitted some details that would have cluttered the diagram of the probe. For example, omissions on the copper shield were the holes in the top and sides of the shield along with the threads it mounts to on the Observe deck. Other omissions are the insulator (a thin Teflon^{TM} sheet) between the coils and supporting (and tuning) rods. All of the capacitors are rated for cryogenic

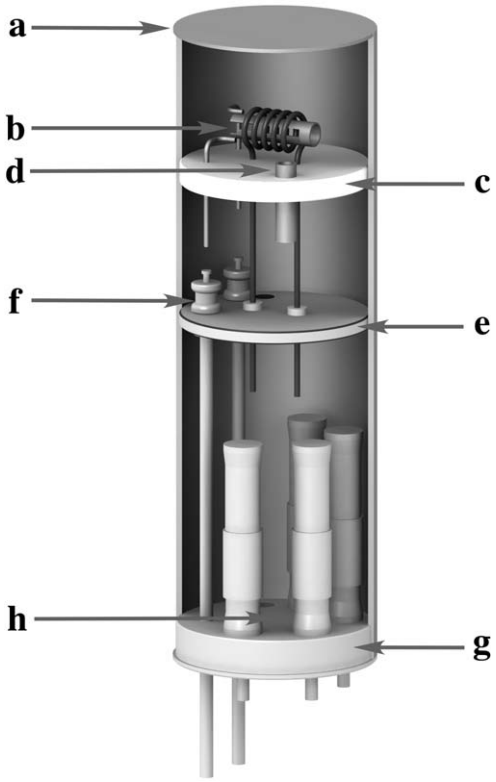

Fig. 1. Engineering cutaway of the top portion of our low-temperature NMR probe with (a) copper shield can, (b) cross-coil assembly, (c) Teflon^{TM} coil deck, (d) copper enclosure for the Cernox^{TM} resistor, (e) the stainless steel ^{1}H deck, (f) ^{1}H tune and match capacitors, (g) stainless steel observe deck, and (h) the tune and match capacitors for the low- and mid-frequency channels.

temperatures and have the ability to be tuned at cryogenic temperature without binding or simply breaking.[25] The coil platform is constructed with Teflon^{TM}, while in previous designs we used stainless steel.

However, at low temperatures we observed significant shifts in the resonance due to the susceptibility of the metal deck. With the Teflon^{TM} deck, the resonance frequencies are virtually invariant to temperature. Another important point in the coil deck is the location of a Cernox^{TM} resistor.[26] The resistor is seated in a cold finger made of copper. The purpose of the resister is to provide a measurement of the temperature as close to the sample as possible without significant coupling to the coils.

At first thought the use of high-power RF in an He atmosphere seems like a recipe for arcing. There is no doubt that conditions can be found that will generate coronal arcs, however, there are a broad range of conditions where the cross-coil structure is stable to the RF fields generated. To avoid generating too much voltage across the coil structure you have to reduce the RF power (which in turn limits the

available RF fields). Having done that, you also have to select the materials that are used for the coils carefully.[24] The reason for this is that at cryogenic temperatures the Q of the coils increases dramatically. High Q's are great for sensitivity but if the Q becomes too large ($\geqslant 400$), tuning instabilities can arise. For these reasons, the solenoid coil depicted in Fig. 1 is made out of brass. Such a coil has a Q on the order of 150 at 10 K ($\sim$70 at room temperature) and can generate RF fields of 50 kHz with 50 W of power.[27] The proton coil, while still made of copper, has a low temperature Q of 200–300 due to the dielectric losses introduced by the tuning elements of the circuit. This coil typically generates 50 kHz with $\sim$65 W of power (at 10 K). Once the power has been reduced, the critical factors become pressure and flow.

2.3. Polarization-transfer experiments

As discussed above, cryogenic temperatures have provided a potential gain in S/N on the order of 159 over a room temperature experiment. However, as we pointed out that gain is not sufficient for our needs. As a result polarization transfer from an abundant proton bath is used as the means to create transverse magnetization in our experiments. Specifically, we employ cross-polarization (CP) experiments to further enhance our S/N.[28,29] In this experiment, the enhancement could be as high as γ_H/γ_X (for ^{25}Mg and ^{67}Zn this ratio is about 16). The combination of low temperatures and CP methods can provide a theoretical gain of $\sim$2,500 over a conventional Bloch decay experiment (direct observation single pulse experiment with ^{1}H decoupling) at room temperature.

We assume at this point that the sample of interest is embedded at the molecular level in an environment containing ^{1}H's and that it can tolerate cryogenic temperatures. By tolerate, we mean the sample is stable (reversible) to thermal cycling. Further, the user must understand that there are possible phase transitions that can occur, and as such you must be sensitive to their potential existence. While our potential time-saving is now on the order of 6 million, the reality is that the recycle delay in the experiment cannot be ignored. Namely, the cryogenic temperatures have significantly lengthened T_1, the spin lattice relaxation time for nuclei in question. Owing to the fact that we are utilizing a polarization-transfer experiment, we need to only reduce T_1 for the protons. We first address issues associated with spin lattice relaxation, followed by a discussion of the methods for polarization transfer.

2.3.1. *The* T_1 *conundrum*

Most chemists when introduced to the NMR experiment are told that they should avoid paramagnetic impurities in their samples. However, in our case the presence of such an "impurity" is the means by which we avoid the problem of spin lattice relaxation times, which can become prohibitively long at cryogenic temperatures. Here we employ a paramagnetic dopant as a means to reduce the ^{1}H spin lattice relaxation time.[30] For biological investigations utilizing metalloproteins and/or their complexes this solution is straightforward. That is, doping the sample with the

same protein (or a different one) with a paramagnetic metal at its active site. Typical loadings are on the order of 5–10% by weight. So far we have only explored the use of Co^{2+}-substituted proteins as our paramagnetic dopant, e.g. Co^{2+}-substitued carbonic anhydrase (CA). Under optimum conditions, we have been able to employ a recycle delay on the order of 30 s for many of our samples. However, there are several cases where that same sample at one field strength can force us to employ a longer recycle delay at a higher field; for example going from 9.4 to 18.8 T. The reason for this is many fold and central to these issues is the field dependence of the spectral density function for electron relaxation. The optimization of these dopants with respect to metal ion is far from complete and is an area that is ripe for exploitation.

If the sample is not a protein, perhaps an inorganic model compound, then the use of paramagnetic impurities becomes more difficult. In the case of models for Zn^{2+} metalloproteins, the use of pyrazolylborates[31–34] complexes as model ligand systems has been profitable.[30,35] In many instances, the Zn^{2+}-pyrazolylborate can be doped with the corresponding Co^{2+}-pyrazolylborate. In this situation, the doping levels are typically 3–5%. The strategy for developing dopants for bioinorganic models for Mg^{2+} is more complicated, as substituting another paramagnetic metal for the Mg^{2+} often yields a different compound from the desired one. For the paramagnetic dopant to work, the dopant and the compound of interest must be "mixed" at the molecular level. Thus a physical mixing or grinding of the two compounds together is generally not sufficient for the doping to work. In the absence of a suitable dopant then the presence of methyl groups will facilitate ^{1}H relaxation through tunneling.[36] A T_1 minimum can be found under these conditions, typically between 30 and 50 K.

2.3.2. *Polarization-transfer methods*

The CP experiment of Pines *et al.*[28,29] is beautiful in its simplicity allowing the transfer of polarization from an abundant spin (usually ^{1}H's) to a rare spin. The gain in S/N in the CP experiment is on the order of γ_H/γ_X. Part of the beauty of the experiment is the thermodynamic analogies that can be drawn from the basic experiment. Recall, the CP experiment involves a $\pi/2$ pulse followed by spin locking the ^{1}H's and then allowing the contact between the ^{1}Hs and the rare spins. During this contact time, the rare spin magnetization grows and the abundant spin's magnetization decreases. After the maximum transfer has occurred the contact is broken and the rare spin magnetization is detected. The $\pi/2$ pulse and spin lock of the abundant spin is equivalent to cooling those spins. The resulting spin temperature is equal to $T_L(H_{1rot}/H_0)$, where T_L is the temperature of the lattice and H_{1rot} and H_0 are the strengths of the magnetic field in the rotating and the laboratory frames, respectively. For typical values of H_{1rot} and H_0, the spin temperature can become on the order of few tens of mK on a time scale of a few μs (which is on the order of ^{1}H T_2) and be held at this temperature for times comparable to $T_{1\rho}$, the spin lattice relaxation time in the rotating frame. At this point, the rare spin magnetization is "hot", corresponding to little if any polarization. Putting these two reservoirs in

"contact" leads to a cooling of the rare spin reservoir (an increase in magnetization) and a warming of the reservoir of the abundant spins (a decrease in magnetization). The amount of warming and cooling is related to the relative heat capacity of the two reservoirs. The contact is provided by the dipolar interaction between the abundant and rare spins.

The transfer is most efficient under the condition when the two rotating frames (one each for the abundant and rare spins) are rotating at the same frequency. This situation is known as the Hartmann–Hahn[37] condition and is given by

$$\gamma_{\mathrm{H}} B_{1\mathrm{H}} = \alpha \gamma_{\mathrm{X}} B_{1\mathrm{X}}, \tag{5}$$

where

$$\alpha = [I(I+1) - m(m-1)]^{1/2}. \tag{6}$$

Here, I refers to the nuclear spin of the quadrupolar nuclide X and the quantum number m refers to the nature of the transition in the quadrupolar spin system. Typically, the transition of interest is the $\pm\frac{1}{2}$ transition and as a result $m = \frac{1}{2}$.

A closer examination of the nature of the spin temperature[38] can bring the reader into some fascinating concepts. One such idea is important in the context of our discussion, namely the idea of adiabatic transfers.[39–42] In some early papers from the Pines group they explored the idea of "total cross polarization" (TCP).[43] Our interest in these experiments arises from the potential of further gains over and above those expected by CP alone. The previous applications of these experiments involved spin-$\frac{1}{2}$ systems. Even though the reported gains have been modest (somewhere between a factor of two and three),[44,45] this can represent a significant time-saving of nearly an order of magnitude. In the TCP experiment rather than utilize a spin lock as the means to cool the abundant spins, an adiabatic demagnetization in the rotating frame (ADRF)[41] is used instead. The respective pulse sequences are depicted in Fig. 2.

Comparing a single contact CP (Fig. 2a) with the TCP experiment (Fig. 2b) yields the following expressions for the potential gain in S/N:[43]

Single contact CP (under the Hartmann–Hahn condition):

$$\text{Gain} \propto \left(\frac{\gamma_I}{\gamma_S}\right). \tag{7}$$

Single contact TCP:

$$\text{Gain} \propto \kappa \left(\frac{\gamma_{\mathrm{I}}}{\gamma_{\mathrm{S}}}\right) \left[\frac{N_I I(I+1)}{N_S S(S+1)}\right]^{1/2}. \tag{8}$$

In these two equations we have used the notation that the nuclear spins are denoted as I and S for the abundant and rare spins, respectively, and N_I and N_S denote the number of I and S spins, respectively. This last factor in Eq. (8) arises from the adiabatic nature of the transfer. It is important to note that the transfer is done adiabatically and not under the conditions of the usual isoenergetic Hartmann–Hahn conditions. Hence, the transfer rates (for the adiabatic case) are slower and more susceptible to relaxation effects, notably $T_{1\mathrm{D}}$, the relaxation time

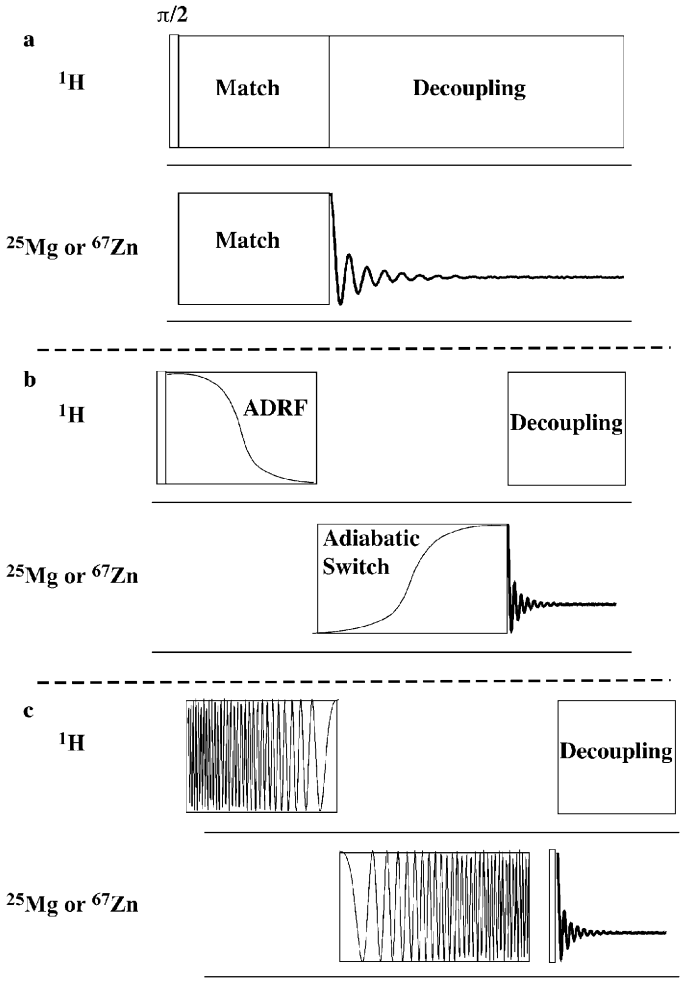

Fig. 2. Polarization-transfer pulse sequences: (a) Hartmann–Hahn CP, (b) ADRF sequence where X application of power is sudden ($\kappa = \frac{1}{2}$) or adiabatic ($\kappa = 1$), and (c) adiabatic laboratory frame transfer with ^{1}H frequency swept from off- to on-resonance and the observe channel swept from on-resonance to off-resonance.

corresponding to the loss of dipolar order.[46] In Eq. (8), the term κ is 1 if the rare spin power is turned on adiabatically and is equal to $\frac{1}{2}$ if it is turned on suddenly. If we recognize that S is $\frac{5}{2}$ for either ^{25}Mg or ^{67}Zn, then Eq. (8) becomes

$$\text{Gain} \propto \kappa \left(\frac{\gamma_I}{\gamma_S}\right) \left(\frac{3}{35}\right)^{1/2} \left[\frac{N_{\text{H}}}{N_{\text{X}}}\right]^{1/2}. \tag{9}$$

In a protein the factor of $N_{\text{H}}/N_{\text{X}}$ could easily be $>1{,}000$. Combining this with the numerical factor leads to a *potential* gain by the adiabatic experiments over that of a

conventional CP experiment of nearly an order of magnitude (with $\kappa = 1$). Given this possibility it is worthwhile comparing the adiabatic and normal CP experiments for ^{67}Zn with the aim to apply the best method to our protein systems.

Another version of the adiabatic experiments is also summarized in Fig. 2. This version of the experiment is performed in the lab frame (as opposed to a rotating coordinate system). There is a commonality in all of the polarization-transfer experiments we have discussed. The first phase involves cooling the abundant spins (in our case protons). The second phase relies on the existence of the dipolar coupling between the abundant spins and the system of interest, the rare spins. The lab frame version of this experiment is no different. The first stage is accomplished by sweeping the frequency of the abundant spins from off-resonance (in our case about 250 kHz) to an on-resonance condition. This process will convert Zeeman magnetization into dipolar order and at the same time cools the abundant spins. The next phase is creating Zeeman magnetization of the rare spin. To accomplish this we again sweep the frequency but now of the rare spin and we do this by going from an on-resonance condition to off-resonance. The new magnetization grows along the ''offset'' field along the lab frame Z-axis; the effectiveness of this process depends upon the lineshape of the rare spins.[45]

In fact when experiments based on the pulse sequences depicted in Fig. 2b and c are performed, the results are no better than those obtained via standard CP experiments (Fig. 2a). Further, the gain we observe does not depend on κ. At this point the exact reason for this failure is unclear and could arise from several factors, one of which is the selective nature of our pulses (a difference between a spin $\frac{1}{2}$ system and the broad resonances associated with quadrupolar spins systems). Another possibility is associated with our lineshape as opposed to the narrower and near Gaussian-shaped resonances observed previously.[44,45] We are still exploring these experiments; however, as a result of these shortcomings, the remainder of the discussion will be based on the standard CP experiment.

As an aside, there are several other methods used to enhance the central transition of a quadrupolar nuclide, notably the rotor-assisted population transfer (RAPT)[47,48] and double frequency sweeps (DFS)[49–51] pulse sequences. A review of these methods is described by Siegal *et al.*[52] All of these experiments are variations on a similar theme: namely perturb the populations of the outer transitions, and observe the consequences of this perturbation on the $\pm\frac{1}{2}$ transition, Le Chatelier's principal for spins. These experiments offer a significant time-saving when CP is not available, e.g. when there are no protons in the material. Why not combine these latter experiments with CP or on adiabatic variations to obtain a further gain in S/N? In the DFS experiment, rapid sweep is used to perturb the populations of outer transitions which in turn forces the population of the energy levels associated with m values of $\pm\frac{1}{2}$ to change yielding an enhanced population for this transition which would correspond to gain a factor of $\sim$2. This enhanced population corresponds to magnetization along the Z-axis for the quadrupolar spin. In either the normal CP or the adiabatic variations, the magnetization from these experiments comes about from the dipolar interaction between the protons and the quadrupole. Hence, as in the spin-$\frac{1}{2}$ case of CP where temperature alternation is needed to prevent spin-locked

"normal magnetization" from contaminating the magnetization from the polarization transfer, the magnetization that arises from the perturbed outer transitions will only serve to contaminate the magnetization from the polarization transfer.

Another point of potential interest is the use of paramagnetics as a means to significantly enhance the sensitivity in our experiment via dynamic nuclear polarization methods (or DNP).[53,54] The details of the DNP experiment are outside the scope of the present discussion. Basically, the existence of these radicals (different from those employed at present) that are coupled to the nuclear spins provide a means to enhance the nuclear polarization. For example, the maximum gain in ^{1}H polarization is ~660. This polarization can now be transferred to the rare spins of interest via a CP experiment yielding significant gains in sensitivity. It is an experiment we are interested in persuing in the future as a means to further extend the applicability of NMR methods to the investigation of metal sites in metalloproteins.

2.4. Spin echo methods

As was previously discussed, we employ low-temperature experiments (taking advantage of the Boltzmann factor) in combination with CP methods to overcome the dilution of the metal in the protein. The combination of low-temperature (10 K) and CP methods increases our S/N over conventional room-temperature experiments by a factor of ~2,000. The approximate nature reflects differences between ideal factors and what we realize experimentally. However, this combination of methods still has insufficient sensitivity to obtain a broad lineshape that is reflective of the desired quadrupole couplings. We could gain perhaps another factor of 10 (or more) in S/N if we could use a method such as MAS. This increase arises because the broad lineshape is broken into a series of narrow sidebands separated by the spinning frequency. The amplitude (and lineshape) of each sideband is encoded with the tensor information. An analysis of the sideband lineshapes and intensities yield the desired couplings. However, as mentioned above we have avoided MAS methods due principally to the reduced sample volume and therefore lower number of observable spins. To circumvent this problem, while still gaining nearly a factor of 10 (or more) in S/N, we have taken advantage of some properties of a spin echo train.[55] The top of each echo within the train refocuses all of the inhomogeneous (in the sense of Portis[56]) interactions (shielding and quadrupole tensors) and the decay of each half-echo has encoded within it the details of these tensors and their relative orientation. Fourier transformation of the echo train yields a spectrum, which after analysis yields the desired couplings.

2.4.1. *Spikelet echo or QCPMG detection*

The basic method is to acquire the induced signals that result from an echo train that was generated as a Carr–Purcell Meiboom–Gill sequence (CPMG).[57,58] The transverse magnetization in the echo train was, as mentioned above, created by a CP sequence. Since we are examining the NMR spectroscopy of a quadrupolar

nuclide, the experiment has been termed a CP/QCPMG experiment or simply the spikelet experiment. The pulse sequence is summarized in Fig. 3.

The reason for the collection of the entire echo train is outlined in Fig. 4. The left-hand side of Fig. 4 depicts an expansion of the first few echoes in a simulated induced signal. The echo spacing, τ_e (from top to bottom) increases such that in the lower left, the spacing has become infinite, analogous with changing the spinning speed in an MAS experiment. Fourier transformation of the time-domain signals results in a powder lineshape where the spike separation is equal to $(\tau_e)^{-1}$ With a simple lineshape, such as that depicted it is easy to follow the tops (connect the dots) of the spikes and recover the lineshape. However, in the presence of noise and more than one lineshape the problem becomes more difficult. As can been seen from Fig. 4, the decreased spike separation makes the lineshape more apparent, but at a cost of S/N per unit time. That is to say the lineshape is divided into more and more spikes decreasing the S/N in a given spike for a given time period.

The reader will note that the spin echo only refocuses inhomogeneous interactions (chemical shielding and quadrupole effects). It does not refocus interactions that are homogeneous, i.e. dynamics and homonuclear couplings. At 10 K the dynamic effects (with some caution) can be ignored which leaves homonuclear couplings. In principle, the couplings manifested in this experiment are dipolar in nature. These dipolar couplings are proportional to the inverse cube of the internuclear distance. Typical couplings are small (a few Hz) due to the metal–metal distances in proteins. However, the presence of such couplings can be ascertained,

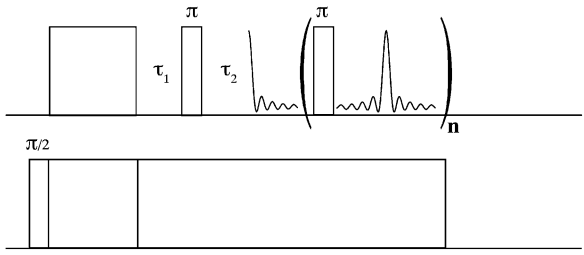

Fig. 3. Schematic diagram of the CP/QCPMG sequence.

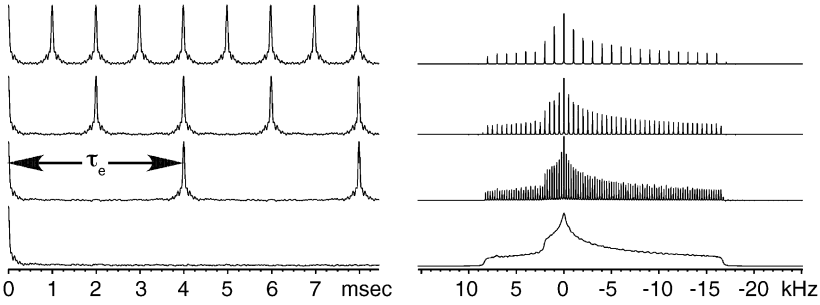

Fig. 4. Influence of τ_e in the time domain on the frequency domain.

in principle, by following the width of a given spikelet depending on the type of experiment being performed.

2.4.2. *Data collection*

We have already discussed the advantages to a QCPMG detection scheme in the previous section. Now we must turn our attention to the practical aspects of this experiment, namely what considerations are there to running such an experiment? What follows here is a discussion that we hope will prove independent of spectrometer vendor and software.

To begin one must have the timing of the sequence understood, including all the deadtimes and filter delays. We suggest starting with a sample of high S/N that can be readily observed in a short amount of time (say less than a few minutes so that parameter optimization can be performed), with the spectrometer set-up to collect a single echo with the ADCs running at or near their maximum rate and the audio filters set where you expect the actual analytes to be (this may be within the lineshape which will be explained in a moment). Now you will need to run the experiment and adjust τ_2 (see Fig. 3) so that the first point acquired is the top of the echo formed. You do NOT want to use left shifting to get to the top of the echo, this error would be propagated by the echo train and introduce timing errors. It is normal if τ_2 exceeds τ_1, and will depend on what the audio filters are set to. For example, if the filters are set to 200 kHz (or $\pm$100 kHz) one can expect an additional filter delay on the order of the inverse of 200 kHz or 5 μs. This can be verified by acquiring an FID with a filter setting and then again with a value half as wide. The echo maximum should move corresponding to the change you made. Knowing this delay (call it $d\tau$ or the time τ_2 exceeds τ_1) one will have to account for it in coding the pulse sequence. The reason for this is that there are required delays surrounding the π pulses to prevent digitizing RF breakthrough (or probe ringing). These delays must be symmetric to keep the timing on the signal consistent and should be kept close to the original τ's, which were presumably chosen to minimize artifacts. The difference is that instead of τ_1 one will need to compensate for the delay $d\tau$. Doing this compensation keeps the pulse train synchronized with the echo formation in the probe, not when it is actually detected with the ADC's. This is shown schematically in Fig. 5.

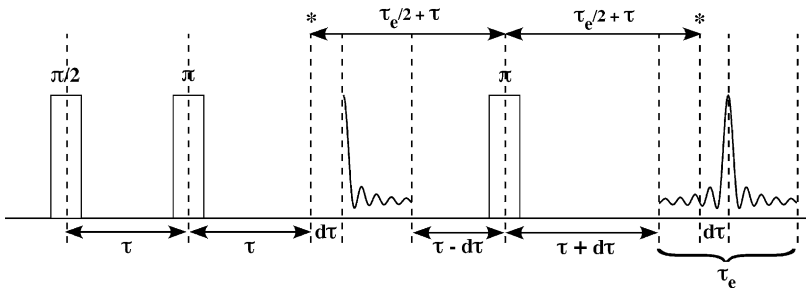

Fig. 5. Timing diagram of the QCPMG sequence.

The next thing is to decide the spikelet spacing required. The practical aspects of this are twofold: first how broad do you expect your lineshape to be and second how much sensitivity gain is desired? As we have seen in the previous section the more spikes generated in the transformed data the more accurately the lineshape is described, but at a trade-off of S/N per unit time. For example, you would not want your lineshape described by only four spikes, as it will be almost impossible to extract any NMR parameters. The parameter being adjusted here is τ_e whose inverse is the separation in frequency. There are two ways to make this change, by altering either the number of points in the echo or by the dwell time. Remember that we want to accurately represent the lineshape and that the half-echo contains this information. So choose a balance that will not oversample too much, the transformed spikes can be quite narrow and you will need a very large Fourier number in the transform to keep the digital resolution adequate to describe the peaks. For example, do not choose a 5 MHz spectral width if the lineshape is 50 kHz wide and the spikes are each only 10 Hz wide. As a good starting point we suggest a 1 MHz sampling rate with audio filters at 100 kHz (you do not want the filters much larger than the excitation bandwidth) and τ_e of 500 μs (a 2 kHz spike separation).

Next decide how many echoes to acquire. There are a few considerations here, especially if you require proton decoupling. The major concern here is sample heating. With a long T_2 one might be tempted to run the echoes out until there is no more signal to be had. However, this can easily exceed 100 ms making the decoupling portion of the experiment almost CW in nature. Be sure to have some method of heat dissipation near the sample area, such as body air or in the case of a cryostat a large flow of the cooling gas. Without proper airflow this experiment has generated enough heat to vaporize samples, liquefy plastic, or even melt solder and detach the RF coil. The other limitation here is the spectrometer, as there may be a limit to the number of points the instrument can acquire. Once you decide on the number of echoes you are now ready to acquire a data set.

The final detail the reader will need to put this into practice is the choice of RF field strength. Assuming one is utilizing cross polarization to generate magnetization the excitation bandwidth is already limited to the matching field required. However, it is not necessary that the train of π pulses be set to the same RF field strength. With a modest to small value of C_q, too strong a π pulse will severely distort[59] the resulting data set such that it does not resemble a pure quadrupole lineshape (and may prevent a simulation optimization from converging). The regimes to *avoid* are where the RF field strength (ω_{RF}) for the π pulses is comparable to the quadrupolar splitting, i.e.

$$0.2 < \left| \frac{\omega_Q}{\omega_{RF}} \right| < 3. \tag{10}$$

and where the ω_{RF} is less than the second-order quadrupolar lineshape, i.e.

$$\frac{2\omega_Q^2}{\omega_0 \omega_{RF}} > 0.1. \tag{11}$$

Here ω_Q is defined as

$$\omega_Q = \frac{2\pi C_q}{4I(2I-1)}. \tag{12}$$

or $C_q/40$ for $I = \frac{5}{2}$. This is exemplified in the ^{25}Mg spectra of Fig. 6. The top two spectra are magnesium acetate acquired with CP and a π pulse of 4 μs and an optimized simulation with quadrupole parameters of $C_q = 3.02$ and $\eta_q = 0.72$. The bottom spectra are the same sample acquired utilizing a 15 μs π pulse width and its respective simulation calculated with $C_q = 2.81$ MHz with $\eta_q = 0.68$. These parameters were independently optimized showing that by using an exact density matrix calculation one can approximate the lineshape to extract values of C_q and η to within 10% error. However, these numbers would be less reliable for those nuclides that have significant shift anisotropy contributions to the lineshape, such as $^{63/65}$Cu[60–62] or $^{87/89}$Rb,[63–65] as well as distortions due to pulse width. It is also worth noting that there are values of C_q where one cannot fulfill the inequalities mentioned above. All of the simulations employed within the manuscript were carried using the program SIMPSON.[115]

When C_q is large enough that the width of the lineshape exceeds the excitation bandwidth, then one is forced to perform multiple experiments so that the complete lineshape can be reconstructed. The whole lineshape is divided into bins, each bin corresponding to an excitation bandwidth. The reader should note that some overlap is desired such that there are no breaks due to non-uniform excitation. The transmitter is then arrayed to these frequencies and the subspectra collected. Typically, the probe needs retuning every ~50 kHz to maintain the "nominal" Hartmann–Hahn[37] match conditions. The resulting phase-corrected subspectra are re-referenced (by either left or right shifting the *spectrum* the number of points corresponding to the offset or equivalently performing a frequency shift in the *time*

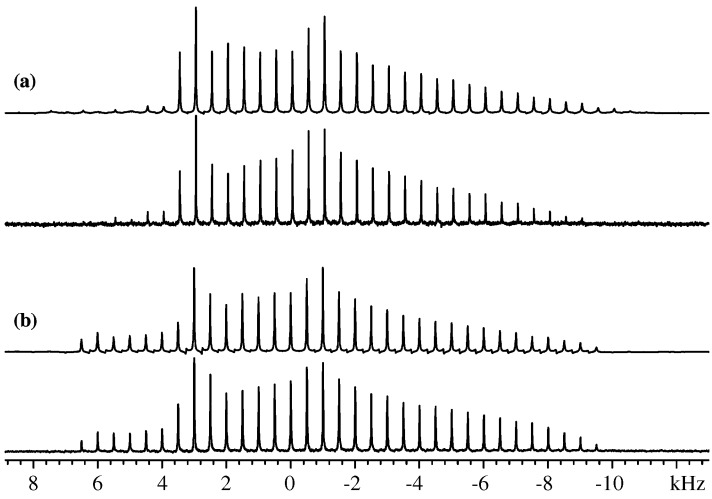

Fig. 6. Finite pulse width effects in the ^{25}Mg NMR of $Mg(OAc)_2 \cdot 4H_2O$ at 50 K/9.4 T with (a) 42 kHz RF and (b) 11 kHz RF fields with their respective simulations above.

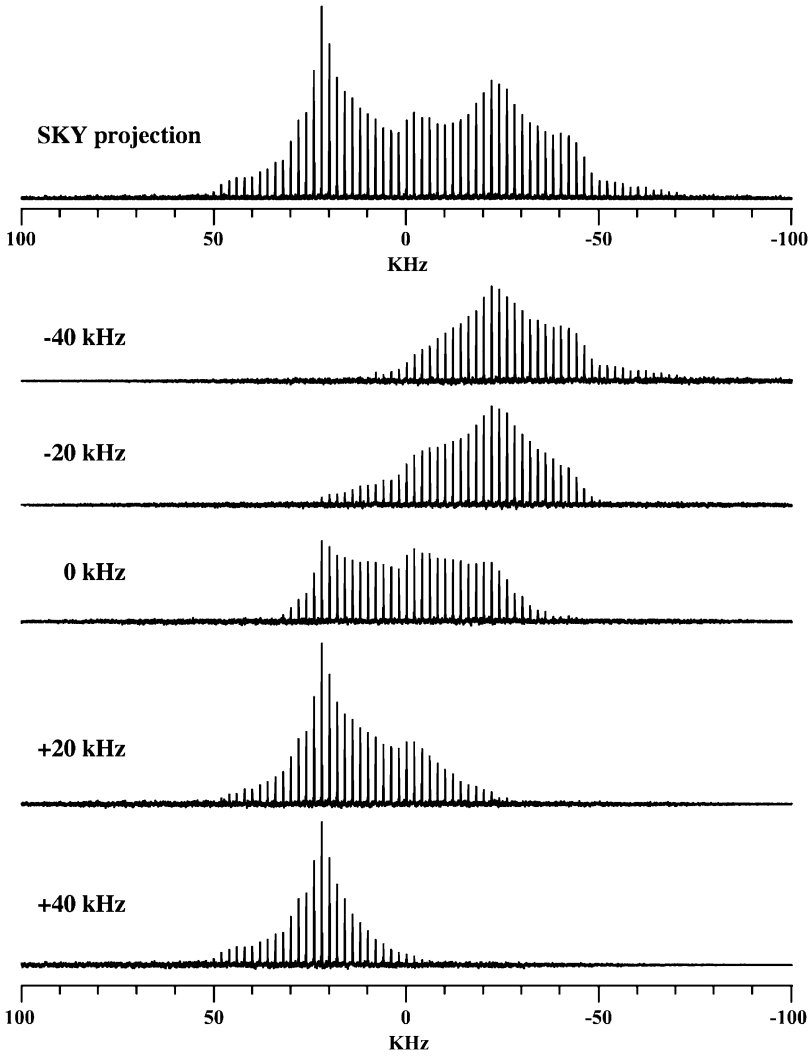

Fig. 7. Frequency shifted ^{67}Zn NMR experiments on [HB(3-^{t}Bu-5-Me-pz)$_3$]ZnI doped with 2 wt.% of its Co analog at 10 K/9.4 T with the resulting sky projection. Transmitter offsets were as indicated on each subspectrum.

domain[66]). The data are then combined to form a sky projection.[67] Fig. 7 depicts one such projection and the subspectra that were used in its construction. It is important to note that projections are utilized to combine the data sets, NOT a summation.

2.4.3. *Post processing and data manipulation*

At this point the reader should be able to acquire a QCPMG-detected "FID" with "N" echoes of spacing τ_e. A typical method for further increasing S/N is to apply

some form of apodization, such as exponential line broadening. For a single decay this is adequate, however, a train of echoes has two time constants. Aside from the T_2 decay of the train there is also the decay of each half-echo and then the rise of the next echo formation. If only the first half-echo were acquired then the line broadening applied would be a match to this decay. For the periodic nature of this data set a function can be defined to match this rapid decay, then the function inverted to rise again, and finally this new function can be replicated "N" times to match the complete train. Following this function a second apodization for the second time constant can be applied to the whole "FID". Examples of these functions and their effect on the data are depicted in Fig. 8.

What further manipulations might be desired other than matched apodization functions? There is also the possibility of changing the echo spacing after the data has been collected or collapsing all the echoes into a single half-echo to generate a high S/N powder pattern. At this point the reader is referred back to Fig. 4 in Section 2.4.1 to see the relationship between echo spacing in the time vs. frequency domains. Now suppose the data set collected was too coarse on the choice of spike spacing, rather than collect the data again with more transients (finer frequency spacing will cost in S/N), one could instead zerofill between the echoes in the time domain to adjust the width of τ_e. Of course, the inverse also applies in that if too fine a spacing was collected then points could be removed from between the echoes for a gain in S/N in the transformed spectrum. Further, one could collapse the echo train itself by combining all the individual echoes where each full echo is summed and then split, inverted (so each half is a decay), and finally summed again to form a single half-echo. In principle, assuming little or no T_2 decay, this method affords a

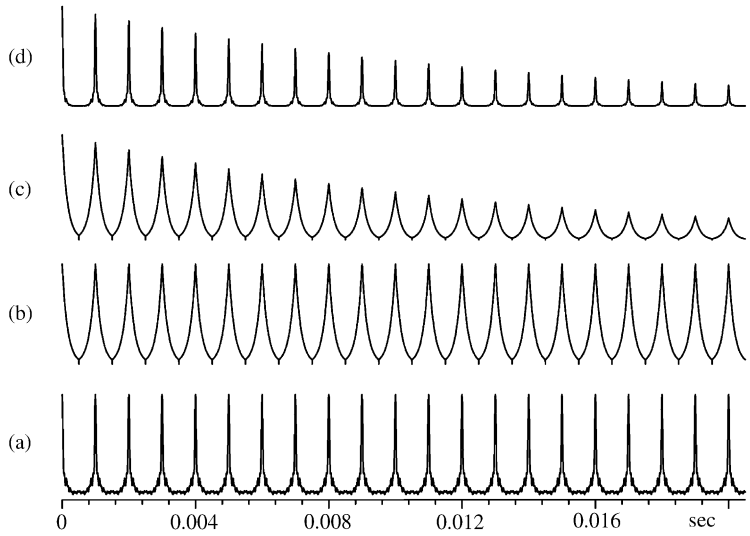

Fig. 8. Simulated "FID" and apodizations where (a) is the "raw" data, (b) the matched apodization function with a 2 kHz time constant, (c) the matched function combined with a 25 Hz exponential decay, and (d) the resulting "FID" with the apodization applied.

S/N gain over a single echo proportional to $\sqrt{(1+2N)}$, where N is the number of echoes in the train.[68]

To summarize the section thus far: we have walked the reader through our method of setting up the QCPMG detection (this is independent of how the initial magnetization was generated), practical considerations for excitation bandwidth for both large and small values of C_q, as well as some different ways the acquired data can be treated. The following section will deal with interpreting the resulting data. There are a few points that are unique to the spectroscopy of metals in proteins.

2.4.4. *Data interpretation*

To review, when investigating half-integer quadrupolar nuclides by solid-state NMR methods the principal observable is the central or $\pm\frac{1}{2}$ transition for that spin. The experiment we are utilizing is CP[28] followed by a CPMG train of π pulses.[57,58] Consider a spin $\frac{5}{2}$ nucleus, such as ^{67}Zn or ^{25}Mg with an unknown value of C_q; there are two possible extremes that one can find with these experiments: first, for a small value of C_q where the central transition lineshape is narrow and totally contained within the excitation region, and second that C_q is large and the expected lineshape is quite broad (requiring several subspectra at different offsets to reconstruct the complete spectrum[30]). A further question is the selectivity of these experiments for the $\pm\frac{1}{2}$ transition. These transitions ($|\frac{3}{2}| \leftrightarrow |\frac{1}{2}|$; $|\frac{5}{2}| \leftrightarrow |\frac{3}{2}|$) all overlap as indicated in the simulated data in Fig. 9, where the top spectrum is a spin $\frac{5}{2}$ lineshape with an η of 1 and the lower spectrum is the same except with an η of 0. One can see that for $\eta = 1$ there is significant overlap of intensity centered on the $\pm\frac{1}{2}$ transition. This becomes important for the investigation of quadrupolar metals in proteins, as each protein investigated thus far has exhibited a value of η_q of 1. In one sense this is helpful in that there is now one less parameter to optimize in simulating these lineshapes. However, in the case where there is low S/N or significant static

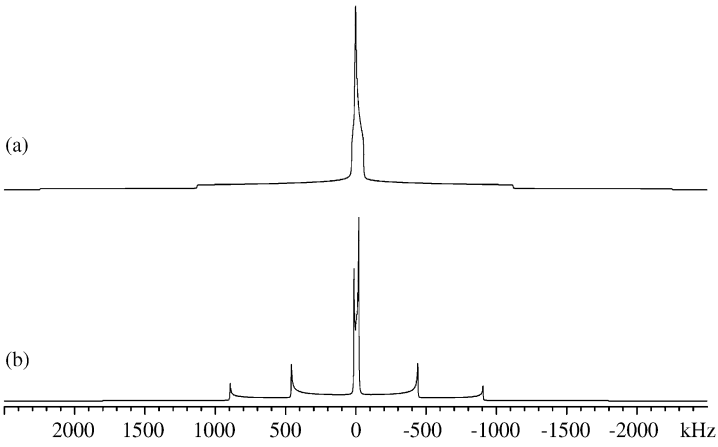

Fig. 9. Simulated spectra of a spin $\frac{5}{2}$ with a 6 MHz C_q with η of (a) 1.0 and (b) 0.0 at a 31.3 MHz resonance frequency (^{67}Zn at 11.7 T).

disorder, the edges of the central transition can be difficult to estimate inducing uncertainty in the extracted value of C_q. The question of selectivity further complicates these determinations as the outer transitions are also excited (even with selective pulses). The $\left|\frac{3}{2}\right| \leftrightarrow \left|\frac{1}{2}\right|$ transition has a Hartmann–Hahn match condition very close to the $\pm\frac{1}{2}$ transition.[69–72] Recall from the Hartmann–Hahn condition (Eqs. (5) and (6)) that the factor α for a $\frac{5}{2}$ spin (like ^{67}Zn or ^{25}Mg) is 3 for the $\pm\frac{1}{2}$ transition, however for the $\left|\frac{3}{2}\right| \leftrightarrow \left|\frac{1}{2}\right|$ transition this factor is $\sqrt{8}$. To analyze these data, an exact calculation was performed utilizing finite pulse widths and a complete density matrix. The results of that calculation demonstrated that the QCPMG train also populates the outer transitions even with selective π pulses. To simulate more closely how the experiment is actually performed the transmitter frequency in the simulation was moved every 20 kHz (from -200 to $+200$ kHz, and in coarser steps outside that range), a data set "acquired" using a QCPMG sequence (no CP), followed by a sky projection of the data to reconstruct it. The resulting simulation of a 10 MHz C_q is compared with a simulated lineshape of only the central transition in Fig. 10a.

Armed with the knowledge that the outer transitions of the ^{67}Zn (or other quadrupolar nuclides) can also be observed rather than simply the $\pm\frac{1}{2}$ transition, one can devise a strategy for distinguishing the desired $\pm\frac{1}{2}$ transition from any extraneous resonance(s)/features arising from the outer transitions (specifically the $\left|\frac{3}{2}\right| \leftrightarrow \left|\frac{1}{2}\right|$). The simplest method is to simulate the lineshape using only the central transition as in Fig. 10a and b and compare the width of the central portion of the lineshapes to see if the calculated spectrum adequately describes the breadth of this feature. If not (as in Fig. 10b) the likelihood is that the outer transitions are also being observed. The spectrum can also be acquired at higher field (i.e. from 9.4 to

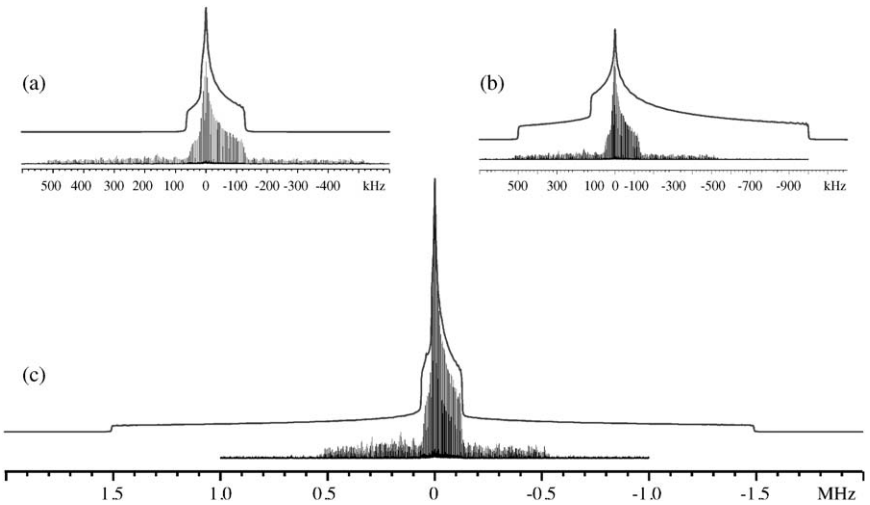

Fig. 10. Simulated stepped frequency QCPMG data with superimposed simulations of (a) $\pm\frac{1}{2}$ transition with C_q of 10 MHz, (b) $\pm\frac{1}{2}$ transition with C_q of 28 MHz, and (c) all the transitions of a C_q of 10 MHz at 11.7 T.

18.8 T), which allows the separation of the second-order quadrupolar lineshape from the first-order lineshape of the outer transitions. By doubling the field the central transition lineshape has half of the width of the lower field, while the $\left|\frac{3}{2}\right| \leftrightarrow \left|\frac{1}{2}\right|$ contribution remains the same (thus dropping in intensity relative to the central transition). If the comparison of the relative intensities (central peak vs. plateau) is invariant, then the outer transitions are not contributing.

The previous discussion for the most part only applies to metals in a protein; however, crystalline, small molecules are not constrained to any asymmetry parameter. Likewise, thus far there has been no mention of contributions from the shielding tensor. As a suggested strategy one should attempt to simulate the lineshape using only the quadrupole interaction, however if this is not satisfactory then two possibilities present themselves: namely chemical shielding anisotropy (CSA) or sample purity. To distinguish between these two options one has to make use of at least one more magnetic field (as large a difference from the first as possible). Owing to the linear nature of the field dependence of the CSA and the corresponding inverse dependence of the quadrupolar contributions to the lineshape, the utilization of multiple fields becomes necessary for disentangling each of the interactions and their relative orientations. If the lineshape does not follow the predicted field dependence then most likely is the presence of another species. This assumes one has performed the simulations accounting for finite pulse width effects and allowed for the presence of static disorder (especially in protein samples). As for sample purity there are again a few possibilities, such as impurities, phase transitions, reaction products, equilibrium states (such as a pH dependence), or non-specific binding. We leave it to the reader to determine the quality of their sample, however, the data can still be interpreted in the same manner if each species is distinct. The case of non-specific binding presents a further challenge as these species are not distinct and will often manifest as an ensemble of overlapping lineshapes that cannot be simulated.

2.5. Sample considerations

2.5.1. *Static disorder*

Setting aside the native disorder that exists within proteins,[73] low-temperature experiments are notorious for inducing problems associated with static disorder.[74] For a given value of I, the width of the quadrupole lineshape in our experiments is proportional to C_q^2/ω_0, where typical values of C_q can be tens of MHz. Hence, the disorder is being averaged in some fashion over an interaction that spans several MHz. This problem is less severe when compared to those observed in EPR spectroscopy. In this case the quantity being averaged is the electron spin spectrum, which can cover many GHz. The problem of *reducing* the consequences of static disorder in EPR spectroscopy has been solved. This was accomplished by utilizing a cryosolvent composed of 30% glycerol/water. There are still outstanding issues associated with the details of systems which benefit from annealing the frozen

solution or not, but the utilization of this solvent system has given us the best lineshapes we have observed for our protein systems. This cryosolvent has enabled us to be able to finally address issues associated with the separation and relative quantitation of multiple species within a given lineshape. This, in turn, has led us to be able to make sensible comments relative to stoichiometry, pK_a, and speciation.

2.5.2. *Non-specific binding: consequences and potential solutions*

As mentioned in Section 1, there is a key difference between Mg^{2+} and Zn^{2+}: namely the nature of the binding they have to their respective proteins. The binding constants for Zn^{2+} are usually reflective of tight binding, whereas for Mg^{2+} the binding is typically weak to modest. Such a difference has no consequences in an X-ray scattering experiment, because the experiment is sensitive to long-range order and as a result does not "see" the non-specifically bound Mg^{2+}. This is not the case in the NMR experiment, the experiment observes *all* of the Mg^{2+}. Hence, a strategy has to be developed to distinguish between specifically and non-specifically bound Mg^{2+}.

Non-specific binding can be thought of simply as an undesired background signal that must be removed. The typical method for removing a background signal is to have a blank sample that has the same measurements performed on it and the result is subtracted from the analyte. The challenge is to create a proper blank for this type of system. For Mg^{2+}-dependent proteins, the approach we have taken is to utilize site-specific mutations to remove all of the Mg^{2+}-binding sites of interest. The caveat is that the mutant protein should fold into a similar structure as the native protein such that no alternative metal-binding sites are created. In the case where a substrate is present in the analyte, the blank should also contain the substrate. For example, a DNA-binding protein should contain DNA in the blank as well (preferably bound in the same manner to the native protein). This ensures that the blank contains as many of the same non-specific binding opportunities as possible to mimic the analyte.

Once this proper blank has been identified then the spectroscopy proceeds as one might expect. The first stage is to obtain ^{25}Mg NMR spectra on each sample at the desired Mg^{2+} stoichiometry, pH, and if applicable substrate concentration. The difference spectrum should yield a spectrum consistent with Mg^{2+} bound to the site(s) of interest uncluttered by non-specific binding effects. This statement is true even in the presence of DNA as long as the blank contains the same DNA. Note that if the substrate is DNA then salting the DNA with high amounts of K^+ before adding the Mg^{2+} in sample preparation would be prudent. Recall that within the cell the relative amounts of K^+ to Mg^{2+} are ~4–5 and ~400 for free and bound, respectively.[75]

We illustrate this procedure using the protein alkaline phosphatase (AP). AP typically binds three metals (two Zn^{2+} and a Mg^{2+}), which are considered tightly bound and stable to dialysis. However, in the ^{25}Mg NMR spectrum there is also evidence for non-specifically bound Mg^{2+} that is distorting the center of the lineshape, shown in Fig. 11. The blank chosen in this example was the D153 H mutant,

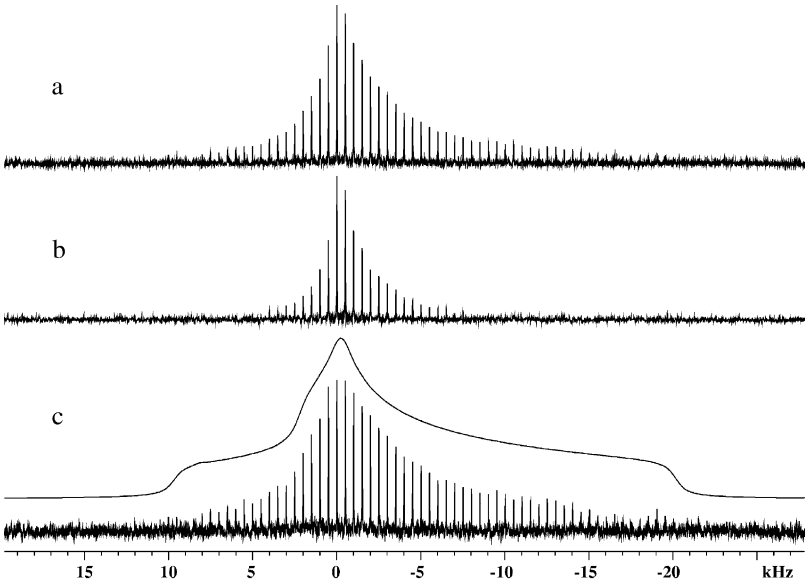

Fig. 11. ^{25}Mg NMR spectrum of (a) native AP at pH 7 in the presence of excess Mg^{2+}, (b) D153H mutant of AP, and (c) the difference spectrum. Superimposed on the difference spectrum is the fit (using ideal pulses) with a C_q of 3.59 ± 0.08 MHz.

which removes the critical residue for Mg^{2+} binding. One obvious distinction between the blank and the native protein's NMR spectrum is that the blank has a narrow lineshape compared with the analyte. This can be seen in Fig. 11 along with the difference spectrum.

To make this strategy work requires high S/N in both experiments. Further the difference entails an arbitrary amount of the blank to be subtracted from the analyte. This can only be determined empirically. There are obvious limits such as if negative resonances are generated in the difference spectrum. The reader will have to use judgment based on what is consistent with a theoretical lineshape. In a determination of an unknown stoichiometry at least an additional two experiments will need to be performed each at different loadings.

3. COUPLING SPECTROSCOPY WITH STRUCTURAL INFORMATION

We have seen in the previous sections a method for acquiring high-sensitivity data for half-integer quadrupolar nuclides as well as strategies for interpreting the results. These experiments allow a direct measurement of the quadrupole coupling constant, or the zz-element of the field-gradient tensor, however it is often difficult to interpret these results. What is needed is to bridge the gap between any structural

data and the NMR results. This can mean refining the structure with distance measurements or restraints generated from the introduction of dipolar couplings into the experiment. Analysis of dipolar-coupled spectra can lead to distance determination and orientations within the molecular frame. Further, as we have previously stated, the value of C_q is sensitive to the electrostatics around the nucleus in question. Utilizing molecular theory to contrast predicted C_q's of models of the system of interest, one can generate a comprehensive description of the center of interest. This includes determining the presence or absence of a charge in the coordination sphere or locating hydrogen-bonding networks. The following sections detail these methods for extracting or inferring structural information from the experiment.

3.1. Homonuclear dipolar couplings

Typical distance measurements by solid-state NMR methods are accomplished by means of a rotational double resonance experiment (REDOR).[76,77] This involves rotor-synchronized π pulses on the I-spins for varying cycles followed by the same experiments with synchronized π pulses on the S-spins. The two sets of experiments are subtracted to create a set of difference spectra, which decay based on the strength of the dipolar interaction. Similarly the same type of data sets can be created for a static case with a spin echo double resonance[78] (SEDOR) experiment. These two methods are effective for the case of a heteronuclear spin pair, but do not work for homonuclear coupling. Engelsberg and Yannoni[79] used a CPMG train to remove the inhomogeneous broadening while preserving the dipolar interaction. The tops of the echoes from the CPMG train are Fourier-transformed to give a Pake[80] doublet from which the internuclear distance can be inferred. This is analogous to homonuclear-coupled ^{1}H's displaying J-modulation of the time-domain response to a train of π pulses,[81] where the echo tops can be Fourier-transformed to recover the J-coupling between the spins. Engelsberg and Yannoni[79] also noted the presence of a spin lock component in their spectra. If the couplings are small this component can dominate the spectrum leading to an inability to measure the couplings.

Consider now this experiment applied to a pair of quadrupoles, for two like spins the truncated dipole–dipole Hamiltonian is given by

$$H_D^{\text{Trunc}} = -2D \cdot P_2(\cos\,\theta)\left[I_{1z}I_{2z} - \frac{1}{4}(I_1^+I_2^- + I_1^-I_2^+)\right]. \tag{13}$$

Here D is given by

$$D = \frac{\gamma_1\gamma_2}{r_{12}}h, \tag{14}$$

and

$$P_2(\cos\,\theta) = \frac{1}{2}(3\cos^2\theta - 1). \tag{15}$$

Using these terms and considering only the $\pm\frac{1}{2}$ transitions, the energy of the triplet states are given by

$$t_0 = \frac{1}{2} D \cdot P_2(\cos\ \theta)\left[\frac{5}{4} + I(I+1)\right]. \tag{16}$$

$$t_{\pm 1} = -\frac{1}{2} D \cdot P_2(\cos\ \theta). \tag{17}$$

Inclusion of the Zeeman energy leads to the following expressions for the total energy:

$$E_+ = \omega_0 - \frac{1}{2} D \cdot P_2(\cos\ \theta), \tag{18}$$

$$E_0 = \frac{1}{2} D \cdot P_2(\cos\ \theta)\left[\frac{5}{4} + I(I+1)\right], \tag{19}$$

$$E_- = -\omega_0 - \frac{1}{2} D \cdot P_2(\cos\ \theta). \tag{20}$$

Taking the differences $E_+ - E_0$ and $E_0 - E_-$, yields

$$E_+ - E_0 = \omega_0 - \frac{1}{2} D \cdot P_2(\cos\ \theta)\left[\frac{9}{4} + I(I+1)\right]. \tag{21}$$

and

$$E_0 - E_- = \omega_0 + \frac{1}{2} D \cdot P_2(\cos\ \theta)\left[\frac{9}{4} + I(I+1)\right]. \tag{22}$$

These differences represent the observed transitions for the lineshape, and the frequency difference between symmetry-related points (for example between the perpendicular horns) within the lineshape, Δ, is given by

$$\Delta = -D \cdot P_2(\cos\ \theta)\left[\frac{9}{4} + I(I+1)\right]. \tag{23}$$

If we select the perpendicular horns ($\theta = \pi/2$) and let $I = \frac{1}{2}$, we obtain the expected relationship that the separation between the perpendicular horns is given by $\frac{3}{2}D$. If rather we have I being a $\frac{5}{2}$ nuclide, the following interesting result is obtained: the distance between the perpendicular horns yields $\frac{11}{2}D$. That is, for the *same* coupling the splitting over that for the spin $\frac{1}{2}$ case has increased by a factor of $\frac{11}{3}$. This scaling of the dipolar splitting allows relatively small coupling to be interrogated for higher I values. For example, given a pair of ^{25}Mg spins ($I = \frac{5}{2}$) that are separated by 3.4 Å corresponding to $D = -11.47$ Hz the splitting would be ~63 Hz for the inner horns.

Another option presents itself with data of this type, why not simply transform the entire echo train. This can potentially give a wealth of information if the

couplings are resolved. Aside from the envelope of spikes retaining the shape of the inhomogeneous interaction; be it CSA, quadrupolar, or both, each side band will contain dipolar information as well as an orientation dependence. Taking all this information together orients the tensor information in the dipolar frame and by extension to the structure. In the case where couplings may not be resolvable the width of the spikes could be utilized to set a lower limit on the distance between two spins. This line broadening can be verified as dipolar coupling by repeating the experiment with a train of $\pi/2$ pulses following the initial echo, which serve to remove any dipolar interactions.[82,83] However, like the previous experiments this too suffers from a spin lock component that cannot be removed at this time.

3.2. Heteronuclear dipolar couplings

As mentioned above Engelsberg and Yannoni[79] noticed that homonuclear dipolar modulation could be seen in an echo train performed on compounds with ^{13}C–^{13}C coupling. In the heteronuclear case each π pulse refocuses this coupling, but as in a SEDOR experiment a π pulse on the coupled spin can restore it. Therefore, simultaneous π pulses in a QCPMG experiment should result in all the echoes being modulated by the dipolar interaction. The tops of each echo can be Fourier-transformed to give a direct measure of the dipolar coupling or as above the complete train could, in principle, be Fourier-transformed to give an envelope describing the powder pattern where each spike is split. The splitting of those peaks would contain the orientation dependence of the interaction measured in the dipolar frame. Fig. 12 depicts an expansion plot of a zinc spin coupled with a single nitrogen where the zinc has a C_q of 6.0 MHz, an η of 1.0, a dipolar coupling of 100 Hz (Zn–N distance of 1.97 Å) at a sampling of orientations indicated on each simulated spectrum. The angle β is the polar angle between the internuclear vector

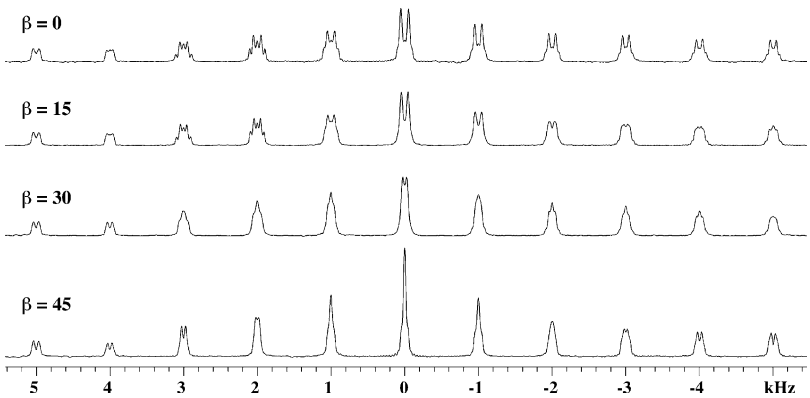

Fig. 12. Expansion plots of a dipolar recoupled ^{67}Zn QCPMG spectrum for a ^{67}Zn-^{15}N spin system with $C_q = 6.0$ MHz, $\eta = 1.0$, 100 Hz dipolar coupling, and a β dependence as indicated.

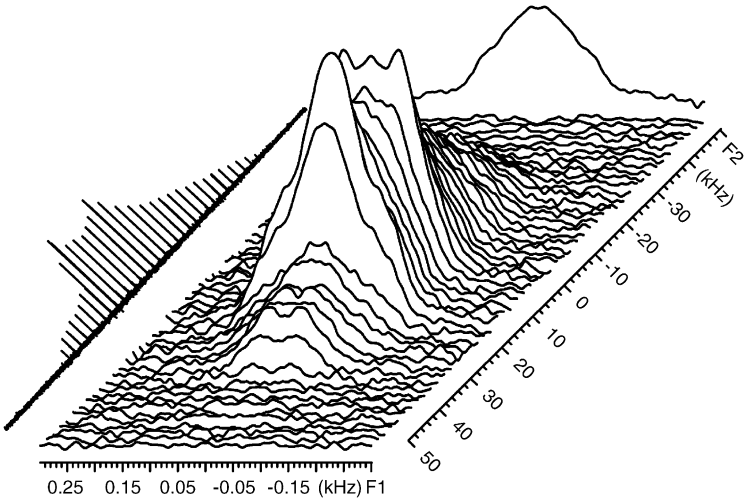

Fig. 13. 2D ^{67}Zn experiment correlating quadrupolar lineshape with dipolar coupling, DIPQUAD, for $ZnIm_2OAc_2$, collected at 21 T and room temperature.

and the V_{zz} element of the EFG tensor. A fit of this type of data would yield C_q as well as the angle and the internuclear distance.

While this data seems ideal to extract the information desired, there is a complication (also seen in the earlier work) in that the experimental data contains a spin lock component that cannot be removed at this time. However this information can be extracted if the experiment is extended in a second dimension in a separated local field (SLF)[84–87] experiment, such as a DIPSHIFT[88–90] or DIPQUAD[91–93] for quadrupolar nuclei. A preliminary version of this experiment on zinc diimidazole diacetate is shown in Fig. 13. The direct dimension shows the QCPMG spectrum and each spike corresponds to a dipolar splitting for those orientations compressed into that isochromat. The challenge in extracting the information for this experiment is the computational resources required in simulating the spin system. This model system has uniformly labeled imidazole, which adds the extra parameters (and dimensionality) of ^{15}N homonuclear couplings that must be taken into account. These computations are underway as well as a search for a method to selectively remove the unnecessary complexity of the homonuclear couplings.

3.3. Molecular theory

One can also utilize molecular theory to describe the system in question in an attempt to reconcile observed properties with structural questions. There will be no attempt here to compare available software packages, so the reader is free to make their own determination. What will be discussed in the following section is a variety of strategies that have proven useful in solving problems of various sizes. The ''simplest'' case is where a structure has been determined and a calculation is being

used to verify that theory can adequately describe the system (this proves useful for establishing confidence when working with unknowns). Another situation is trying to understand an unknown or partial structure, such as a derivative or reaction intermediate. The next type of case would be that of a lattice or periodic structure such as a surface. The last and potentially largest system to be described here is a protein molecule, which includes extensive hydrogen-bonding networks.

3.3.1. *Single point calculations*

In the case where a crystal structure is known (all atom positions determined) one can perform a single point calculation using the method of choice, restricted Hartree–Fock (RHF) or density functional theory (DFT). The size of the calculation will depend upon the number of atoms included as well as the size/quality of the basis set. The reader should be prepared to run several single point calculations to calibrate the dependence on these factors. When calculating NMR properties the property should converge with increasing complexity of the basis set utilized. There is also the caveat that the calculation is in fact a gas-phase simulation and there could be interactions with next nearest neighbors that must be accounted for.

There are several alternatives to perform the calculations. Assume for the moment that the X-ray structure provides the positions of the hydrogen as well as the heavy atoms. Then calculations can be performed on the X-ray geometry and compared to that where the geometry has been optimized via an *ab initio* method. If the structure does not provide the positions of the protons, then usually they can be added but the geometry must then be optimized. Here again there are choices, the geometry can be optimized for all of the atoms or simply the proton positions can be optimized. Again, the reader is advised to perform several such calculations to gain confidence, to determine which method is better for your own systems. Generally, the basis set used for the geometry optimization is not the same as used for the property calculation. That is, for geometry optimization a basis set at the so-called double-ζ is sufficient while a property calculation should be performed at the triple-ζ level.

As an example consider the molecule zinc tetrakis thiophenol, $Zn[SC_6H_5]_4[N(CH_3)_4]_2$, which has a known structure.[94] The solid-state ^{67}Zn NMR spectrum was measured at ambient temperature in a 21 T magnetic field and C_q was found to be 4.00 ± 0.05 MHz, with an η of 0.59 ± 0.02, as well as a contribution from the shielding tensor.[95] The EFG tensor was calculated from *ab initio* methods using RHF as well as DFT with the exchange-correlation functional defined as the local spin density approximation (LSDA or LDA) utilizing Slater's local spin density exchange[96] and the VWN V local spin density correlation functional,[97] as well as Becke's[98] three parameter hybrid functional using the Lee, Yang, and Parr (LYP) correlation functional,[99] B3LYP. All of the calculations were performed using either of two triple-ζ basis sets,[100,101] and the results are listed in Table 2. Note that it is not until the next nearest counterions were included that C_q and η both approach the experimental values (at least for the LDA method). Even at this level it would seem that there is more that could be included to accurately represent the system.

Table 2. Predicted quadrupole parameters for $Zn(SPh)_4$ using molecular theory

Complex	Basis[a]	Method	C_q	η_q
$Zn(SPh)_4$ (−2)	Ahlrichs VTZ[100]	RHF	6.475	0.675
$Zn(SPh)_4$ (−2)	Ahlrichs VTZ	DFT/LDA	−4.505	0.830
$Zn(SPh)_4$ (−2)	Ahlrichs VTZ	DFT/B3LYP	4.849	0.915
$Zn(SPh)_4$ (−2)	Ahlrichs TZV[101]	RHF	6.219	0.721
$Zn(SPh)_4$ (−2)	Ahlrichs TZV	DFT/LDA	−4.507	0.781
$Zn(SPh)_4$ (−2)	Ahlrichs TZV	DFT/B3LYP	4.718	0.973
$Zn(SPh)_4[NMe_4]_2$	Ahlrichs VTZ	RHF	9.108	0.409
$Zn(SPh)_4[NMe_4]_2$	Ahlrichs VTZ	DFT/LDA	7.751	0.360
$Zn(SPh)_4[NMe_4]_2$	Ahlrichs VTZ	DFT/B3LYP	8.153	0.432
$Zn(SPh)_4[NMe_4]_2$	Ahlrichs TZV	RHF	8.723	0.417
$Zn(SPh)_4[NMe_4]_2$	Ahlrichs TZV	DFT/LDA	7.516	0.381
$Zn(SPh)_4[NMe_4]_2$	Ahlrichs TZV	DFT/B3LYP	7.908	0.445
$Zn(SPh)_4[NMe_4]_6$ (+4)	Ahlrichs VTZ	RHF	6.065	0.744
$Zn(SPh)_4[NMe_4]_6$ (+4)	Ahlrichs VTZ	DFT/LDA	−3.848	0.638
$Zn(SPh)_4[NMe_4]_6$ (+4)	Ahlrichs VTZ	DFT/B3LYP	−4.261	0.939
$Zn(SPh)_4[NMe_4]_6$ (+4)	Ahlrichs TZV	RHF	5.665	0.796
$Zn(SPh)_4[NMe_4]_6$ (+4)	Ahlrichs TZV	DFT/LDA	−3.701	0.652
$Zn(SPh)_4[NMe_4]_6$ (+4)	Ahlrichs TZV	DFT/B3LYP	−4.126	0.934

[a]See Refs. 100 and 101 for the definitions of the basis sets; these calculations employed the polarization functions defined within the reference.

This example merely underscores the importance of utilizing all of the information at hand when attempting to contrast theory with experiment to understand the electrostatics present.

3.3.2. *Periodic systems*

When dealing with a periodic or polymeric system the approach taken by Zhang *et al.*[102] seems effective and straightforward to implement with available packages. The method, self-consistent charge field perturbation (SC-CFP), involves treating the first coordination sphere as real atoms, while the next set of the repeating monomer units are reduced to point charges. These point charges are Mulliken charges computed from the first coordination shell. The process is iterated until the calculated point charges converge to within 0.01*e*. This can be done in the context of a unit cell as well, with the next nearest neighbor molecules treated as point charges.

Another way to treat a solid is to make use of the periodic nature of the unit cell using the full-potential linearized-augmented plane wave (LAPW or FLAPW) bandstructure method.[103–105] The method consists of dividing the unit cell into two parts, atomic spheres and an interstitial region. The interstitial part has the wavefunctions expanded into plane waves and inside the spheres the plane waves are augmented with a linear combination of radial functions and an atomic-like spherical harmonics expansion as well as ''local orbitals''.

3.3.3. *Proteins*

The difficulty in protein systems lies in the sheer magnitude of the calculation. The number of atoms makes a complete calculation with a decent size basis set impractical. There are a few options that can be explored depending upon whether the answer desired is qualitative or quantitative. The first choice is to build a model of the active site trying to include the minimal number of atoms to mimic the active site of interest. This usually involves steps, such as replacing histidine with methyl imidazole or aspartic acid with acetic acid and so on. A geometry optimization with a modest basis set followed by a property calculation on the converged geometry with a larger basis set will give a qualitative number for C_q. By making small changes, such as replacing water with hydroxide, and repeating the calculation one can predict trends that might be observed experimentally.

Another method is to trim the protein around the desired metal site to include only the residues of interest. However, the question here is how much does one need to include to adequately describe the system. One must take into account not just the first coordination sphere, but the hydrogen-bonding interactions of at least the second coordination sphere as well as any residues or substrates that are also implicated in any reaction chemistry. Having a complete set of coordinates for a protein is also a challenge as proton positions are usually not determined from X-ray crystallography and solution NMR structures do not see the metals. It can be utilized as a starting point with the understanding that an optimization/minimization of some kind will be required before proceeding to a high-level property calculation. Depending on the number of atoms in the trimmed down system even a cheap basis optimization may take several weeks of CPU time. An alternative is to utilize a force field minimization and/or a molecular dynamics run with the system solvated in water. This model should closely approximate the complete native system.

A final alternative is to utilize a similar methodology used in the periodic systems above where most of the external system is reduced to point charges. This method is referred to as combined or hybrid quantum mechanics and molecular mechanics or QM/MM.[106–109] The strategy is basically the same as the previous one where the protein is minimized using force fields such as AMBER, the desired region is defined as quantum and the rest of the protein is reduced to point charges. This can be followed by further minimizations/optimizations or again the triple-ζ property calculation. We are currently exploring this type of method in our laboratory where we are varying the size of the quantum region.

4. SUMMARY AND CONCLUSIONS

In Section 1, we raised some questions relative to the electrostatics around a metal site in a metalloprotein, i.e. can a determination of the pK_a be made on Zn^{2+}-bound water in a resting enzyme? From the perspective of a chemist, central to this question is the ability to distinguish and contrast the difference between charged and

neutral ligands, the classic example is water vs. hydroxide. The spectroscopy should enable the determination of the relative amounts of the Zn-OH_2 and Zn-OH forms in the protein of interest, enabling the *direct* determination of the pK_a of the bound water on the Zn^{2+}. Such an observation allows the testing and verification of the central paradigm of Zn^{2+} metallobiochemistry for hydrolytic enzymes, namely that Zn^{2+} significantly lowers the pK_a of the bound water from a value of nominally 14 to values that are appropriate for physiological environments. Such an experiment has not been accomplished before and this represents an important and unique contribution by this form of NMR spectroscopy.

The potential to determine the pK_a for the bound water of a Zn^{2+} was the driving motivation for our initial experiments on human CA.[110] The proposed mechanism of action of CA has been extensively reviewed,[111] and can be summarized as water bound to Zn^{2+} as a tris-imidazole Zn(II) aquo species, which loses a proton to form the corresponding hydroxide. This species, in turn, reacts with

$$[EZnOH]^{1+} \underset{CO_2}{\rightleftharpoons} [EZnHCO_3]^{1+} \underset{H_2O}{\rightleftharpoons} [EZnOH_2]^{2+} + HCO_3^-$$

CO_2 forming bicarbonate bound to Zn^{2+}. This bicarbonate then reacts with water to reform the Zn^{2+}-bound water displacing the bicarbonate as a product. The catalytic cycle then continues. We examined the pH dependence of the ^{67}Zn NMR spectrum and found, in contrast to what would be expected, no pH dependence. From a comparison with electronic structure calculations, the data was consistent with hydroxide bound to the Zn^{2+} over a range of pH values from 5 to 9. No experimental evidence was found for the presence of bound water. These observations lent support for an alternative mechanism of action of CA originally put forth by Merz *et al.*[112] In this mechanism, water is never bound to Zn^{2+} in the absence of CO_2, consistent with our experimental observations.

Theory played a significant role in the analysis of our experimental data, in so much as the theory correctly predicted the value of C_q for the Zn^{2+} with bound OH^- (8.7–10.4 MHz) compared to the experimental value of 10 MHz. Theory also predicted a value of C_q for Zn^{2+} with water bound to be in the range 25–35 MHz. We had sufficient sensitivity to observe such a coupling, yet it was not observed. The level of theory utilized in these calculations was not as sophisticated as we would employ now or what was described above. We are in the process of re-examining those calculations employing a more realistic model for the active site of CA to further explore the rationale for the lack of observed pH dependence for the ^{67}Zn NMR spectroscopy. Further, we are planning additional experiments on CA and some of its mutants.

In summary, we have presented a detailed description of the low-temperature solid-state NMR experiment, which enables a unique perspective of the metal sites in metalloproteins. This experiment provides complementary information to that extracted from X-ray diffraction experiments. We are currently addressing the questions (and others) posed above. Although we have discussed these experiments in terms of Mg^{2+} and Zn^{2+} chemistry, the methods are more general and are

applicable to any system, which is amenable to cryogenic temperatures and a polarization-transfer experiment.

ACKNOWLEDGMENTS

The authors would like to express their gratitude to the members of the magnetic resonance group and members of their Environmental Molecular Sciences Laboratory (EMSL) for their encouragement and support. In particular we would like to acknowledge the many stimulating discussions with Drs. M. Bowman, H. Cho, and R. Wind. Likewise, we are grateful for the superb technical assistance of J. Sears. The research summarized here was supported in part by the NIH through GM 26295 and EB 002050, the DOE by KP-01-01 24931 and 41055, and the EMSL operations budget. Some of the research described here was performed in the EMSL (a national scientific user facility sponsored by the Biological and Environmental Research Directorate of the DOE) located at Pacific Northwest National Laboratory and operated by Battelle for the DOE.

REFERENCES

1. P. D. Ellis, *Science*, 1983, **221(4616)**, 1141–1146.
2. M. F. Summers, *Coord. Chem. Rev.*, 1988, **86**, 43–134.
3. P. Gettins and J. E. Coleman, *Fed. Proc.*, 1982, **41(13)**, 2966–2973.
4. J. E. Coleman, *Curr. Opin. Chem. Biol.*, 1998, **2(2)**, 222–234.
5. K. A. McCall, C. C. Huang and C. A. Fierke, *J. Nutr.*, 2000, **130(5)**, 1437S–1446S.
6. J. J. R. F. da Silva and R. J. P. Williams, *The Biological Chemistry of the Elements. The Inorganic Chemsitry of Life*, 1st ed., Oxford University Press, New York, 1991.
7. R. H. Holm, P. Kennepohl and E. I. Solomon, *Chem. Rev.*, 1996, **96(7)**, 2239–2314.
8. S. J. Lippard and J. M. Berg, *Principles of Bioinorganic Chemistry*, 1st ed., University Science Books, Mill Valley, CA, 1994, 411.
9. J. A. Cowan, *Biometals*, 2002, **15**, 225–235.
10. K. E. Hightower and C. A. Fierke, *Curr. Opin. Chem. Biol.*, 1999, **3**, 176–181.
11. R. G. Matthews and C. W. Goulding, *Curr. Opin. Chem. Biol.*, 1997, **1(3)**, 332–339.
12. J. E. Penner-Hahn, *Ind. J. Chem. Sect. A – Inorg. Bio-Inorg. Phys. Theor. Anal. Chem.*, 2002, **41(1)**, 13–21.
13. The term "low-gamma" is not well defined. Within the context of the discussions here we mean those nuclei with a gyromagnetic ratio, such that the ratio of the proton resonance frequency to that of the nucleus in question is greater than 10.
14. H. Pelletier, M. R. Sawaya, A. Kumar, S. H. Wilson and J. Kraut, *Science*, 1994, **264(5167)**, 1891–1903.
15. W. A. Beard and S. H. Wilson, *Structure*, 2003, **11**, 489–496.
16. W. A. Beard and S. H. Wilson, *Chem. Rev.*, 2006, **106(2)**, 361–382.
17. M.H. Cohen, and F. Reif, *Solid-State Physics*, F. Seitz and D. Turnbull, eds., New York: Academic Press, 1957, **5**.
18. P. Styles, N. F. Soffe, D. A. Scott, R. Cragg, D. J. White and P. C. White, *J. Magn. Reson.*, 1984, **60**, 397.
19. P. Styles and N. F. Soffe, *J. Magn. Reson.*, 1989, **84**, 376.
20. Y. W. Kim, W. L. Earl and R. E. Norberg, *J. Magn. Reson.*, 1995, **Series A 116**, 139–144.
21. The models we employ are Oxford Instruments CF-1200 and Spectrostat CF DY cryostats.

22. A. Samoson, T. Tuherm, J. Past, A. Reinhold, T. Anupold and I. Heinmaa, *Topics in Current Chemistry*. Springer, Berlin, 2004, **246**, 15–31.
23. A. S. Lipton, J. A. Sears and P. D. Ellis, *J. Magn. Reson.*, 2001, **151(1)**, 48–59.
24. A. S. Lipton, R. W. Heck, J. A. Sears and P. D. Ellis, *J. Magn. Reson.*, 2004, **168(1)**, 66–74.
25. All of the capacitors are manufactured by Voltronics (www.voltronics.com); the specific part numbers for the capacitors we employ are summarized as: The 1H channel — Tune: NMKT10-HVK Match: NMKT25-HVK, The X and Y channels — Tune and Match: NMCD-5CK.
26. The interested reader should consult the following web site for more details: http://www.lakeshore.com/temp/sen/crtd.html.
27. Using such low power can potentially introduce another experimental problem‘; namely amplifier stability. Most amplifiers for solid-state NMR experiments are designed to be operated at several hundred watts of power. A small variation in input voltage will normally have little consequences on the output power. However, at such low powers the amplifier is being operated outside of its normal input power regime. As a result a small fluctuation in input voltage can produce a large change in the output power shifting the experiment off a cross-polarization condition or simply providing an unexpected result such as an arc. The important message here is to make sure amplifiers have been stabilized.
28. A. Pines, M. G. Gibby and J. S. Waugh, *J. Chem. Phys.*, 1972, **56**, 1776.
29. A. Pines, M. G. Gibby and J. S. Waugh, *J. Chem. Phys.*, 1973, **59(2)**, 569–590.
30. A. S. Lipton, T. A. Wright, M. K. Bowman, D. L. Reger and P. D. Ellis, *J. Am. Chem. Soc.*, 2002, **124(20)**, 5850–5860.
31. S. Trofimenko, *J. Am. Chem. Soc.*, 1967, **89(24)**, 6288–6294.
32. R. Alsfasser, S. Trofimenko, A. Looney, G. Parkin and H. Vahrenkamp, *Inorg. Chem.*, 1991, **30(21)**, 4098–4100.
33. G. Parkin, *Chem. Rev.*, 2004, **104(2)**, 699–767.
34. G. Parkin, *Chem. Commun.*, 2000, **20**, 1971–1985.
35. A. S. Lipton, C. Bergquist, G. Parkin and P. D. Ellis, *J. Am. Chem. Soc.*, 2003, **125(13)**, 3768–3772.
36. R. A. Wind, S. Emid, D. J. Ligtghelm and J. F. J. M. Pourquie, *Bull. Magn. Reson.*, 1984, **6**, 71–88.
37. S. R. Hartmann and E. L. Hahn, *Phys. Rev.*, 1962, **128(5)**, 2042–2053.
38. M. Goldman, *The International Series of Monographs on Physics*, W.a.W. D. H. Marshall, ed., Oxford at the Clarendon Press, Oxford, 1970, 246.
39. A. G. Redfield, *Phys. Rev.*, 1955, **98(6)**, 1787–1809.
40. C. P. Slichter and W. C. Holton, *Phys. Rev.*, 1961, **122(6)**, 1701–1708.
41. A. G. Anderson and S. R. Hartmann, *Phys. Rev.*, 1962, **128(6)**, 2023–2041.
42. W. I. Goldburg, *Phys. Rev.*, 1962, **128(4)**, 1554–1561.
43. A. Pines, J. J. Chang and R. G. Griffin, *J. Chem. Phys.*, 1974, **61(3)**, 1021–1030.
44. A. Pines and T. W. Shattuck, *J. Chem. Phys.*, 1974, **61(3)**, 1255–1256.
45. J. -S. Lee and A. K. Khitrin, *J. Magn. Reson.*, 2005, **177(1)**, 152–154.
46. M. Mehring, *Principles of High Resolution NMR in Solids*, 2nd ed., Springer, Berlin, 1983, 342.
47. Z. Yao, H. -T. Kwak, D. Sakellariou, L. Emsley and P. J. Grandinetti, *Chem. Phys. Lett.*, 2000, **327**, 85–90.
48. R. W. Schurko, I. Hung and C. M. Widdifield, *Chem. Phys. Lett.*, 2003, **379**, 1–10.
49. E. V. Veenendaal, B. H. Meier and A. P. M. Kentgens, *Mol. Phys.*, 1998, **93(2)**, 195–213.
50. A. P. M. Kentgens and R. Varhagen, *Chem. Phys. Lett.*, 1999, **300**, 435–443.
51. D. Iuga, H. Schafer, R. Verhagen and A. P. M. Kentgens, *J. Magn. Reson.*, 2000, **147**, 192–209.
52. R. Siegal, T. Nakashima and R. E. Wasylishen, *Concepts Magn. Reson. Part A*, 2005, **26A(2)**, 47–61.
53. R. A. Wind, M. J. Duijvestijn, C. V. D. Lugt, A. Manenschijn and J. Vriend, *Prog. Nucl. Magn. Reson. Spectrosc.*, 1985, **17(3)**, 33–67.
54. J. H. Ardenkjaer-Larsen, B. Fridlund, A. Gram, G. Hansson, L. Hansson, M. H. Lerche, R. Servin, M. Thaning and K. Golman, *Proc. Natl. Acad. Sci. U.S.A.*, 2003, **100**, 10158–10163.
55. E. L. Hahn, *Phys. Rev.*, 1950, **80(4)**, 580–594.
56. A. M. Portis, *Phys. Rev.*, 1953, **91(5)**, 1071–1078.

57. H. Y. Carr and E. M. Purcell, *Phys. Rev.*, 1954, **94(3)**, 630–638.
58. S. Meiboom and D. Gill, *Rev. Sci. Instrum.*, 1958, **29(8)**, 688–691.
59. F. H. Larsen, H. J. Jakobsen, P. D. Ellis and N. C. Nielsen, *Mol. Phys.*, 1998, **95(6)**, 1185–1195.
60. S. Kroeker and R. E. Wasylishen, *Can. J. Chem.*, 1999, **77(11)**, 1962–1972.
61. P. R. Bodart, J. -P. Amoureux, Y. Dumazy and R. Lefort, *Mol. Phys.*, 2000, **98(19)**, 1545–1551.
62. J. V. Hanna, A. S. Lipton, and G. A. Bowmaker. Manuscript in preparation.
63. J. T. Cheng, J. C. Edwards and P. D. Ellis, *J. Phys. Chem.*, 1990, **94(2)**, 553–561.
64. J. M. Koons, E. Hughes, H. M. Cho and P. D. Ellis, *J. Magn. Reson. Series A*, 1995, **114(1)**, 12–23.
65. T. Vosegaard, J. Skibsted, H. Bildsoe and H. J. Jakobsen, *J. Magn. Reson. Series A*, 1996, **122(2)**, 111–119.
66. J. C. Hoch and A. S. Stern, *NMR Data Processing*, Wiley, New York, NY, 1996.
67. W. E. Hull, Two-Dimensional NMR Spectroscopy: Applications for Chemists and Biochemists, W. R. Croasmun, R. M. K. Carlson, eds., *VCH Publishers*, New York, NY, 1994.
68. J. Z. Hu and R. A. Wind, *J. Magn. Reson.*, 2003, **163**, 149–162.
69. S. Vega, *Phys. Rev. A*, 1981, **23(6)**, 3152–3173.
70. T. H. Walter, G. L. Turner and E. Oldfield, *J. Magn. Reson.*, 1988, **76(1)**, 106–120.
71. R. K. Harris and G. J. Nesbitt, *J. Magn. Reson.*, 1988, **78(2)**, 245–256.
72. A. J. Vega, *Solid State NMR*, 1992, **1(1)**, 17–32.
73 W. Min, B. P. English, G. Luo, B. J. Cherayil, S. C. Kou and X. S. Xie, *Acc. Chem. Res.*, 2005, **38**, 923–931.
74. R. W. Martin and K. W. Zilm, *J. Magn. Reson.*, 2003, **165**, 162–174.
75. M. E. Maguire and J. A. Cowan, *Biometals*, 2002, **15**, 203–210.
76. T. Gullion and J. Schaefer, *J. Magn. Reson.*, 1989, **81**, 196–200.
77. T. Gullion and J. Schaefer, *Advances in Magnetic Resonance*, W. S. Warren, ed., Academic Press, San Diego, CA, 1989, 57–83.
78. D. E. Kaplan and E. L. Hahn, *J. Phys. Radium.*, 1958, **19**, 821.
79. M. Engelsberg and C. S. Yannoni, *J. Magn. Reson.*, 1990, **88**, 393–400.
80. G. E. Pake, *J. Chem. Phys.*, 1948, **16(4)**, 327–336.
81. R. Freeman, *Spin Choreography*, Oxford University Press, Oxford, Chapter 4, 1998.
82. J. S. Waugh and C. H. Wang, *Phys. Rev.*, 1967, **162(2)**, 209–216.
83. R. Siegel, T. Nakashima and R. W. Wasylishen, *J. Phys. Chem. B*, 2004, **108**, 2218–2226.
84. J. S. Waugh, *Proc. Natl. Acad. Sci. U.S.A.*, 1976, **73(5)**, 1394–1397.
85. R. K. Hester, J. L. Ackerman, B. L. Neff and J. S. Waugh, *Phys. Rev. Lett.*, 1976, **36(18)**, 1081–1083.
86. E. F. Rybaczewski, B. L. Neff, J. S. Waugh and J. S. Sherfinski, *J. Chem. Phys.*, 1977, **67(3)**, 1231–1236.
87. M. Linder, A. Hohener and R. R. Ernst, *J. Chem. Phys.*, 1980, **73(10)**, 4959–4970.
88. M. G. Munowitz, R. G. Griffin, G. Bodenhausen and T. H. Huang, *J. Am. Chem. Soc.*, 1981, **103(10)**, 2529–2533.
89. M. Munowitz, W. P. Aue and R. G. Griffin, *J. Chem. Phys.*, 1982, **77(4)**, 1686–1689.
90. M. G. Munowitz and R. G. Griffin, *J. Chem. Phys.*, 1982, **76(6)**, 2848–2858.
91. E. R. H. van Eck and M. E. Smith, *J. Chem. Phys.*, 1998, **108(14)**, 5904–5912.
92. J. Grinshtein, C. V. Grant and L. Frydman, *J. Am. Chem. Soc.*, 2002, **124(45)**, 13344–13345.
93. J. Grinshtein and L. Frydman, *J. Am. Chem. Soc.*, 2003, **125(24)**, 7451–7460.
94. H. Zaima, N. Ueyama, H. Adachi and A. Nakamura, *Biopolymers*, 1995, **35(3)**, 319–329.
95. A. S. Lipton and P. D. Ellis, manuscript in preparation.
96. J.C. Slater *Quantum Theory of Molecular Solids*, Vol. 4, McGraw-Hill, New York, NY, 1974.
97. S. H. Vosko, L. Wilk and M. Nusair, *Can. J. Phys.*, 1980, **58(8)**, 1200–1211.
98. A. D. Becke, *J. Chem. Phys.*, 1993, **98**, 5648.
99. C. Lee, W. Yang and R. G. Parr, *Phys. Rev. B*, 1988, **37**, 785.
100. A. Schafer, H. Horn and R. Ahlrichs, *J. Chem. Phys.*, 1992, **97(4)**, 2571–2577.
101. A. Schafer, C. Huber and R. Ahlrichs, *J. Chem. Phys.*, 1994, **100(8)**, 5829–5835.
102. Y. Zhang, S. Mukherjee and E. Oldfield, *J. Am. Chem. Soc.*, 2005, **127(8)**, 2370–2371.

103. P. Blaha, K. Schwarz and P. Herzig, *Phys. Rev. Lett.*, 1985, **54(11)**, 1192–1195.
104. P. Blaha, K. Schwarz, W. Faber and J. Luitz, *Hyperfine Interact.*, 2000, **126(1–4)**, 389–395.
105. K. Schwarz, P. Blaha and G. K. H. Madsen, *Comput. Phys. Comm.*, 2002, **147(1)**, 71–76.
106. A. Warshel and M. Levitt, *J. Mol. Biol.*, 1976, **103(2)**, 227–249.
107. U. C. Singh and P. A. Kollman, *J. Comput. Chem.*, 1986, **7(6)**, 718–730.
108. A. Warshel, *Computer Modeling of Chemical Reactions in Enzymes and Solutions*, Wiley, New York, 1997, 256.
109. J. Gao, *Reviews in Computational Chemistry*, K. B. Lipkowitz and D. B. Boyd, eds., VCH Publishers, New York, NY, 1995, 119–185.
110. A. S. Lipton, R. W. Heck and P. D. Ellis, *J. Am. Chem. Soc.*, 2004, **126(14)**, 4735–4739.
111. D. W. Christianson and C. A. Fierke, *Acc. Chem. Res.*, 1996, **29(7)**, 331–339.
112. K. M. Merz, R. Hoffmann and M. J. S. Dewar, *J. Am. Chem. Soc.*, 1989, **111(15)**, 5636–5649.
113. P. Pyykko, *Z. Naturfors. Sect. A – J. Phys. Sci.*, 1992, **47(1–2)**, 189–196.
114. P. Pyykko, *Mol. Phys.*, 2001, **99(19)**, 1617–1629.
115. M. Bak, J. Rasmussen and N. C. Nielsen, *J. Magn. Reson.*, 2000, **147**, 262–275.

NMR Methods for Characterising Ligand-Receptor and Drug–Membrane Interactions in Pharmaceutical Research

DAVID A. MIDDLETON

Faculty of Life Sciences, University of Manchester, Sackville Street, Manchester M60 1QD, UK

A common strategy in drug discovery is to identify small molecules that interact with a specific target receptor and then to perform iterations of structural optimisation to produce high-affinity lead compounds to progress into pre-clinical development. The last decade has witnessed the development of several sensitive,

ANNUAL REPORTS ON NMR SPECTROSCOPY
VOLUME 60 ISSN 0066 4103
DOI 10.1016/S0066-4103(06)60002-1

high-throughput NMR that have helped to rejuvenate NMR as a valuable tool for screening and characterising receptor-ligand interactions in the early stages of the drug discovery process. This chapter highlights the recent advances in NMR methods and technology that are now being implemented widely in pharmaceutical research for probing receptor-ligand interactions, and describes some of the emerging techniques that promise to be of value in the future. The NMR methods reviewed fall conveniently into two broad categories, namely, methods that detect the ligands and methods that observe the receptor target. Most of these methods can be implemented on conventional liquid-state spectrometers, but this chapter also draws attention to some recent examples of how solid-state NMR methods are providing information about ligand interactions with insoluble protein targets such as membrane-embedded receptors. It is also shown how NMR methods for characterising drug-membrane interactions are also proving useful in the structural optimisation of pharmaceutical lead compounds, as drug lipophilicity has implications for absorption, distribution and metabolism. The range of methods and their applications covered in this review, although not exhaustive, provide testament to the versatility of NMR, an advantage that will help to secure its future as an important and evolving technique in drug discovery.

1. INTRODUCTION

1.1. Drug discovery

Modern drug discovery is a multidisciplinary and technology-driven process that draws upon a wide range of chemical and biological methods with the goal of identifying drug candidates to progress to preclinical development and, ultimately, to the patient. The search for pharmaceutical leads involves screening numerous chemical compounds in animal models of disease or cell- or target-based bioassays, to assess their biological and pharmacological activity against a set of predefined criteria. Recent technological advances in bioassay development have yielded a variety of sophisticated methods for identifying synthetic ligands of a specific biomolecular target protein or polynucleotide with high throughput and sensitivity. When these methods are combined with parallel organic synthesis, vast numbers of compounds can be screened for ligand activity in a fraction of the time taken 20 years ago. Lead compounds may be identified serendipitously by cross-screening compounds from existing corporate repositories.[1] An increasingly attractive, and potentially more effective, strategy is to screen small drug-like fragments to identify weakly binding ligands, which are structurally optimised to generate high-affinity leads for further refinement.[2]

In the midst of the technological improvements brought about within bioassay development and high-throughput screening, NMR has maintained a presence as a valuable tool for drug discovery that has adapted well to the evolving strategies and priorities for drug discovery. The versatility and adaptability of NMR has rekindled interest in the technique as an attractive complementary tool that can contribute to the many different stages of the drug-discovery process, from screening weak

receptor–ligand interactions through to the structural assessment of receptor–ligand complexes and the detection of biomarkers of disease. In particular, the ability of NMR to provide information about how ligands interact with a target receptor is a valuable asset that can help to guide the medicinal chemistry towards compounds with a higher target affinity.

This review will give an account of some recent developments in NMR, many of which have become part of the standard repertoire in pharmaceutical research, and will also describe some of the emerging techniques that promise to be of value for identifying high-affinity lead compounds. The content of the review focuses specifically on the NMR methods for screening and characterising receptor–ligand interactions, although the utility of NMR clearly extends far beyond this particular application. The chapter is organised into sections reviewing methods that observe the ligand and methods that observe the receptor target. A sizeable section of the review reflects the mounting interest and the considerable recent advances in solid-state NMR, which is emerging as a tool for drug discovery owing to its ability to provide information about membrane protein targets and amyloidogenic proteins. Finally, a section is included that reviews some recent NMR methods for characterising drug–membrane interactions. The structural optimisation of lead compounds often involves increasing lipophilicity to exploit hydrophobic contacts[3] and interactions between lipophilic drug candidates and cellular membranes can have either deleterious or advantageous effects on the efficacy of the drug. The chapter leaves aside the vast field of metabolomics and the NMR analysis of biofluids, which has become a widely used approach for identifying markers of disease and for monitoring temporal changes in response to treatment of animal models with drug candidates. Current perspectives on this latter application of NMR can be found in recent reviews.[4,5]

1.2. NMR methods for ligand screening and characterisation

The primary screening of a library of chemical compounds for biological activity usually utilises a range of molecular- or cellular-level assays or involves assessment of *in vivo* efficacy in a suitable animal model. Molecular-level assays may rely on the compound(s) having some observable effect upon the behaviour of the target biomolecule. In other cases, the assay detects the interaction between the target biomolecule and the compounds, for example by monitoring changes in fluorescence or by using microcalorimetry, ELISA, Biacore or immunoblotting techniques. Often none of these approaches is satisfactory, either because the target (or ligand) lacks a suitable probe such as a fluorophore with which to detect the interaction between them, or because the interaction is too weak to observe. As a result, ligands that bind to a target with micromolar or millimolar affinities may not be detected in the early stages of drug discovery and potential drug candidates may be overlooked.

NMR is ideally suited to detecting weak receptor–ligand interactions and, indeed, many of the experiments described in the following sections work best when the

ligand has micromolar- or millimolar-binding affinities for the target.[6,7] A variety of solution-state ^{1}H NMR methods have been developed to identify synthetic ligands of specific targets and for providing quantitative information about binding affinities, the location of binding sites and the structure of the receptor–ligand complex formed. These methods can be roughly divided into two categories, namely, those that observe the ligand and those that observe the receptor. Ligand-observed NMR screening methods are attractive and cost-effective in the early stages of drug discovery since they do not demand the preparation of isotopically labelled receptor targets. Such methods can also be used to map epitope regions of ligands, identify ligands in a mixture of compounds and provide structural constraints. Protein-detected screening methods are more resource-intensive, requiring the preparation of isotopically labelled recombinant proteins, but can provide detailed information about the location(s) of bound ligands. Protein-detected screening methods, when used at later stages in the drug-discovery process, have helped in the design of leads with nanomolar affinities for the targets.

2. LIGAND-DETECTED SCREENING METHODS

2.1. Theoretical considerations

Several NMR methods of interest in drug discovery exploit the proton signals from solutions of small molecules, either alone or in mixtures, to screen for receptor–ligand interactions and to provide quantitative information about ligand-binding affinities and conformations. Each method has its limitations depending upon sample availability, solubility and, importantly, the size of the receptor target. The choice of an appropriate method is therefore dictated largely by the demands of the sample. It is useful to consider the implications of a small molecule ligand interacting with a (usually much larger) receptor. Most compounds of pharmaceutical relevance are water-soluble small molecules that bind reversibly to the target either in aqueous solution or, in the case of membrane receptors, embedded in what is effectively a solid support.

The binding equilibrium of a non-covalent ligand L in the presence of a receptor R to form a complex RL is first considered. The affinity of the ligand for the receptor, defined by the dissociation constant K_D, is a function of the on-rate (with rate constant k_{on}) and off-rate (having velocity constant k_{off}) of the ligand, according to $K_D = k_{off}/k_{on}$. If the association of a ligand with its receptor is diffusion-controlled, k_{on} is typically on the order of $10^8\,M^{-1}\,s^{-1}$ and the dissociation constant is dominated by the off-rate.[8] Low-affinity interactions ($K_D \geqslant 0.1$ mM) therefore usually involve rapid rates of dissociation ($k_{off} > 100\,s^{-1}$) of the ligand from its binding site and the ligands are classified as weakly binding. Higher affinity ligands ($K_D \leqslant 10\,\mu M$) usually undergo slower dissociation from their targets (Fig. 1) and are classified as strongly binding. The weak-binding situation is favourable for the majority of ligand-observed NMR screening methods because the ligand can be

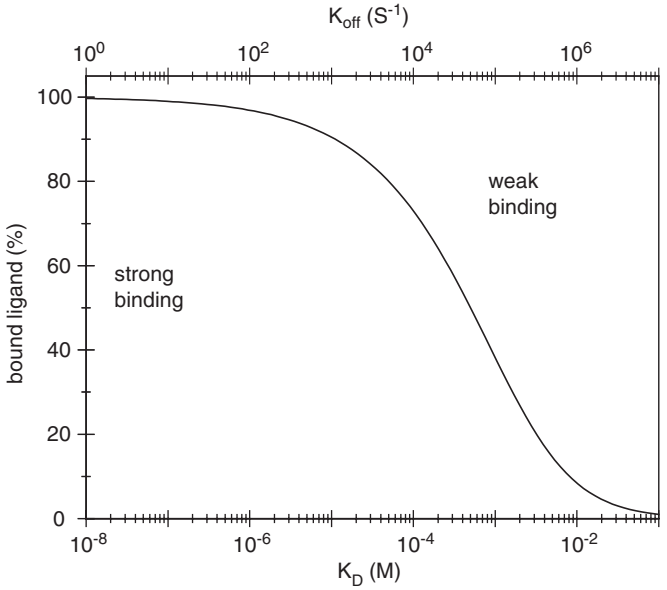

Fig. 1. The predicted relationship between weak binding, strong binding, dissociation constant (K_D) and off-rate (defined by velocity constant k_{off}) for a ligand and receptor in equimolar concentration, when association of the ligand is diffusion-limited (i.e., $k_{on} = 10^8\,M^{-1}\,s^{-1}$).

detected in solution while exploiting various physical properties of the ligand that are modulated by its transitory association with the receptor. The fraction f of the total ligand bound to a receptor is a function of K_D and the total concentrations of ligand and receptor, $[L]_T$ and $[R]_T$, according to

$$f = \frac{1}{2[L]_T}\left\{K_D + [L]_T + [R]_T - \sqrt{(K_D + [L]_T + [R]_T)^2 - 4[L]_T[R]_T}\right\} \qquad (1)$$

A corollary of this equation, which is implicit in the plot of [RL]eq versus K_D in Fig. 1, is that weakly binding ligands must be added in large excess over the receptor in order to saturate the available binding sites.

The dissociation constants of strongly binding ligands ($k_{off} < 100\,s^{-1}$ $K_D < 1\,\mu M$) can, in favourable situations, be estimated from an NMR spectrum of a receptor–ligand solution by integrating the peaks for the free and bound ligand at different ligand concentrations. Peak areas can be measured accurately only if the chemical shifts of the free and bound ligand are resolved from each other, the peaks are relatively sharp and are situated away from the protein signals. A ligand undergoing slow rates of dissociation from its receptor gives rise to a free induction decay in which the time-dependent NMR signal M from a specific nuclear spin in a ligand reflects the two resonance frequencies of the free and bound species, ω_f and

ω_b, according to

$$M(t) = f \exp\left[\left(-\frac{1}{T_2^b} + i\omega_b\right)t\right] + (1-f)\exp\left[\left(-\frac{1}{T_2^f} + i\omega_f\right)t\right] \quad (2)$$

where T_2^b and T_2^f are the transverse relaxation times for the bound and free species, respectively. Peak intensities can, in principle, be measured from the spectrum after complex Fourier transformation of the free induction decay. In practice, however, the line widths of peaks for the bound ligand are usually severely broadened as a result of the rapid transverse relaxation rates for proton spins within the slow tumbling macromolecular complex. The proton transverse relaxation rate R_2 for an inflexible ligand bound tightly to a rigid-body globular protein in aqueous solution undergoing isotropic rotational diffusion is estimated as

$$R_2 = \frac{1}{T_2} = \left[\frac{3\hbar^2\gamma^4}{20r^6}\right]\left[3\tau_c + \frac{5\tau_c}{1+\omega^2\tau_c^2} + \frac{5\tau_c}{1+4\omega^2\tau_c^2}\right] \quad (3)$$

where τ_c is the rotational correlation time for the macromolecular complex and r the average proton–proton distance. The correlation time is related to the hydrodynamic radius a of the ligand–target complex through the Debye equation

$$\tau_c = \frac{4\pi a^3 \eta}{3kT} \quad (4)$$

where η is the solvent viscosity at the experimental temperature and k the Boltzmann constant. It is worth noting that 30% of all proteins are embedded in a cell membrane and undergo anisotropic rotational diffusion. The rotational diffusion within the lipid bilayer[9]

$$\tau_c \approx \frac{4\pi a^2 h\eta}{3kT} \quad (5)$$

where a is the cross-sectional diameter and h the height of the transmembrane domain. In Fig. 2 is shown a plot of predicted T_2 relaxation times for ligands bound to protein targets of different molecular weights, calculated from the empirically derived relationship between the hydrodynamic radius and the molecular weight of a selection of globular proteins. The plot implies that signals from tightly bound ligands ($k_{off} < 100\,s^{-1}$) are generally too broad to be directly detected in the binding site of targets of above about 100 kDa unless sophisticated isotope labelling and NMR experiments are employed.[10] If the target is embedded in a membrane, the line broadening effects of anisotropic molecular motions can be eliminated by using solid-state magic-angle spinning (MAS) and high-power proton decoupling to observe ^{13}C or ^{15}N signals from an isotope-enriched ligand or receptor. Further details of this approach will be considered later on.

Next is considered the case of a weak ligand with an off-rate that is much greater than the difference in resonance frequencies of the free and bound species (e.g., $k_{off} > 10^3\,s^{-1}$). Weakly binding ligands are likely to be encountered in the first iterations of ligand screening. The NMR signal $M(t)$ from a specific nuclear spin within the ligand now reflects a weighted average of the resonance frequencies of the

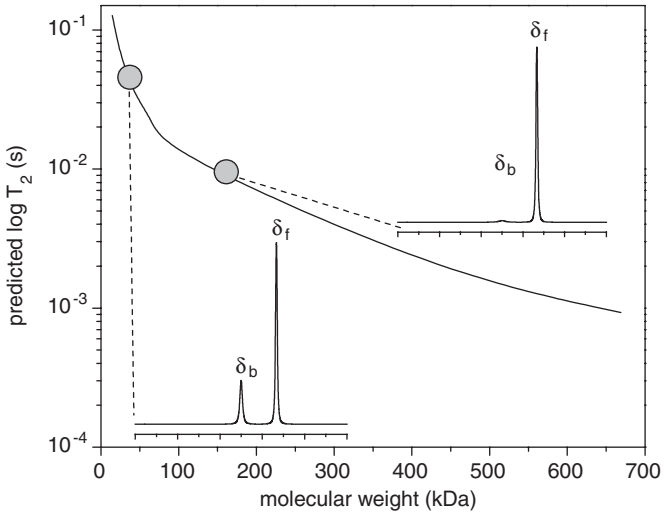

Fig. 2. An idealised plot of the relationship between protein molecular weight and ^{1}H transverse relaxation rate at 25°C, predicted using Eqs. (3) and (4) from a survey of the experimentally determined hydrodynamic radii of 20 globular proteins of different molecular weights. Calculations are for a proton Larmor frequency of 600 MHz. The inset shows simulated peaks for a small ligand molecule in which half of the ligand is free in aqueous solution and half is strongly bound to the receptor ($K_D = 0.1\,\mu M$), with chemical shifts δ_f and δ_b for the free and bound species separated by 70 Hz. In the favourable situation when the receptor target is small (20 kDa), a narrow peak for the free ligand and a broader peak for the bound ligand can be observed and K_D can be calculated by integration of the two peaks (left inset). When the target is large (150 kDa), the peak for the bound ligand is broadened beyond detection and it is no longer possible to measure K_D (right inset).

free and bound species, i.e.,

$$M(t) = \exp\left[\left\{-\frac{1}{T_2^{obs}} + i(f\omega_b + (1-f)\omega_f)\right\}t\right] \tag{6}$$

where the observed relaxation time $T_2^{obs}$is given by[11]

$$\frac{1}{T_2^{obs}} = \frac{f}{T_2^b} + \frac{(1-f)}{T_2^f} + f(1-f)^2\frac{4\pi^2(\omega_f - \omega_b)}{k_{off}} \tag{7}$$

Hence, after complex Fourier transformation of the free-induction decay, peaks from a ligand interacting weakly with a receptor will appear in a spectrum at frequencies that are determined by the chemical shifts of the free and bound species and by the fraction f of the ligand that is bound to the receptor. In this situation, simple inspection of the spectrum together with peak integration is not sufficient to detect and quantify ligand binding. For this reason more sophisticated experiments have been designed, which exploit certain spin interactions or other physical

properties of the ligand, such as relaxation or diffusion, that are modulated by association of the ligand with its receptor.

2.2. Screening approaches

A common feature of all ligand-observed screening methods is that rely upon some NMR property of a weakly binding ligand being perturbed or manipulated as a result of the ligand associating with the target protein. Two general approaches in ligand-detected screening are used. One approach is to measure a specific property of the ligand, such as relaxation, diffusion or chemical shift. At the fast exchange limit, the observed property O_{meas} represents a weighted average of the values for the free and bound ligand according to the general equation,

$$O_{\text{meas}} = fO_{\text{bound}} + (1 - f)O_{\text{free}} \tag{8}$$

where f is the fraction of bound ligand. If, in a mixture of compounds and a receptor target, one of the compounds is a weak ligand, the magnitude of O_{meas} for the ligand reflects its transitory association with the target, whereas O_{meas} for non-binding compounds is simply the value observed for the compounds alone in solution, O_{free}. Ligands can therefore be discriminated from non-ligands in a mixture of compounds together with a receptor, provided the spectrum of the mixture can be deconvoluted and assigned to the individual components of interest. The second approach is to transfer magnetisation from the receptor target to the ligand for the period in which the ligand resides in the binding site. The transferred magnetisation is then carried with ligand as it dissociates into solution from where the NMR signal is observed. Examples of both approaches are described in the following sections.

The ability to observe signals for a weak ligand in the presence of a large (>100 kDa) macromolecular receptor – and to detect ligand binding – depends upon the interrelationship between T_2^{obs}, k_{off} and the ligand concentration. The corollary of this relationship is that NMR experiments to detect weak binding ligands must be carried out with the ligand in sufficiently large excess over the receptor to prevent the line widths from being dominated by the short relaxation times of the receptor–ligand complex. It is equally important, however, that the concentration of ligand is low enough to ensure that weak interactions between receptor and ligands give rise to an observable response from the measured NMR property.

2.3. Relaxation-based screening

A simple strategy for distinguishing ligands from non-binding compounds is to exploit the differences in relaxation properties of receptor-bound ligands and small molecules that are free in aqueous solution. Hajduk and colleagues[12] used relaxation-editing to detect ligand binding by applying a CPMG spin-lock to eliminate the signals from bound molecules without affecting the signals from non-binding molecules. By doing so, a ligand with 200 μM affinity for the receptor FKBP could be

readily identified from a mixture of nine compounds. Short spin-lock times are used to preferentially detect high-affinity ligands, while longer spin-lock times are necessary for detecting weaker ligands. Earlier, Rossi and co-workers[13] showed how measurements of T_1 relaxation times could be used to detect ligand–DNA interactions. A relaxation-based strategy called TINS (target immobilised NMR screening) was recently described, which detects ligand binding by exploiting the fast transverse relaxation rates of receptors that have been attached to solid supports.[14] One advantage of this method is that, because the target is attached to an insoluble matrix, the receptor can be readily isolated from the compound mixture and recycled for further screening. The application of relaxation-based methods is, however, limited to simple screening of receptor–ligand interactions and does not provide details of ligand-binding affinities or give information about binding surfaces, for example. Consequently, relaxation based approach has been largely superseded by other, more advanced methods that provide additional information about the receptor–ligand complex.

2.4. Saturation transfer

Meyer and Mayer[15] described the saturation transfer difference (STD) NMR method for detecting weak receptor–ligand interactions in solution. In the STD approach, ^{1}H magnetisation from the protein target is saturated by low-power irradiation by a shaped pulse at a frequency well away from the ligand resonance frequencies (<1 ppm and >10 ppm) (Fig. 3). Selective saturation of the target spins gives rise to spin-diffusion across the network of protons within the target. The saturation effect is transferred to a ligand during the period for which it is associated with the receptor-binding site (Fig. 4). For a ligand in fast exchange between free and bound environments, the transferred saturation is carried with the ligand when it dissociates from the receptor into the free state. In practice, one spectrum is obtained with saturating pulses and a second spectrum is obtained either without saturating pulses or with a shaped pulse that is off-resonance with respect to both the protein and ligand (Fig. 3). When one spectrum is subtracted from the other, the remaining peaks correspond only to compounds that bind weakly to the target. Signals from molecules having micromolar to millimolar affinity for the receptor are observed, and the method allows ligands to be discriminated from non-ligands in a mixture of compounds. The method is also straightforward to implement and is rather sensitive, requiring nanomolar quantities of the protein target, and can be combined with other standard ^{1}H NMR methods such as TOCSY.[16]

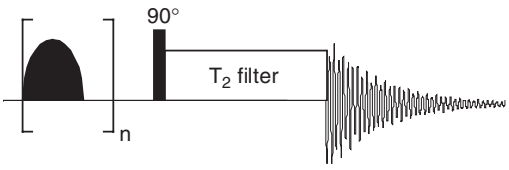

Fig. 3. Pulse scheme for a basic saturation transfer experiment.

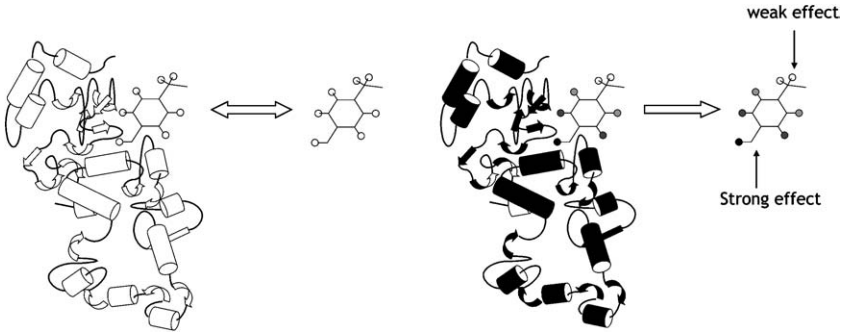

Fig. 4. An illustration of how the saturation transfer difference method can be used to map ligand-binding surfaces. A ligand is in dynamic equilibrium between free and bound states in fast chemical exchange ($k_{off} > 100\,s^{-1}$) (left). If the magnetisation of the receptor is saturated, the saturation effect is transferred to the bound ligand at a rate depending on the distances between the ligand and receptor protons: saturation is transferred most rapidly to the ligand protons in closest contact with the protein. The saturation effect is then carried with the ligand as it dissociates from the binding site. Recently, Hadjuk and co-workers[22] have introduced a saturation transfer NMR-based method called SOS-NMR, which exploits selectively deuterated proteins to define the amino acid composition of the binding site and, when the target protein structure is known, determine the structure of the receptor–ligand complex.

The extent of saturation has been defined by a saturation amplification factor, F, where[17]

$$F = ((I_0 - I_{sat})/I_0)[L]_{ex} \tag{9}$$

and $[L]_{ex}$ is the concentration of ligand in excess, I_0 the intensity of ligand peaks in the absence of saturation and I_{sat} the intensity after saturation. The value of F increases as the ligand concentration is increased until a plateau is reached, typically at rather long saturation times of 1 s or more when the ligand is weak and in large excess over the receptor. The saturation time giving the optimal amplification factor is a function of the T_1 relaxation times of the free and bound ligand and the off-rate of the complex. The amplification factors for proton spins at different sites in the ligand depend upon which functional groups of the ligand interact most strongly with the target. This effect has been exploited to reveal ligand-binding epitopes, or regions of the ligand that come into closest contact with residues within the receptor-binding site.[18] The group epitope mapping approach was developed further to characterise the binding interactions in more detail using as a model system a lectin agglutinin and its galactose-based ligands.[17] Analysis of the saturation transfer effects of methyl beta-D-galactoside showed that the H2, H3 and H4 protons experienced the greatest saturation giving evidence of their close proximity to the lectin-binding site.

The STD method has also been shown to be suitable for screening ligands of immobilised proteins, including membrane proteins.[19,20] A human integrin subunit assembly $\alpha_{IIb}\beta_3$, possessing two short transmembrane regions, was embedded into liposomes and screened for interactions with peptides presenting the peptide recognition

sequence (RGD) found in fibrinogen.[20] The STD method was also implemented as a double difference technique to characterise binding interactions of cell surface proteins within living cells.[21] The STD method is not limited to receptor–ligand interactions, however, and has also been applied to examine interactions between small RNA fragments and the clinically important ribosomal RNA binding antibiotic paromomycin.[23] Examples of other recent applications of STD-NMR are summarised in Table 1.

The correct implementation of STD experiments and the interpretation of amplification factors are influenced by non-ideal experimental conditions and unfavourable NMR properties of the sample. Jayalakshmi and Rama Krishna[24] report a rigorous theoretical analysis of STD that considers sources of errors in the analysis of STD data arising from deviations from ideal conditions. They suggest that caution should be taken when relating amplification factors to ligand epitope regions, owing to non-uniform spin-diffusion. Another theoretical study demonstrated how rapid T_1 relaxation could distort the epitope map derived by STD, which can be particularly serious when the ligand protons have a range of T_1 relaxation times.[25] It was suggested that relaxation times should be measured carefully to compensate for distortions to the epitope map. Conducting STD experiments on RNA-binding ligands in D_2O lengthens the time taken to reach steady state between relaxation and saturation, with the effect that saturation factors are increased by over 100% compared to the saturation observed in H_2O.[23] A serious concern problem is the

Table 1. A summary of various applications of STD for ligand screening and characterisation

Receptor	Ligand(s)	Details	Reference
DNA fragment	Spermine; ethidium bromide and others	Differential frequency STD used to distinguish between different modes of ligand binding	[27]
Monoclonal antibody	Sialyl Lewis(x)	Identified epitope regions on the pyranose rings	[28]
HIV-inactivating protein cyanovirin-N	Oligosaccharides	Mapping binding surfaces	[29]
Bovine serum albumin	Halothane	Detection of anaesthetic binding to proteins	[30]
RNA	Phenothiazines	Mapping binding surfaces	[31]
Factor Xa	Compound library	Identification of micromolar ligands from compound mixtures	[32]
Antibody	Polysaccharides	ID TOCSY experiment to identify cell wall fragment–antibody interactions	[33]
Agglutinin	Disaccharide	Ligand conformation by tNOE and epitope region by STD	[34]

effect of non-specific binding, which is promoted by the high concentrations of ligand that are usually necessary to conduct the STD experiment under optimal conditions. The use of deuterated proteins has been shown to improve the reliability, ligand screening and reduce the effects of non-specific binding, provided it is known which residues within the binding site come into contact with the ligand.[26]

2.5. Water saturation methods

An alternative approach to STD is the water-ligand observed via gradient spectroscopy (waterLOGSY) method.[35] In this experiment, the magnetisation from bulk water is transferred selectively to the receptor and to the bound ligand and, like saturation transfer, the effects are carried with the ligand as it dissociates into bulk solution. In Fig. 5 is shown a pulse scheme used in the waterLOGSY experiment, which starts with the selective excitation of water followed by a mixing period τ_m to allow magnetisation transfer from water to the protein. There are various mechanisms for the transfer of magnetisation from water to the ligand, including via chemical exchange of protons from water to the OH and NH groups of the bound ligand and protein amino acids. The net result of transfer process is that the peaks for non-binding compounds in the waterLOGSY spectrum are of opposite sign and weaker than those for ligands. A variant of this scheme (not shown) has an additional 180° pulse in the centre of the mixing period to avoid relaxation of the spins to the equilibrium state and a selective water flip-back pulse.[36] The advantage of the waterLOGSY experiment is that it is sensitive and suitable for protein targets that cannot be over-expressed in large quantities, but initial optimisation of the pulse sequence parameters is important.

2.6. Diffusion methods

Pulsed field gradient (PFG) diffusion NMR techniques such as the pseudo-two-dimensional method DOSY (diffusion-ordered spectroscopy) have been used widely as a means of separating signals from a mixture of small molecules according to their molecular weights.[37] The relationship between the diffusion constant and

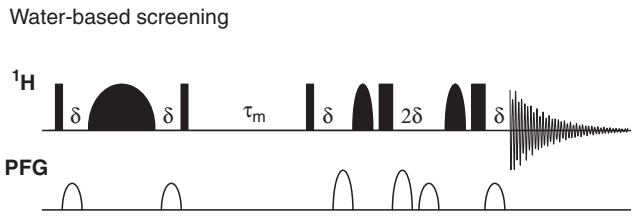

Fig. 5. A pulse scheme for the basic experiment used in the water-based screening method waterLOGSY. The bulk water magnetisation is first excited selectively and stored longitudinally for a mixing time τ_m during which magnetisation is transferred from water to the protein.

the hydrodynamic radius of a molecule also allows for detecting the interactions of small molecules with larger macromolecular targets and, in favourable cases, it is also possible to measure ligand binding constants. The ability of PFG-NMR to probe receptor–ligand interactions was reported in 1997 by Shapiro and co-workers,[38,39] who used a method combining PFG-NMR and TOCSY to identify interactions between small organic compounds in a mixture. The method was later used to observe D-amino acid peptide ligands binding to vancomycin[40] and to identify ligand interactions with DNA fragments.[41]

In the PFG experiment, the peak intensity I for a molecule diminishes exponentially as a function of the gradient amplitude G, the translational diffusion coefficient D (e.g., Ref. [42])

$$I = I_0 \exp\left[-D(\gamma\delta G)^2(\Delta - \delta/3)\right] \tag{10}$$

where I_0 is the peak intensity in the absence of a PFG, δ the duration of the gradient pulse and Δ the diffusion time. D for the observed species is defined by the Stokes–Einstein equation

$$D = \frac{kT}{6\pi\eta a} \tag{11}$$

Hence a plot of $\ln I$ as a function of G^2 is, in principle, linear with gradient yielding the value of D_{obs}, which is diagnostic of the strength of ligand binding. It follows that the dissociation constant K_D for a receptor–ligand complex in the fast ligand exchange regime can be expressed as a function of diffusion constants[43]

$$K_D = [R]_T\left(\frac{D_b - D_o}{D_o - D_f}\right) + [L]_T\left(\frac{D_o - D_b}{D_b - D_f}\right) \tag{12}$$

where D_o, D_b and D_f are the observed diffusion-, bound ligand diffusion- and free ligand diffusion coefficient, respectively.

In practice, two basic diffusion-editing PFG methods are commonly used for ligand screening (Fig. 6). One is the pulsed gradient spin-echo (PGSE), which is generally applied for species with long T_2 relaxation times and with no J modulation during the echo period.[44] The other method is the stimulated echo (STE), which stores the magnetisation longitudinally during the diffusion interval and is therefore preferable for species with long T_1 relaxation times.[45] Additional modifications to the basic pulse sequences to simplify NMR spectra, for example by rejecting the resonances of coupled spins, have also been reported.[46] Moreover, it has been shown to be important to suppress or subtract the background signal from the receptor target to provide accurate measurements of diffusion constants.[47]

Measurements of diffusion coefficients alone do not directly provide information about the binding site, structure or epitope region of a ligand. It has been noted, however, that diffusion plots for ligands in the presence of receptor often deviate from linearity when the diffusion measurements are performed with STE-based experiments.[48] The observed curvature of the plots arises from transferred NOEs from the target to ligand protons during the STE diffusion period. The extent of non-linearity has been shown to be site-specific, since chemically distinct protons in the ligand

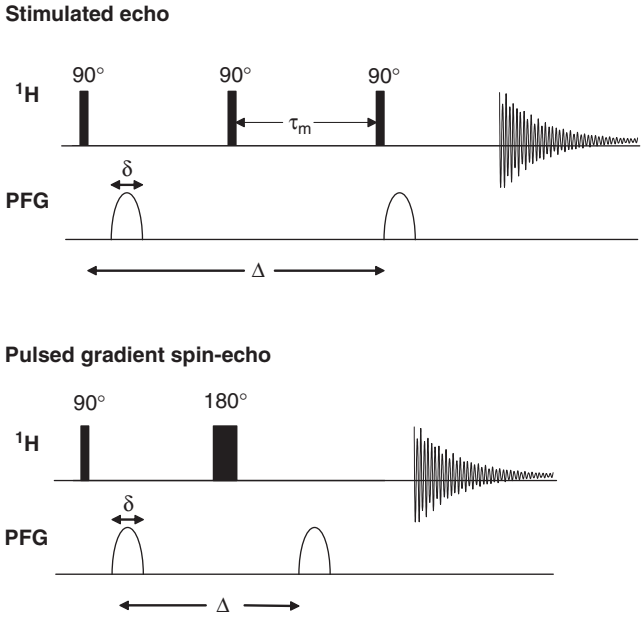

Fig. 6. Simple versions of the two main PFG-NMR pulse sequences used for diffusion-based ligand screening.

undergo different rates of cross-relaxation with proton spins within the target according to their disposition in the binding site. This observation was exploited as a tool for epitope mapping by PFG-NMR, the first example of which was demonstrated by experiments on trimethoprim binding to the dihydrofolate reductase.[49] Epitope mapping by this method to characterise interactions of ligands with human serum albumin (HSA) has also been reported.[50] In this work, NOEs between dansylglycine and caprylate ligands were detected in the diffusion analysis, which provided insight into the ligand conformations in the common HSA binding pockets. The epitope map most reliably reflects the regions of the ligand in contact with the binding site when the off-rate is much faster than the rate of cross-relaxation; when the two rates are comparable the non-linear deviations in the diffusion plots are moderated by spin-diffusion.

2.7. NOE pumping

An alternative PFG-NMR-based method to discriminate ligands from non-binding compounds in solution is the NOE pumping experiment.[51] In this approach, an STE or longitudinal eddy-current delay (LED) is applied to the sample to suppress all signals from the rapidly diffusing ligand molecules, while preserving signals from the macromolecular target. Signals from bound ligands are then recovered using a standard NOE mixing interval following the diffusion filter, to allow magnetisation to be transferred from the receptor to the ligand. Since the ligand coherence is

destroyed by the diffusion experiment at the beginning of the NOE experiment, any ligand signals detected at the end of the NOE mixing interval arise from polarisation transferred from the receptor. In the fast exchange regime, the ligands dissociate from the target macromolecule and the transferred magnetisation is retained as a result of the longer T_1 of the ligands in the free state. A modification to this experiment, referred to as reverse NOE pumping, has been proposed as a means of countering the adverse T_2 relaxation times of ligands associated with large macromolecules.[52] This method uses T_2 filters instead of field gradients to achieve the desired discrimination between ligands and non-binding compounds.

2.8. Transferred NOEs

The nuclear Overhauser enhancements observed for a molecule undergoing isotropic reorientation in solution are related to the correlation times τ_c, defining the rate of global molecular rotational diffusion. For an isolated spin pair, the observed NOEs can be approximated as[53]

$$NOE = \left(\frac{\mu_0}{4\pi}\right)^2 \left[\frac{\gamma^4 \hbar^2}{10r^6}\right] \left[\frac{6\tau_c}{1 + 4\omega^2\tau_c^2} - \tau_c\right] \tag{13}$$

Typical protein targets, with rotational correlation times of up to hundreds of nanoseconds in the case of large, multiple sub-unit complexes, give rise to strong negative NOEs; small organic compounds in solution produce small positive NOEs, zero NOEs or small negative NOEs. Small compounds that act as weak ligands undergoing fast exchange ($k_{off} > 300\,s^{-1}$) between free and bound states accrue negative NOEs when bound to the receptor, which are transferred with the ligand as it dissociates from the binding site into the bulk aqueous environment provided k_{off} is faster than the longitudinal relaxation rate of the ligand in the free state. The principles of tNOEs are well established and the subject of many detailed theoretical treatments (e.g., Ref. [54]) over the past 30 years. Meyer and co-workers recognised that tNOEs observed for small organic molecules in the presence of a receptor provides a useful basis for distinguishing ligands from non-ligands according to the sign of cross-peaks in a NOESY experiment.[55] Modifications to the standard NOESY sequence, such as introducing spin-lock steps to eliminate protein background signal and dephase unwanted zero quantum coherences,[56] have improved the reliability of the method for ligand screening purposes.

The principal advantage of tNOE methods over other screening methods for drug discovery lies in their ability to analyse the conformations of ligands in the bound state, specifically in situations where the size of the receptor-ligand complex is too large to be observed directly by NMR. Experiments exploiting tNOEs have been used to characterise a variety of receptor-ligand interactions and the subject has been treated in much detail by several reviews (e.g., Ref. [57]). Like the other methods described earlier in this section, tNOE methods rely upon the ligand being present in solution in large excess (10–50-fold) over the target receptor, so that the

peaks for the ligand are biased towards the favourable line widths for the free ligand. Structural information about the ligand in its bound state is derived from the analysis of NOESY-type experiments, in which the initial build-up of cross-peak intensities is proportional to proton–proton distances of up to about 5 Å. Table 2 summarises some of the applications of tNOE methods in the analysis of receptor–ligand complexes to demonstrate the diversity of systems that are amenable to this approach; a few additional examples are worth mentioning here in more detail, however. Moore and colleagues have exploited simple NOESY experiments alongside other NMR screening methods in the so-called SHAPES strategy, which generates leads by detecting weakly binding ligands from mixtures of small, drug-like fragments.[58] In this application, conformational constraints for the ligands are less important than the observation of interligand NOEs that indicate that two or more of the fragments in the mixture bind to the target in close proximity to each other. By chemically linking such fragments together, it is possible to generate ligands with much higher affinity for the target. Interligand NOEs also form the basis for a recent method called INPHARMA (interligand NOEs for pharmacophore mapping).[59] The INPHARMA strategy relies upon spin diffusion mediated by the protons of the target, and detects NOEs between ligands that bind to the same site of the target competitively and consecutively. In another example, Dinsmore and co-workers[60] report the conformational analysis of macrocyclic inhibitors of farnesyltransferase, which demonstrated how interproton distances combined with

Table 2. A summary of some recent applications of tNOE experiments for ligand screening and characterisation

Receptor	Ligand(s)	Details	Reference
Angiotensin-converting enzyme	Amino acid derivatives	Identification of ligands from compound mixtures	[66]
Streptococcus monoclonal antibody	Oligosaccharides	Combination of tNOE and STD to determine binding conformation and epitope region	[67]
$\alpha_5\beta_1$ integrin	Cyclic peptide	Conformational analysis by ^{15}N-edited tNOEs	[68]
Bacterial 70S ribosomes	Oxazolidinones	Conformational analysis	[69]
Synthetic fragment of lipopolysaccharide binding protein	Peptidic lipopolysaccharide	Conformational analysis of complex led to the design a peptide with increased inhibitory properties	[70]
Hepatitis C NS3 protease	Tetrapeptide inhibitors	Determined the orientation of aryl substituents of inhibitors and designed new inhibitors with increased potency	[71]
HCVNS5B polymerase	Thiophene-2-carboxylic acids	Analysis of bioactive conformation	[72]

energy minimisation was able to refine the structure of a flexible lead compound and produce an entropically favourable restrained ligand. Furukawa and co-workers[61] used tNOE measurements to determine the conformation of inhibitors bound to the muscarinic acetylcholine receptor, demonstrating the potential of this technique for examining the large proportion of drug targets that are embedded in cell membranes. More recently, Reif and co-workers used a combination of tNOE and transferred residual dipolar coupling measurements to analyse the conformation of inhibitors bound to β-amyloid fibrils.[62] These insoluble protein deposits are implicated in neurodegenerative diseases including Alzheimer's and Parkinson's and have long being intractable to study. Solution- and solid-state NMR measurements of amyloid proteins and their interactions with ligands promise to help in the search for new generations of drugs in the treatment of these diseases.

The quantitative analysis of tNOEs, to provide structural information about bound ligands, should be treated with some caution. One important consideration is the possibility of non-specific, or extraneous, binding, which is exacerbated by requirement for the ligand to be present in large molar excess over the target. The most common approach to eliminate the effects of non-specific binding is to conduct a control experiment with a second ligand that binds competitively to the target site.[63] Another consideration is the contribution of multiple spin systems to the dipolar cross-relaxation pathway, manifest as intermolecular spin diffusion. Such effects have been considered in detailed relaxation matrix analyses of multiple spin systems.[64] The accuracy of the analysis of NOE build-up curves is compromised by intermediate ligand exchange with respect to the cross-relaxation rate, which becomes more a significant problem with increasing size of the receptor target.[65] Moreover, the free ligand should ideally give negligible NOEs, which limits the size of the ligand to under about 5 kDa.

2.9. Cross-polarisation magic-angle spinning NMR

Over half of the targets of marketed drugs are membrane-embedded receptors, ion channels, enzymes and transporters, which usually must be isolated in their native membrane to preserve their structure and function.[73] The size and insolubility of biomembranes can present considerable experimental difficulties for observing receptor–ligand interactions by conventional solution NMR methods. Strongly binding ligands undergoing slow dissociation rates from membrane receptors cannot be detected directly by conventional NMR methods because the resonance lines are broadened by chemical shift anisotropy (CSA) and dipolar interactions within the binding site. Moreover, the heterogeneity of membrane assemblies may introduce susceptibility discontinuities and give rise to extensive non-specific interactions in the presence of a large excess of weakly binding ligands.

Cross-polarisation magic-angle spinning (CP-MAS) is a solid-state NMR method that is also capable of detecting the interactions of ligands with membrane proteins, regardless of size or function, and with nanomolar to millimolar binding affinities.[74] In conventional CP-MAS NMR, Hartmann–Hahn cross-polarisation is used to enhance the signal from an observed low-gamma nucleus (e.g., ^{13}C or ^{15}N) and to

reduce recycle times, by transferring magnetisation from protons which have higher sensitivity and more favourable (i.e., shorter) T_1 relaxation times. Over short cross-polarisation contact times (<10 ms), magnetisation transfer between heteronuclear spins is mediated predominantly by dipole–dipole interactions. For rigid solids, cross-polarisation can produce theoretical gains in signal intensity of up to 4-fold for ^{13}C, although this level of enhancement is rarely achieved in practice because of competing relaxation processes. For a solid material the signal intensity S for ^{13}C spins after a contact time t_c can be approximated as[75]

$$S = S_0\left(1 - \frac{T_{HC}}{T_{1\rho H}}\right)^{-1}\left[\exp\left(-\frac{t}{T_{1\rho H}}\right) - \exp\left(\frac{t}{T_{HC}}\right)\right] \tag{14}$$

where S_0 is the theoretical maximum signal intensity attainable, T_{HC} the cross-polarisation rate and $T_{1\rho H}$ the proton rotating frame relaxation time.

The CP-MAS method has been adapted to examine interactions between suitably isotopically labelled (e.g., ^{13}C, ^{15}N or ^{19}F) ligands and receptors in membrane samples. Using Hartmann–Hahn cross-polarisation to transfer magnetisation from protons to a less-sensitive spin, such as ^{13}C, it is possible to discriminate between free and bound substrate molecules because of the differences in the motional characteristics of substrate in the two environments. Heteronuclear dipolar interactions within the free ligand are averaged to zero by rapid isotropic reorientation and the rate of cross-polarisation is negligible compared to the rate for the receptor-bound ligand, which undergoes slow reorientation. Ligand binding is detected when the membrane sample is in a non-frozen, fluid state, allowing receptor-ligand interactions to be characterised under physiologically relevant conditions that are intractable to other methods of analysis. Moreover, magic-angle spinning eliminates or reduces the line broadening effects of CSA and dipolar interactions, and susceptibility effects, so that both strongly and weakly binding ligands can be observed equally well without adjustment of the experimental conditions. Spooner *et al.*[76] first demonstrated how CP-MAS could be used to detect interactions between ^{13}C-labelled L-glucose and the bacterial sugar transporter GalP in partially purified *Escherichia coli* membrane samples at 4°C. This development provided the incentive for further studies in which bacterial transporters were nitroxide spin-labelled at unique cysteine residues in order to locate residues close to the substrate binding site. It was shown that the strong magnetic dipole of the electron spin broadened the peaks from the bound substrates and permitted distances between the labelled residues and the bound ligand to be estimated.[77]

It was shown recently that CP-MAS is able to provide quantitative information about ligand-binding affinities for receptors in fluid membranes. In this new development, peak intensities from different concentrations of an isotope-labelled ligand in the presence of a membrane receptor are measured at increasing cross-polarisation contact times.[78] The magnetisation M transferred from the proton spins to the observed nucleus after contact time t is given by

$$M_C(t_c) = \sum_N\left[\int_0^{t_1}\frac{dm_C^1}{dt} + \int_{t_1}^{t_2}\frac{dm_C^2}{dt} + \int_{t_2}^{t_3}\frac{dm_C^1}{dt}\cdots\right] \tag{15}$$

where each integral represents the magnetisation transferred during episodes of ligand binding to, and dissociation from, the receptor. The build up of peak intensities at different ligand concentrations is highly sensitive to binding affinity and the experimental data are compared with curves calculated for an ensemble of molecules to extract values of K_D. One advantage of this method is that the K_D value can be checked independently by measuring the peak intensities after displacement of the labelled ligand by titration of an unlabelled ligand. Another attractive feature of this method is that the cross-polarisation procedure can be "tuned" to eliminate the signal from non-specifically bound ligand. Variable contact time CP-MAS has since been used to measure K_D values for the interactions of glucuronide sugars with the bacterial transport protein GusB[78] (Fig. 7), ouabain analogues with the Na^+/K^+-ATPase[79] and the antidepressant drug trifluoperazine (TFP) with gastric H^+/K^+-ATPase.[80] In the latter work, the intrinsic ^{19}F signal of TFP was exploited to measure ligand-binding affinities.

2.10. Strongly binding ligands

A limitation of the NMR methods outlined above is that they are effective only for detecting relatively weak ligands undergoing fast exchange between free and receptor-bound states. Moreover, the NMR measurements alone offer no indication of the biological significance of the interactions taking place; simply identifying a receptor–ligand interaction does not guarantee that the interaction will generate a drug-like response. These shortcomings have been addressed with the advent of competition-binding strategies, in which a weak reference ligand with known biological activity is exploited as a reporter molecule. Solution NMR measurements of the reporter ligand L_{ref} together with the receptor R are carried out in the presence of a compound mixture. The presence in the mixture of one or more compounds competing with the reference ligand for the binding site will lower the concentration of the complex RL_{ref}, which will have a concomitant effect upon the measured NMR properties of the observed reporter ligand. This approach was demonstrated by Dalvit and co-workers,[81] who used T_1 and T_2 relaxation measurements of reporter ligands to identify ligands with affinities in the nanomolar range from compound mixtures. In principle, the competition-binding strategy can be applied to any of the NMR screening methods described in this section, and examples have been reported of competition waterLOGSY[82] and STD[83] experiments.

Solid-state CP-MAS NMR methods have been used to examine the molecular conformations of ligands bound tightly ($K_D < 1\ \mu M$) to receptors embedded in lipid membranes. The structural information comes in the form of internuclear distances, torsional angles and bond orientations relative to a fixed reference frame. A variety of heteronuclear and homonuclear dipolar recoupling (DR) experiments have been applied to receptors prepared in disordered membranes; these methods manipulate the nuclear spin systems to restore the weak, but structurally informative, dipolar interactions that are otherwise removed by magic-angle spinning.[84] The dipolar

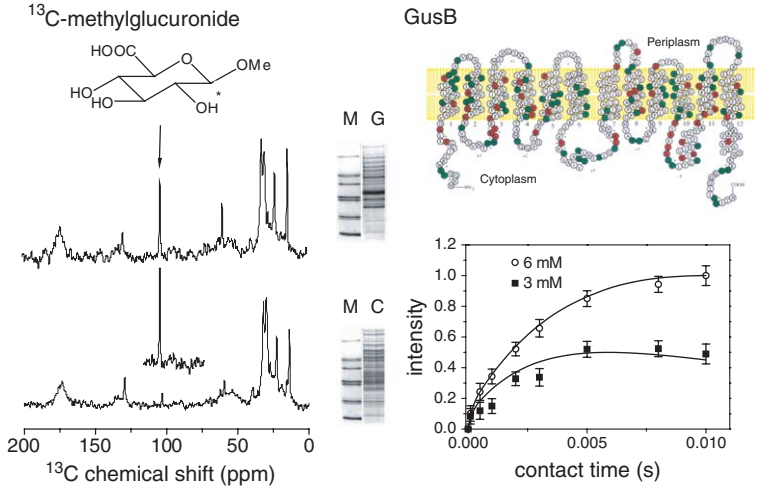

Fig. 7. An example of how ligand-binding affinities can be estimated using variable contact time ^{13}C CP-MAS NMR. Using a single Hartmann–Hahn contact time of 10 ms, binding of the substrate [^{13}C]methylglucuronide to *E. coli* membranes containing the overexpressed bacterial sugar transport protein GusB can be detected from the signal in the ^{13}C spectrum at 100 ppm from as little as 20 nmoles of protein (top left spectrum). This spectrum was obtained in less than 20 min at 4°C. A polyacrylamide gel of the membrane sample (marked G) shows that GusB represents less than 30% of the total membrane protein. The peak at 100 ppm can be assigned to substrate binding only to GusB and not to other membrane proteins by conducting a control experiment on membranes containing natural expression levels of GusB. The spectrum of the control membranes (bottom left) shows that the peak from the substrate is absent. By comparing the peak intensities for the ligand at different contact times with calculated peak intensity profiles it is possible to estimate the binding affinity of the substrate for GusB (bottom right). Figure adapted from Ref. [78]

coupling constant d_{IS} is given by

$$d_{IS} = -\left(\frac{\mu_0}{4\pi}\right)\frac{\gamma_I \gamma_S \hbar}{r_{IS}^3} \tag{16}$$

where r_{IS} is the internuclear distance and all other terms have their usual meanings. Many such experiments have been devised including rotational resonance NMR, which restores and measures homonuclear couplings, REDOR for heteronuclear couplings and a range of experiments to measure H–C–H, H–C–N–H and N–C–C–N torsional angles (e.g., Ref. [85]). In addition, an alternative solid-state NMR method called MAOSS (magic-angle-oriented sample spinning) has been used to measure bond orientations in the retinal chromophore of rhodopsin.[86] Williamson and coworkers used CP-MAS and broad line ^{2}H NMR to probe the interaction of an acetylcholine derivative with the nicotinic acetylcholine receptor (*n*AChR), the ligand-gated cation channel that mediates synaptic transmission, to provide clues about how the ligand interacts with the binding pocket (reviewed in Ref. [87]). Deuterium NMR

experiments on uniformly aligned membranes containing [^{2}H]bromoacetylcholine indicated that the ligand is positioned in the binding site with the quaternary ammonium group facing outwards and oriented at about 40° with respect to the membrane normal. Further, CP-MAS spectra of the ^{13}C-labelled acetylcholine ligand in the receptor binding site showed an up-field perturbation in chemical shift relative to the free ligand in solution which was consistent with a ring current effect of aromatic residues that are believed to line the binding pocket.

Similar structural measurements have been reported for inhibitors of the P-type ATPases, an important class of therapeutic targets. The gastric H^+/K^+-ATPase is a proton pump responsible for secretion of acid into gastric glands, and is a target for drugs in the treatment of gastric ulcer disease. Reversible inhibitors of the proton pump include the aryl-substituted imidazopyridines, which are reasonably potent ($IC_{50}\sim1\,\mu M$) but have undesirable toxicological properties. A known imidazopyridine inhibitor of gastric H^+/K^+-ATPase was modified to incorporate ^{19}F into the aryl ring substituent and ^{13}C into the *N*-methyl group. Measurements of ^{19}F–^{13}C dipolar couplings from the bound inhibitor provided structural constraints defining the relative orientations of functionally important groups within the bound inhibitors.[88,89] These constraints were used to model the inhibitor in the binding site and also suggested structural refinements leading to the design of a new inhibitor with 100-fold higher potency. A similar strategy was adopted to examine how high-affinity cardiac glycoside inhibitors interact with their receptor, the cardiac Na^+/K^+-ATPase (Fig. 8). Cardiac glycosides have been used for over 200 years in the treatment of congestive heart failure. More recently, multidimensional solid-state NMR experiments have been used to solve the structure of a fragment of the peptide ligand neurotensin bound to its G-protein-coupled receptor,[91] a pharmaceutically important class of membrane-embedded receptors.

3. TARGET-DETECTED NMR SCREENING METHODS

3.1. Solution NMR methods

Protein-observed NMR screening methods in general exploit perturbations in the chemical shifts for the target protein in solution that occur as a result of changes in structure or microenvironment accompanying ligand binding. Studies of this kind usually rely upon having fully or extensively assigned spectra and, ideally, a crystal structure of the protein target in order to relate chemical shift perturbations to the location and three-dimensional structure of the ligand–target binding interface.[92] For small proteins of molecular weight under 30–40 kDa, the simplest most common approach is to monitor ^{1}H/^{15}N backbone amide chemical shifts while titrating a single compound or a mixture into the solution. The protein target must be expressed recombinantly to incorporate NMR isotopes, with uniform ^{15}N labelling being the minimum requirement. Heteronuclear correlation spectra (e.g., ^{1}H/^{15}N-HSQC or derivatives thereof) are then recorded in the absence and presence of potential ligand compounds. For larger protein targets it is often necessary to adopt

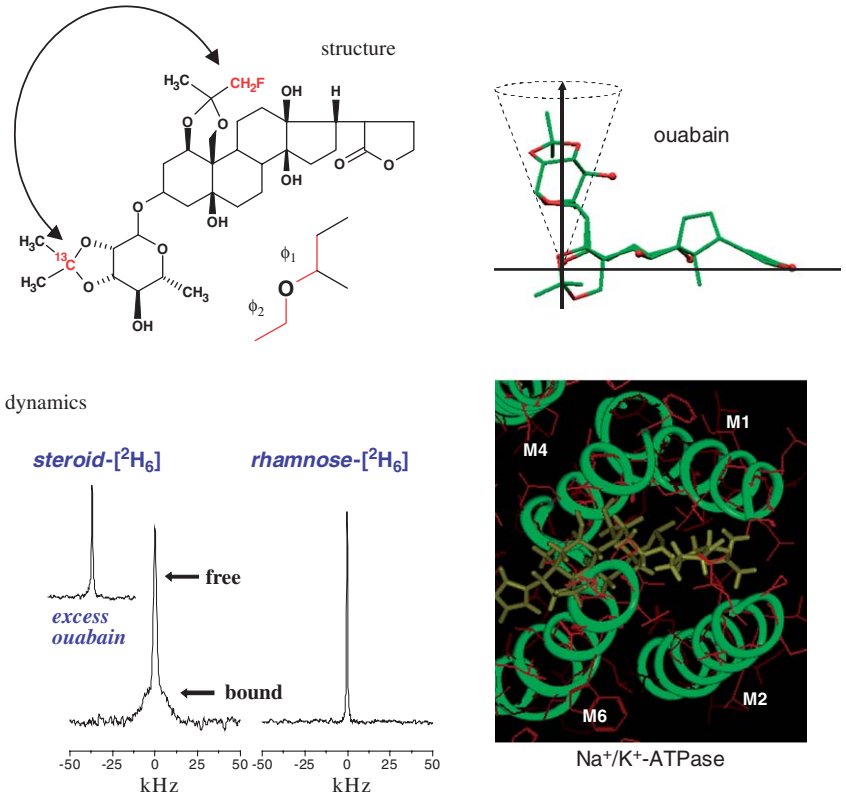

Fig. 8. Determination of the structure and orientation of a cardiac glycoside in the binding site of Na^+/K^+-ATPase, the digitalis receptor, using solid-state NMR. The inhibitor ouabain was modified to incorporate ^{19}F into the steroid and ^{13}C into the rhamnose sugar moiety. The C–F dipolar coupling, which is a function of the torsional angles ϕ_1 and ϕ_2, was measured by REDOR NMR. These measurements, taken together with deuterium NMR measurements of dynamics of the rhamnose sugar and steroid moieties with ^2H incorporated, indicated that the functionally redundant sugar group faced away from the surface of the protein with the functionally important steroid group aligned across the protein surface. Adapted from Ref. [90]

more sophisticated multiple isotope-labelling strategies (see below), combined with NMR methods such as transverse relaxation-optimised spectroscopy (TROSY) or SEA (solvent-exposed amide)-TROSY at high magnetic fields to enhance sensitivity and resolution.[93,94] Alternatively, fractional labelling can improve the sensitivity and reduce the complexity of standard HSQC spectra of larger protein targets at moderate field strengths. For example, selective ^{13}C labelling of valine, leucine and isoleucine has been shown to be a cost-effective method to obtain sensitive $^1H/^{13}C$-HSQC spectra of targets with molecular weights of up to 110 kDa.[95]

An advantage of the protein-observed screening approach is its ability to locate the binding sites of ligands and to identify any "hot spots" on protein surfaces, that

is, regions that interact preferentially with ligands and contribute a disproportionate amount of the energy involved in ligand binding. Hajduk and co-workers used heteronuclear NMR methods to characterise ligand interactions with 23 target proteins. The study revealed that over 90% of the ligands identified bound to the targets at sites that were already known to interact with small molecules, suggesting that protein surfaces contain highly selective ligand-binding regions.[96] From this observation it was shown that a model derived from the binding site characteristics of proteins can be used to predict experimental screening success rates and to assess the probability that high-affinity leads can be found for a particular target.

An important breakthrough in the development of target-detected NMR methods came with the linked-fragment strategy, first reported as the structure–activity relationship (SAR) by NMR method, by Fesik and colleagues in 1997.[97] In this approach, libraries of up to 10,000 small, drug-like fragments are first screened by heteronuclear NMR to identify low- to medium-affinity ligands ($K_D > 10\,\mu M$) and to locate primary binding sites on the target. A follow-up NMR screening is then performed to identify weak ligands that bind to a second site in close proximity to the first. Ligands of sites 1 and 2 are selected from the screening hits and, after subjecting to some further structural refinement the two ligands are coupled together with a linker. In favourable cases lead compounds can be designed with significantly higher affinities than the component fragments, with typical K_D values often in the nanomolar range. This simple strategy has led to the developments of lead compounds for several important therapeutic targets including the Bcl-2 family, a regulator of programmed cell death and a target for cancer,[98] and tyrosine phosphatase, a target for diabetes treatment.[99] The contribution of this NMR approach to fragment-based screening has been reviewed recently by Hajduk and colleagues[100] and some general examples of protein-detected ligand screening are shown in Table 3.

3.2. Solid-state NMR methods

Chemical shift mapping of ligand binding sites has until recently been limited to relatively small water-soluble proteins. As noted earlier, many drug targets are either large macromolecules or exist in preformed assemblies such as membrane proteins and amyloid fibrils, which are not amenable to solution NMR studies. Recent advances in sample preparation techniques and in NMR methodology in the solid-state are promising to overcome some of these difficulties and extend the molecular weight range and diversity of ligand–target complexes that can be examined for drug-discovery purposes. There is also mounting interest, however, in the possibility of mapping ligand binding sites within smaller soluble proteins in the solid state using methods analogous to those used in solution NMR. Solid-state NMR has the advantage of circumventing difficulties that might arise from examining these proteins in solution, such as aggregation or unfavourable dynamics of intrinsically unstructured regions.

Table 3. A summary of some recent applications of protein-detected NMR screening experiments in drug discovery

Receptor	Ligand(s)	Details	Reference
Tyrosine phosphatase 1B	Synthetic compounds	Heteronuclear correlation experiments identified catalytic site-binding fragments which were linked and refined to produce nanomolar K_i inhibitors	[101]
Papillomavirus E2 protein	Synthetic compounds	Compounds binding close to the DNA recognition helix were identified and refined to produce a lead compound for developing antiviral agents	[102]
Subunit of glutamate mutase	Fragment of natural co-factor	Demonstration of a method for mapping-binding interfaces between an unlabelled ligand and $^{13}C/^{15}N$-labelled protein from inter- and intramolecular NOEs	[103]
ED-B domain of fibronectin	Synthetic compounds	Identification of a lead compound that binds to the ED-B domain.	[104]
Stromelysin	Synthetic compounds	Example of a linked fragment approach leading to a 15 nanomolar inhibitor	[105]

Chemical shift analysis by solid-state NMR is critically dependent on the resolution that can be achieved from the macromolecular target in a solid preparation. The line narrowing that can be achieved is dependent in part on the degree of molecular order that can be attained within the sample, with the assistance of NMR pulse sequences to remove line broadening effects associated with scalar coupling and heterogeneity, for example. Most of the work reported to date has focused on developmental studies on a small number of well-characterised proteins including ubiquitin, BPTI and the α-spectrin SH3 domain,[106] in order to identify conditions and design methodologies to enable full or extensive assignment of NMR spectra in the solid-state. The general procedure involves preparing the protein in microcrystalline or other precipitated form using a range of precipitants or lyoprotectants such as polyethyleneglycol or ammonium sulphate. A similarity in chemical shifts for the precipitated protein and the same protein in solution is a good indication that the structure of the solid protein reflects its conformation in solution.[107] Further enhancement of resolution can be accomplished by fractional or selective isotopic labelling that can simplify the spectrum and reduce line widths by removing strong homonuclear couplings.

Recent published examples of solid-state NMR methods for the mapping of ligand-binding sites have demonstrated methodological developments using relatively small or well-characterised complexes. McDermott and co-workers used solid-state ^{13}C–^{13}C correlation experiments to observe peptide and small organic molecule ligand binding to a precipitated preparation of the uniformly ^{13}C-labelled anti-apoptotic protein Bcl-xL.[108] In this study it was suggested that chemical shift changes of as little as 0.1 ppm in the presence of ligand were meaningful and indicative of ligand binding. More recently, Jovanovich and McDermott used a selective ^{15}N, ^{13}C-labelling approach that relied upon the unique sequential occurrence of a Leu–Phe pair in a cytochrome *P450* complex to provide site-specific evidence of binding of the substrate *N*-palmitoylglycine.[109] These emerging approaches along with improvements in pulse sequences are promising to open the door to the characterisation of many drug targets that are currently inaccessible to NMR or crystallographic analysis (Table 4).

4. ISOTOPE-LABELLING STRATEGIES FOR LIGAND SCREENING

4.1. Macromolecular targets

NMR methods for the detailed structural characterisation of receptor–ligand complexes and chemical shift mapping of interfacial or binding sites rely upon isotopic (^{15}N, ^{13}C, ^{2}H) labelling of the target receptor to simplify the spectrum by reducing crowding and for line narrowing.[115] It is then possible to take advantage of a range of isotope editing or filtering experiments to generate the appropriate sub-spectra.[116] There are numerous strategies for isotope labelling recombinant proteins expressed in a suitable cellular or cell-free system depending upon the growth media utilised by the cells before and after expression has been induced. The labelling strategy employed, and, hence, the choice of growth medium, depends on the level of simplification necessary to assign the spectrum and obtain the relevant structural constraints. In many cases, uniform ^{15}N labelling of the target is sufficient, but it is often necessary to adopt more sophisticated labelling approaches to resolve and assign resonances from amino acid residues around the ligand-binding site. Amino acid-specific labelling is one attractive option, with valine and tryptophan being particularly useful probes of ligand binding; these amino acids are frequently present in active sites and ^{13}C-labelled side groups are useful markers of ligand binding.[117] Selective ^{19}F labelling of Trp side groups has provided a sensitive probe of protein–ligand interactions.[118] An extension of the amino acid-selective labelling approach is to select a pair of sequentially contiguous amino acids located close to a ligand-binding site. The target is then expressed in a minimal growth medium supplemented with an excess of the two amino acids, one ^{13}C labelled and the other ^{15}N labelled. If the contiguous sequence occurs only once in the target protein, it can be identified unambiguously using a HNCO correlation experiment.[119] Further examples of methods for isotope labelling are listed in Table 5 and several extensive reviews on the subject are recommended.[120,121]

Table 4. A summary of some recent applications of solid-state NMR methods suitable for the analysis of receptor–ligand interactions

Receptor	Method of preparation	Description	Reference
Bovine pancreatic trypsin inhibitor	Crystallised by dialysis against deionised water for 1 week at room temperature	Partial NMR assignments	[110]
Ubiquitin	Lyophilised	One of the first strategies for assignment of fully labelled proteins in the solid state	[111]
SH3 domain	Various conditions: lyophilised with and without PEG-800 and precipitated from NH_3SO_3 solution	Sample optimisation and identification of signal patterns of amino acid side chains	[112]
Ubiquitin	Crystalised by slow addition of 2-methylpentanediol to sodium citrate solution	Global structure determination	[113]
Immunoglobulin binding domain of protein G	Precipitation conditions determined by hanging drop method	Chemical shift assignments and conformational analysis	[114]

4.2. Isotope-labelled ligands

An attractive feature of ligand-detected screening methods is that ^{1}H spectra of the ligands can be observed without isotope filtering when the ligands are weakly binding and the receptor is soluble, thereby avoiding expensive and labour-intensive chemistry. There are, however, situations in which it is advantageous to exploit nuclear spins other than protons to provide the desired information. One common alternative is to observe ^{19}F. It is estimated that over 30% of compounds generated in drug-discovery programmes contain one or more fluorine atoms[128] and, as a spin-half nucleus, ^{19}F has a number of attractive properties that are suitable as a probe of ligand binding. Fluorine is not naturally present in proteins or other biological materials and hence the ^{19}F NMR spectrum is assigned readily and unambiguously. Moreover, ^{19}F is sensitive having a high gyromagnetic ratio, a wide chemical shift dispersion, favouring the detection of changes in chemical environment, and a large chemical shielding anisotropy that makes a significant contribution to transverse relaxation when a ligand is bound to a macromolecular target. Dalvit and co-workers[129,130] exploited fluorinated ligands as reference compounds in competition-binding NMR experiments to identify hits from high-throughput screens of chemical mixtures. The method was adapted to screen for biologically active enzyme inhibitors and to measure their IC_{50} values, by using native enzyme substrates modified with CF_3 groups as the reporter ligands.[131] The hits identified by this method, called

Table 5. Commonly used isotope-labelling strategies for protein-detected ligand screening

Labelling agent	Incorporation sites	Reasons for use	Reference
[$^{13}C_6$]glucose	Uniform ^{13}C	General routine	Numerous
[1-^{13}C]glucose	Alternate ^{12}C–^{13}C–^{12}C and methyl ^{13}C	Simplification of relaxation analysis; removal of ^{13}C–^{13}C scalar coupling effects	[122]
[$^{13}C_6$, d_7]glucose	Uniform ^{13}C and perdeuteration	Simplification; improvement of resolution	[123]
[d_4]acetate	Perdeuteration	Improvement of resolution	[124]
[$^{13}C_2$]acetate	Uniform^{13}C	Alternative carbon source to glucose	[125]
[4,4′-$^{13}C_2$]-α-ketoisovalerate	Selective methyl labelling: [^{13}C-δ-Me]Leu, [^{13}C-γ-Me]Val	Simplification and assignment	[95]
[3,3′-$^2H_2$,4-^{13}C]-α-ketobutyrate	($^{13}C^1H$-δ_1-Me)Ile and selective methyl protonation	Simplification	[126]
[2-^{13}C]glycerol	Fractional ^{12}C–^{13}C–^{12}C	Simplification of relaxation analysis; removal of ^{13}C–^{13}C scalar coupling effects	[127]

3-FABS (three fluorine atoms for biochemical screening) are biologically relevant as they compete with the labelled substrate for the active site of the enzyme. By using reporter ligands with three or more magnetically equivalent fluorine labels the sensitivity of the experiment allows low enzyme concentrations to be used.[132]

Solid-state NMR methods for characterising receptor-ligand complexes have tended to avoid observing proton signals directly because the high gyromagnetic ratio and abundance of protons gives rise to strong coupling networks and homogeneous line broadening. When it is not possible to exploit fluorine or other NMR active nuclei present in the ligand it is necessary to label the ligand specifically with suitable isotopes (^{13}C, ^{15}N or ^2H). This is clearly resource-intensive and often a challenge for organic chemists who must introduce the labels at chemically feasible positions which are informative, well resolved from the background signal and, if structural information is required, at sites separated by one or more flexible torsional angles. For CP-MAS measurements of ligand-binding affinities (e.g., Fig. 7), however, it is only necessary to obtain a single labelled reporter ligand that can be exploited many times in competition-binding experiments to identify hits from mixtures of unlabelled ligands. Small reporter molecules are often commercially available with ^{13}C or ^{15}N labels,[78] or else can be synthesised by substituting labelled reagents into the standard synthetic route.[133] When performing structural investigations from labelled ligands (e.g., Fig. 8) it is necessary to use a range of

sophisticated NMR methods to extract multiple distance and angular information from what may be a limited number of isotope-labelled sites.[134]

5. TECHNOLOGICAL ADVANCES IN NMR FOR LIGAND SCREENING

Sensitivity and throughput are major considerations in both protein- and ligand-observed NMR screening methods and considerable resources have been committed by instrument manufacturers and users to develop new hardware and pulse sequence methodology to streamline the NMR screening process. Astonishing gains in sensitivity have been made following the development of cryogenic probes and flow probes[135] (reviewed earlier in this series by Martin[136]), which have enabled protein solutions of less than 50 μM to be examined routinely at a 600 MHz field. Fesik[137] reports a strategy in which compound libraries are screened in groups of 100 compounds in which a single hit ($K_D < 10$ mM) among non-ligands can be readily detected. This approach potentially enables 200,000 compounds to be screened in less than a month.

An interesting new method is the so-called RAMPED-UP (rapid analysis of experimentally discriminated uniquely labelled proteins) NMR approach, which increases throughput by screening for ligand binding to a mixture of protein targets and anti-targets.[138] The method exploits unique amino acid selective isotope labelling patterns for each of the different proteins in the mixture, which also helps to reduce the possibility of detecting false-positive hits. The detection of false positives is one drawback of NMR-based screening methods and Huth and co-workers have reported a method called ALARM (a La assay to detect reactive molecules) NMR which identifies false hits resulting from molecules that oxidise or alkylate the macromolecular target.[139]

6. ANALYSIS OF DRUG–MEMBRANE INTERACTIONS

6.1. Background

The interactions between an administered drug compound and cellular membranes play a critical part in the absorption, distribution, metabolism and excretion (ADME) properties of the drug. The physical association between pharmaceutical compounds and cellular membranes may also assist in the delivery to the pharmacological target. In some cases, the drug may act directly on the plasma membrane, while in other, the accumulation of a drug at the membrane surface may counter pharmacological efficacy by lowering the effective concentration of the drug and reducing its bioavailability. Consequently, there is much interest within preclinical drug discovery to develop methods to quantify the lipid solubility of drug candidates and to characterise drug–membrane interactions in further detail.

Among these methods, NMR has a useful role to play in quantifying drug lipophilicity and in probing the mechanisms of drug–membrane interactions at the molecular level.

Drug lipophilicity is routinely quantified as a partition coefficient (defined as K_p, P or $\log P$) representing the molecular distribution in a binary isotropic solvent system such as *n*-octanol/water. Octanol/water partition coefficients are not always reliable predictors of drug lipophilicity, however. Basic aromatic amines, for example, tend to partition into phospholipid membranes more readily than is suggested by their octanol/water partition coefficients.[140] Consequently, NMR methods have been developed to examine drug partitioning into model membranes such as phospholipid vesicles, which are generally more reliable than organic solvent systems as predictors of lipophilicity.

6.2. NMR methods for determining membrane partition coefficients

Membrane partition coefficients can be measured by titrating an aqueous drug solution into an aqueous suspension of lipid vesicles. For weakly lipophilic drug candidates undergoing rapid ($>100\,s^{-1}$) exchange between the insoluble membrane phase and the aqueous environment, membrane partition coefficients may be determined by measuring chemical shift values, or another property such as relaxation rates, for the drug at different lipid concentrations [L]. The term $\Delta\delta$ is the observed change in a chemical shift value for a drug at different lipid concentrations relative to the chemical shift of the drug in aqueous solution (i.e., δ_{obs}–δ_{aq}) and is related to the partition coefficient (defined here as K_p) according to the simple relationship[141]

$$\Delta\delta = \frac{K_P \Delta\delta_{max}[L]}{K_P[L] + [W]} \tag{17}$$

where [W] is the molar concentration of water and $\Delta\delta_{max}$ the maximum change in the observable NMR quantity. Values of $\Delta\delta_{max}$ and K_p are calculated by non-linear least squares fitting to a plot of $\Delta\delta$ versus [L]. In practice, this approach works best when using small unilamellar vesicles (SUVs) of phospholipids as the model membranes, as the relatively rapid tumbling time of the vesicles gives rise to relatively narrow line widths for the drug with respect to the chemical shift changes observed. Omran *et al.*[141] used ^{19}F NMR to measure partition coefficients for fluorinated phenothiazine compounds in SUVs of phosphatidylcholine lipids. More recently, A similar method was used to measure partition coefficients of fluorinated drugs in large phospholipid vesicles that are more representative of cell membranes.[142] Changes in spin-lattice relaxation rates (ΔT_1) were measured rather than chemical shift values so as to overcome problems with broad line widths arising from the long rotational correlation times of the large vesicles.

For drugs in slow exchange (at a rate τ_{ex} of 10^{-3} s or slower) between model membrane and aqueous phases, ^2H NMR has been useful for measuring K_p values and for providing additional information abut the mechanism with which drugs

associate with the lipid bilayer.[143,144] A suitably deuterated-labelled lipophilic drug when added to lipid vesicle suspension will give rise to two components in the ^{2}H NMR spectrum provided the exchange rate is slow with respect to the residual quadrupole interaction of the membrane-bound drug. In the slow exchange regime, a narrow central line corresponding to the free drug is superimposed on a broad quadrupolar powder pattern representing the membrane partitioned drug. Simulation of the two components provides the areas of the two components from which a value of K_p can be calculated (Fig. 9).

6.3. Further characterisation

Like the drug screening methods described in the earlier sections, NMR can provide information about how drugs interact with phospholipid bilayers. The reader is

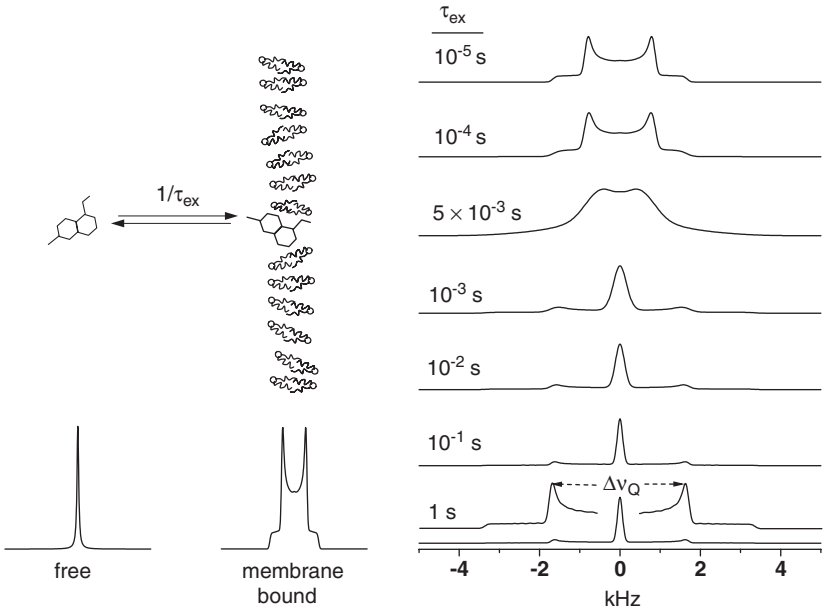

Fig. 9. Simulated ^{2}H NMR spectra of a small molecule, containing a single deuteron, undergoing exchange between an aqueous phase and a lipid bilayer at a rate of $1/\tau_{ex}$. The simulated spectra on the right assume identical equilibrium populations of the free and bilayer-associated small molecule and a residual quadrupolar splitting ($\Delta\nu_Q$) of 3.5 kHz for the bilayer-associated molecule. Individual components from the free and bilayer-associated populations can be observed only when exchange is slow compared to the residual splitting (i.e., $1/\tau_{ex} > \Delta\nu_Q$). In the slow exchange regime ($\tau_{ex} > 10^{-3}\,s^{-1}$), the membrane partition coefficient K_p of the molecule can be measured from the areas A_b and A_f of the two components representing the free and bound molecule according to the equation $K_p = A_b V_a / A_f V_b$, where V_a and V_b are the volumes of the aqueous and bilayer fractions, respectively. At faster exchange rates the two components coalesce into a single line.

referred to more extensive reviews of this subject,[145] but two NMR methods for characterising drug–membrane interactions are described here in more detail.

The ^{2}H NMR spectrum of a deuterated drug compound can provide information about drug lipophilicity as described above, but the shape of the broad powder pattern component (e.g., Fig. 10) can also report on the orientational preference of drug molecules within the lipid bilayer. Analysis of the spectra of an ^{2}H-aryl substituted imidazopyridine in membrane suspensions have shown that the membrane affinity of the compound increased as the proportion of unsaturated hydrocarbon chain lipids increased (Fig. 10). The quadrupole splitting values $\Delta\nu_Q$ for the drug depended upon the ratio of unsaturated and saturated lipids, which indicated that the orientation of the deuterated aryl group was highly sensitive to the composition of the membranes. Information about structure and orientation is particularly important when the mode of drug action involves membrane

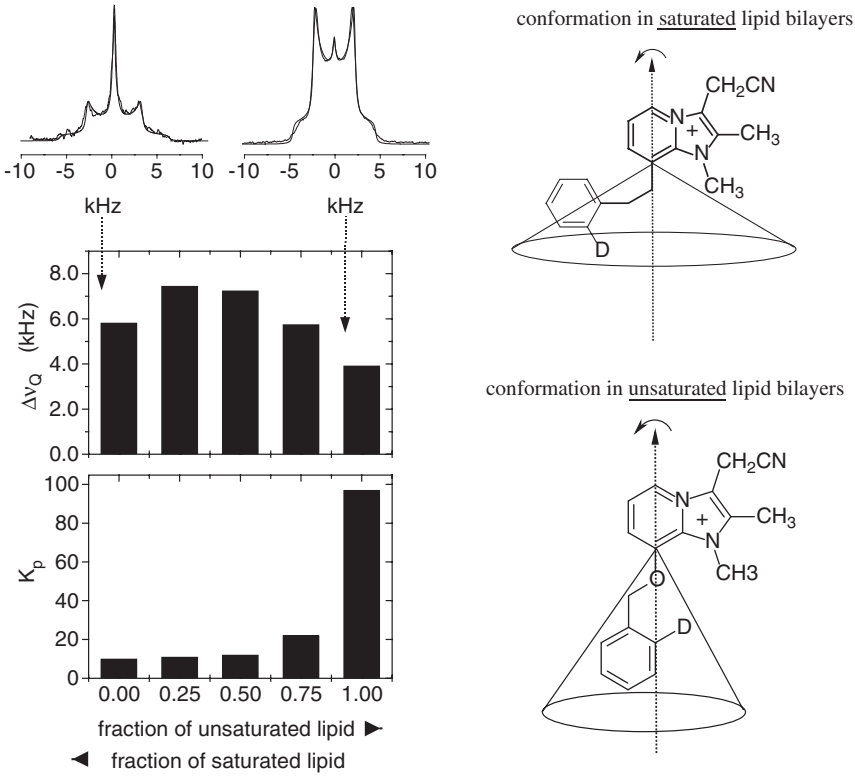

Fig. 10. A summary of the measurements from ^{2}H NMR spectra of a deuterated imidazopyridine in aqueous suspensions of membranes consisting of different mole fractions of the unsaturated phospholipid DOPC and saturated phospholipid DMPC. The ratio of the components of the spectra (typical spectra shown at the top) provide values of K_p in the different membranes, whereas values of $\Delta\nu_Q$ report on the orientation and amplitude of motion of the ^{2}H-aryl group of the drug in the different membranes. Adapted from Ref. [144]

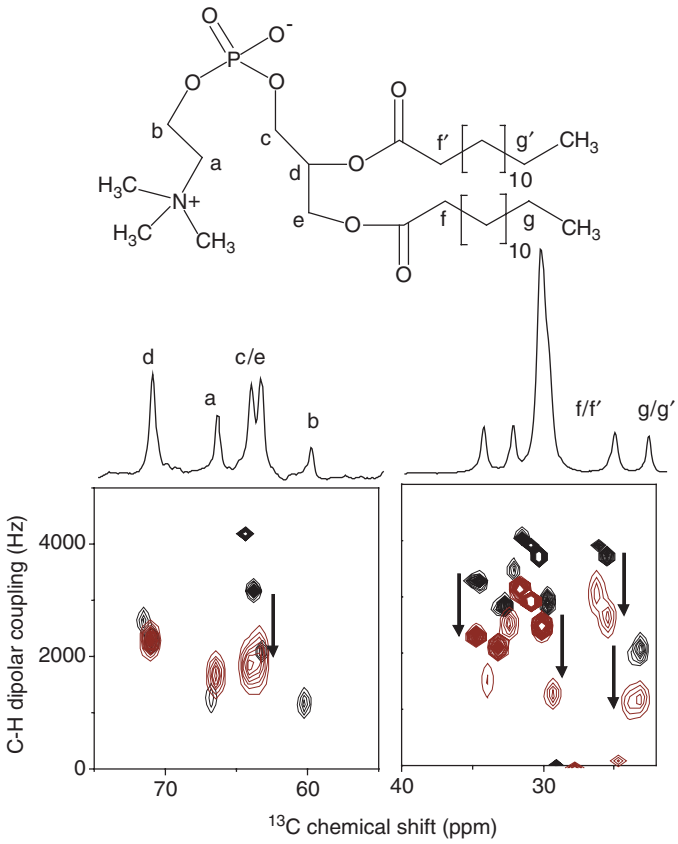

Fig. 11. A plot correlating apparent ^{1}H–^{13}C dipolar couplings (d^{app}) and ^{13}C chemical shifts compiled from 10 membrane lipid samples before (black contours) and after the addition of the lipophilic drug trifluoperazine (grey contours). The values of d^{app} corresponding to the various sites (a–g) in the lipid molecule are reduced after the addition of trifluoperazine, which is consistent with the known membrane-destabilising effect of the drug. The width of the contours in the second dimension reflects the standard error of the d^{app} values measured from the 10 samples.

interactions or when its association with the lipid bilayer assists in directing the drug to its pharmacological target.

The disadvantage of the ^{2}H NMR method is the requirement for a deuterium label to be incorporated into the drug compound. An alternative method for characterising drug–membrane interactions has been described, based upon ^{13}C CP–MAS NMR, to detect and characterise the interactions between small molecules and peptides and biomembranes.[146] In this method, a series of spectra from natural abundance ^{13}C nuclei in the phospholipids is converted into a single profile representing ^{13}C–^{1}H dipolar interactions at different sites in the lipid molecule. By combining profiles from replicate samples, it is possible to observe site-specific modulations of dipolar interactions arising from perturbations in membrane

fluidity after the addition of lipophilic compounds such as drugs. Such changes carry information about how the drug additives interact with the membranes at the molecular level (Fig. 11).

7. OUTLOOK

This chapter has reviewed some of the principal NMR methods for drug discovery that have gained prominence in the past decade. The sheer variety of the methods and applications cited here, together with many other aspects of the technique not included but reviewed elsewhere,[4,5,8,43,74] provide a measure of the versatility of NMR in pharmaceutical research. The future of NMR as a tool for drug discovery will be assured if new approaches are developed that continue to provide information of value to medicinal chemists that cannot be obtained readily by other means. For example, over half of the targets for currently marketed drugs are proteins that function within the cell membrane and the pipeline of drugs in clinical development suggests that this proportion will rise significantly in the future. Solution NMR methods like STD are already proving to be capable of detecting weak ligand binding to proteins within biomembranes and whole cells. Solid-state NMR could become an established technique for screening and resolving the structures of ligands bound to membrane-embedded receptors, but significant improvements in sensitivity and throughput must be made before the potential of this technique becomes fully realised.

REFERENCES

1. H. Kubinyi, *Nat. Rev. Drug. Discov.*, 2003, **2**, 665.
2. E. R. Zartler and M. J. Shapiro, *Curr. Opin. Chem. Biol.*, 2005, **9**, 366.
3. M. Vieth, M. G. Siegel, R. E. Higgs, I. A. Watson, D. H. Robertson, K. A. Savin, G. L. Durst and P. A. Hipskind, *J. Med. Chem.*, 2004, **47**, 224.
4. J. L. Griffin, *Curr. Opin. Chem. Biol.*, 2003, **7**, 648.
5. A. P. Watt, R. J. Mortishire-Smith, U. Gerhard and S. R. Thomas, *Curr. Opin. Drug Discov. Dev.*, 2003, **6**, 624.
6. E. R. Zartler, J. Yan, H. Mo, A. D. Kiline and M. J. Shapiro, *Curr. Top. Med. Chem.*, 2003, **3**, 25.
7. H. O. Villar, J. Yan and M. R. Hansen, *Curr. Opin. Chem. Biol.*, 2004, **8**, 387.
8. B. Meyer and T. Peters, *Angew. Chem. Int. Ed.*, 2003, **42**, 864.
9. D. Marsh and L. I. Horváth, *Advanced EPR. Applications in Biology and Chemistry*, A. J. Hoff, ed., Elsevier, Amsterdam, 1989, 707.
10. C. Fernandez and G. Wider, *Curr. Opin. Struct. Biol.*, 2003, **13**, 570.
11. L. -Y. Lian and G. C. K. Roberts, *NMR of Macromolecules*, in: G. C. K. Roberts ed., Oxford University Press, Oxford, UK, 1993, p. 153.
12. P. J. Hadjuk, E. T. Olejniczak and S. W. Fesik, *J. Am. Chem. Soc.*, 1997, **119**, 12257.
13. C. Rossi, A. Donati and M. R. Sansoni, *Chem. Phys. Lett.*, 1992, **189**, 278.
14. S. Vanwetswinkel, R. J. Heetebrij, J. van Duynhoven, J. G. Hollander, D. V. Filippov, P. J. Hajduk and G. Siegal, *Chem. Biol.*, 2005, **12**, 207.
15. M. Mayer and B. Meyer, *Angew. Chem. Int. Ed.*, 1999, **38**, 1784.
16. M. Vogtherr and T. Peters, *J. Am. Chem. Soc.*, 2000, **122**, 6093.
17. R. Meinecke and B. Meyer, *J. Med. Chem.*, 2001, **44**, 3059.

18. T. Haselhorst, T. Weimar and T. Peters, *J. Am. Chem. Soc.*, 2001, **123**, 10705.
19. J. Klein, R. Meinecke, M. Mayer and B. Meyer, *J. Am. Chem. Soc.*, 1999, **121**, 5336.
20. R. Meinecke and B. Meyer, *J. Med. Chem.*, 2001, **44**, 3059.
21. B. Claasen, M. Axmann, R. Meinecke and B. Meyer, *J. Am. Chem. Soc.*, 2005, **127**, 916.
22. P. J. Hadjuk, J. C. Mack, E. T. Olejniczak, C. Park, P. J. Dandliker and B. A. Beutel, *J. Am. Chem. Soc.*, 2004, **126**, 2390.
23. M. Mayer and T. L. James, *J. Am. Chem. Soc.*, 2002, **124**, 13376.
24. V. Jayalakshmi and N. Rama Krishna, *J. Magn. Reson.*, 2002, **155**, 106.
25. J. L. Yan, A. D. Kline, H. P. Mo, M. J. Shapiro and E. R. Zartler, *J. Magn. Reson.*, 2003, **163**, 270.
26. M. Pellechia, D. Meininger, Q. Dong, E. Chang, R. Jack and D. S. Sem, *J. Biomol. NMR*, 2002, **22**, 165.
27. S. DiMicco, C. Bassarello, G. Bifulco, R. Riccio and L. Gomez-Paloma, *Angew. Chem. Int. Ed.*, 2006, **45**, 224.
28. L. Herfurth, B. Ernst, B. Wagner, D. Ricklin, D. S. Strasser, J. L. Magnani, A. J. Benie and T. Peters, *J. Med. Chem.*, 2005, **48**, 6879.
29. C. Sandstrom, O. Berteau, E. Gemma, S. Oscarson, L. Kenne and A. M. Gronenborn, *Biochemistry*, 2004, **43**, 13926.
30. J. H. Streiff, N. O. Juranic, S. I. Macura, D. O. Warner, K. A. Jones and W. J. Perkins, *Mol. Pharmacol.*, 2004, **66**, 929.
31. M. Mayer and T. L. James, *J. Am. Chem. Soc.*, 2004, **126**, 4453.
32. L. Fielding, D. Fletcher, S. Rutherford, J. Kaur and J. Mestres, *Org. Biomol. Chem.*, 2003, **1**, 4235.
33. M. A. Johnson and B. M. Pinto, *J. Am. Chem. Soc.*, 2002, **124**, 15368.
34. T. Weimar, B. Bukowski and N. M. Young, *J. Biol. Chem.*, 2000, **275**, 37006.
35. C. Dalvit, P. Pevarello, M. Tatò, M. Veronesi, A. Vulpetti and M. Sundström, *J. Biomol. NMR*, 2000, **18**, 65.
36. C. Dalvit, G. Fogliatto, A. Stewart, M. Veronesi and B. Stockman, *J. Biomol. NMR*, 2001, **21**, 349.
37. M. D. Pelta, H. Barjat, G. A. Morris, A. L. David and S. J. Hammond, *Angew. Chem. Int. Ed.*, 1998, **36**, 706.
38. M. F. Lin, M. J. Shapiro and J. R. Wareing, *J. Org. Chem.*, 1997, **62**, 8930.
39. M. F. Lin, M. J. Shapiro and J. R. Wareing, *J. Am. Chem. Soc.*, 1997, **119**, 5249.
40. K. Bleicher, M. F. Lin, M. J. Shapiro and J. R. Wareing, *J. Org. Chem.*, 1998, **63**, 8486.
41. R. C. Anderson, M. F. Lin and M. J. Shapiro, *J. Comb. Chem.*, 1999, **1**, 69.
42. B. Antalek, *Concepts Magn. Reson.*, 2002, **14**, 225.
43. L. H. Lucas and C. K. Larive, *Concepts Magn. Reson.*, 2004, **20A**, 24.
44. E. O. Stejskal and J. E. Tanner, *J. Chem. Phys.*, 1965, **42**, 288.
45. R. M. Cotts, T. Sun, J. T. Marker and M. J. R. Hoch, *J. Magn. Reson.*, 1989, **83**, 252.
46. W. H. Otto and C. K. Larive, *J. Magn. Reson.*, 2001, **153**, 273.
47. T. S. Derrick, E. F. McFord and C. K. Larive, *J. Magn. Reson.*, 2002, **115**, 217.
48. L. H. Lucas, J. Lan, C. K. Larive, E. R. Zartler and M. J. Shapiro, *Anal. Chem.*, 2003, **75**, 627.
49. J. L. Yan, A. D. Kline, H. P. Mo, E. R. Zartler and M. J. Shapiro, *J. Am. Chem. Soc.*, 2002, **124**, 9984.
50. L. H. Lucas, K. E. Price and C. K. Larive, *J. Am. Chem. Soc.*, 2004, **126**, 14258.
51. A. Chen and M. J. Shapiro, *J. Am. Chem. Soc.*, 1998, **120**, 10258.
52. A. Chen and M. J. Shapiro, *J. Am. Chem. Soc.*, 2000, **122**, 414.
53. S. Macura and R. R. Ernst, *Mol. Phys.*, 1990, **41**, 95.
54. G. M. Clore and A. M. Gronenborn, *J. Magn. Reson.*, 1983, **53**, 423.
55. B. Meyer, T. Weimar and T. Peters, *Eur. J. Biochem.*, 1997, **246**, 705.
56. T. Weimar, *Magn. Reson. Chem.*, 2000, **38**, 315.
57. C. B. Post, *Curr. Opin. Struct. Biol.*, 2003, **13**, 581.
58. J. Fejzo, C. A. Lepre, J. W. Peng, G. W. Bemis, Ajay, M. A. Murcko and J. M. Moore, *Chem. Biol.*, 1999, **6**, 755.
59. V. M. Sánchez-Pedregal, M. Reese, J. Meiler, M. J. J. Blommers, C. Griesinger and T. Carlomagno, *Angew. Chem. Int. Ed.*, 2005, **44**, 4172.

60. C. J. Dinsmore, M. J. Bogusky, J. C. Culbertson, J. M. Bergman, C. F. Homnick, C. B. Zartman, S. D. Mosser, M. D. Schaber, R. G. Robinson, K. S. Koblan, H. E. Huber, S. L. Graham, G. D. Hartman, J. R. Huff and T. M. Williams, *J. Am. Chem. Soc.*, 2001, **123**, 2107.
61. H. Furukawa, T. Hamada, M. K. Hayashi, T. Haga, Y. Muto, H. Hirota, S. Yokoyama, K. Nagasawa and M. Ishiguro, *Mol. Pharmacol.*, 2002, **62**, 778.
62. Z. J. Chen, G. Krause and B. Reif, *J. Mol. Biol.*, 2005, **354**, 760.
63. N. Murali, G. K. Jarori, S. B. Landy and B. D. N. Rao, *Biochemistry*, 1993, **32**, 12941.
64. J. Zheng and C. B. Post, *J. Magn. Reson.*, 1993, **101**, 262.
65. R. E. London, M. E. Perlman and D. G. Davis, *J. Magn. Reson.*, 1992, **97**, 79.
66. M. Mayer and B. Meyer, *J. Med. Chem.*, 2000, **43**, 2093.
67. M. A. Johnson, M. Jaseja, W. Zou, H. J. Jennings, V. Copie, B. M. Pinto and S. H. Pincus, *J. Biol. Chem.*, 2003, **278**, 24740.
68. L. Zhang, R. H. Mattern, T. I. Malaney, M. D. Pierschbacher and M. Goodman, *J. Am. Chem. Soc.*, 2002, **124**, 2862.
69. C. C. Zhou, S. M. Swaney, D. L. Shinabarger and B. J. Stockman, *Antimicrob. Agent Chemother.*, 2002, **46**, 625.
70. P. Pristovsek, S. Simcic, B. Wraber and U. Urleb, *J. Med. Chem.*, 2005, **48**, 7911.
71. N. Godreau, D. R. Cameron, P. Bonneau, V. Gorys, C. Plouffe, M. Poirier, D. Lamarre and M. Llinas-Brunet, *J. Med. Chem.*, 2004, **47**, 123.
72. L. Chan, O. Pereira, T. J. Reddy, S. K. Das, C. Poisson, M. Courchesne, M. Proulx, A. Siddiqui, C. G. Yannopoulos, N. Nguyen-Ba, C. Roy, D. Nasturica, C. Moinet, R. Bethell, M. Hamel, L. Heureux, M. David, O. Nicolas, P. Coutemanche-Asselin, S. Brunette, D. Bilimoria and J. Bedard, *Bioorg. Med. Chem. Lett.*, 2004, **14**, 797.
73. J. Drews, *Science*, 2000, **287**, 1960.
74. A. Watts, *Nat. Rev. Drug Discov.*, 2005, **4**, 555.
75. W. Kolodziejski and J. Klinowski, *Chem. Rev.*, 2002, **102**, 613.
76. P. J. R. Spooner, N. Rutherford, A. Watts and P. J. F. Henderson, *Proc. Natl. Acad. Sci. USA*, 1994, **91**, 3877.
77. P. J. R. Spooner, L. M. Veenhoff, A. Watts and B. Poolman, *Biochemistry*, 1999, **38**, 9634.
78. S. Patching, A. Brough, R. Herbert, P. Henderson and D. A. Middleton, *J. Am. Chem. Soc.*, 2004, **126**, 3072.
79. M.P. Boland, Ph.D. Thesis, University of Manchester, 2006.
80. M. Boland and D. A. Middleton, *Magn. Reson. Chem.*, 2004, **42**, 204.
81. C. Dalvit, M. Flocco, S. Knapp, M. Mostardini, R. Perego, B. J. Stockman, M. Veronesi and M. Varasi, *J. Am. Chem. Soc.*, 2002, **124**, 7702.
82. C. Dalvit, M. Fasolini, M. Flocco, S. Knapp, P. Pevarello and M. Veronesi, *J. Med. Chem.*, 2002, **45**, 2610.
83. Y. -S. Wang, D. Liu and D. F. Wyss, *Magn. Reson. Chem.*, 2004, **42**, 485.
84. S. Dusold and A. Sebald, *Annu. Rep. NMR Spectrosc.*, 2000, **41**, 185–264.
85. X. Feng, Y. K. Lee, D. Sandstrom, M. Eden, H. Maisel, A. Sebald and M. H. Levitt, *Chem. Phys. Lett.*, 1996, **257**, 314.
86. G. Gröbner, I. J. Burnett, C. Glaubitz, G. Choi, A. J. Mason and A. Watts, *Nature*, 2000, **405**, 810.
87. P. T. F. Williamson, B. H. Meier and A. Watts, *Eur. Biophys. J.*, 2004, **33**, 247.
88. D. A. Middleton, R. Robins, X. Feng, *et al.*, *FEBS Lett.*, 1997, **410**, 269.
89. J. A. Watts, A. Watts and D. A. Middleton, *J. Biol. Chem.*, 2001, **276**, 43197.
90. S. Luca, J. F. White, A. K. Sohal, D. V. Filippov, J. H. van Boom, R. Grisshammer and M. Baldus, *Proc. Natl. Acad. Sci. USA*, 2003, **100**, 10706.
91. D. A. Middleton, S. Rankin, A. Watts and M. Esmann, *Proc. Natl. Acad. Sci. USA*, 2000, **97**, 13602.
92. E. R. Zartler and M. J. Shapiro, *Curr. Pharm. Des.*, 2005, **11**, 295.
93. M. J. S. Kelly, J. J. Ball, C. Krieger, Y. H. Yu, M. Fischer, S. Schiffman, P. Schmieder, R. Kuhne, W. Bermel, A. Bacher, G. Richter and H. Oschkinat, *Proc. Natl. Acad. Sci. USA*, 2001, **98**, 13025.

94. M. Pellechia, D. Meininger, A. L. Shen, R. Jack, C. B. Kasper and D. S. Sem, *J. Am. Chem. Soc.*, 2001, **123**, 4633.
95. P. J. Hadjuk, D. J. Augeri, J. Mack, R. Mendoza, J. Yang, S. F. Betz and S. W. Fesik, *J. Am. Chem. Soc.*, 2000, **122**, 7898.
96. P. J. Hajduk, J. R. Ruth and S. W. Fesik, *J. Med. Chem.*, 2005, **48**, 2518.
97. S. B. Shuker, P. J. Hajduk, R. P. Meadows and S. W. Fesik, *Science*, 1996, **274**, 1531.
98. T. Oltersdorf, S. W. Elmore, A. R. Shoemaker, R. C. Armstrong, D. J. Augeri, B. A. Belli, M. Bruncko, T. L. Deckwerth, J. Dinges, P. J. Hajduk, M. K. Joseph, S. Kitada, S. J. Korsmeyer, A. R. Kunzer, A. Letai, C. Li, M. J. Mitten, D. G. Nettesheim, S. Ng, P. M. Nimmer, J. M. O'Connor, A. Oleksijew, A. M. Petros, J. C. Reed, W. Shen, S. K. Tahir, C. B. Thompson, K. J. Tomaselli, B. L. Wang, M. D. Wendt, H. C. Zhang, S. W. Fesik and S. H. Rosenberg, *Nature*, 2005, **435**, 677.
99. A. M. Petros, J. Dinges, D. J. Augeri, S. A. Baumeister, D. A. Betebenner, M. G. Bures, S. W. Elmore, P. J. Hajduk, M. K. Joseph, S. K. Landis, D. G. Nettesheim, S. H. Rosenberg, W. Shen, S. Thomas, X. L. Wang, I. Zanze, H. C. Zhang and S. W. Fesik, *J. Med. Chem.*, 2006, **49**, 656.
100. J. R. Huth, C. H. Sun, D. R. Sauer and P. J. Hajduk, *Methods Enzymol.*, 2005, **394**, 549.
101. G. Lui, Z. L. Xin, H. Liang, H. C. Abad-Zapatero, P. J. Hajduk, D. A. Janowick, B. G. Szczepankiewicz, Z. H. Pei, C. W. Hutchins, S. J. Ballaron, M. A. Stashko, T. H. Lubben, C. E. Berg, C. M. Rondinone, J. M. Trevillyan and M. R. Jirousek, *J. Med. Chem.*, 2003, **46**, 3437.
102. P. J. Hajduk, J. Dinges, G. F. Miknis, M. Merlock, T. Middleton, D. J. Kempf, D. A. Egan, K. A. Walter, T. S. Robins, S. B. Shuker, T. F. Holzman and S. W. Fesik, *J. Med. Chem.*, 1997, **40**, 3144.
103. C. Eichmuller, W. Schuler, R. Konrat and B. Krautler, *J. Biomol. NMR*, 2001, **21**, 107.
104. J. Scheuermann, A. Volonterio, O. Zerbe, M. Zanda and D. Neri, *Drug Dev. Res.*, 2003, **58**, 268.
105. P. J. Hajduk, G. Sheppard, D. G. Nettesheim, E. T. Olejniczak, S. B. Shuker, R. P. Meadows, D. H. Steinman, G. M. Carrera, P. A. Marcotte, J. Severin, K. Walter, H. Smith, E. Gubbins, R. Simmer, T. F. Holzman, D. W. Morgan, S. K. Davidsen, J. B. Summers and S. W. Fesik, *J. Am. Chem. Soc.*, 1997, **119**, 5818.
106. F. Castellani, B. van Rossum, A. Diehl, M. Schubert, K. Rehbein and H. Oschkinat, *Nature*, 2002, **420**, 98.
107. H. B. R. Cole, S. W. Sparks and D. A. Torchia, *Proc. Natl. Acad. Sci. USA*, 1988, **85**, 6362.
108. S. G. Zech, A. J. Wand and A. E. McDermott, *J. Am. Chem. Soc.*, 2005, **127**, 8618.
109. T. Jovanovic and A. E. McDermott, *J. Am. Chem. Soc.*, 2005, **127**, 13548.
110. A. McDermott, T. Polenova, A. Bockmann, K. W. Zilm, E. K. Paulsen, R. W. Martin and G. T. Montelione, *J. Biomol. NMR*, 2000, **16**, 209.
111. S. K. Straus, T. Bremi and R. R. Ernst, *J. Biomol. NMR*, 1998, **12**, 39.
112. J. Pauli, B. van Rossum, H. Forster, H. J. M. de Groot and H. Oschkinat, *J. Magn. Reson.*, 2000, **143**, 411.
113. S. G. Zech, A. J. Wand and A. E. McDermott, *J. Am. Chem. Soc.*, 2005, **127**, 8618.
114. W. T. Franks, D. H. Zhou, B. J. Wylie, B. G. Money, D. T. Graesser, H. L. Frericks, G. Sahota and C. M. Rienstra, *J. Am. Chem. Soc.*, 2005, **127**, 12291.
115. M. Kainosho, *Nat. Struct. Biol. Suppl.*, 1997, **4**, 858.
116. A. L. Breeze, *Prog. Nucl. Magn. Reson. Spectrosc.*, 2000, **36**, 323.
117. R. A. Rodriguez-Mias and M. Pellecchia, *J. Am. Chem. Soc.*, 2003, **125**, 2892.
118. M. Leone, R. A. Rodriguez-Mias and M. Pellecchia, *ChemBioChem*, 2003, **4**, 649.
119. J. Weigelt, M. J. van Dongen, J. Uppenberg, J. Schultz and M. Wikstrom, *J. Am. Chem. Soc.*, 2002, **124**, 2446.
120. L. -Y. Lian and D. A. Middleton, *Prog. NMR Spectrosc.*, 2001, **39**, 171.
121. J. Weigelt, M. Wikstrom, J. Schultz and M. J. van Dongen, *Comb. Chem. High Throughput Screen*, 2002, **5**, 623.
122. M. Hong and K. Jakes, *J. Biomol. NMR*, 1999, **14**, 71.
123. B. Leiting, F. Marsilio and J. F. O'Connell, *Anal. Biochem.*, 1998, **265**, 351.
124. R. A. Venters, C. C. Huang, B. T. Farmer, R. Trolard, L. D. Spicer and C. A. Fierke, *J. Biomol. NMR*, 1995, **5**, 339.
125. R. A. Venters, T. L. Calderone, L. D. Spicer and C. A. Fierke, *Biochemistry*, 1991, **30**, 4491.

126. K. H. Gardner and L. E. Kay, *J. Am. Chem. Soc.*, 1997, **119**, 7599.
127. D. M. LeMaster and D. M. Kushlan, *J. Am. Chem. Soc.*, 1996, **118**, 9255.
128. H. J. Bohm, D. Banner, S. Bendels, M. Kansy, B. Kuhn, K. Muller, U. Obst-Sander and M. Stahl, *ChemBioChem*, 2004, **5**, 637.
129. C. Dalvit, M. Flocco, M. Veronesi and B. J. Stockman, *Comb. Chem. High Throughput Screen*, 2002, **5**, 605.
130. C. Dalvit, P. E. Fagerness, D. T. A. Hadden, R. W. Sarver and B. J. Stockman, *J. Am. Chem. Soc.*, 2003, **125**, 7696.
131. C. Dalvit, E. Ardini, M. Flocco, G. P. Fogliatto, N. Mongelli and M. Veronesi, *J. Am. Chem. Soc.*, 2003, **125**, 14620.
132. C. Dalvit, G. Papeo, N. Mongelli, P. Giordano, B. Saccardo, A. Costa and M. Veronesi, *Drug Dev. Res.*, 2005, **64**, 105.
133. S. G. Patching, P. J. F. Henderson, D. A. Middleton and R. B. Herbert, *Org. Biomol. Chem.*, 2003, **1**, 2057.
134. D. A. Middleton, C. Le Duff, X. Peng, D. G. Reid and D. Saunders, *J. Am. Chem. Soc.*, 2000, **122**, 1161.
135. R. L. Haner, W. Llanos and L. Mueller, *J. Magn. Reson.*, 2000, **143**, 69.
136. G. E. Martin, *Annu. Rep. NMR Spectrosc.*, 2005, **56**, 1.
137. P. J. Hajduk, T. Gerfin, J. -M. Boehlen, M. Häberli, D. Marek and S. W. Fesik, *J. Med. Chem.*, 1999, **42**, 2315.
138. E. R. Zartler, J. Hanson, B. E. Jones, A. D. Kline, G. Martin, H. Mo, M. J. Shapiro, R. Wang, H. Wu and J. Yan, *J. Am. Chem. Soc.*, 2003, **125**, 10941.
139. J. R. Huth, R. Mendoza, E. T. Olejniczak, R. W. Johnson, D. A. Cothron, Y. Y. Liu, C. G. Lerner, J. Chen and P. J. Hajduk, *J. Am. Chem. Soc.*, 2005, **127**, 217.
140. R. P. Austin, A. M. Davis and C. N. Manners, *J. Pharm. Sci.*, 1995, **84**, 1180.
141. A. A. Omran, K. Kitamura, S. Takegami, M. Kume, M. Yoshida, A. A. Y. El-Sayed, M. H. Mohamed and M. Abdel-Mottaleb, *J. Pharm. Biomed. Anal.*, 2002, **30**, 1087.
142. M. P. Boland, Ph.D. Thesis, University of Manchester, 2006.
143. D. M. Fraser, L. C. M. van Gorkom and A. Watts, *Biochim. Biophys. Acta*, 1991, **1069**, 53.
144. D. A. Middleton, D. G. Reid and A. Watts, *J. Pharm. Sci.*, 2004, **93**, 507.
145. J. K. Seydel and M. Wiese, *Methods and Principles in Med. Chem.*, Vol. 15, R. Mannhold, H. Kubinyi and G. Folkers, eds, Wiley, Weinheim, 1–349.
146. D. A. Middleton, E. Hughes and J. Madine, *J. Am. Chem. Soc.*, 2004, **126**, 9478.

Recent Advances in NMR Studies of Cyclophanes

LUDGER ERNST

Department of Chemistry, Technical University of Braunschweig, 38106 Braunschweig, Germany

This review on the application of NMR spectroscopy to the field of cyclophanes follows earlier ones by Smith (covering the period up to 1964), by Mitchell (up to late 1981), by Ernst (1982–1999), and by Ernst and Ibrom (2000 to early 2003). It covers the literature from the beginning of 2003 until the end of 2005. To facilitate the access to information relating to particular molecules, the material is arranged according to classes of compounds. The review is not intended to be exhaustive but includes only those references in which NMR spectroscopy is a topic of its own and not used simply to characterize cyclophane molecules. Owing to the specific nature of cyclophanes, unusual ^1H chemical shifts caused by the magnetic anisotropy of aromatic systems and the mobility of cyclophane bridges are ever-recurring motifs. The mobility of short bridges is often restricted and thus brings the rate of existing conformational processes into the range observable by dynamic NMR spectroscopy.

1. INTRODUCTION AND SCOPE

An abundance of papers exist that deal with NMR spectroscopy of cyclophanes and a number of reviews have covered the field until the beginning of 2003. In 1964, Smith already reviewed the subject in his book ''Bridged aromatic compounds''.[1] An often-cited two-volume book edited by Keehn and Rosenfeld[2] includes a chapter by Mitchell on the NMR properties and conformational behaviour of

ANNUAL REPORTS ON NMR SPECTROSCOPY
VOLUME 60 ISSN 0066 4103
DOI 10.1016/S0066-4103(06)60003-3

cyclophanes,[3] which treats the literature up to the end of 1981. This book also contains chapters on [*n*]cyclophanes,[4] heterophanes,[5] nonbenzenoid cyclophanes[6] and multilayered cyclophanes,[7] in which the authors discuss the NMR aspects of their respective classes of compounds. The author of the present chapter has summarized the literature on NMR spectroscopy of cyclophanes that appeared between 1982 and mid-1999[8] and between 1999 and early 2003.[9] Consequently, we now only cover the subsequent period until the end of 2005. Still, in view of the limited space available, a number of restrictions had to be made with respect to the literature references included. As in our previous reviews,[8,9] the focus is directed on the NMR properties of the cyclophanes themselves, not on the changes that occur when the cyclophanes interact with other molecules. Thus host–guest or supramolecular interactions upon NMR spectra are covered only in a few cases, i.e. when they appear to constitute very instructive examples (cf. Sections 6 and 8). Accordingly, crownether derivatives of cyclophanes and their thio analogues, polyazacyclophanes, calixarenes and analogous compounds, the cavitands, the carcerands, the spherands or the rotaxanes, are usually not treated, for the main interest in these compounds lies in their suitability for such interactions. Also, cyclophanes possessing only bridges spanning *ortho*-positions are not considered proper cyclophanes, because most of them do not show the characteristic NMR spectroscopic properties usually associated with cyclophanes, such as shielding of protons positioned above/below the planes of aromatic rings. Orthocyclophanes are therefore also omitted.

Chemical Abstracts online searches (through SciFinder) were carried out for papers containing the combination of the terms "NMR" and "phane" or "cyclophane" (or related terms). The latest such search was performed on 19th December 2005. Also "Current Contents: Physical, Chemical and Earth Sciences" was searched in a similar fashion for the years 2003–2005. A few earlier papers that came to our attention by other ways and which had not been treated in Refs. 8 or 9 were also included. Thus, the literature reviewed here spans the period from the beginning of 2003 to approximately the end of 2005. The type of search carried out implies that the respective author must have considered the NMR-related content of his/her paper important enough to mention it in the title, abstract or keywords. The papers found by this method were then inspected whether they contained interesting enough information to be included in this review. Admittedly, certain personal preferences may have influenced the selection process.

Also in line with our earlier cyclophane reviews, the material presented in this article is arranged according to classes of compounds. This makes it easy for the reader to find information related to specific molecules. Cross-references to other sections are given when papers deal with compounds belonging to different classes.

2. [*n*]PHANES

[*n*]Phanes are aromatic systems bridged by a single alkane chain of length *n*. We found only relatively few literature references that fall into this category and are of interest from an NMR point of view. As stated above, phanes containing

ortho-bridges only were not considered. In a very careful study of 13-methyl-2, 6-dithia[7]metacyclophane (**1**), Mitchell *et al.*[10] calculated the ground state energies (DFT) and the ^{1}H and ^{13}C chemical shifts (GIAO-HF/6-31G*) of all relevant conformers involved in the conformational equilibrium of this compound. At 175 K, the unsymmetrical conformer **1a** can be observed in slow exchange and is also calculated to dominate the equilibrium (87%). At 300 K its mole fraction is calculated to be 67% with the next two higher energy conformers at 18% and 11%. The computed internal shift differences of both the major conformer and of the averaged ensemble (according to the calculated mole fractions) agreed well with the experimental findings. The authors concluded that this agreement is good evidence that the calculated geometry is close to the experimental structure. The most characteristic chemical shift is that of H-4a: $\delta = -1.79$ (measured at 175 K) and -1.92 ppm (computed for **1a**), which is caused by the position of this proton in the strongly shielding region of the aromatic ring current. The experimental and calculated shifts of H-4b are $\delta = 1.18$ (175 K) and 0.71 ppm, respectively. Variable temperature spectra were also recorded: two ^{1}H and two ^{13}C signal coalescences consistently resulted in a barrier $\Delta G^{\ddagger}$ of 40.4 ± 0.2 kJ mol^{-1}. The process observed was assumed to be the interconversion of **1a** into its enantiomer through a symmetrical intermediate. It was anticipated that the overall good performance of the calculations would improve the confidence level that organic chemists would have in such calculations.

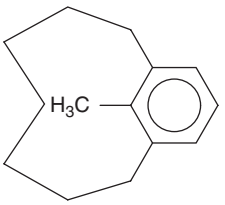

1

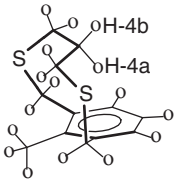

1a

Another series of metacyclophanes, **2a–2d**, with nine-, eight-, seven-, and six-membered methylene bridges was investigated by Nitta *et al.*[11] with respect to the conformational behaviour of the compounds. Whereas **2a–2c** show chemically equivalent geminal methylene protons at room temperature which indicates rapid bridge flipping between the two faces of the pyridone ring, the geminal protons in **2d** are nonequivalent and no bridge flipping can be effected up to at least 423 K. Lowering the temperature slows down the pseudo-rotational movement of the bridge depicted by formulae **2dA** and **2dB**. In each of these conformers, one of the protons on the two central bridge carbon atoms is situated over the aromatic ring and hence strongly shielded ($\delta = -0.74$ ppm). The $\Delta G^{\ddagger}$ values of the pseudo-rotational movement amounts to 43.9 kJ mol^{-1} at the coalescence temperature of 243 K. When **2c** was cooled down, the flipping of its seven-membered bridge could be stopped, and $\Delta G^{\ddagger}$ was determined to be 50.2 kJ mol^{-1} at 273 K. The chemical shifts of the protons of the central methylene group at 183 K were observed to be $\delta = -0.83$ (*endo*) and 1.35 ppm (*exo*). They average to $\delta = 0.37$ ppm at room temperature. Overall, the conformational behaviour of **2c** and **2d** was found to be very similar to that of the corresponding 6-phenyl[*n*](2,4)pyridinophanes which had

previously been described by the same authors[12,13] (also cf. Ref. 8).

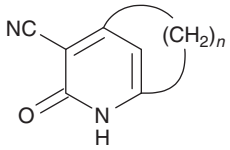

2	*n*
a	9
b	8
c	7
d	6

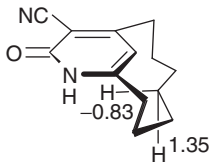

2c (at 183 K)

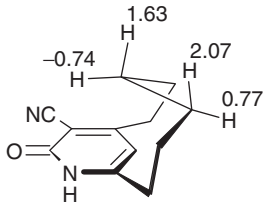

2dA

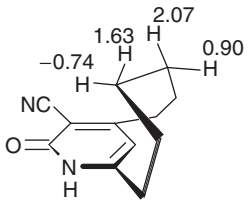

2dB

In continuation of their earlier work[14] on the evaluation of the effect of strain on the reduction of pyrene, Aprahamian *et al.*[15] reduced the two curved systems **3** and its benzoannelated homologue **4** with lithium metal in THF-d_8 and followed the reduction process by NMR spectroscopy. In contrast to the behaviour of pyrene and 2,7-dimethylpyrene themselves, **3** and **4** both form dimeric anions **5** and **6**, respectively, via the radical anions of **3** and **4**. The structures of **5** and **6** were derived from H,C-HSQC and -HMBC spectra. In **5** both C-6 and H-6 are strongly shielded ($\delta = 48.3$ and 3.22 ppm, respectively) and ^1J(C-6,H-6) has a value of 128.2 Hz, which showed the rehybridization of C-6 from sp^2 to sp^3. The observation of a long-range correlation (^2J) between C-6 and H-6′ in the HMBC spectrum and a ^3J(H-6,H-6′) coupling constant of 10.3 Hz in the ^{13}C satellites of the sensitivity-enhanced HSQC spectrum proved that dimerization had taken place. Compound **6** had NMR properties similar to **5**. Both **5** and **6** are of intermediary nature and are further reduced to **7** and **8** already described earlier[14] and discussed in our previous review,[9] where the structural formula of **7** (**20** in Ref. 9) is in error. The behaviour of (2,7)pyrenophanes with longer tethers was studied in a later paper.[16] Like **3**, [8]phane **9a** undergoes one-electron reduction and dimerizes but, opposed to **5**, the dimeric anion is not converted into a structure analogous to **7**. Reduction of the higher phanes **9b** and **9c** via short-lived paramagnetic radical anions, which give no ^{1}H NMR spectra, leads to dimers analogous to **5** followed by the formation of dianionic antiaromatic species $\mathbf{9b}^{2-}$ and $\mathbf{9c}^{2-}$, respectively, which eventually cleave the solvent in order to turn into the aromatic species **10b** and **10c**. In this respect, the relatively strain-free phanes **9b** and **9c** behave in a similar fashion as pyrene itself. The influence of the

antiaromaticity of **9b**$^{2-}$ and **9c**$^{2-}$ on the ^{1}H chemical shifts of these ions is remarkable. The former is given as an example. At temperatures of 200 K or lower, the dynamic process of the tether is slow ($\Delta G^{\ddagger} = 36.0 \pm 0.9\,\mathrm{kJ\,mol^{-1}}$) and hence lowers its symmetry such that the protons of each methylene group become, at least in principle, diastereotopic. The most dissimilar chemical shifts are found for the protons at C-14, namely $\delta = 2.58$ and 7.98 ppm when the counterions are Li^{+}, and $\delta = 3.22$ and 9.93 ppm when they are K^{+}. These protons point to opposite directions, one away from the paramagnetic electron current and the other towards it. The averaged pyrene proton shifts in **9b**$^{2-}$ amount to $\delta = 1.44$ and 2.58 ppm, for H-1 and H-10, respectively, in the case of the lithium salt.

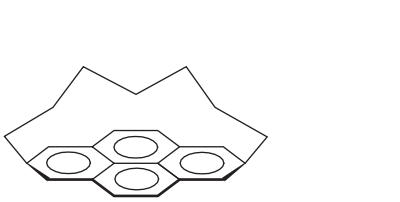

3

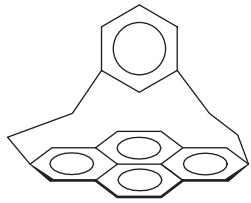

4

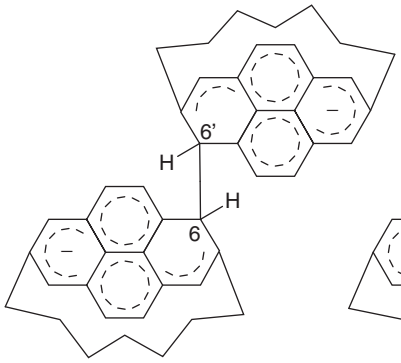

5

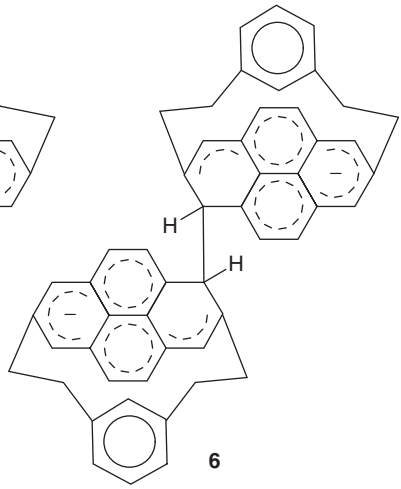

6

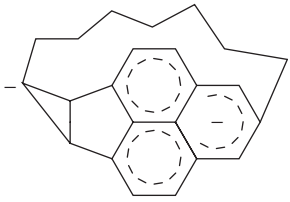

7

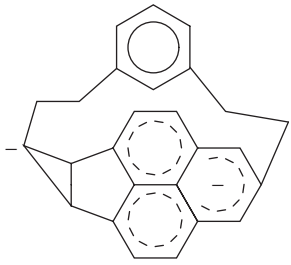

8

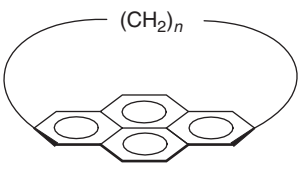

9	n
a	8
b	9
c	10

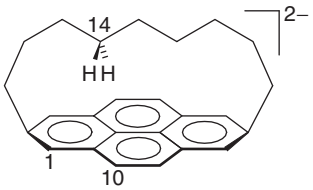

9b^{2-}

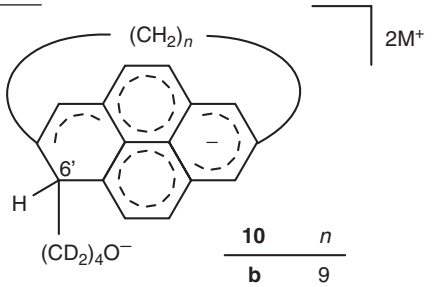

10	n
b	9
c	10

A stereochemically very interesting system containing two [10]paracyclophanes connected in a biphenyl fashion was introduced by Bringmann *et al.*[17] In this system, the biaryl axis connects the constitutionally identical but oppositely configured planar-chiral paracyclophane moieties. It is therefore a (planar-chiral)–(axially chiral)–(planar-chiral) molecule which, when biaryl rotation is fast on the NMR timescale, constitutes a *meso*-compound and, at slow biaryl rotational rates, a chiral molecule of C_1-symmetry. At room temperature, rotation about the biphenyl axis in **11a** is slow and the two halves of the molecule are not symmetry-related. Hence they possess different chemical shifts, for example, the two aryl protons show an enormous shift difference of $\Delta\delta = 0.50$ ppm (in $CDCl_3$). To achieve a coalescence of these signals, the ^{1}H NMR spectra at elevated temperatures had to be recorded on a 80 MHz spectrometer. Coalescence was observed at 416 K from which, with $\Delta\nu = 38.1$ Hz (in $C_2D_2Cl_4$), $\Delta G^{\ddagger}$ was calculated to be 87 kJ mol^{-1}. Compound **11b** behaves similarly to **11a**. Its aryl protons display an even larger shift difference of 0.63 ppm. Further, four different OH proton signals were observed (in DMSO-d_6) and 32 out of the theoretically possible number of 36 ^{13}C NMR signals.

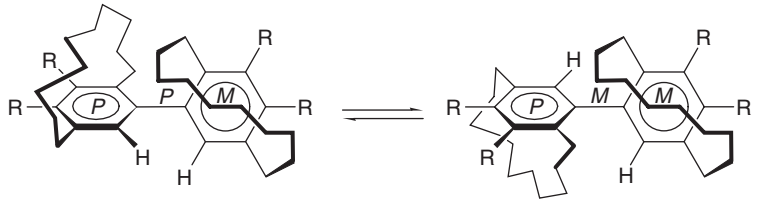

(p*P*, a*P*, p*M*) **11a** (R = CO_2Me) **11b** (R = CH_2OH) (p*P*, a*M*, p*M*)

3. [2.2]PHANES

Regarding the number of references found for this class of compounds, the [2.2]phanes are the most popular among the different cyclophane varieties covered in this article. This is certainly due to the fact that the [2.2]bridges are the shortest ones that can conveniently be prepared, so the [2.2]phanes have the highest degree of cyclophane properties of the classes of compounds considered. Two papers[15,16] dealing with [2.2]phanes have already been discussed in Section 2. From an NMR point of view, not many novel aspects were reported for [2.2]metacyclophanes. Georghiou and coworkers[18] described a [2.2](1,3)naphthalenophane system for which there is the possibility of a *transoid* (**12**) and a *cisoid* (**13**) arrangement of the nonbridged (outer) aromatic rings. The chemical shifts of these isomers are rather similar which is understandable in view of the large distances between the outer rings of the naphthalene moieties. The chemical shifts of the bridge protons are $\delta = 3.95$, 3.72, 2.24, and 2.00 ppm for **12** and $\delta = 3.97$, 3.72, 2.16, and 2.01 ppm for **13**. The patterns of the ^{1}H multiplets of both isomers were described to be "dramatically different". This should not be really surprising because in the *cisoid* isomer **13** the two bridges are different, one constituting an AA′XX′ and the other a BB′YY′ spin system such as in *anti*-[2.2]metacyclophane[19] itself (where, of course, the bridges are equivalent). In the *transoid* isomer **12**, the bridges are equivalent, but the four protons in each bridge are chemically nonequivalent, so the two bridges give a common ABXY spectrum. The authors did not give specific assignments of the bridge proton shifts. Some dithia[3.3](1,3)naphthalenophanes, which were synthetic precursors to **12** and **13**, are discussed in Section 4.

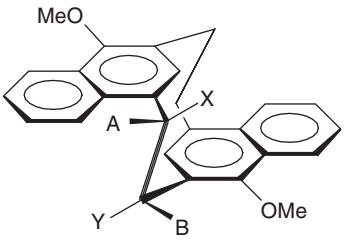

12

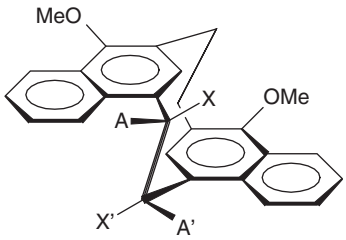

13

A few papers deal with [2.2]metacyclophanedienes (CPD) which can be switched photochemically or thermally to convert the two isolated 6π systems of the *meta*-substituted benzene rings (the olefinic bridges being orthogonal to the aromatic systems) into a 14π dihydropyrene (DHP). The DHPs can be photochemically switched back to CPDs. Mitchell and coworkers[20] followed the DHP (**14**)→CPD (**15**) conversion by NMR for approximately a dozen compounds that differed by the aromatic systems annelated to one or both of the olefinic bridges. We just mention one example, viz. the pair **16/17**. By following the isomerization with ^{1}H NMR at various temperatures between 233 K and 263 K, E_a for the process **16** → **17** was determined to be 84.1 ± 2.9 kJ mol^{-1}. This means a half-life time of 400 min at 233 K and of 1–2 s at 293 K. The ^{1}H methyl chemical shift is $\delta = -3.41$ ppm for **16** and

+1.07 ppm for **17**. Molecules were also described containing two or three DHP/CPD switches simultaneously. Later, Mitchell[21] also studied the equilibrium **18/19** and concluded that the effect of the annelated cyclopentadienide was consistent with it being less aromatic than benzene (cf. the δ_H values given with the formulae). The ^{7}Li NMR spectrum of the associated cation showed a chemical shift of −1.02 ppm (in THF-d_8 solution) after UV irradiation, when only the DHP form was present, and an averaged shift of −2.72 ppm after irradiation with visible light for the photostationary state of 85% CPD and 15% DHP. When the solvent was C_6D_6, the behaviour was more complex.

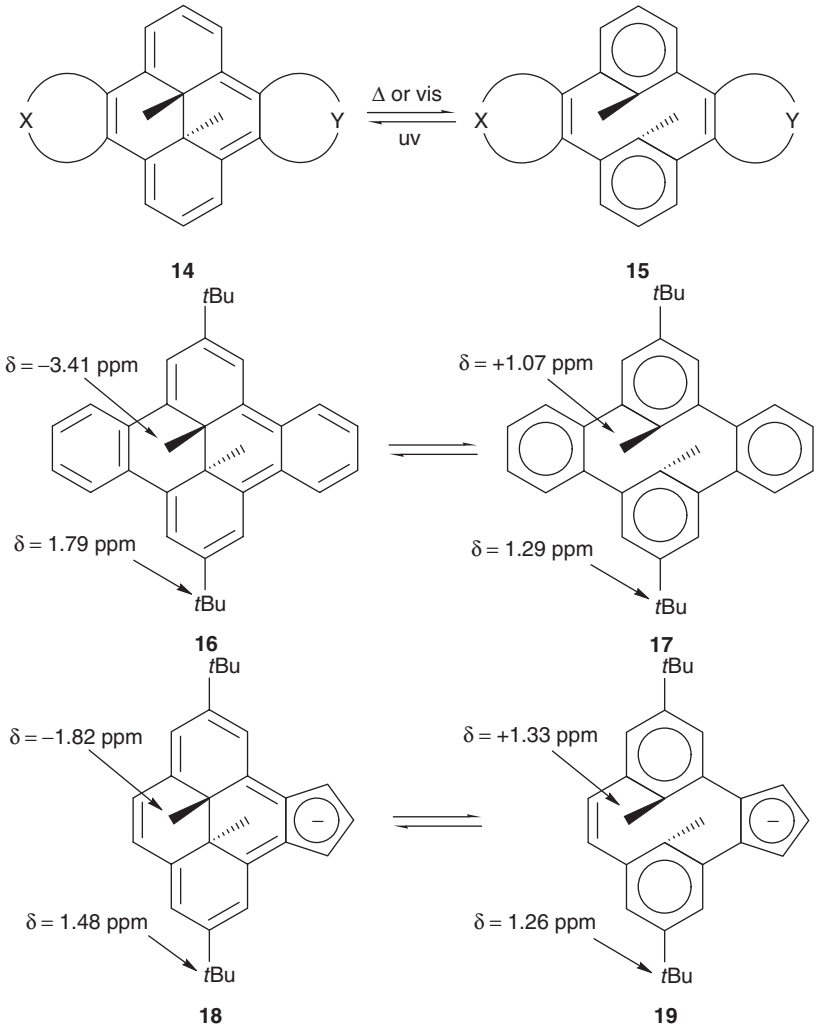

On the way to a DHP with a bulky internal substituent, Ting and Lai[22] obtained 8-methyl-16-(2-naphthyl)-CPD **20**. The conformation depicted in the formula was assumed to be the most favourable one because it avoids the close approach of the

outer naphthalene and the opposite benzene ring. The relatively high shielding of H-4,6 ($\delta = 6.14$ ppm) and H-5 ($\delta = 6.22$ ppm) was attributed to the effect of the naphthyl ring, and H-4′ ($\delta = 7.46$ ppm) is also appreciably shielded by the opposite benzene ring relative to the other naphthalene protons.

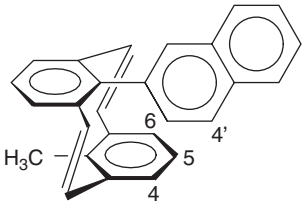

20

[2.2]Paracyclophanes are the most common variety of the [2.2]phanes covered in this section. The (2-pyridinyl)[2.2]paracyclophane **22** was obtained by the reaction of nitrone **21** with (*E*)-1,2-dibenzoylethene.[23] The (*E*) configuration of the starting material **21** was secured by H{H} nuclear Overhauser enhancement (NOE) measurements and the structure of **22** by extensive 1D and 2D ^{1}H and ^{13}C NMR experiments yielding full signal assignments. Another paper from the same group[24] described diastereomeric pseudo-geminally substituted bis(propargylic alcohols) **23**. These were dehydrated to give the meso (**24m**) and chiral (**24c**) ethers, the configuration of which followed from the symmetry or nonsymmetry of their NMR spectra. The second conceivable *meso*-isomer (ether bridge pointing towards the *ortho*-CH_2CH_2 bridge) was not observed. Diols **25** also occurred as one meso and one chiral diastereomer, and these had surprisingly different chemical shifts of their substituents; **25m**: $\delta_C = 26.9$ (CH_3), 67.4 (CH), $\delta_H = 1.75$ (CH_3), 5.26 (CH) ppm; **25c**: $\delta_C = 24.4$, 27.1 (CH_3), 66.6, 71.4 (CH), $\delta_H = 1.15$, 1.36 (CH_3), 4.70, 5.16 (CH) ppm.

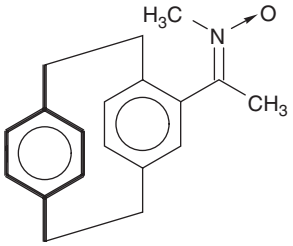

21

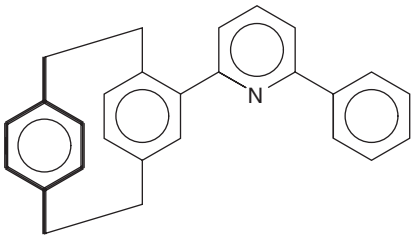

22

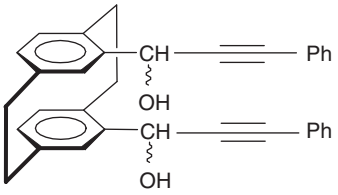

23

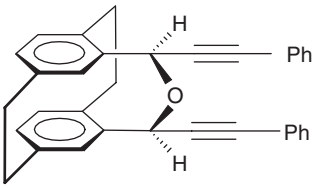

24m

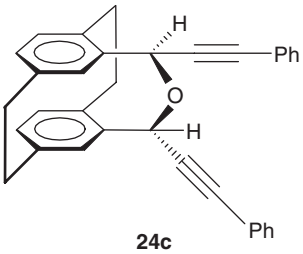

24c

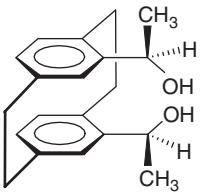

25m

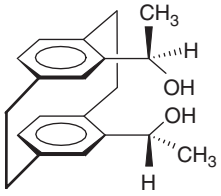

25c

Roche and coworkers[25] presented, for the first time, the complete assignment of the ^{19}F, ^{13}C, and ^{1}H NMR spectra of an *aryl*-monosubstituted [2.2]paracyclophane with perfluorinated bridges, 4-amino-1,1,2,2,9,9,10,10-octafluoro[2.2]paracyclophane (**26**). The unambiguous assignments were achieved through the combination of F,H-HOESY, H,H-COSY, and F,F-COSY. The assignment started with the H-5 signal (the only one without an *ortho*-H,H coupling), this signal showed an NOE to a fluorine signal that was therefore assigned to the spatially close F-9 s (*syn* to the NH_2 substituent), which then from F,F-COSY gave F-9a (*anti*). The ^{2}J(F,F) couplings are characteristically large, of the order of 240 Hz. F-9a exhibited an NOE to H-7, which showed an H,H-COSY interaction to H-8, which displayed an NOE to F-2a. F-2a from F,F-COSY gave F-2 s, which also gave an NOE to the NH_2 signal. Thus the hydrogens and fluorines on the lower deck of **26** were assigned. Of the several possible ways to gain entry into the upper deck, the following one was chosen. It made use of the weaker NOE between H and F atoms on the same side of the molecule but on different decks (e.g., F-9 s to H-16; note that the numbering of the upper deck differs from that used in Ref. 25 in order to achieve consistency within the present article). Starting at F-9 s that showed a strong NOE to H-5 and a weaker NOE to a signal that was assigned to H-16, from the H,H-COSY H-16 revealed H-15 (pseudo-geminal to NH_2). H-15 exhibited an NOE to F-1 s, which from F,F-COSY led to F-1a. The latter displayed an NOE to H-13, which from H,H-COSY gave H-12. H-12 revealed an NOE with F-10a, which from F,F-COSY gave F-10 s. F-10 s showed an NOE back to H-16, which completed the ^{19}F and ^{1}H assignments. In the absence of ^{19}F-decoupling, small or unresolved ^{4}J(F,H) couplings generally prevented the observation of ^{4}J(H,H) couplings which normally would have facilitated the proton assignments. C,H-HETCOR experiments optimized for $^{1}J(C,H) = 140$ and for $^{3}J(C,H) = 8$ Hz were carried out to achieve assignment of the signals of the proton-bearing and

quaternary carbon atoms, respectively. C,F-HETCOR optimized for $^{3}J(F,C) = 7$ Hz showed preferred *anti*-$^{3}J(F,C)$ couplings, for example, from C-13 to F-1 s but not to F-1a. During the ^{19}F studies it was observed that H/D exchange was taking place between the NH_2 substituent and the deuterated acetone used as the solvent. Deshielding isotope effects of the ND_2 group upon ^{19}F chemical shifts were found to decrease in the following order: F-2 s (0.08 ppm) > F-2a (0.01 ppm) ≈ F-1 s (0.01 ppm) > F-9 s (< 0.01 ppm).

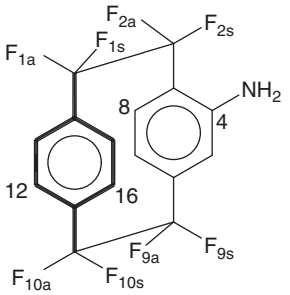

26

Another report from the Roche group[26] describes compounds containing two octafluoro[2.2]paracyclophanyl (OFP) groups on a *para*-phenylene (**27**) or a biphenyl-4,4′-diyl (**28**) spacer. Both compounds display only one set of ^{1}H and ^{19}F signals from which the authors concluded that there is no evidence of significant line broadening due to restricted rotation. It does, however, also mean that the meso and chiral diastereomers, which are principally possible and are most likely formed in the synthesis, have spectra so similar that they cannot be distinguished. A reasonable explanation would be that the two chiral OFP subunits in the diastereomers are too far apart to influence each other to a noticeable amount.

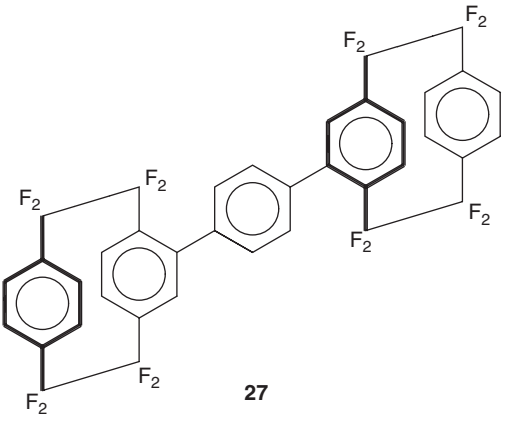

27

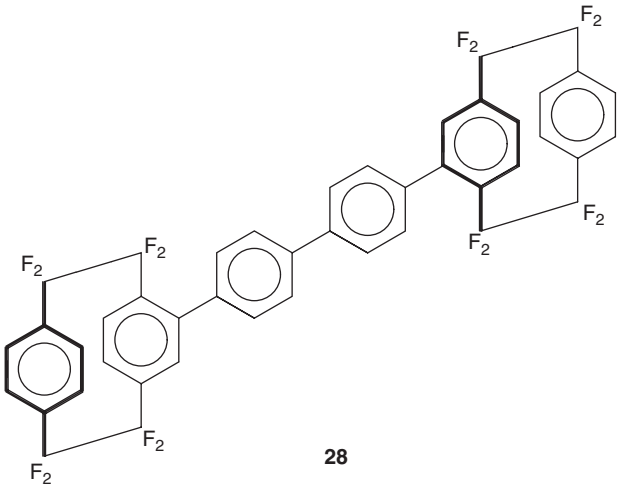

28

Dolbier and coworkers[27] reported the novel octafluoro[2.2]naphthalenophanes (**29** and **30**) and -anthracenophanes (**31** and **32**). They provided full ^{1}H and ^{13}C signal assignments for these compounds, only the ^{13}C NMR spectrum of **32** could not be obtained because of low solubility. The ^{19}F NMR chemical shifts and $^{2}J(F,F)$ coupling constants for **29–32** were also given, however without specific assignments. The *anti*-configurations of **30** and **32** were deduced from the higher shieldings of H_a (**30**: $\delta = 6.41$ ppm, **32**: $\delta = 6.07$ ppm) relative to H_b in the *para*-phenylene derivatives (**29**: $\delta = 7.45$ ppm, **31**: $\delta = 7.37$ ppm).

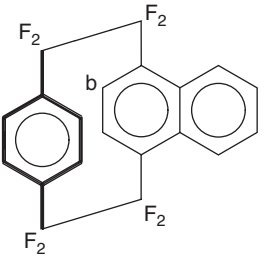

29

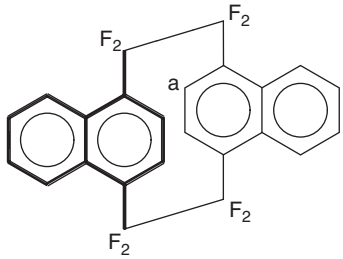

30

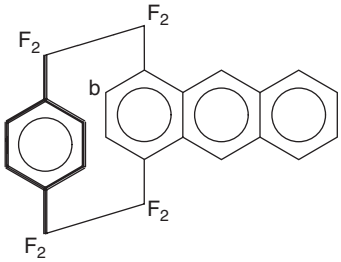

31

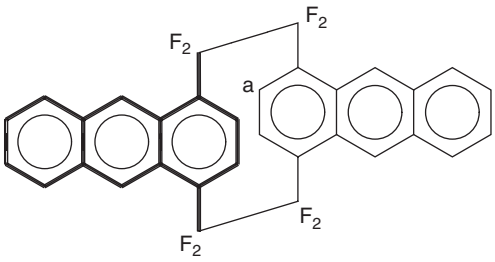

32

Pseudo-ortho-[2.2]paracyclophanediol ("PHANOL", **33a**) and its *para*-substituted derivatives **33b–d** were found to catalyse, among others, Diels–Alder cycloadditions of conjugated aldehydes or ketones with dienes.[28] The mode of catalysis is via double hydrogen bonding to the two sp^2 lone pairs of a carbonyl group. The order of activity correlates with the expected H-bond donor strength. In contrast, *ortho*-substituted PHANOLs **34a–c** are not catalytically active due to steric interference with the double hydrogen-bonding mode. The double hydrogen-bonding mode is supported by IR spectra and by the chemical shifts of the OH protons. The OH shifts are $\delta \approx 8.5$–8.9 ppm for **33a** and **33c–d** and 10.83 ppm for **33b**, while they amount to only 4.34–5.84 ppm for **34a–c**. Intramolecular H-bonds in the PHANOLs can be excluded because the phenolic O···O separation of ca. 4.0 Å is too large.

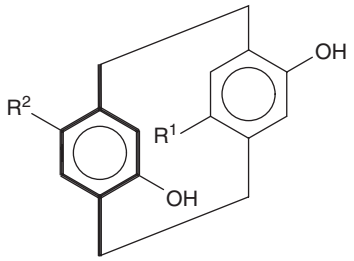

33	R^1	R^2
a	H	H
b	NO_2	NO_2
c	Br	H
d	SO_2NEt_2	SO_2NEt_2

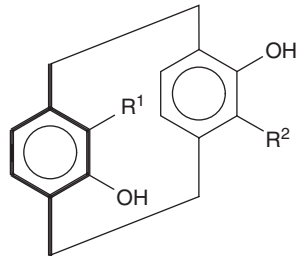

34	R^1	R^2
a	*n*-C_5H_{11}	*n*-C_5H_{11}
b	H	Et
c	H	*t*-CH=CH–C_3H_7

^{1}H NMR spectroscopy was used to study coordination equilibria between [2.2]paracyclophane and bis(diene)rhodium and -iridium complexes.[29] Both mono- (**35**) and dimetalated paracyclophane (**36**) were observed. Iridium was found to better coordinate to [2.2]paracyclophane than rhodium.

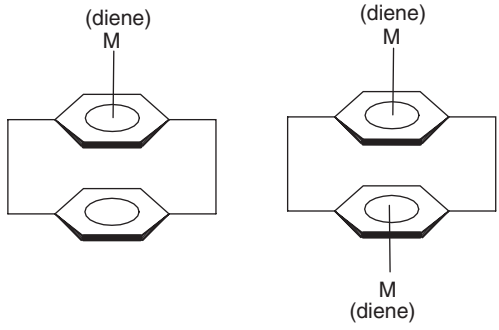

35 **36**

M= Rh or Ir
diene = 1,5-cyclooctadiene or norbornadiene

An older paper not previously reviewed concerns deuterium isotope effects of the CD_3 group in 4-(trideuteriomethyl)[2.2]paracyclophane **(37a)** upon the pseudo-geminal carbon C-15 of the opposite ring.[30] Unlike the majority of cases reported,[31–33] the isotope effect of CD_3 on C-15, $\Delta(\text{C-15}) = \delta(\mathbf{37a}) - \delta(\mathbf{37b}) = +0.035$ ppm, is positive, i.e. deshielding. Obviously, this is a through-space effect as it becomes smaller when the aromatic inter-ring distance is increased such as in the pair of [3.3]paracyclophanes **38a–b**, where $\Delta(\text{C-17}) = +0.020$ ppm. The isotope effect exerted by CD_3 is identical to the difference of the substituent effects (SEs) of a CD_3 and a CH_3 group, and a systematic study of other compounds in which CD_3 groups affect the chemical shifts of nearby carbon nuclei led to the conclusion that through-space isotope effects (TSIE) of CD_3 are shielding (negative) if the SE of CH_3 is deshielding (positive) and that TSIE are deshielding if SE is shielding. Expressed differently, a CD_3 group has an algebraically smaller SE than a CH_3 group, in line with the shorter bond length of C–D relative to C–H.

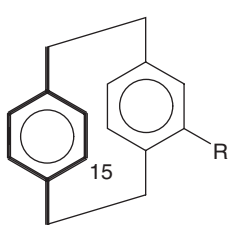

37a, R = CD_3
37b, R = CH_3

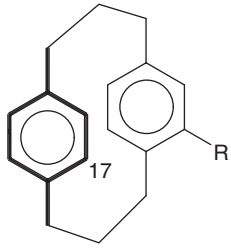

38a, R = CD_3
38b, R = CH_3

A plethora of synthetic compounds related to [2.2]paracyclophane has been reported by the group of Minuti and Taticchi. All their papers contain detailed NMR studies, the aim of which is the elucidation of the structures of reaction products and the determination of their stereochemistry. They investigated the Diels–Alder addition, under pressures of 6–9 kbar, of 5-ethenyl[2.2]indenoparacyclophane with *para*-benzoquinone, *N*-phenylmaleimide or 2-inden-1-one which gave products **39–42**.[34] Extensive NMR investigations (H,H-COSY, one-bond and long-range C,H-HETCOR, H{H}-NOE) were undertaken for the purposes mentioned and ^3J(H,H) coupling constants were exploited additionally in order to secure the configurations of the products. For example, in **39** the coupling constants $^3J(\text{H-4a,17c}) = 4.8$ Hz and $^3J(\text{H-17b,17c}) = 4.7$ Hz secured the *cis*-arrangement of the three protons involved while the NOE experienced by H-20 and H-21 when the signal of H-17b was irradiated, indicated the *cis*-relationship between H-17b and the unsubstituted arene ring of the paracyclophane unit.

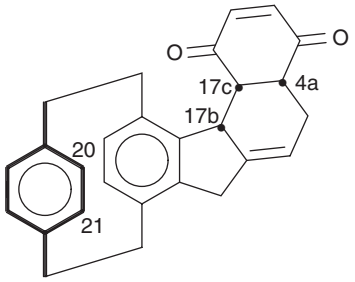

39

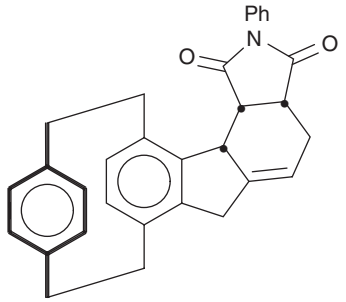

40

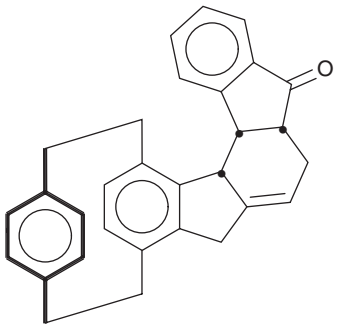

41

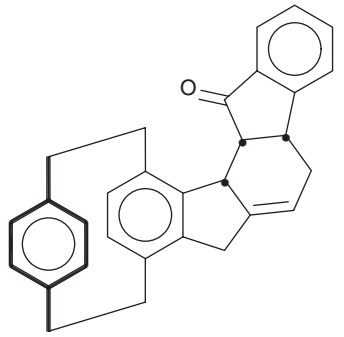

42

Also by Diels–Alder cycloadditions under elevated pressure, this time using 4-(2-propenyl)[2.2]paracyclophane as the diene component and *N*-phenylmaleimide or maleic anhydride as the dienophiles, compounds **43a–b** were synthesized and dehydrogenated to the [2.2](1,4)naphthalenoparacyclophanes **44a–b**.[35] ^{1}H and ^{13}C NMR signal assignments and elucidation of the 3D structure were achieved using the techniques mentioned above. Aromatization of the cycloadducts **43a–b** to give **44a–b** increased the shielding of H-10 by 0.85 ppm and that of H-11 by 1.1 ppm (on average), for example δ(H-10) = 6.43, δ(H-11) = 6.79 ppm in **43b** while δ(H-10) = 5.57 and δ(H-11) = 5.66 ppm in **44b**. Cycloadditions of the same dienophiles and of *N*-methylmaleimide to diene **45** yielded cyclophanes **46a–c**, which were dehydrogenated to give aromatic compounds **47a–c** again fully characterized by the proven methods.[36] The same paper also reports on the NMR study of adduct **48**, prepared from **45** and 1,4-naphthoquinone. When dehydrogenation of **46a–b** was attempted with DDQ, the unexpected chloro derivatives **49a–b** were obtained.[37] The stereochemistry of H-16 followed from the NOE between this hydrogen and H-11 and H-14.

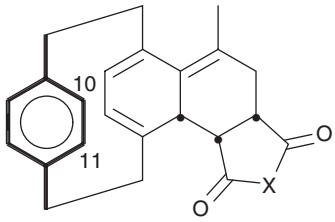

43a, X = NPh
43b, X = O

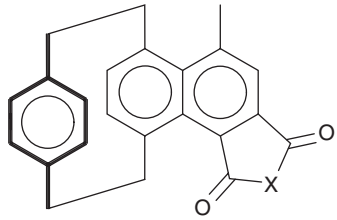

44a, X = NPh
44b, X = O

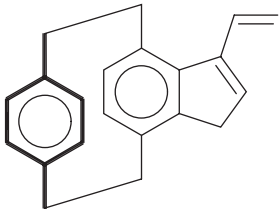

45

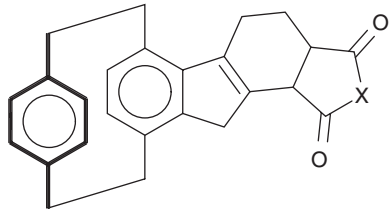

46a, X = NMe
46b, X = NPh
46c, X = O

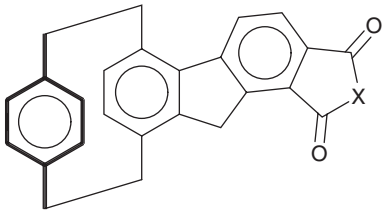

47a, X = NMe
47b, X = NPh
47c, X = O

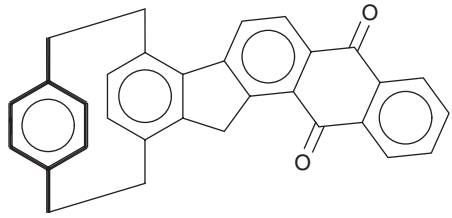

48

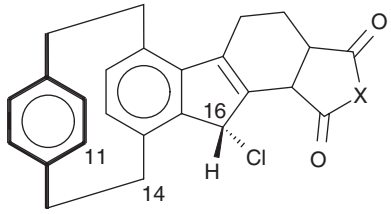

49a, X = NMe
49b, X = NPh

Work along similar lines described the structural elucidation of isomeric cycloadducts **50** and **51** together with that of the fully aromatic helicenophane **52** and the side

product **53**.[38] Here also, long-range heteronuclear correlations and H{H}-NOEs gave the decisive hints as to the constitutions and configurations of these products. The NOEs showed that the angular hydrogens in **50** (one) and **51** (two) point toward the unsubstituted ring of the paracyclophane unit. In **52**, irradiation of H-7 produced enhancements of the H-6 and H-9 signals and saturation of H-18 gave NOEs at H-1 and H-15. The same group of authors also dealt with the NMR spectra of coumarinoparacyclophane **54**, its cycloadducts **55a–b**, and dibenzofuranophanes **56a–b**.[39] High-pressure acid-catalysed addition of quinoline-5,8-dione and 1,4-naphthoquinone to 4-ethenyl[2.2]paracyclophane resulted in compounds **57** and **58** whose structures were also derived from their ^{1}H and ^{13}C NMR spectra including many selective H{H}-NOE spectra.[40] A new type of angularly annelated [2.2]paracyclophane **(59)** has been synthesized by Diels–Alder reaction of 4-(2-propenyl)[2.2]paracyclophane with 1,4-benzoquinone under high-pressure conditions.[41] Semiempirical MO calculations and extensive NMR studies including the complete assignment of all ^{1}H and ^{13}C resonances were carried out to determine the structure of this compound. The rather high-field shift of the protons at ring B and of the methylene protons at C-16 were indicative of the olefinic nature of this ring. The C-16 and H-16 chemical shifts differ markedly from those of the other bridge methylenes and from the methylene shifts of **44a–b** that were used for comparison. To conclude the report of NMR-related cyclophane work by the Italian/Hungarian research group, we mention two unexpected products, **60** and **61**, from the reaction of 4-(2-propenyl)[2.2]paracyclophane with 2-inden-1-one and 1,4-benzoquinone, respectively.[42,43] The characteristic shielding of H-19, H-20, and H-21 ($\delta = 5.73$, 5.71, and 5.38 ppm, respectively) and the lack of extra shielding of H-5 and H-6 ($\delta = 7.26$ and 7.30 ppm, respectively) showed **60** to possess a [2.2]metaparacyclophane skeleton. H,C-HMBC correlations and H{H}-NOEs ascertained the mode of fusion of rings B–E. Compound **61** also has a *para*- and a *meta*-substituted aromatic ring but, formally, constitutes a [3.2]metaparacyclophane. Still, its ^{1}H chemical shifts resemble the data published for [2.2]metaparacyclophane.[44] Protons H-6, H-11 and H-12 absorb at $\delta = 5.48$, 6.23, and 5.96 ppm, respectively, in **61** while the corresponding values for [2.2]metaparacyclophane are $\delta = 5.37$, 5.79, and 5.79 ppm. The structure elucidation of **61** also relied most heavily on long-range H,C-correlations and H{H} nuclear Overhauser effects. AM1 semiempirical calculations predicted the geometry of **61** to be in satisfactory agreement with the structure deduced from the NMR experiments.

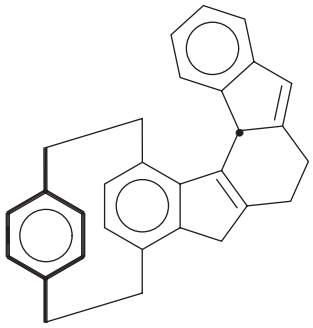

50

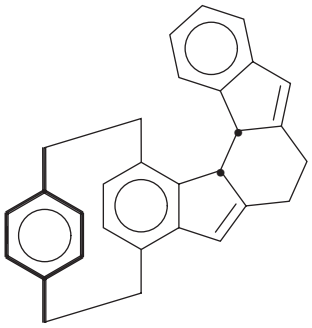

51

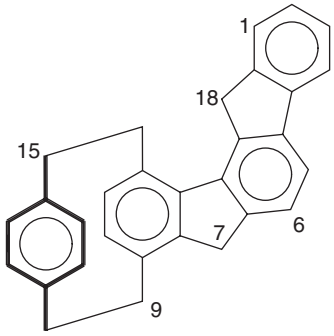

52

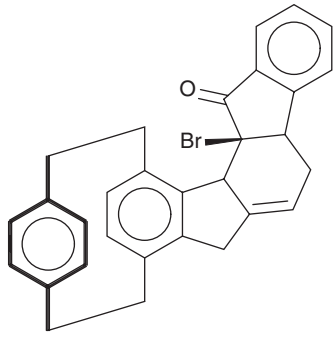

53

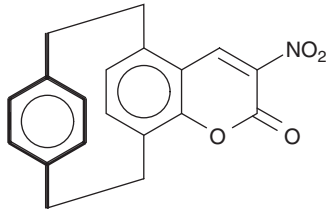

54

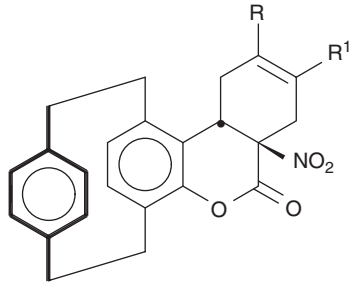

55a, R = R^1 = Me
55b, R = Me, R^1= H

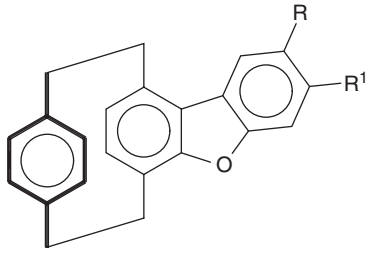

56a, R = R^1 = Me
56b, R = Me, R^1=H

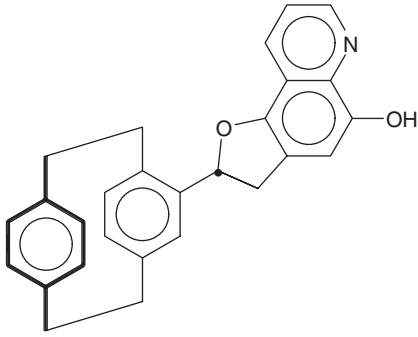

57

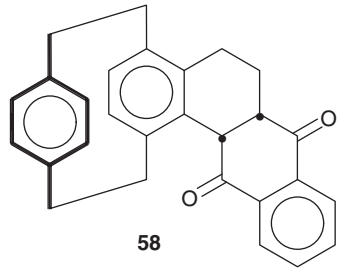

58

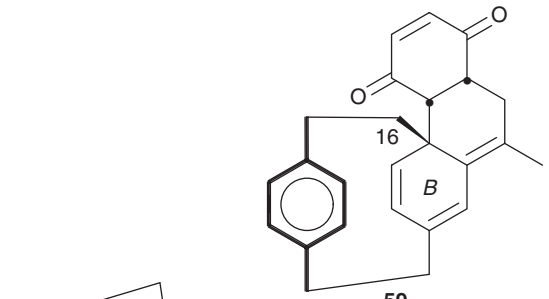

59

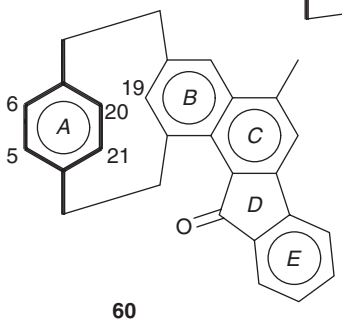

60

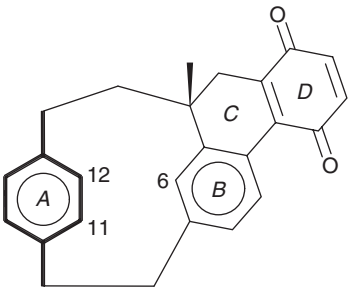

61

In continuation of the earlier work Tani *et al.*[45] studied [2.2]phane **62** consisting of the electron-rich carbazole and the electron-poor terephthalate subunits fixed in a distinct geometry. The ^{1}H NMR chemical shifts were compared with those of model compounds 9-ethyl-3,6-dimethylcarbazole and dimethyl terephthalate. The relative chemical shifts are given in formula **62** and demonstrate the mutal shielding of the two halves of the molecule. The unsymmetry with respect to the chemical shifts of both the terephthalate and the carbazole parts show that rotation of the terephthalate moiety is restricted at room temperature. These results agree with those reported previously for the analogous compound without the ester groups.[46] In the diselena[3.3]phane **63**, the synthetic precursor of **62**, the chemical shift effects are much smaller due to the increased distance between the aromatic planes. As a consequence of this larger distance, free rotation of the terephthalate moiety is observed at room temperature. This was deduced from the averaged chemical shifts of its two aromatic protons and from those of the left and right halves of the carbazole part.

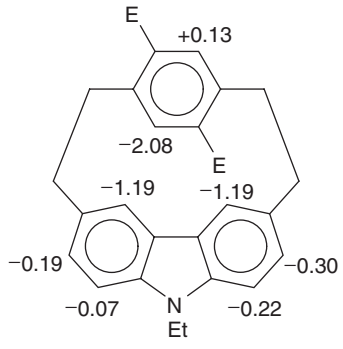

62

(E = CO_2CH_3)

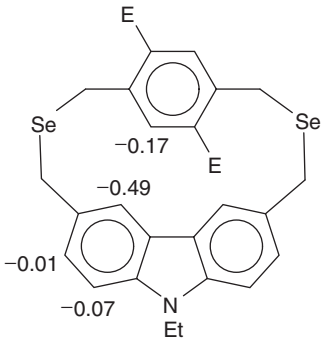

63

Tsuge's group[47] continued their work on [2.2]fluorenophanes. They prepared a number of symmetrical and unsymmetrical phanes **64a–g** whose subunits carried bridges at the 1,8-, 2,7-, and 1,7-positions. Some ^{1}H NMR data of these compounds were given, viz. bridge proton and H-9 (central methylene) shifts. It was concluded that all compounds have a rigid fixed conformation at room temperature and that marked upfield shifts of H-9 protons were only found in the unsymmetrical compounds **64b** and **64e**. Unfortunately, the conformations were not discussed in any more detail. For the precursor dithia[3.3]phanes, see Section 4.

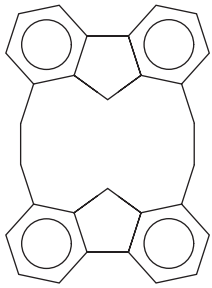

64a

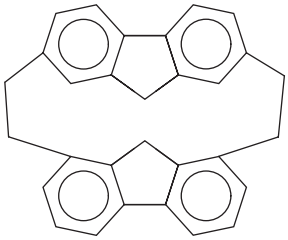

64b

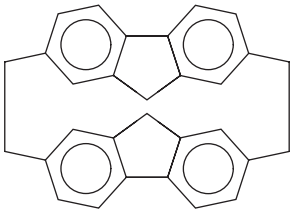

64c

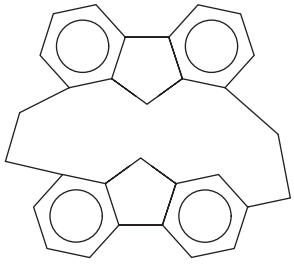

64d

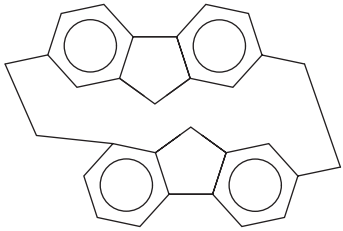

64e

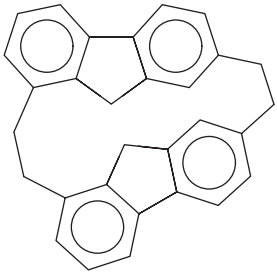

64f

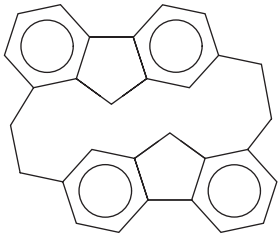

64g

The McMurry reaction of 2,7-diformylfluorene led to [2.2](2,7)fluorenophanediene **65** and the corresponding trimer (see Section 8).[48] The protons at

C-9 are strongly anisochronous: $\delta = 3.26$ (H-9_{exo}) and 2.35 ppm (H-9_{endo}), $^2J = 20.9$ Hz, in $CDCl_3$. This behaviour is similar to what is known for the compound with saturated bridges. The dianion $\mathbf{65}^{2-}$ is stable in DMSO-d_6 solution at room temperature for more than three months whereas, under the same conditions, the H-9 signal of the fluorenyl anion **66** itself disappears smoothly through H/D exchange with the solvent within a short time. The reason for this behaviour lies in the easy approach of bases and solvent to only the 9-*exo* protons. The 9-*endo* protons are left intact because of the tightly layered structure of $\mathbf{65}^{2-}$. The high-field shifts of the fluorene ring protons in $\mathbf{65}^{2-}$ relative to those of the model compound **66** are explained in terms of anisotropy effects due to the stacking structure of the two fluorenide rings in close proximity.

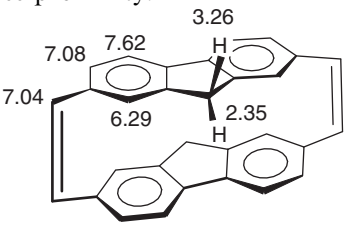

65

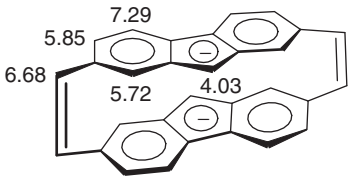

$\mathbf{65}^{2-}$

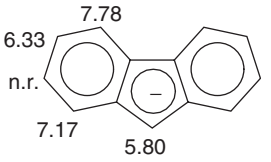

66

The ^{1}H NMR chemical shifts of the novel *anti*-[2.2](1,4)biphenylenophane (**67**) were assigned[49] from H{H} NOEs observed between bridge proton H_b and the aromatic *ortho*-proton H_c and between bridge proton H_a and the aromatic *peri*-proton in a derivative of **67**. No specific assignment was performed for the protons of the outer aromatic rings in **67**. Protons H_c on the inner rings showed a remarkable shielding of $\delta = 5.92$ ppm.

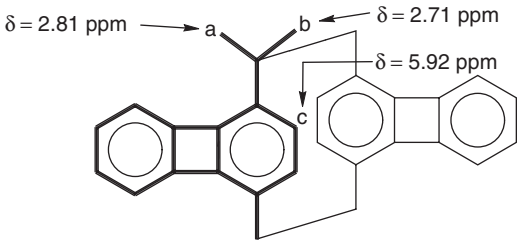

67

The groups of Hopf and Haley[50] recently reported on compounds **68–69**, which are hybrids of [2.2]paracyclophane and dehydro[14]annulene. These compounds were used to measure the induced ring current, i.e. the aromaticity of the dehydro[14]annulene system. As the protons H-15,16 of the upper deck of the paracyclophane unit lie above the annulene ring, they can function as a probe of the diamagnetic anisotropy of the latter. The shielding effect of the aromatic system formed upon cyclization leads to a marked upfield shift of H-15,16 compared to the corresponding resonances in the acyclic precursors, in which the bond between the central C–C triple bonds does not yet exist. Comparison of δ(H-15,16) in **68** with the value in its precursor gives a shielding effect $\Delta\delta$ of -0.37 ppm, indicative of a diatropic ring current in the [14]annulene unit. The upfield shift is considerably more pronounced when **69** is compared with its acyclic precursor, $\Delta\delta = -0.92$ ppm. This is in line with the common notion that aromaticity of annulenes is decreased by fused benzene rings, i.e. the stronger aromatic annulene unit in **69** exerts a stronger shielding effect on H-15,16.

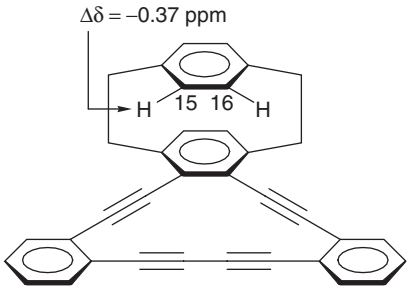

68

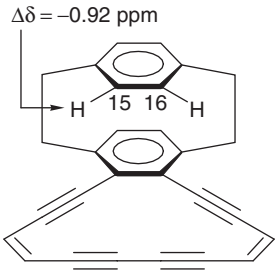

69

Diastereomerically pure (*R*,*R*)-2,2′-biquinolinophane **70** and (*R*,*R*)-1,1′-biisoquinolinophane **71** were investigated with respect to their favoured conformations by ^{1}H NMR spectroscopy and molecular mechanics calculations.[51] For **70** a strong NOE between H-9s and H-3′ pointed to an essentially planar central 2,2′-biquinoline unit in a *transoid* arrangement. A weak NOE between H-10s and H-3′ appeared to indicate a slight preferred rotation about the C2–C2′ bond so that H-3′ points to the middle of the C9–C10 bridge. MMFF94 force field calculations brought a very similar result, yielding a preferred conformation with a dihedral angle N–C–C–N of -173°. The situation proved to be very different for **71**. Here the chemical shifts of H-15 and H-16 are moved to significantly higher frequencies ($\Delta\delta = 0.1$–0.2 ppm) relative to **70**. This is consistent with an almost perpendicular arrangement of the two C1–C1′-bonded isoquinoline moieties, with H-15 and H-16 of one isoquinolinophane moiety falling into the deshielding zone of the other. Moreover, the two bridge protons turned toward the heterocyclic ring (H-9s and H-10s) resonate at abnormally high field ($\delta = 0.88$ and 1.96 ppm, respectively) compared with the corresponding protons in **70** ($\delta = 4.55$ and 3.2 ppm, respectively). The most plausible explanation is that the two isoquinoline moieties are rotated about the

C1–C1′ bond by a substantial dihedral angle such that H-9s and H-10s of one isoquinolinophane unit fall into the shielding zone of the other. Thus, H-9, the most deshielded bridge proton in **70** becomes the most shielded proton in **71**. NOE experiments confirmed this hypothesis: a substantial NOE was observed between H-3 and H-10′ and a smaller one between H-4 and H-9′. Therefore the (*R*,*P*,*R*) conformation (*P* referring to the biaryl axis) could be assigned to **71**. Force field calculations agreed with the NMR results and predicted the most stable conformer to possess a dihedral angle of 72° and prevailing to the extent of 91% at room temperature.

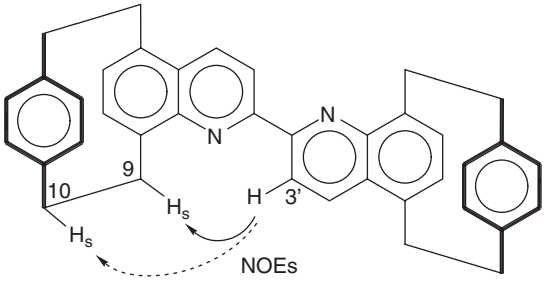

70

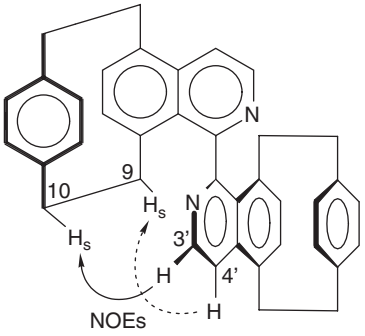

71

4. [3.3]PHANES

For easy cross-referencing we mention here some papers that have already been discussed in Section 3 but also contain information on [3.3]phanes, namely on compounds **38**[30] and **63**.[45]

[3.3]Metacyclophanes and 2,11-dithia[3.3]metacyclophanes are known to prefer the *syn*- to the *anti*-conformation.[3,8,9] Vermeij[52] studied a number of 6,15-disubstituted 2,11-dithia[3.3]metacyclophanes, **72**, by dynamic ^{1}H and ^{13}C NMR spectroscopy. Here the aromatic rings were also in the *syn*-conformation, and at temperatures below 223 K a freezing of the interconversion of the *chair,*

chair (*c,c*) into the *boat,chair* (*b,c*) conformation of the bridges was observed. The *boat,boat* (*b,b*) conformation was not detectable. Inspection of the ^{1}H chemical shifts and of the splitting patterns of the benzylic proton signals indicated that, at low temperature, the *b,c*-conformer still underwent rapid *syn* to *syn′* interconversion. Thus there is a slow equilibration *syn-c,c*-**72**/*syn-b,c*-**72** with an energy barrier of 42–46 kJ mol^{-1} and a fast one *syn-b,c*-**72**/*syn′-b,c*-**72** with a barrier too small to measure by the techniques applied. The equilibrium ratios $K = [syn\text{-}c,c\text{-}\mathbf{72}]/[syn\text{-}b,c\text{-}\mathbf{72}]$ were found to be substituent-dependent. While in the case of electron-withdrawing substituents (R = CO_2Et) K was 0.67, it was 1.6 for the parent compound (R = H) and 2.3 for the compound with electron-donating substituents (R = OAc). Correlations of chemical shift differences $\Delta\delta_H = \delta_H(\text{cyclophane}) - \delta_H(\textit{meta}\text{-xylene})$ with Hammett constants or Taft's dual-parameter system led to the conclusion that inductive SEs are far more important in determining K than are resonance effects.

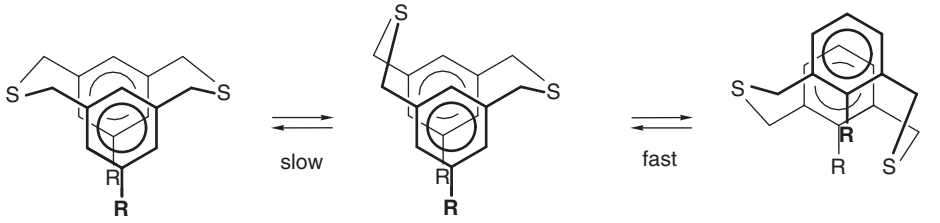

syn-chair, chair ***syn***-boat, chair ***syn'***-boat, chair

72 (R= CO_2Et, H, OAc)

A heterocyclic [3.3]*meta*-type cyclophane, **73**, and its bis(phenylene) homologue **74** were reported by Mashraqui *et al.*[53] In both compounds, conformational mobility seems to be little restricted as the methylene proton signals remain singlets down to a temperature of 218 K. A low-temperature ^{1}H NMR study of [3.3](2,6)pyridinophane **75**[54] with disiloxa bridges showed that the interconversion of the chair and boat conformations of the three-membered bridges in the *syn*-arrangement of the aromatic rings becomes slow on the NMR time scale below 208 K (at 300 MHz), when the methyl signal splits into two resonances ($\Delta\nu = 26.8$ Hz). This behaviour resembles that of **72** discussed above. The activation barrier $\Delta G^{\ddagger}_{208}$ for bridge inversion in **75** is 43.2 kJ mol^{-1}.

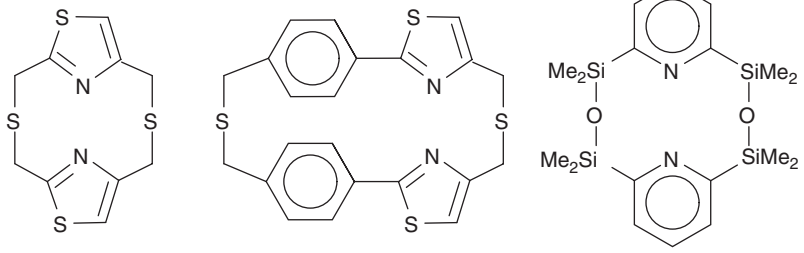

73 **74** **75**

Ting and Lai[22] prepared some dithia[3.3]metacyclophanes, **76a** and **76b** (only *syn* isomers shown), with a naphthyl group as the internal substituent. Both *syn*- and *anti*-isomers were formed in the synthesis. They were distinguished by the strong shielding of the methyl protons in the *anti*-isomers ($\delta = 1.59$ and 1.61 ppm in *anti*-**76a** and *anti*-**76b**, respectively) as opposed to the more normal shifts in the *syn*-isomers ($\delta = 2.52$ and 2.62 ppm in *syn*-**76a** and *syn*-**76b**, respectively). This group also synthesized **77**, which was isolated as the *anti*-isomer.[55] Here also, the stereochemistry could be deduced from the shift of the internal methyl protons ($\delta = 1.64$ ppm). A dynamic ^{1}H NMR study showed different chemical shifts for the H-1′ and H-3′ protons ($\delta = 7.90$ and 8.75 ppm, respectively) of the DHP moiety at 233 K, due to restricted rotation about the aryl–aryl bond and the different distance of H-1′ and H-3′ from the opposite benzene ring of the metacyclophane unit. The barrier to aryl–aryl rotation was determined by the coalescence method to be $\Delta G^{\ddagger} = 53.5\,\text{kJ mol}^{-1}$ (temperature not given).

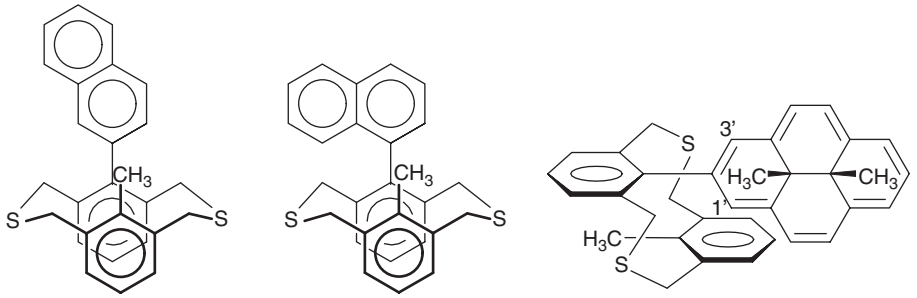

76a **76b** **77**

(*syn*-isomers shown)

Georghiou[18] described a number of dithia[3.3](1,3)naphthalenophanes, **78–79**, which occurred both in the *syn*- and in the *anti*-isomeric forms and also had a *cisoid* or *transoid* arrangement of the outer rings of the naphthalene systems. When the naphthalene systems are *anti*, the methoxy protons are shielded by the ring current of the opposite aromatic ring ($\delta_{OMe} = 2.93$ in **78a** and 2.92 ppm in **79a**), while they show normal shifts in the *syn*-isomers ($\delta_{OMe} = 3.57$ in **78s** and 3.56 ppm in **79s**). A characteristic difference between **78s** and **79s** lies in the chemical shift of H-5. This proton is more shielded in **78s** ($\delta_{H-5} = 6.96$ ppm) by the outer ring of the opposite naphthalene unit than it is in **79s** ($\delta_{H-5} = 7.46$ ppm). All proton signals in the four compounds were carefully assigned from their coupling constants and from NOE difference spectra. The *anti*- and *syn*-forms of **78** and **79** are conformationally stable at room temperature as can be seen from the diastereotopicity of all benzylic protons.

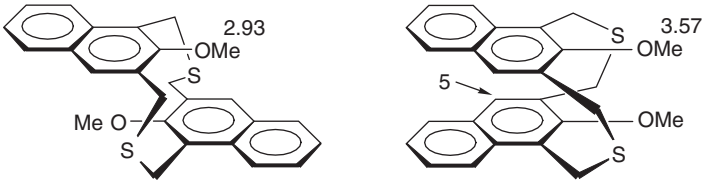

78a (*anti*, transoid) **78s** (*syn*, transoid)

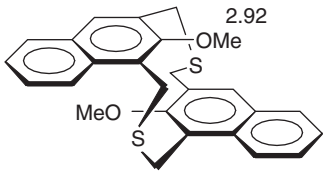

79a (*anti*, cisoid)

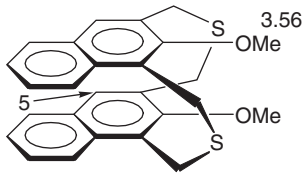

79s (*syn*, cisoid)

A [3.3]metacyclophane, **80**, composed of a phenol unit and a fluorobenzene unit was synthesized as a simple model for the investigation of the C–F···H–O hydrogen bond.[56] The cyclophane skeleton is suitable for realizing the ideal F···H–O distance and the appropriate angles. Compounds **81** (without fluorine) and **82** (without the hydroxy group) were studied for comparison. The factors taken as evidence for an intramolecular C–F···H–O hydrogen bond were (a) deshielding of the OH proton in **80** ($\delta = 4.60$ ppm in methylcyclohexane-d_{14} and 4.86 ppm in $CDCl_3$) relative to **81** ($\delta = 4.21$ ppm in methylcyclohexane-d_{14} and 4.58 ppm in $CDCl_3$), (b) spin coupling between OH and F [J(OH,F) = 6.6 Hz in methylcyclohexane-d_{14} and 6.0 Hz in $CDCl_3$], and (c) shielding of fluorine in **80** ($\delta = -120.3$ ppm in methylcyclohexane-d_{14} and -119.9 ppm in $CDCl_3$) relative to **81** ($\delta = -118.7$ ppm in methylcyclohexane-d_{14} and -118.9 ppm in $CDCl_3$). When **80** was dissolved in DMSO-d_6, no spin coupling was observed between OH and F, because solvent molecules successfully compete with the fluoro substituent in forming a hydrogen bond with the OH group.

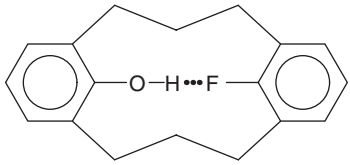

80

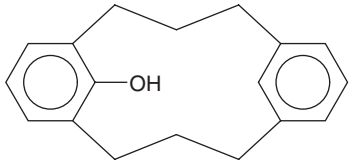

81

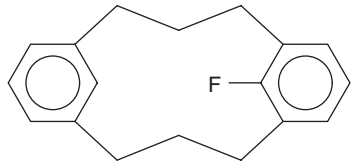

82

Dithia[3.3]metaparacyclophanes, **83**, containing a 9,10-bridged anthracene moiety were reported by Tsuge's group.[57] Compounds **83a** and **83e–f** with no internal substituent R^1 are flexible, i.e. undergo rapid flipping of the *meta*-substituted ring at room temperature as could be deduced from the appearance as a singlet of the methylene bridge protons. The internal proton in these molecules is highly shielded because it plunges deeply into the shielding region of the anthracene unit

($\delta_H = 3.29$,* 4.25, and 4.03 ppm for **83a**, **83e**, and **83f**, respectively). Compounds **83b–d** with an internal substituent are rigid and show AX patterns for the bridge protons. The protons of the internal methoxy group in **83b** are substantially shielded ($\delta = 2.73$ ppm). Heating **83b–d** "in the range of the conventional temperatures" (probably to ca. 423 K) did not lead to signal coalescence.

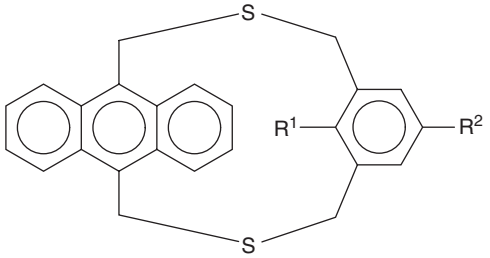

83	R^1	R^2
a	H	H
b	OMe	H
c	NO_2	H
d	NH_2	H
e	H	NO_2
f	H	NH_2

Tsuge's group[58] also investigated a series of dithia[3.3](4,9)pyrenometacyclophanes, **84a–i**. These compounds are conformationally rigid as they show nonequivalent methylene protons, the signals of which did not show coalescence within "conventional temperatures" (see above). The authors concluded that compounds **84f–i** with a substituent at the inner position of the *meta*-phenylene ring ($R^1 \neq H$) assume a conformation in which the pyrene and the *meta*-phenylene units are parallel to each other. Compounds **84a–e** without an internal substituent ($R^1 = H$) prefer a conformation with a perpendicular orientation of the *meta*-phenylene and pyrene systems. The internal protons in **84a–e** are strongly shielded (e.g. $\delta = 3.77$ ppm in **84a**) because they penetrate deeply into the pyrene π-cloud. The conclusions regarding the preferred conformations were based on the fact that the compounds with $R^1 = H$ showed only three kinds of pyrene proton signals while those with $R^1 \neq H$ showed six. Moreover, the methoxy protons in **84f** have almost the same chemical shift ($\delta = 2.72$ ppm) as the methoxy protons in 8-methoxy-*anti*-[2.2]metacyclophane, where the aromatic rings are known to assume a parallel orientation.

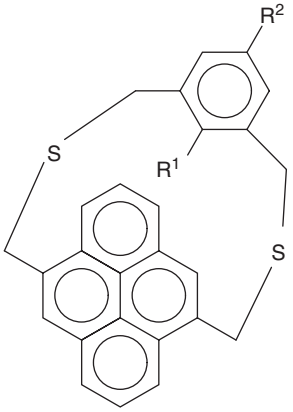

84	R^1	R^2
a	H	H
b	H	CH_3
c	H	OMe
d	H	NO_2
e	H	NH_2
f	OMe	H
g	NO_2	H
h	NH_2	H
i	F	H

*The chemical shift value of 3.29 ppm for **83a** appears to be in error when compared with the values for **83e** and **83f**.

A number of dithia[3.3]fluorenophanes, **85a–d**, was reported to have flexible structures, i.e. the fluorene units can pass one another freely, as was deduced from the singlet signals of the benzylic protons at room temperature, whereas others, **85e–g**, have rigid structures on the NMR timescale up to 423 K as shown by their anisochronous benzylic protons.[47] By variable temperature ^{1}H NMR conformational barriers for the flexible isomers were determined to be 36.8 kJ mol^{-1} at 198 K (**85a**), 41.8 kJ mol^{-1} at 213 K (**85b**), 49.0 kJ mol^{-1} at 253 K (**85c**), and 47.1 kJ mol^{-1} at 243 K (**85d**). The nature of the conformational processes was not discussed.

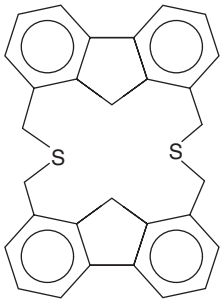

85a

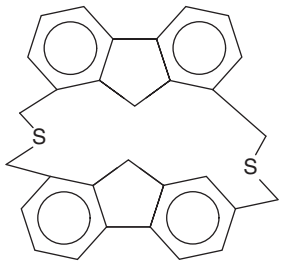

85b

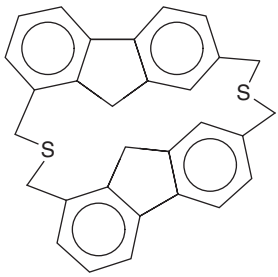

85c

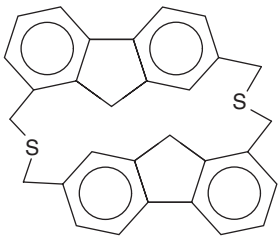

85d

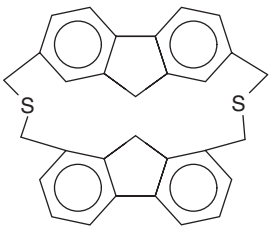

85e

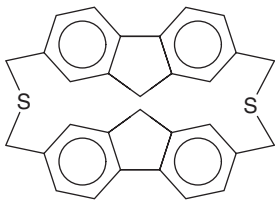

85f

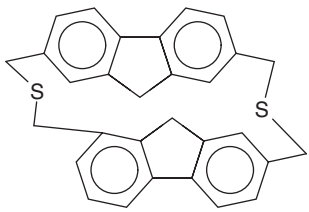

85g

The [3.3]metaparacyclophanes **86a–c** were described by Yamato *et al.*[59] These compounds assume a step-like structure in which the internal proton or substituent lies over the *para*-phenylene ring and experiences extra shielding [$\delta = 5.37$ (H), 1.69 (CH_3), and 3.26 ppm (OMe) for **86a**, **86b**, and **86c**, respectively]. Likewise, the

protons of the *endo*-half of the *para*-phenylene ring are shielded ($\delta = 5.99$ ppm) while those of the *exo*-half have chemical shifts close to normal values ($\delta = 6.88$ ppm). When the *para*-bridged ring carries another substituent, e.g. an acetyl group, stable *endo*- and *exo*-rotamers are possible. They can be distinguished by the chemical shifts of the *para*-phenylene ring and its substituent. For example, the protons of the *endo*-acetyl group in **87** have a chemical shift of $\delta = 2.13$ ppm and the two *ortho*-protons on the same ring absorb near $\delta = 6.96 \pm 0.02$ ppm, while the *exo*-acetyl group in **88** is found at $\delta = 2.68$ ppm and the two *ortho*-protons at $\delta = 6.11$ ppm.

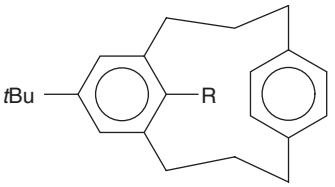

86	R
a	H
b	CH_3
c	OMe

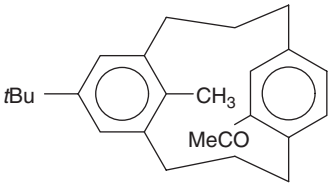

87

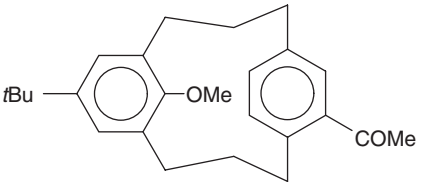

88

A new [3.3]paracyclophane, **89**, with bridges consisting only of boron and nitrogen atoms was synthesized by Paetzold and his group.[60] The aromatic protons absorb at $\delta = 6.27$ ppm and are distinctly shielded relative to model compound **90**, which has $\delta = 6.8$ ppm.

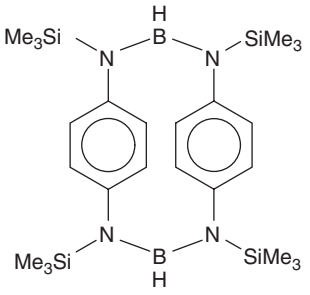

89

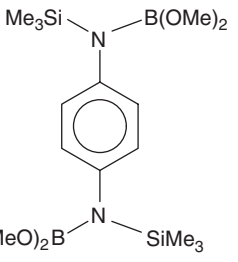

90

Lai and coworkers[61] synthesized dithia[3.3]pyridinophenanthrolinophane **91**. This [3.3]phane is conformationally mobile on the NMR timescale at room

temperature on account of its two ^{1}H NMR singlets for the two types of benzylic methylene groups. At 183 K the spectrum indicated the presence of only one frozen conformation, which according to PM3 semiempirical MO calculations was thought to be *syn–cis* (*syn* relating to the arrangement of the aromatic systems and *cis* to that of the sulphur atoms). The benzylic protons gave rise to one AB and one AX spectrum. Coalescence occurred at 193 and 206 K, respectively, and the barrier to conversion of *syn–cis*-**91** to *syn′–cis*-**91**, presumably via an *anti–trans* intermediate, was determined to be 36.5 kJ mol^{-1}.

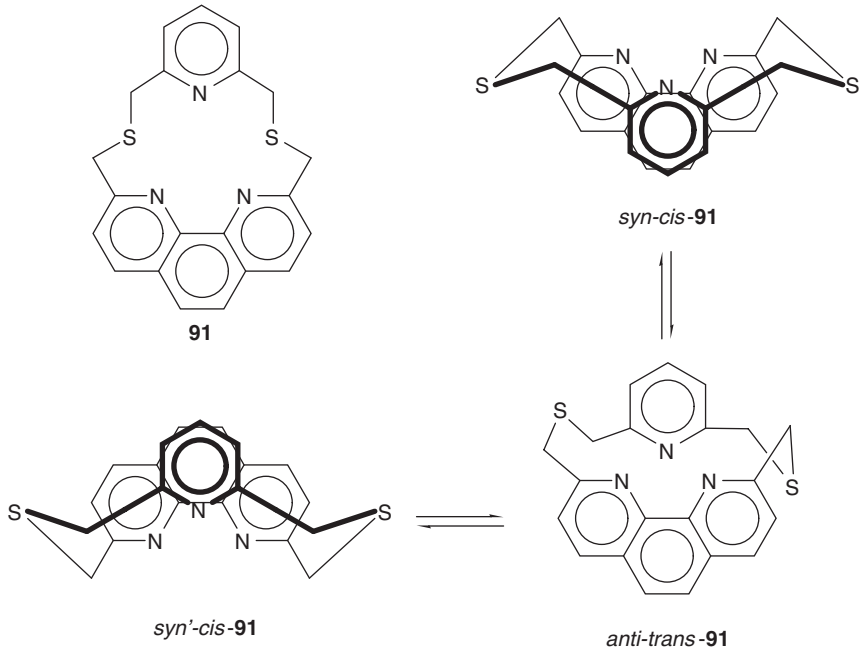

As the final examples of [3.3]phanes, oxa[3.3]phenanthrenophanes **92** and **93** as well as oxa[4.3]phenanthrenophane **94** are mentioned, which were investigated by Nishimura and coworkers.[62] While the synthesis of **92** gave the *anti*-isomer only, **93** and **94** were obtained as *anti*/*syn*-mixtures with the *anti*- outweighing the *syn*-isomers. The aromatic protons of *syn*-**93** and *syn*-**94** were almost equally shifted upfield relative to those of their precursors (carrying two –CH_2OH groups instead of the –CH_2OCH_2– bridge). This observation demonstrated that the two phenanthrene units were wholly overlapped with each other. In contrast, the aromatic protons of *anti*-**92–94** ranged over a wider region. Among the aromatic protons of *anti*-**92** and *anti*-**94**, H-6–H-8 were hardly shifted while H-1 and H-10 were strongly shifted upfield (to $\delta = 6.52$ and 6.19 ppm, respectively, in *anti*-**92**), indicating that these protons are located above the opposite phenanthrene unit, most likely over its central aromatic ring. The ^{1}H chemical shifts of *anti*-**93** suggested that this compound possesses a less overlapped structure as also indicated by MM2 calculations.

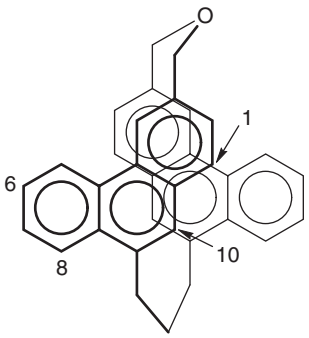

anti-**92**

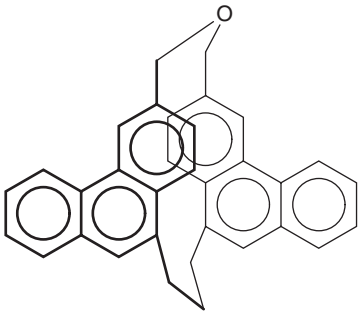

anti-**93**

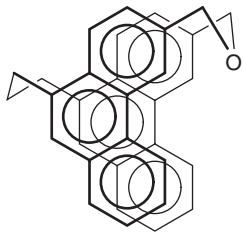

syn-**93**

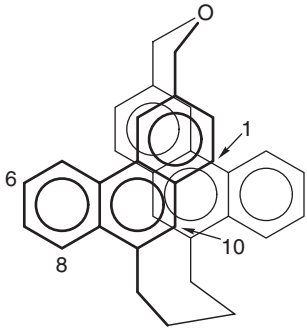

anti-**94**

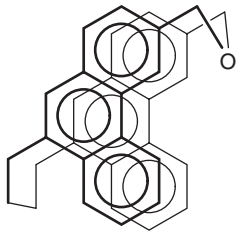

syn-**94**

5. [*m.n*]PHANES ($m > 2$, $n \geqslant 2$)

In this section, [*m.n*]phanes are treated which have one bridge of at least two and another bridge of at least three members. They will be discussed in the order [*m.n*]metaphanes, [*m.n*]paraphanes, and other [*m.n*]phanes. The two [3.2]metacyclophanes, **95** and **96**, have different preferred conformations.[63] Compound **95** having an 1,2-dimethylene-ethano bridge prefers the *syn*-conformation, which is visible from the (''normal'') chemical shift of the intra-annular aromatic protons, $\delta = 6.92$ ppm, while in the *anti*-conformation of **96** with its 1,2-dimethyl-etheno bridge the internal aromatic protons are shielded ($\delta = 5.68$ ppm) due to the ring current of the opposite benzene ring. The protons of the benzylic CH_2 groups in **95** give two multiplets at $\delta = 2.28$ and 3.14 ppm, while those of the central CH_2 group have $\delta = 1.32$ and 1.83 ppm. This spectrum proves the absence of a rapid *syn–syn* interconversion, which would exchange H_A and H_B of each CH_2 group. At 303 K, the signals of the benzylic protons coalesced and the energy barrier to conformational ring flipping was estimated to be 58.6 kJ mol^{-1}. For **96** the coalescence temperature amounted to 343 K, and the conformational barrier was determined as 65.3 kJ mol^{-1}.

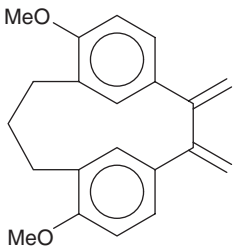

95

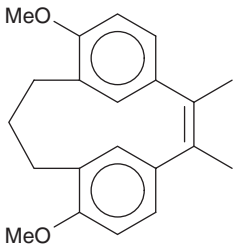

96

A [4.4](2,4)thiazolophane, **97**, containing two lactone bridges was described by Mashraqui and Lele.[64] The authors' attempt to convert **97** into the corresponding [2.2]phane by twofold decarboxylation was not successful. The room temperature ^{1}H NMR spectrum of **97** revealed sharp signals of singlet multiplicity at $\delta = 4.20$, 5.65, and 7.78 ppm for the $-CH_2CO-$, $-CH_2OCO-$, and thiazole protons, respectively. No conformational movement could be slowed down on the NMR timescale down to 218 K and any conformational barrier was estimated to lie below 50 kJ mol^{-1}. Other [4.4]cyclophanes studied by these authors had shown similar behaviour.

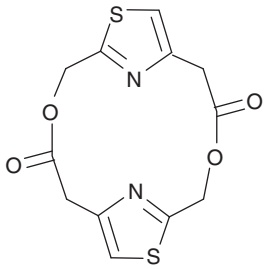

97

Compounds **98a–e** are macrocyclic bis(hydroxynaphthoic amides) connected by an achiral or chiral diamine.[65] They can be regarded as [6.3]-, [7.3]-, or [8.3]metacyclophanes. The two hydroxynaphthalenes in the macrocycle adopt a twisted conformation because of their mutual steric hindrance. Variable temperature ^{1}H NMR spectra showed that flipping of the hydroxynaphthalenes past one another is possible against an activation barrier, the height of which depends on the length and stiffness of the diamine link and its substituents. Thus, **98e** is rather mobile ($\Delta G^{\ddagger}_{223} = 44.7$ kJ mol^{-1}) requiring a low temperature (223 K) for decoalescence of the geminal methylene proton signals, while in **98a** these protons are already diastereotopic at room temperature and need heating to 343 K for coalescence, from which $\Delta G^{\ddagger}_{343} = 67.6$ kJ mol^{-1}. Compounds **98b–d** have very rigid frameworks and show no coalescence of their CH_2 signals up to 453 K. Hence, $\Delta G^{\ddagger}_c$ must be larger than 91 kJ mol^{-1} for all of them.

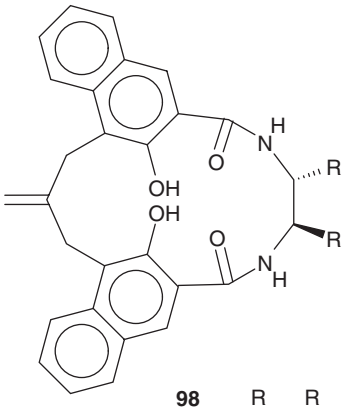

98	R	R
a	H	H
b	Ph	Ph
c	$(CH_2)_4$	
d	$OC(CH_3)_2O$	

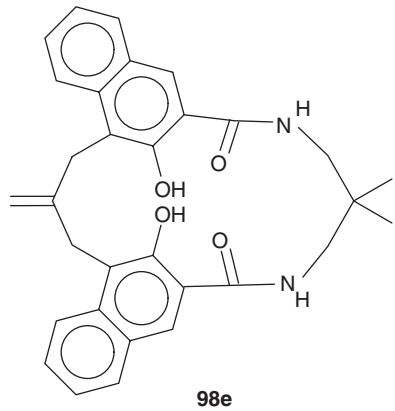

98e

A somehow related topic was presented in two papers by Nelson and collaborators.[66,67] They determined the effect of macrocycle size and substitution on the configurational stability of some bisindolylmaleimides, **99** and **100**, which may be considered [*n*.2]metacyclophanes ($n = 6$–10). Compounds **99** ($n = 10$) with R = phenyl or benzyl are separable atropisomers occurring in the *syn*- and the *anti*-configuration. Careful inspection of their 500 MHz ^{1}H NMR spectra allowed to distinguish them: the protons of the benzylic CH_2 group at the maleimide nitrogen are isochronous (enantiotopic) in the *syn*-, but anisochronous (diastereotopic) in the *anti*-atropisomer. Heating to 433 K for five days did not effect any epimerization, so the interconversion barrier must be higher than 160 kJ mol^{-1}. With no substituents at the 2-indolyl positions, compound **100** ($n = 6$) with a short tether showed decoalescence of the signal of the methylene protons adjacent to the indole nitrogen below 203 K. Molecular modelling studies had shown that for **100** ($n = 6$) the *anti*-conformer is more stable than the *syn*-conformer by more than 20 kJ mol^{-1}, hence the process observed was deemed to be a conversion of the *anti*-conformer into its enantiomer *anti*′, and the barrier for enantiomerization was determined as $\Delta G^{\ddagger}_{203} = 36.6 \pm 0.3$ kJ mol^{-1}. Increasing the length of the tether to **100** ($n = 7$–10) lowered the barrier such that no diastereotopicity of the tether protons could be observed. When the 2-indolyl substituents were methyl groups, viz. in **101** ($n = 9$ and 10), two sets of signals were detected at room temperature and slightly above: *syn*- and *anti*-conformers were present in unequal proportions. Temperature-dependent ^{1}H NMR spectra allowed the barriers to isomerization of the *anti*-conformers to be determined as 70.3 ± 0.3 kJ mol^{-1} for **101** ($n = 10$) and 74.3 ± 0.3 kJ mol^{-1} for **101** ($n = 9$). For **102** ($n = 6$–8) with shorter tethers only the *anti*-conformer was populated at 298 K. The benzylic proton signals did not coalesce up to 373 K, but the racemization barrier was measured to be >90 kJ mol^{-1} by chiral analytical high-performance liquid chromatography (HPLC).

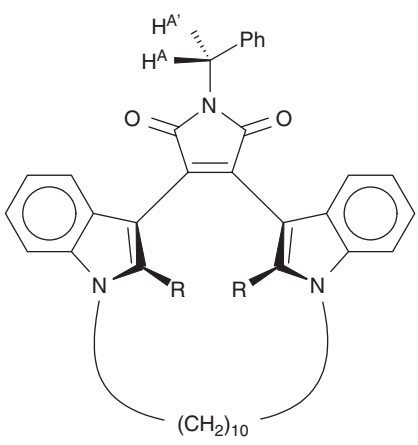

syn-**99**

(R = Ph or CH_2Ph)

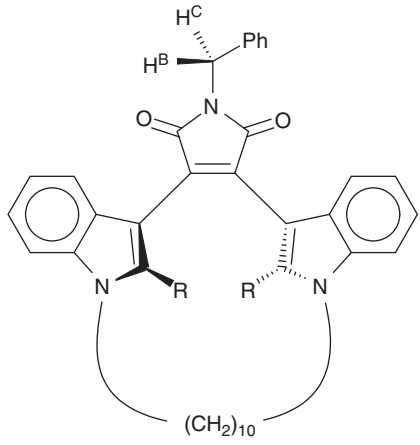

anti-**99**

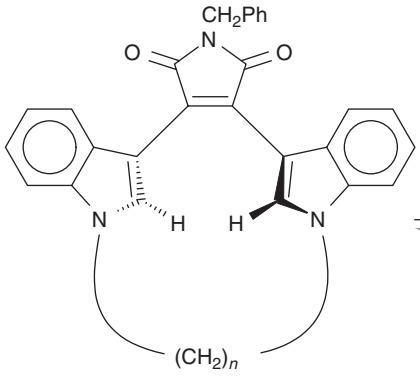

anti-**100**

(n = 6–10)

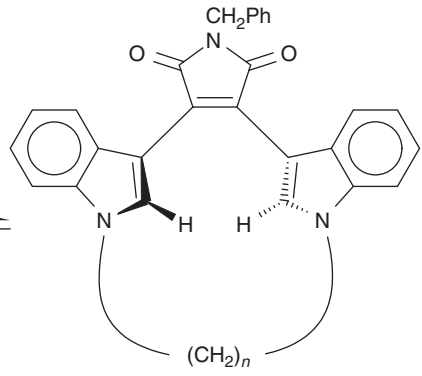

anti'-**100**

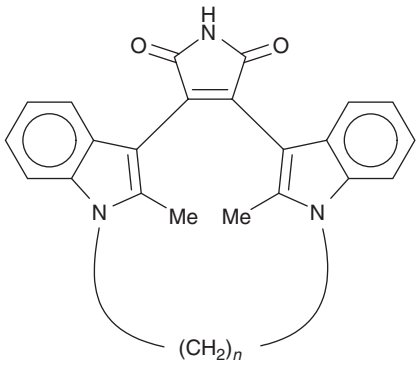

101(n = 9–10)

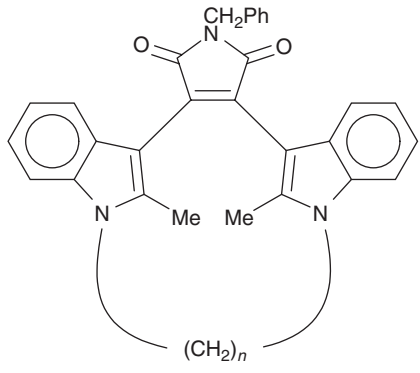

102 (n = 6–8)

The [7]- and [8](4,4′)stilbenophanes, or [7.2]- and [8.2]paracyclophenes, **103** and **104**, represent conformationally restricted cyclic analogues of the mitotic agent deoxycombretastatin A-4 **(105)**.[68] They show simple NMR spectra with a single signal for each chemically equivalent set of protons or carbons such as both methoxy groups, the aromatic proton pairs or the potentially diastereotopic hydrogens of the methylene groups. A comparison of the proton chemical shifts of the macrocycles with those of noncyclized **105** shows significant shielding of the aromatic protons and deshielding of the olefinic ones: $\Delta\delta(\text{cyclic}-\text{open}) = -0.45\ldots-0.56$ (H-2′,6′), $-0.42\ldots-0.58$ (H-2,6), and $+0.35\ldots+0.51$ ppm (H-olefinic). This suggests, in agreement with X-ray diffraction results, a close to parallel disposition of both aromatic rings in **103** and **104** (see **103A**), whereas in the noncyclized molecule the aromatic rings are nearly orthogonal. The same group of authors prepared compound **106**,[69] in which the stilbene C = C double bond is formally dihydroxylated. The ^{1}H NMR spectrum showed two broad singlets for the four aromatic protons ($\delta = 6.55$ and 5.74 ppm) and two signals for the four methoxy groups ($\delta = 3.83$ and 3.56 ppm), whereas the two hydroxylated methines resonated as a singlet at $\delta = 4.61$ ppm. Such a spectrum can, in principle, be explained by a conformationally locked *trans*-glycol **106A** or by a *cis*-glycol in fast exchange of the two possible conformers (not shown). Consideration of the large chemical shift difference of the aromatic protons ($\Delta\delta = 0.81$ ppm) and of the ROEs observed, on one hand, between the deshielded aromatic hydrogen (H_{ar}) and the deshielded methoxy group (OMe) and between the shielded H_{ar} and the shielded OMe and, on the other, between both aromatic protons and the hydroxylated methines led to the conclusion that the spectra are much better explained by the arrangement depicted in **106A**.

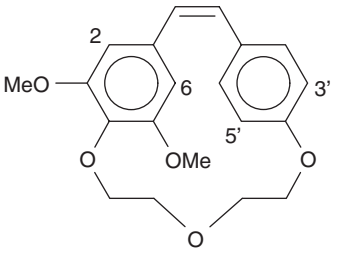

103

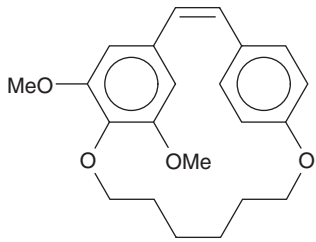

104

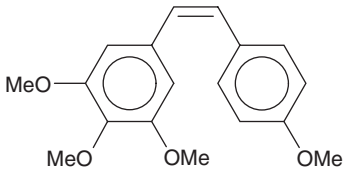

105

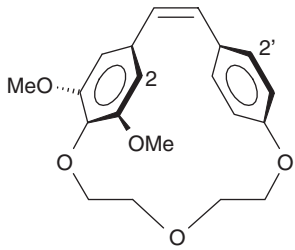

103A

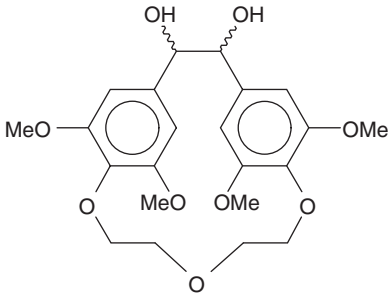

106

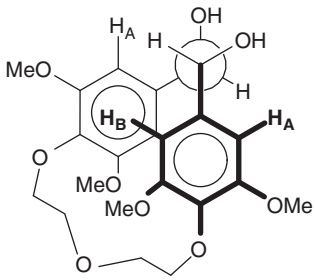

106A

The chemical shifts of the aromatic protons of tetraoxa[5.5](1,4)naphthalenophane **107**[70] in comparison with model compound **108** clearly indicated a preference for the *anti*-conformation of **107** as the protons *ortho* to the five-membered bridges (H-12,13) were shielded by 0.76 ppm, while those *ortho* to the methoxy groups only showed a 0.19 ppm shielding. H-12,13 must therefore lie over the second naphthalene unit of the molecule.

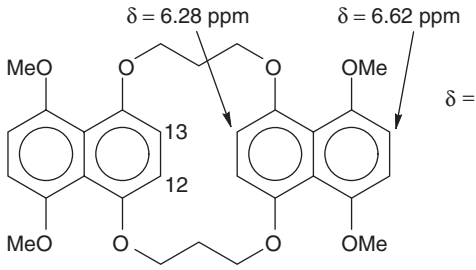

107

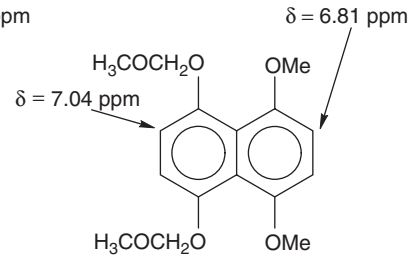

108

Photocycloaddition of various macrocyclic bis(chalcones) gave, among other products, the double cyclophanes **109** and **110**.[71] Phane **109** has a 7-and a 13-membered bridge to connect the *para*-phenylene rings while **110** has two 10-membered bridges. For the determination of the configuration of the central cyclobutane ring, it proved helpful that the shorter, seven-membered bridge in **109** resulted in restricted rotation, at room temperature, of the phenylene rings to which it was connected. This made the *ortho*-protons H-2′ and H-6′ chemically non-equivalent such that they gave separate crosspeaks in a 2D NOESY spectrum. It was found that H-2′ gave an NOE exclusively with H-1 of the cyclobutane ring whereas H-6′ interacted with H-2 of the cyclobutane. This proved the 1,2-*trans*-configuration of the cyclobutane unit. The 10-membered bridge in **110** no longer prevented the internal rotation of the *para*-phenylene rings in question. Hence, the NOESY experiments described above could not be applied to elucidate the cyclobutane stereochemistry in this compound. As the coupling patterns of the cyclobutane AA′XX′ spin systems of **109** and **110** were, however, very similar, the stereochemistry of **109** and **110** could be assumed to be the same.

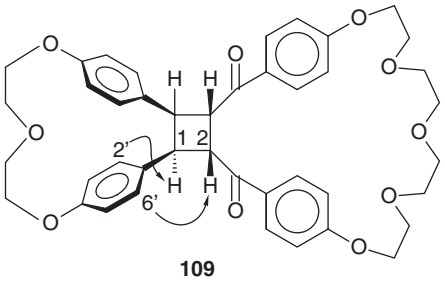

109

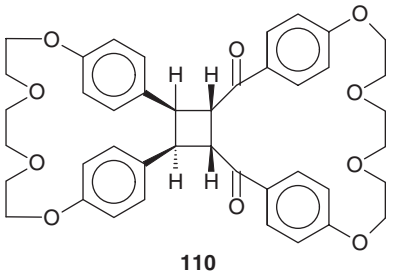

110

Nine macrocyclic cyclophanes of different ring size and aromatic substitution pattern, all containing 1,3-dioxane-*cis*-2,5-diyl building blocks as part of the rings, have been reported by a French–Romanian research group.[72] Here we only mention [7.7]paracyclophane **111** which has been studied in particular detail. It is known that aryl groups at position 2 of 1,3-dioxane prefer the axial orientation and also an orthogonal orientation with respect to the heterocycle (i.e. the line connecting C-2 and C-6 of the aryl group is parallel to the line connecting the dioxane oxygens). During the synthesis of **111**, one of the 1,3-dioxane rings must invert in order to permit closure of the macrocyclic ring. Thus in **111** *para*-phenylene ring C is at the same time equatorial with respect to 1,3-dioxane ring A and axial relative to 1, 3-dioxane ring B. The unfavourable interaction in **111** of the axial methyl group at ring A with the axial hydrogens H-4 and H-6 may be released by a chair inversion of ring A, which, however, can only take place if dioxane ring B inverts simultaneously. This tandem ring inversion **111**→**111′** may be regarded as a rocking chair movement (in one direction) with respect to aromatic ring C as the reference (support). Since **111′** has analogous steric disadvantages to **111**, the rocking chair movement goes back and the equilibrium is degenerate. At room temperature, the rocking motion is fast on the NMR time scale (^{1}H NMR at 500 MHz) such that only one set of averaged chemical shifts is observed for the two 1,3-dioxane rings. The conformational process **111/111′** was studied by detailed low-temperature ^{1}H NMR including 2D NOESY/ROESY/exchange spectra. A conformational barrier was not reported.

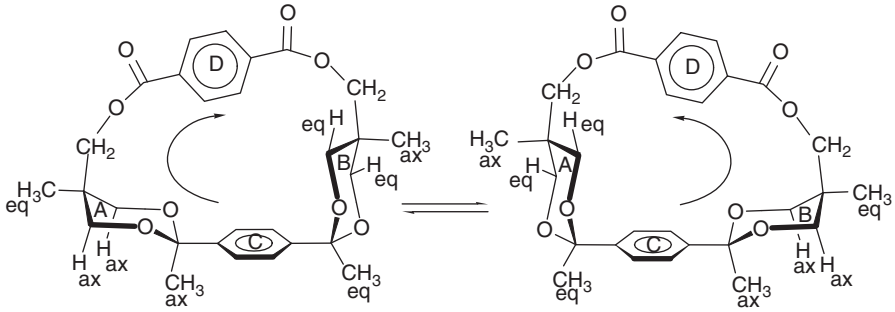

111 **111'**

A series of three macrocyclic 2,7-dioxyfluorenonophanes, **112**, possessing [7.7]- (**112a**), [10.10]- (**112b**), and [13.13]oligo(ethylenglycol) bridges (**112c**), was presented by Lukyanenko *et al.*[73] These long bridges permit free rotation of the fluorenone fragments about their long axes. According to force field calculations, the most stable conformers are the *syn*- and *anti*-forms with parallel arrangements of the fluorenone units. As these conformers are of comparable energies, the observed chemical shifts are probably averages over these conformers. When the chemical shifts of the aromatic protons of **112a–c** were compared with those of **113** as the reference compound, shieldings of $-0.16\ldots-0.39$ ppm were found which advocate predominantly parallel and closely located fluorenone units in solution as predicted by the force field calculations and also observed in the solid state by X-ray diffraction.

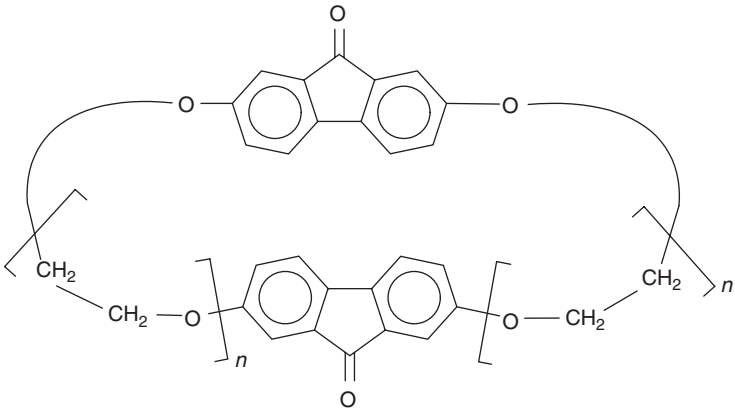

112	*n*
a	2
b	3
c	4

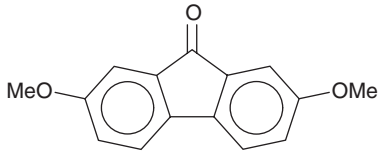

113

This section closes with a series of cyclophane-like quinquethiophenes, **114a–e**, with the bridges consecutively increased from two to six methylene groups, which have been studied as π-dimer models.[74] The double-decker structures of these compounds were verified by upfield shifts (up to −0.26 ppm) of the NMR signals of the protons of the inner thiophene groups compared to those of monomeric dimethylquinquethiophene **115** as a reference. It was found that the average upfield shifts of the thiophene protons relative to **115** were stronger for the compounds with odd-numbered bridges (**114b** and **114d**) than for the compounds with even-numbered bridges (**114c** and **114e**). This behaviour was interpreted by *syn*-stacking of the thiophene rings in the former two compounds and by *anti*-stacking in the

latter ones. The reasons for alternate conformations of the homologues were speculated upon.

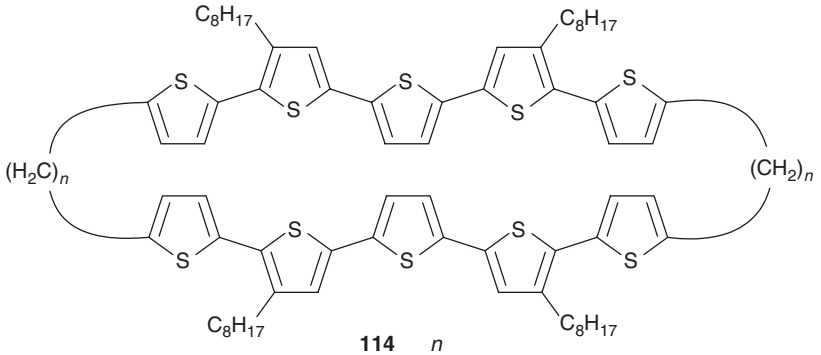

114	*n*
a	2
b	3
c	4
d	5
e	6

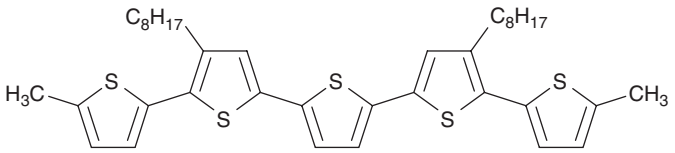

115

6. MULTIPLY BRIDGED PHANES

6.1. Phanes with multiple bridges between aromatic rings

We take the triquinolina triscationic bicyclophane **116**[75] as the first example of this class of compounds. Here, the 1-, 3-, and 5-positions of two benzene rings are mutually connected by bridges containing a 4-aminoquinolinium group. Low-temperature ^{1}H NMR measurements, in a restricted temperature range (298–213 K) for reasons of poor solubility, did not result in any decoalescence of the signals of the two kinds of methylene groups. This was explained by the results of force field/*ab initio* MO calculations, which showed the two enantiomeric C_3 propeller conformers to be of minimum energy. The higher energy conformers could be negleted

because they were calculated to lie at least $8\,kJ\,mol^{-1}$ above the C_3 form. A calculation of the barrier between the C_3 enantiomers resulted in a value of only $25\,kJ\,mol^{-1}$ that explained the failure of slowing down the conformational interconversion sufficiently. The comparison of the ^1H chemical shifts of **116** with those of the open analogue **117**[76] was considered to support the propeller ground state of the title compound. Protons H-2 and H-3 are more shielded in **116** ($\delta_2 = 7.92$, $\delta_3 = 6.57$ ppm) than in **117** ($\delta_2 = 8.57$, $\delta_3 = 6.92$ ppm) whereas H-8 is deshielded in **116** relative to **117** ($\delta_8 = 8.46$ and 7.95 ppm, respectively). The explanation offered was that the restricted mobility of **116** keeps H-2 and H-3 in a location between both benzene rings where these protons are shielded and that H-8 is forced into the deshielding zone of the lower benzene ring.

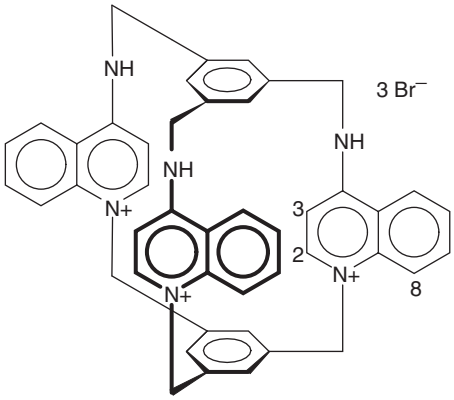

116

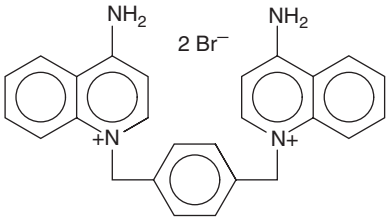

117

Lai and coworkers[77] studied the conformational behaviour of a series of crown-ether-fused dithia[*n*.3.3](1,2,6)cyclophanes, **118** ($n = 10$, 13, and 16), and dithia[*n*.3.3](1,3,5)cyclophanes, **119** (same values of *n*), by X-ray diffraction in the solid state and by ^1H and ^{13}C NMR in solution. The preferred conformations of the thia bridges of **118** were of the *chair–chair* type although it was not possible to rule out the wobbling processes *chair–chair* (*cc*) ⇆ *boat–chair* (*bc*) ⇆ *chair–boat* (*cb*) ⇆ *boat–boat* (*bb*) in solution. Dynamic ^1H NMR at 500 MHz down to 178 K did not permit the observation of a frozen wobbling process of the thia bridges indicating either a low barrier or insignificantly populated conformers with boat participation (*bc*, *cb* or *bb*), perhaps because of electronic repulsion between sulphur and phenolic oxygen. Low-temperature NMR spectra of **119** showed a slowing down of the conformational processes in the crownether ring and a doubling of the methylene proton AB pattern ($\delta = 4.23$ and 3.79 ppm at room temperature) at temperatures below 180 K. The results for the bridge-wobbling barriers of **119a**

($36.8\,kJ\,mol^{-1}$) and **119b** ($38.5\,kJ\,mol^{-1}$) indicated that the length of the crownether bridge is not of much influence.

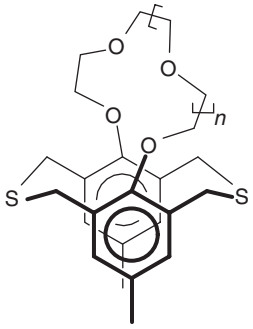

118 (*cc*-conformer)

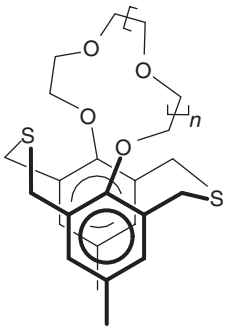

118 (*bc*-conformer)

a $n = 1$
b $n = 2$
c $n = 3$

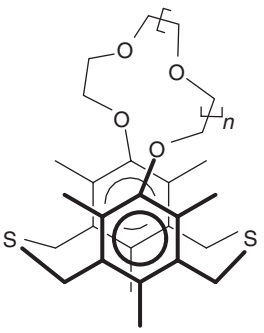

119

The same group also investigated[78] crown-tetrathia[3.3.3.3]metacyclophane **120a** possessing 10-membered crownether tethers and **120b** with 13-membered tethers. The X-ray structure of **120b** showed that the compound adopts a conformation in which two aromatic rings (A and B) are inclined to be perpendicular to the opposite rings (D and C), driving two internal methyl groups (a and c) into the π-clouds of rings A and B. Simultaneously, one benzylic hydrogen of methylene group b comes close to ring B and one proton of group c close to ring A. Also, both hydrogens of group e closely approach ring D. While, in solution, there are three methyl proton shifts at room temperature ($\delta = 2.47$, 2.31, and 1.98 ppm), these signals split on lowering the temperature, and there are 12 methyl signals at 223 K, two of which are indeed substantially shielded ($\delta = 1.36$ and 1.19 ppm). At the same time, a multitude of benzylic proton signals are observed, four of them also shielded [$\delta = 3.17$ (2 H), 2.84 (1 H), and 2.14 ppm (1 H)] and attributed to the protons that have close contact to an opposite aromatic ring. The upfield shifts, at 223 K, of these benzylic protons relative to the room temperature values are 0.47, 0.81, and 1.50 ppm. The low-temperature conformer described above is in exchange with its enantiomer, and the two high-field methyl signals show coalescence at 253 K and 500 MHz, from which the interconversion barrier was determined to be $50.6\,kJ\,mol^{-1}$. Interestingly, the carbon nuclei of the methyl groups undergoing C–H$\cdots\pi$ interactions are deshielded by 0.45 and 1.57 ppm with respect to the room temperature value. Compound **120a** with its shorter crownether tethers was shown by ^{1}H NMR to exist as two noninterconverting conformers at room temperature

and approaching fast exchange at 393 K. At low temperature, the spectra became rather complicated suggesting many possible conformations.

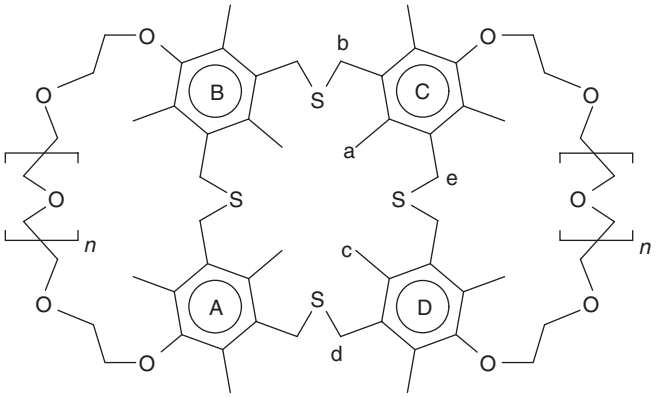

120a, $n = 0$
120b, $n = 1$

A triply bridged cyclophane was prepared by Meier and Karpouk[79] through threefold photochemical dimerization of (*E*,*E*,*E*)-1,3,5-tris(3-phenylpropenoyl)benzene **121a**. Various possible structures of the dimer can be thought of, depending on the regiochemistry (head-to-head or head-to-tail addition) of the dimerization and the conformation(s) of the starting material. H{H}-NOE experiments on a mixed addition product of **121a** and **121b** and an analysis of the spin coupling pattern of the cyclobutane rings proved the structure of the product to be the head-to-head/*anti*-dimer **122** with D_3 symmetry.

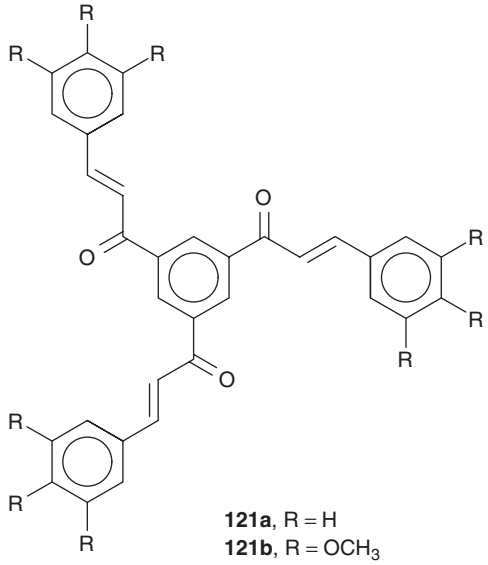

121a, R = H
121b, R = OCH_3

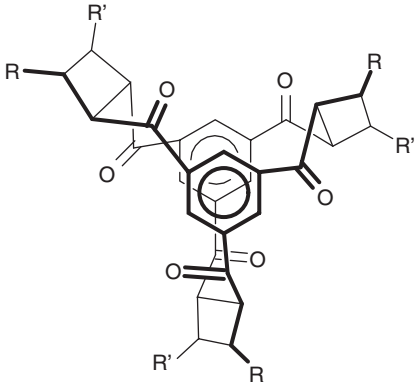

122, R = R' = Ph

When the pseudo-*ortho*-diiodide **123** of octafluoro[2.2]paracyclophane (OFP) was allowed to react with potassium *tert*-butoxide in dibutyl ether (415 K), the two triple bonds of the formal intermediate *syn*-bis(didehydro)OFP, **124**, added to one molecule of anthracene, giving the cage product **125**, which was an octafluoro[2.3.3.2](1,2,3,4)cyclophane derivative.[80] The ^{1}H and ^{13}C NMR spectra (HMQC, HMBC, NOE) of the product were completely assigned. X-ray diffraction showed that the remaining internal anthracene double bond is highly pyramidalized. It is therefore very reactive towards oxygen, chlorine, and bromine although the latter can only add in a *cis*-fashion. The addition products of these agents to the internal double bond of **125** were also characterized by their ^{1}H, ^{13}C, and ^{19}F NMR spectra (structures of these products not shown here).

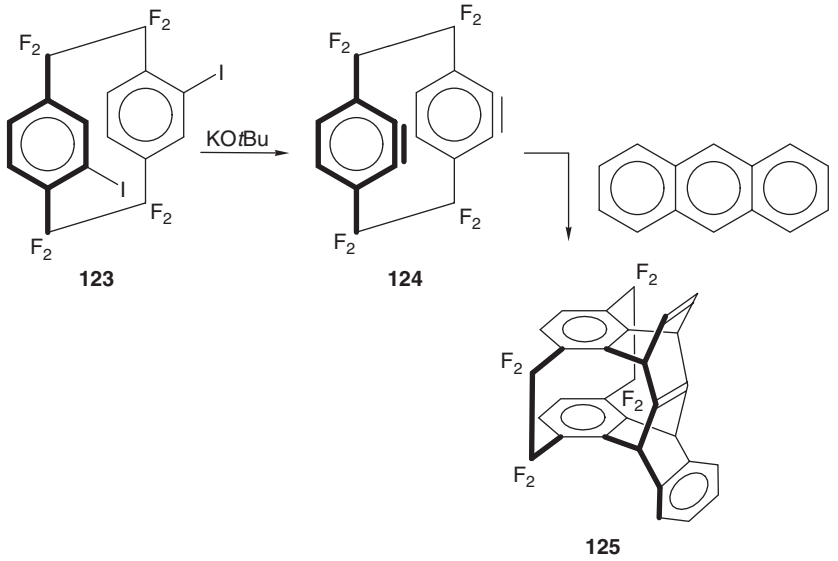

123 **124** **125**

Although, as stated in Section 1, this article is mainly concerned with NMR spectroscopy of cyclophanes themselves and not with the observation by NMR of cyclophane interactions with other molecules, we now refer to a few examples of cryptophane inclusion complexes because we think they are of high scientific interest. Cryptophanes are cage-like host molecules, **126**, which consist of two bowl-shaped cycloveratrylene caps connected by three aliphatic linker groups, $(CH_2)_x$, $(CH_2)_y$, and $(CH_2)_z$. One possible nomenclature enumerates the number of methylene groups in the linkers, e.g. cryptophane-222 is **126** with $x = y = z = 2$. Another nomenclature uses terms such as cryptophane-A or cryptophane-E, which are not self-explanatory. The *x*, *y*, *z* nomenclature is used here because of its greater clarity. Brotin and Dutasta[81] investigated the formation of inclusion complexes Xe@cryp by ^{129}Xe NMR, where cryp stands for the C_2-symmetric cryptophanes-223, -233, and -224 and the xenon atom resides in the cavity of the cryptophane. Cryptophanes-223 and -233 complex xenon efficiently in 1,1,2,2-tetrachloroethane-d_2

solution with binding constants $K = 2{,}810$ and 810/M, respectively, at 278 K. The free and bound xenon atoms were observed separately at room temperature under slow-exchange conditions on the ^{129}Xe NMR timescale. Thus, at 293 K, the ^{129}Xe chemical shifts were $\delta = 225$ for unbound Xe, 61 for Xe@cryptophane-223, and 48 ppm for Xe@cryptophane-233. Also including the previous data for cryptophane-222,[82] a linear relationship was found to exist between the binding constants and the internal volume of the hosts. Under the conditions mentioned, the Xe@cryptophane-224 complex underwent fast exchange on the NMR timescale. The decomplexation activation energies E_a and also $\Delta H^{\ddagger}$ and $\Delta S^{\ddagger}$ were determined from variable temperature 1D-EXSY experiments for Xe@cryptophane-223 and -233. The importance of the size of the cavity of the cryptophanes for guest encapsulation and the extreme sensitivity of the ^{129}Xe chemical shift towards slight structural modifications of the atom's environment were stressed.

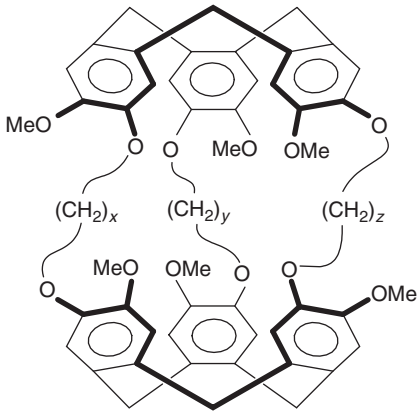

126 (cryptophanes)

Cryptophane-233 was also used to demonstrate the application of a new NMR experiment termed Spin Polarization Induced Rotating Frame NOE (SPIROE).[83] Like in the older Spin Polarization Induced NOE (SPINOE) experiment,[84] proton magnetization is generated by laser-polarized xenon atoms. The magnetization transfer pulse sequence is, however, amended to quench proton spin diffusion, which otherwise does prevent quantitative exploitation of the experiment. The C_2-symmetrical cryptophane-233 is well suited for SPIROE experiments as its dissymetry allows discrimination between the different protons inside the cavity. Thus, while all resonances present in the ^{1}H NMR spectrum also appeared in the SPINOE spectrum, only the aromatic protons, the aliphatic protons in the two-carbon linker and, more weakly, the equatorial protons of the methylene bridge groups were detected in the SPIROE spectrum. This indicated that spin diffusion was indeed suppressed, and the experiment could show that the preferred location of the xenon atom is between the aromatic rings and the two-carbon linker and distant from the three-carbon linkers.

Two diastereomeric cryptophane-222 derivatives were produced by attaching a molecule of (−)-camphanic acid to the parent alcohol (−)-cryptophanol A.[85] Laser-polarized ^{129}Xe and magnetization-transferred ^{1}H NMR spectra were obtained. Binding constants of xenon were found to be different for the diastereomers: xenon had a higher affinity for *anti*-(+)-cryptophane (−)-camphanate than for *anti*-(−)-cryptophane (−)-camphanate. Also, the energy barriers for the binding of xenon in the two host molecules were different. These differences seem to arise from the different abilities of the hosts to adopt their structures to the size of the guest atom.

The inclusion complex of cryptophane-222 and ^{13}C-labelled chloroform in two nonchiral liquid-crystalline environments was investigated by ^{13}C NMR.[86] Ordering of the complexes was manifested by the ^{1}H–^{13}C dipolar splitting of the chloroform ^{13}C-signal. In both solutions, the dipolar splitting for the bound ligands was substantially larger than that obtained for the free ligands, indicating a significant increase in ligand ordering upon complexation despite the absence of direct contact with the oriented solvent molecules. Ordering was enhanced to a similar degree for the aromatic (ZLI 1132) and aliphatic (ZLI 1695) thermotropic nematic liquid crystals used. Line narrowing of the ^{13}C chloroform resonance upon heteronuclear decoupling of the ZLI 1695 solution suggested that a significant component of the observed line broadening might originate from intermolecular coupling between host and guest molecules.

An important question concerning the properties of inclusion compounds is the motion of the guest relative to that of the host ("dynamic coupling"). Sandström and coworkers[87] performed studies of the guest mobility in the inclusion complexes CH_2Cl_2@cryptophane-333 and $CHCl_3$@cryptophane-333 by solid-state NMR techniques. They measured ^{1}H–^{13}C through-space dipolar couplings by separated local field methods under magic angle spinning conditions and compared residual ^{1}H–^{13}C dipolar interactions obtained directly by solid-state NMR and effective ^{1}H–^{13}C couplings estimated indirectly through the ^{13}C relaxation rates in isotropic solution. Although a number of approximations had to be made in the interpretation of the results, the authors were confident in their conclusion that the mobilities of encaged guests in the solid state and of guests inside the host cavity in the isotropic liquid are very similar. In a later paper,[88] the same authors reported on a variable temperature ^{2}H solid-state NMR investigation of the inclusion complexes CD_2Cl_2@cryptophane-333 and $CDCl_3$@cryptophane-333. The ^{2}H line shapes and nuclear spin relaxation rates were analysed in terms of C–D bond orientations and the time scale of the guest dynamics. It was found that encaged chloroform produces broad ^{2}H spectra, and that its reorientation is relatively slow with a correlation time of ca. 0.17 μs at 292 K. In contrast, the ^{2}H line shapes of encaged dichloromethane are narrow and the motion of this guest molecule is fast with a correlation time of ca. 1.4 ps at 283 K. A possible explanation of the different dynamics of the encaged dichloromethane and chloroform guests may be the van der Waals size of dichloromethane, which is ca. 20% smaller than that of chloroform. Another explanation can be sought in the symmetry of the host and the guests and its effect on the host–guest potential: the matching threefold symmetry of

chloroform and cryptophane-333 can perhaps result in a relatively higher barrier to the reorientation of encaged chloroform.

To terminate the report on cryptophane inclusion complexes, we mention a study of host–guest complexation of CHBrClF and CDBrClF by a chiral thiomethylated cryptophane-333, **127**, by means of ^{19}F NMR.[89] ^{19}F NMR T_1 experiments performed on CHBrClF@**127** revealed the presence of ^{19}F–^{1}H CSA-DD cross-correlated relaxation, which was found to be more efficient inside the host cavity. The measurement of ^{19}F–^{1}H CSA-DD cross-correlated relaxation rates at two field strengths allowed the determination of the correlation time τ_C of CHBrClF outside ($\tau_C = 0.27$ ns) and inside the cryptophane ($\tau_C = 0.62$–0.78 ns). These correlation times were confirmed by the measurement of the deuterium quadrupolar relaxation time T_q in the CDBrClF@**127** system. The two methods were in very good agreement and showed that the mobility of the substrate was decreased upon complexation.

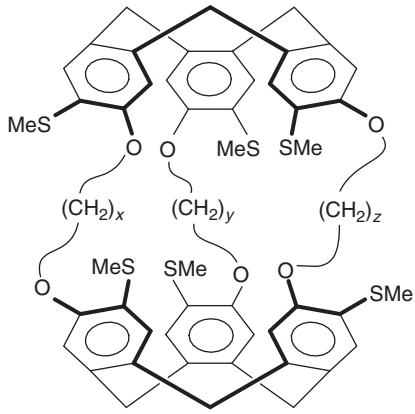

127

6.2. *in*-Phanes

The *in*-cyclophanes are a class of compounds that is of much interest both from the structural and an NMR point of view. They are cage compounds in which a central atom is connected by several (usually three) bridges to the same aromatic framework, and a substituent, hydrogen or lone pair of electrons on the central atom is pointing towards the inside of the cage. Until recently, the largest inside substituent has been fluorine (on silicon as the central atom). In continuation of their previous work, Pascal's group[90] have now successfully constructed compound **128** with an internal methyl group by placing a 9-methyltriptycene cap on 1,3,5-trisubstituted benzene as the base. The protons of the internal methyl group possess a chemical

shift of $\delta = 2.52$ ppm, which means only a modest degree of shielding with respect to the shifts in the precursor molecules **129a** ($\delta = 3.16$ ppm) or **129b** ($\delta = 3.85$ ppm). This was thought to be due to the fact that the methyl *protons* lie above the inside *edge* of the basal aromatic ring and not its centre. In contrast, the *in*-methyl ^{13}C resonance appears at $\delta = 14.8$ ppm, significantly shielded with respect to the values in **129a–b** ($\delta_C \geqslant 18.4$ ppm). The motion of the CH_2–S–CH_2 bridges (interconversion of enantiomeric conformers) in **128** is restricted on the NMR timescale at room temperature, and variable temperature ^1H NMR experiments gave a $\Delta G^{\ddagger}$ of 59.8 kJ mol^{-1} for the enantiomerization.

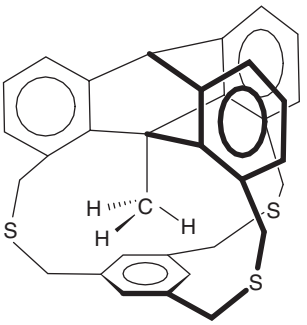

128

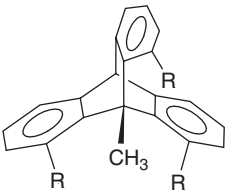

129a: R = CH_3
129b: R = CH_2Br

7. MULTILAYERED PHANES

As their name implies multilayered phanes possess more than two aromatic layers. Formerly these were studied mainly by Misumi.[7] Following Misumi's retirement the subject has only rarely occurred in the literature, so this section can be kept very short. We discuss one paper by Finocchiaro's group,[91] which describes two diastereomeric cyclophanes containing three aromatic layers. The outer layers are, however, not planar as they consist of spirobiindane units. The products were prepared from 1,2,4,5-tetrakis(bromomethyl)benzene (**130**) and two molecules of **131**. The latter attack **130** in a *para*-fashion and as they are chiral, the racemic diastereomer **132r** (*PP* and *MM*) and its *meso*-counterpart **132m** (*PM*) are formed (ratio 7:12). The racemic form **132r** is chiral. Because of its D_2 symmetry all constitutionally equivalent atoms of the spirobiindane units and those of the central tetrakismethylbenzene unit are related by symmetry. Hence, the ^1H, ^{13}C, and ^{31}P NMR spectra should feature only one set of signals for the 4,4′-H, 7,7′-H, four diastereotopic CH_2 bridge protons, etc. Such behaviour was found for the minor product. By way of contrast, **132m** is also chiral but has C_2 symmetry, and the constitutionally equivalent atoms are related pairwise by symmetry. The ^1H, ^{13}C, and ^{31}P NMR spectra should therefore display two sets of signals, which was indeed the case for the major product.

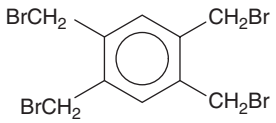

130

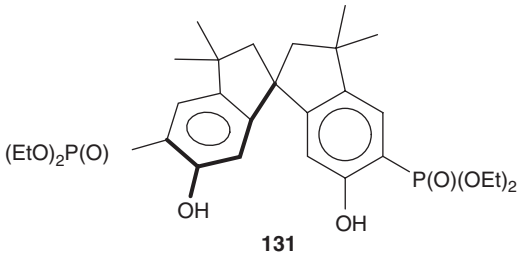

131

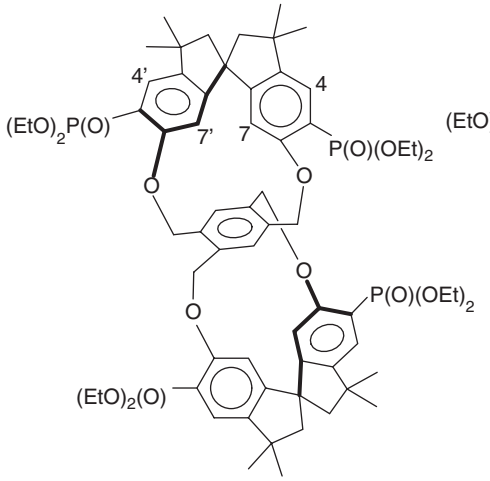

132r(*PP* or *MM*)

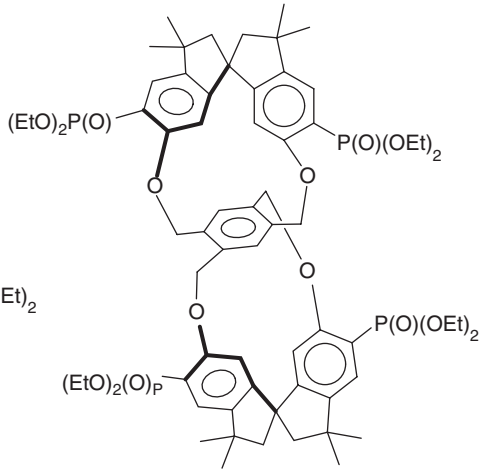

132m(*PM*)

8. [*m.n.o*…]PHANES

This section deals with compounds containing three or more aromatic systems in a cyclic arrangement, separated by aliphatic bridges of lengths *m*, *n*, *o*, … including zero bridge lengths. Besides compound **74** discussed in Section 4, Mashraqui and Kumar[92] investigated further macrocyclic cyclophanes and probed their conformational mobility. Both bis-lactone **133** with two four-membered bridges and its flash vacuum pyrolysis product **134** with two two-membered bridges are conformationally mobile. Their ^{1}H NMR spectra did not show any evidence of restricted rotation of the aromatic rings in the temperature range 408–218 K. Likewise, **135**, the bis-benzo homologue of **133**, and **136**, the dithia[3.3]phane analogue of **135**, were found to be conformationally flexible down to 218 K.[93] Hence, any conformational energy barrier was estimated to be smaller than 40 kJ mol^{-1}.

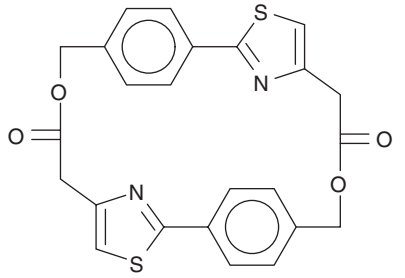

133

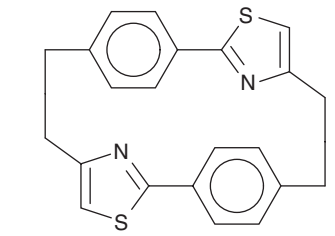

134

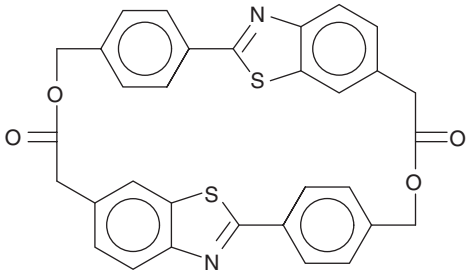

135

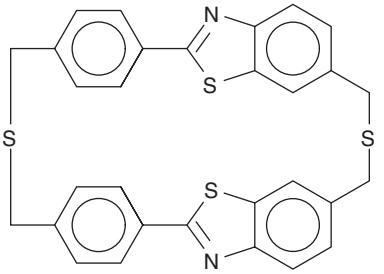

136

[2.2.2](2,7)Fluorenophanetriene **(137)** shows C_3 symmetry in its ^{1}H and ^{13}C NMR spectra at room temperature: H-9 and the olefinic protons each are observed as a singlet at $\delta = 3.38$ and 6.80 ppm, respectively (in $CDCl_3$).[48] No change was observed at low temperatures down to 223 K. Thus the fluorene rings are rotating fast under these conditions. From the ^{13}C satellites of the etheno proton signals the vicinal coupling constant was measured to be 12.5 Hz, indicating all-*cis* geometry of the etheno bridges. Treatment of trimer **137** with KH in DMSO-d_6 generated trianion $\mathbf{137}^{3-}$. The etheno protons ($\delta = 6.46$ ppm) of this trianion were observed at appreciably higher field than those of the corresponding dimer dianion $\mathbf{65}^{2-}$ ($\delta = 6.68$ ppm), suggesting more effective delocalization of the negative charges throughout the molecule.

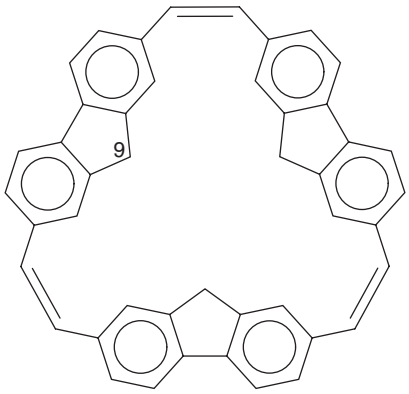

137

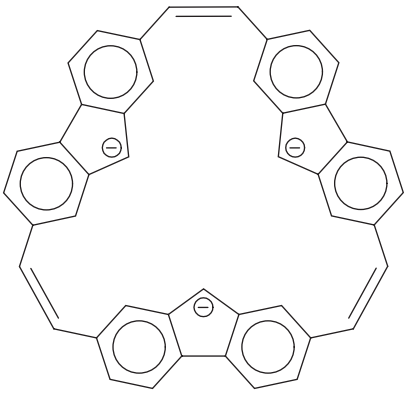

137^{3-}

[2.0.2.0]Metacyclophanediynes **138a–b** possess two axes of chirality on account of their two biphenyl units.[94] For this reason the two diastereomers *dl*-**138** and *meso*-**138** are possible. In compound **138a**, these interconvert rapidly on the NMR timescale even at 173 K. In **138b** with methoxy groups at the 2,2′-positions of the biphenyl units, diastereomerization is rapid at room temperature but signal decoalescence was observed below 223 K at 270 MHz. At a temperature of 213 K, two sets of signals were present with an integral ratio of ca. 5:1. Due to the structural similarity of the *dl*- and *meso*-diastereomers it was not possible to decide which was the major one. The interconversion barrier $\Delta G^{\ddagger}_{223}$ of **138b** is near 50 kJ mol^{-1}. Because of the bending of the triple bonds due to ring strain, the acetylenic carbons in **138a** and **138b** ($\delta \approx 99$ ppm) are deshielded by ca. 10 ppm relative to the strain-free model compounds **139a** and **139b** ($\delta \approx 89$ ppm).

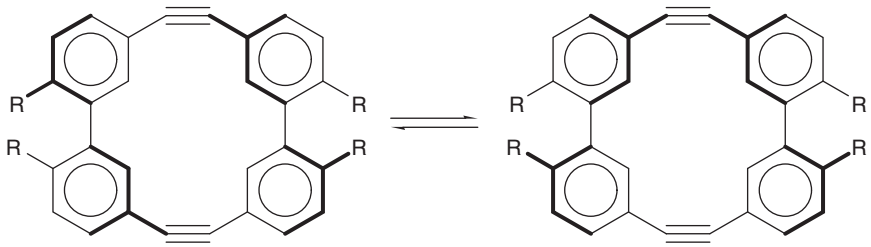

dl-**138** ⇌ *meso*-*138*

138	R
a	H
b	OMe

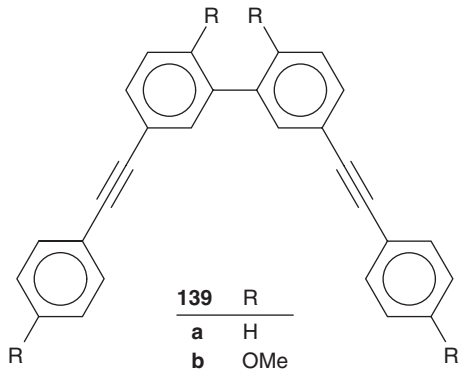

139	R
a	H
b	OMe

The stereochemically very demanding system **140** was reported by Cid, Diederich and their coworkers.[95] The four allene units in the macrocycle give rise to two

achiral diastereomers and two pairs of enantiomers, all of which could not only be isolated in a pure form, but it was also possible to determine their relative configurations. The main product showed four chemically nonequivalent *tert*-butyl groups in its 300 MHz ^{1}H NMR spectrum and was identified as the C_2-symmetric (*M*,*P*,*P*,*P*)/(*P*,*M*,*M*,*M*)-**140**. The spectrum of achiral C_{2h}-symmetric (*M*,*M*,*P*,*P*)-**140** displayed only two different *tert*-butyl signals and the remaining two products, D_4-symmetric (*P*,*P*,*P*,*P*)/(*M*,*M*,*M*,*M*)-**140** and D_{2d}-symmetric (*M*,*P*,*M*,*P*)-**140** each showed a single *tert*-butyl resonance. They were distinguished by X-ray diffraction of the D_4-isomer.

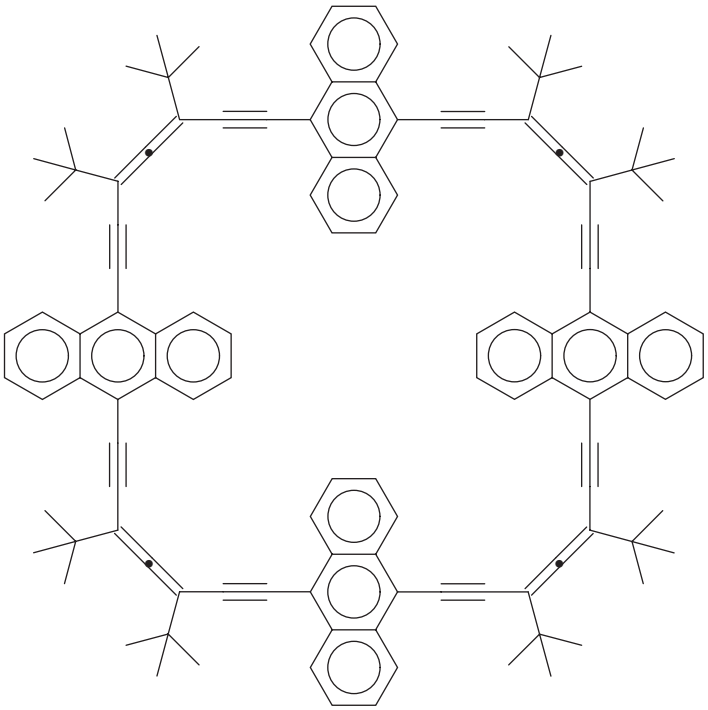

140

Two [2.1.1](2,6)pyridinophanes, **141** and **142**, with and without *gem*-dimethyl substitution of the one-carbon bridges were studied by Vedernikov *et al.*[96] According to its ^{1}H NMR spectrum, pyridinophane **141** shows mirror symmetry. Four chemically equivalent methyl groups indicate only a small barrier to conformational reorientation of one of the pyridine rings to the opposite side of the three-nitrogen plane. In contrast to the free ligand **141**, complex **141•PdCl$_2$** exhibits two

nonequivalent geminal methyl groups because of a rigid symmetric structure resulting from binding to $PdCl_2$. The protons of the ethano bridge form an AA′XX′ spin system, consistent with the rigidity of the molecule. An X-ray diffraction study confirmed that Pd is bound to the nitrogens of rings A and B. No isomerization to the unsymmetrical isomer (Pd bound to the nitrogens of rings B and C) was observed in the ^1H NMR spectrum when heating an acetonitrile solution of **141•PdCl$_2$** to 333 K. Complex **142•PdCl$_2$** showed properties significantly different from those of **141•PdCl$_2$**. It exhibits fluxional behaviour at room temperature because of rapid palladium atom migration between the nitrogens of the A and B rings. The only sharp signal in its ^1H NMR spectrum corresponds to H_{para} of pyridine ring C, all other proton signals being broad at room temperature. These broad signals became resolved as multiplets at 238 K, characteristic of a molecule with no symmetry. Resolved were three triplets of H_{para}, six doublets of H_{meta}, and two sets of AX patterns of CH_2 bridges. Hence, **141•PdCl$_2$** is the unsymmetrical isomer with Pd bound to the nitrogens of rings B and C.

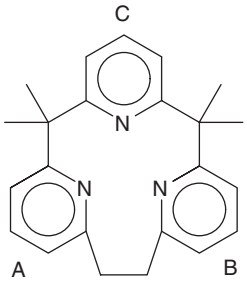

141

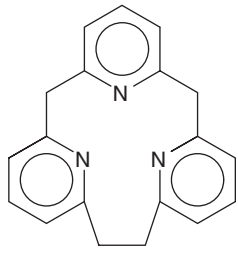

142

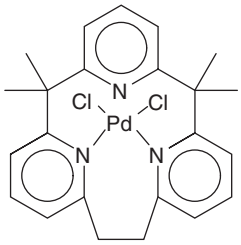

141•PdCl$_2$

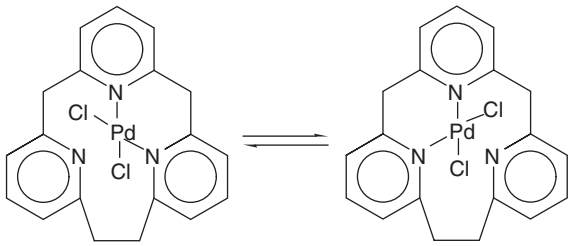

142•PdCl$_2$

Espinosa and his group[97] studied the conformational behaviour of bispyridinium cyclophane **143**, which is akin to their triply bridged compound **116** (Section 6). In compound **143**, the hydrogen atoms displaced symmetrically with respect to the pyridinium nitrogens show substantially different chemical shifts: δ(H-2,6) = 8.36 and 7.85 ppm, δ(H-3,5) = 6.83 and 6.57 ppm (in DMSO-d_6). These shift differences were explained by model calculations which resulted in two minimum energy conformations **143A** and **143B** (and their mirror images), in which the pyridinium rings

are rotated about the N(+)–C(α) and (C4)–N(α) bonds in such a way that their one side is pointing towards the centres of the *para*-phenylene rings while their opposite side is oriented to the outside of the molecule. Raising the temperature to 424 K caused signal coalescence, and from the chemical shift difference $\Delta\nu$ of 204 Hz for H-2,6 an approximate $\Delta G^{\ddagger}_{c}$ value of 85.8 kJ mol^{-1} was determined.

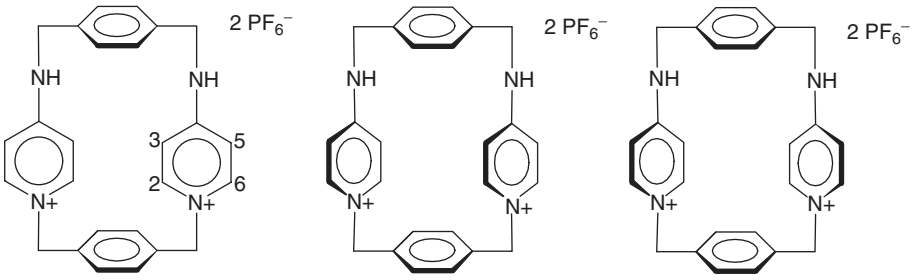

Compound **144** is a calixarene derivative that can dimerize by hydrogen bonding between the imide moieties of two molecules to form an elongated capsule, **144•144**, which is able to include small- to medium-sized guests. Rebek and coworkers found[98] that when **144•144** is offered a solution of CCl_4 and *p*-ethyltoluene (PET) in mesitylene-d_{12} it coencapsulates one of each guest. The 600 MHz ^{1}H NMR spectrum of product **(PET + CCl_4)@144•144** at room temperature showed two sets of resonances representing "social isomers", in which the PET molecule is oriented differently with respect to its neighbour CCl_4. The signals were sharp and well separated, and the exchange rate between isomers was slow on the NMR timescale at room temperature. The size and the shape of the capsule limits the mobility of the guests: they are too large to slip past each other and exchange places, and the PET molecule is too long to tumble within the capsule. The tapered ends of the cavity best accomodate smaller functions, and the isomer with the methyl group pointing away from the CCl_4 molecule is favoured to the extent of 85% at room temperature. Protons residing near the aromatic ends of the capsule are more strongly shielded by ring currents than those near the equator: chemical shifts reported for the major isomer of **(PET + CCl_4)@144•144** are $\delta = +0.2$ (CH_2CH_3) and -2.9 ppm (Ar-CH_3), and those for the minor isomer $\delta = -2.2$ (CH_2CH_3) and -3.7 ppm (CH_2CH_3). Many other coencapsulates of PET, 4-methylanisole, and *N*-methyltoluidine with a large variety of "solvent" molecules (e.g. CH_2Cl_2, $CHCl_3$, benzene, simple alcohols, alkanes, and cycloalkanes) were studied in order to assess the factors governing the relative stability of the social isomers. Explanations are difficult because it is not possible to change a single feature at a time. Every change in molecular shape necessarily comes with changes in size, surface polarity, volume, etc.

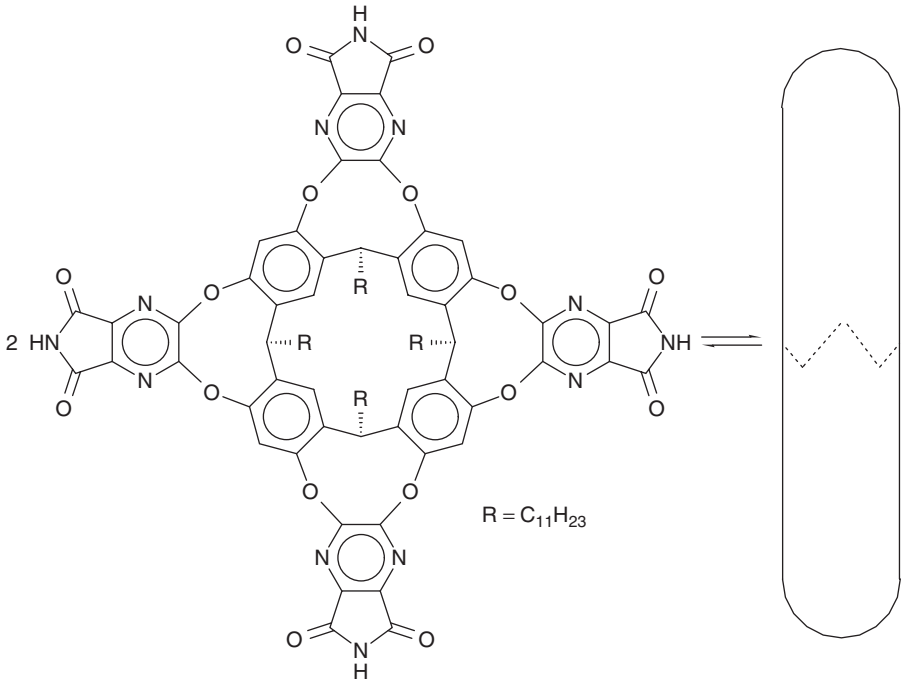

144 **144•144**

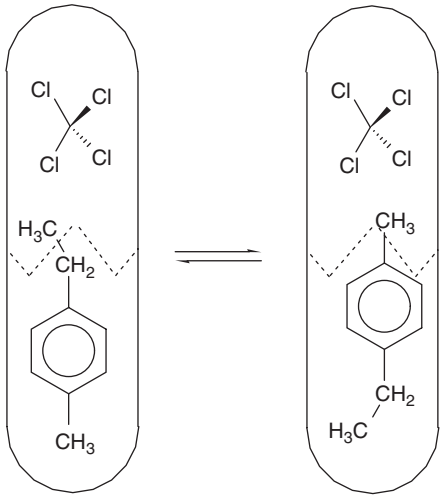

85% **15%**

(PET + CCl_4) @ 144•144

Capsule **144•144** is also able to accommodate [2.2]paracyclophane **(145)**, a guest of congruent shape and size.[99] Compound **145** alone, however, does not complex with the capsule. Only the addition of certain coguests, for example of CCl_4, to the solution causes almost instantaneous encapsulation of **145** leading to **(145 + CCl_4)@144•144**. As the guest in the previous example, the encapsulated [2.2]paracyclophane showed very strongly shielded protons near the end of the capsule, $\delta(CH_2) = -1.5$, $\delta(Ar–H) = 3.4$ ppm, and less strongly shielded protons closer to the equator, $\delta(Ar–H) = 5.1$, $\delta(CH_2) = 1.7$ ppm. (Paracyclophane **145** normally has shifts $\delta = 6.5$ and 3.1 ppm for Ar–H and CH_2, respectively.) This means that **145** is encapsulated with the CH_2–CH_2 bonds perpendicular to the axis of the capsule. In fact, it would not fit any other way for reasons of space. The chemical nonequivalence of certain protons of the host indicated that the spinning rate of **145** along the axis of the capsule was slow on the NMR timescale at room temperature. Variable temperature 2D EXSY experiments gave a barrier to rotation of **145** inside the capsule of 64.0 kJ mol^{-1}. When guests smaller than CCl_4 were coencapsulated with **145**, this barrier decreased slightly. Guests of larger dimensions increased the rotational barrier of **145** somewhat, for example to 66.5 kJ mol^{-1} when the coguest was cyclohexane.

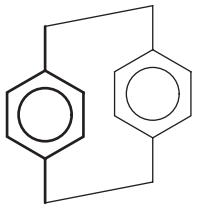

145

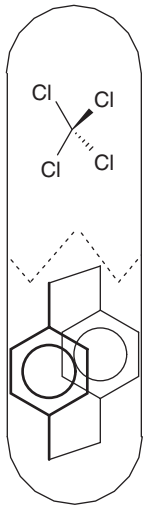

(145 + CCl_4) @ 144•144

Baker and his group[100] reported on a series of azolium-linked cyclophanes **146**. These consisted of two (benz)imidazolium or benzotriazolium groups linked to two benzenoid units (benzene naphthalene, methylbenzenes, or 2,6-pyridine) by methylene groups. The benzenoid units had *ortho*-, *meta*-, or *para*-substitution patterns. The conformations of these compounds were examined in solution by variable temperature ^{1}H NMR and in the solid state by X-ray diffraction.

The paracyclophanes and mesitylene-based meta- and orthometacyclophanes are rigid on the NMR timescale as indicated by sharp ^{1}H NMR spectra at all accessible temperatures. The nonmesitylene-based metacyclophanes and the orthocyclophanes are fluxional on the NMR timescale at high temperatures, but in most cases specific conformers could be frozen at low temperatures (down to 200 K). Many structures deduced from solution studies were consistent with those in the solid state. In all of the identified cyclophane conformations the azolium units were mutually *syn*. The benzenoid moieties in each conformation were either mutually *syn* or *anti*. One example for each is shown in formulae **147** (*syn*) and **148** (*anti*). Because of the extensive material (18 compounds) presented in the paper the interested reader is referred to the original literature for details.

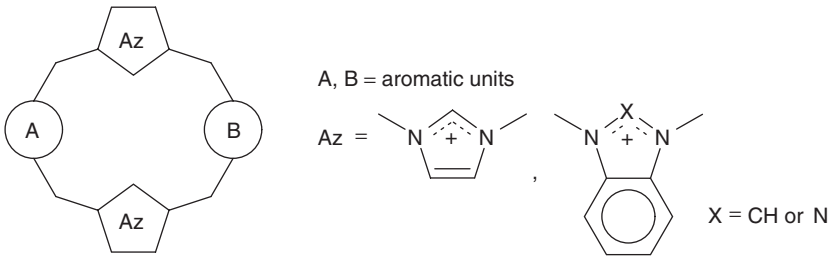

146

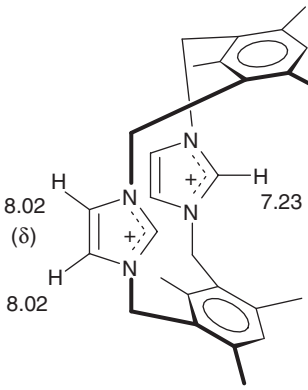

147

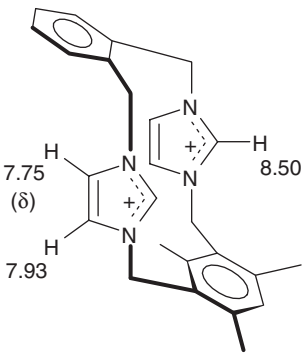

148

Finally, there is a review article by Finocchiaro *et al.*,[101] which is worthy of note and which deals with phosphorylated macrocycles, mainly cyclophanes of the calixarene type or related molecules. These were designed for applications in supramolecular chemistry and are capable of undergoing different binding modes, viz. hydrogen bonding, electrostatic attraction, and π-cation interactions. The NMR characterization of the macrocycles, their stereochemistry in solution and in the solid state, and the use as chiral receptors for biologically relevant molecules are

described. The material contained is too copious to be discussed here in detail. To get a hint of the theme, see compounds **132m** and **132r** in Section 7.

9. METALLOCENOPHANES

Structurally, the metallocenophanes do not have much in common with what organic chemists normally consider a cyclophane. Formally, however, they are cyclophanes as they contain bridges connecting aromatic units. For this formal reason we include them in this review. The overwhelming majority of the metallocenophanes are [*n*]ferrocenophanes, in which an *n*-membered chain connects one cyclopentadienide (cp) ring with the second one within a ferrocene unit. The smallest possible value of *n* is one, and [1]ferrocenophenophanes have enjoyed much popularity recently. The first aluminium-bridged [1]ferrocenophane, **149a**, showed five ^{13}C NMR signals for its two cp rings.[102] The signal of the *ipso*-carbon is broad at room temperature and sharpens when the temperature is lowered to 233 K. It has a chemical shift $\delta = 53$ ppm, i.e. upfield from ferrocene ($\delta_C = 68$ ppm), which is generally accepted to indicate ring strain, but downfield of the other known [1]ferrocenophanes with Si, Ge, Sn or B bridges. The ^{27}Al chemical shift of $\delta = 141$ ppm is in the range for tetracoordinate aluminium. The same group of authors[103] also described the first gallium-bridged [1]ferrocenophane, **149b**, for which δ(C-*ipso*) = 47.2 ppm. This upfield shift relative to ferrocene again indicates tilted cp rings but a simple correlation between ring tilt and δ(C-*ipso*) for all known [1]ferrocenophanes does not seem to exist. A Japanese group[104] used the pentacoordinate sila[1]ferrocenophane **150** as a monomer for ring-opening polymerization. The cp *ipso*-carbon was found to be rather deshielded [δ(C-*ipso*) = 47.2 ppm]. This is at lower field than any silicon-bridged [1]ferrocenophane investigated so far. The ^{29}Si chemical shift of -69.7 ppm supports the pentacoordinate character of the silicon atom in **150**. In contrast, **151**, the synthetic precursor of **150**, has both a relatively high-field cp C-*ipso* shift ($\delta_C = 31.4$ ppm), and a low-field ^{29}Si shift ($\delta_{Si} = -0.3$ ppm), which is appropriate for tetracoordinate silicon. Compound **152** is another example of a sila[1]ferrocenophane with pentacoordinate silicon.[105] Variable temperature ^{1}H NMR showed that **152** is a fluxional molecule in solution. Its behaviour can be explained by an equilibrium between the open (tetracoordinate) form **152b** and the two pentacoordinate species **152a** and **152a′**. At slow exchange rates (173 K, solvent: toluene-d_8), the ^{1}H spectrum displayed eight different cp proton signals, two distinct resonances for the CH_2 protons, and two *N*-methyl signals. Coalescence of the latter at 185 K gave a $\Delta G^{\ddagger}_c$ value of 35.8 kJ mol^{-1} for the coordination/decoordination process. Zirconium-bridged [1]ruthenocenophane **153a** shows an unusual downfield shift of the *ipso*-carbon ($\delta = 162.5$ ppm) of the ruthenocenophane cp ring.[106] The analogous iron compound, **153b**, has δ(C-*ipso*) = 159.0 ppm. As ruthenium is larger than iron, this behaviour is not in line with the rule: strain = upfield shift (see above). An explanation is lacking. However, tin-bridged compound **154a** behaves normally: δ(C-*ipso*) = 31.8 ppm

compared to 38.2 ppm for **154b**. When **154a** is polymerized to **155**, its strain is lifted and δ(C-*ipso*) moves to 76.9 ppm.

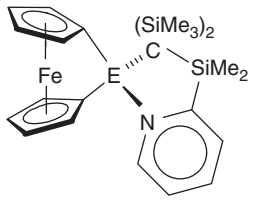

149	E
a	Al
b	Ga

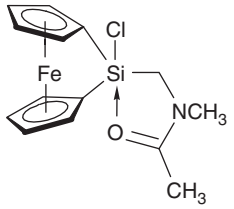

150

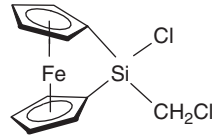

151

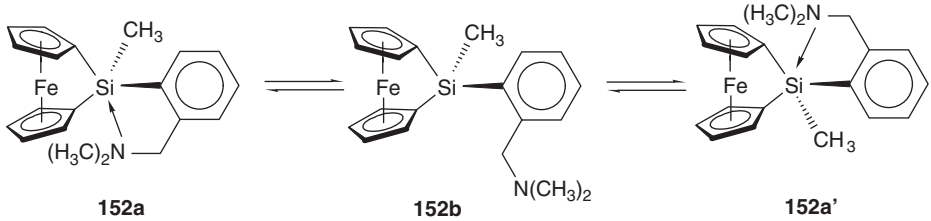

152a **152b** **152a'**

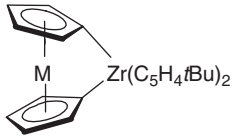

153	M
a	Ru
b	Fe

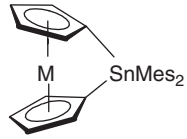

154	M
a	Ru
b	Fe

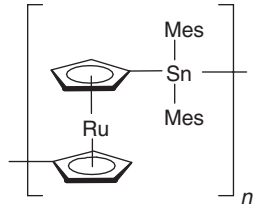

155

Upon UV photoirradiation in the presence of 1,2-diphosphinoethanes, both dimethylsila[1]ferrocenophane and [2]ferrocenophane undergo haptotropic shifts in which one η^5-cp ring is converted into an η^1-cp ring (**156**, **157**).[107] At 233 K, both products show unsymmetrical ^{1}H, ^{13}C, and ^{31}P NMR spectra, which were completely assigned by one- and two-dimensional NMR methods. Near room

temperature, the ^{1}H and ^{31}P signals of **156** appeared very broad. Near 273 K, the signal pairs of **157** underwent coalescence. The fluxional processes taking place in both compounds may involve fast successive 1,2-shifts of the η^1-cp ring and slow coordination mode exchange between the two cp ligands.

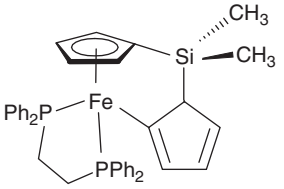

156

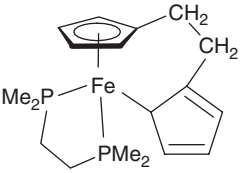

157

A thorough NMR study of the sila[1]ferrocenophanes **158a–e** was undertaken by Wrackmeyer and colleagues.[108] Using the refocussed INEPT technique, they observed ^{13}C, ^{29}Si, and ^{57}Fe satellites in the ^{13}C NMR spectra. The results, in particular the relative small values of $^{1}J(^{13}C\text{-}1,^{13}C\text{-}2) = 31.8$ and $^{1}J(^{29}Si,^{13}C\text{-}1) = 57.8$ Hz, were interpreted in terms of the special bonding situation of C-1. Wrackmeyer and coworkers also published a multitude of papers dealing with the NMR aspects of [3]ferrocenophanes and of a few [4]-, [5]-, and [6]ferrocenophanes. The material is too rich to be discussed here in full detail; hence, we give details of only some papers and restrict ourselves to enumerate the remaining ones. A full multinuclear resonance characterization (^{1}H, ^{13}C, ^{31}P, ^{119}Sn, ^{195}Pt) of 1,3-distanna-2-platina[3]ferrocenophane **159** was undertaken[109] and a large number of all possible heteronuclear coupling constants reported. It is of particular interest that at 298 K fast exchange of the two PPh_3 ligands occurs, resulting in an averaged $^{2}J(^{119}Sn,^{31}P)$ coupling of 680 Hz. At 233 K chemical exchange is slow, allowing the observation of different *cis*- (+206 Hz) and *trans*-couplings (−1574.5 Hz). Comparison of the individual values with their average strongly suggests that they must be of opposite sign. The barrier $\Delta G^{\ddagger}$ to site exchange of the PPh_3 groups is 41.8 ± 2 kJ mol^{-1}. This work was later extended to include complexes **160a–f** containing various chelating diphosphanes.[110] With respect to its dynamic behaviour **160f** resembles **159**, while **160a–e** have more rigid structures. Multinuclear (^{1}H, ^{13}C, ^{15}N, ^{29}Si, ^{119}Sn) magnetic resonance spectra were also recorded for the first 1,3,2-diazastanna[3]ferrocenophane **161**.[111] Sign determinations of one- to four-bond coupling constants involving ^{119}Sn were carried out on the more stable and soluble model compound **162**. Substituting the chloro groups in **161** by alkynyl substituents gave **163**, which reacted with triethylborane to give spirotin compound **164**.[112] Both **163** and **164** were characterized by ^{1}H-, ^{13}C-, ^{15}N-, ^{29}Si-, and ^{119}Sn NMR, **164** in addition by ^{11}B NMR. ^{1}H-detected HMBC served to obtain the ^{15}N and ^{119}Sn data, including the relative signs of some very small coupling constants. Compound **164** (R = $SiMe_3$) was also studied by solid-state ^{13}C-, ^{29}Si-, and ^{119}Sn MAS NMR.

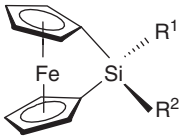

158	R^1	R^2
a	Me	Me
b	Me	Ph
c	Me	Cl
d	Ph	Cl
e	Cl	Cl

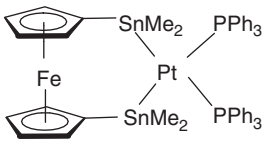

159

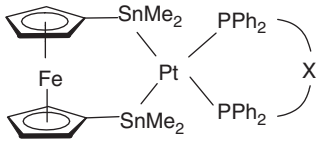

160

160	X
a	$-CH_2-$
b	$-(CH_2)_2-$
c	$-(CH_2)_3-$
d	$-CH=CH-$
e	$(C_5H_4)_2Fe$
f	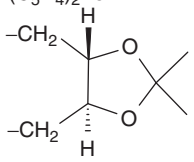

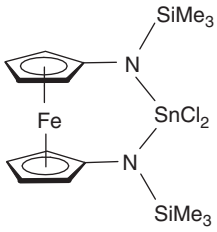

161

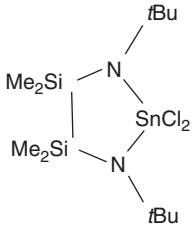

162

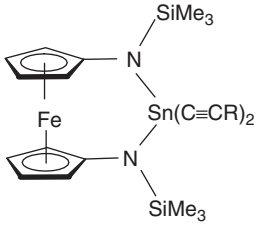

163

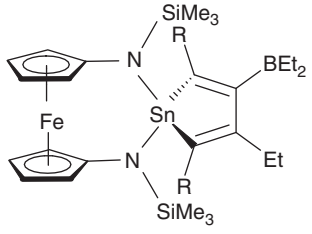

164

(R=*t*Bu or $SiMe_3$)

Other [3]ferrocenophanes investigated by full multinuclear magnetic resonance spectroscopy are 1,3,2-diazaphospha[3]ferrocenophanes **165** (R = *t*Bu, Ph; X = lone pair, O, S, Se),[113] and 1,3,2-diazabora[3]ferrocenophanes **166**[114] and **167**.[115] From the number of signals in the low-temperature ^{1}H, ^{13}C, and ^{29}Si NMR spectra of **166a–c**, it was concluded that the preferred conformations of **166a** and **166b** have the boron atom out of the Fe–C1–C1′ plane and the substituents at the exocyclic nitrogen parallel to the line connecting the two cp ring centres. The barrier to rotation about the exocyclic B–N bond in **166a** was determined to be $\Delta G^{\ddagger}_{273} = 58 \pm 1\,\mathrm{kJ\,mol^{-1}}$ from signal coalescence in the ^{13}C NMR spectrum. The preferred conformation of **166c** is different. Here the boron atom lies in the Fe–C1–C1′–N–N plane and the bonds between the substituents and the exocyclic nitrogen are orthogonal to this plane. Ref. 115 also describes the 1,4,2,3-diazadibora[4]ferrocenophane **168**, which has an unsymmetrical ground state conformation because the four nitrogens of the N_2B–BN_2 moiety avoid to become part of a plane around both boron atoms. 1D and 2D NOE/EXSY ^{1}H NMR spectra were utilized to clarify the fluxional processes taking place in this molecule.

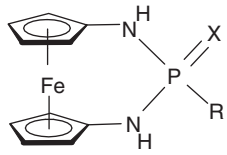

165

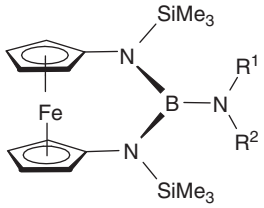

166	R^1	R^2
a	Et	Et
b	Me	CH_2Ph

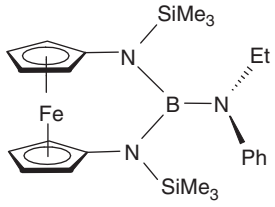

166c

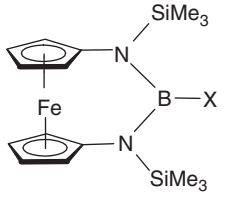

167 (X = H, F, Cl, Br, OPh, Ph)

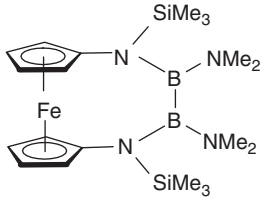

168

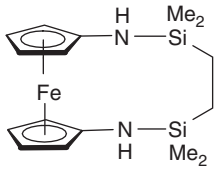

169

In the ^{1}H and ^{13}C NMR spectra of [6]ferrocenophane **169** broad signals were observed at room temperature.[116] Upon cooling two signals each appeared for C-2,5 ($\Delta\delta = 7.5$ ppm), for C-3,4 ($\Delta\delta = 2.9$ ppm), and for the carbons of the $SiMe_2$ groups ($\Delta\delta = 1.9$ ppm), because the six-membered bridge adopts a nonplanar conformation. Coalescence measurements gave a bridge inversion barrier $\Delta G^{\ddagger}_{233}$ of $50 \pm 1\,\mathrm{kJ\,mol^{-1}}$. 1,5,3,2,4-Diazaoxadisila[5]ferrocenophane **170** was studied by ^{13}C and ^{29}Si MAS NMR in the solid state and by ^{1}H, ^{13}C, ^{15}N, and ^{29}Si NMR in solution.[117] X-ray powder diffraction showed that in each molecule of **170** the two

silicon atoms and the four SiMe groups occupy crystallographically different positions. Therefore, two ^{29}Si signals were observed in the ^{29}Si MAS spectrum and three out of the four expected SiMe signals in the ^{13}C MAS spectrum. In the solution spectra the ^{1}H and ^{13}C signals for positions 2/5 and 3/4 of the cp rings were broad at room temperature, while the ^{1}H, ^{13}C, and ^{29}Si signals of the $SiMe_2$ groups were sharp. The broad signals stayed broad down to a temperature of 213 K when the compound became insoluble in toluene-d_8. Cyclophane ring inversion was assumed to be the process responsible for the line broadening observed.

In the context of a study of ^{57}Fe,^{13}C and ^{57}Fe,^{1}H spin–spin coupling in ferrocenes and other cyclopentadienyl iron complexes, 90% ^{57}Fe-labelled [3]ferrocenophane **(171)** was also investigated.[118] It showed $^{1}J(^{57}Fe,^{13}C)$ couplings of $+4.6 \pm 0.2$ Hz for all cp ring carbon atoms and (for some compounds other than **171**) $^{2}J(^{57}Fe,^{1}H)$ couplings < 1 Hz (negative or vanishingly small). The relative signs of $^{1}J(^{57}Fe,^{13}C)$ and $^{2}J(^{57}Fe,^{1}H)$ were obtained from the slopes of the cross-peaks in 2D ^{13}C,^{1}H-HETCOR spectra. Both the sign and magnitude of $^{1}J(^{57}Fe,^{13}C)$ were well reproduced by DFT calculations. The ^{57}Fe resonance of **171** undergoes a large ^{13}C isotope effect, $^{1}\Delta^{12/13}C(^{57}Fe)$, of -0.42 ppm. The ^{57}Fe chemical shifts of several [3]ferrocenophanes were reported and compared with those of ferrocene [$\delta_{Fe} = 1541.7$ ppm relative to $Fe(CO)_5$] and suitably substituted ferrocenes.[119] The iron shifts were discussed in terms of the π-accepting properties of substituents or phane bridges, which cause deshielding of the ^{57}Fe nucleus, and in terms of distortions of the ideal ferrocene geometry (tilting of the cp rings), which causes shielding of ^{57}Fe. The extreme chemical shift values given for the [3]ferrocenophanes were $\delta_{Fe} = 1691.0$ ppm for **172** and $\delta_{Fe} = 1285.5$ ppm for **171**, a shift range of 405 ppm.

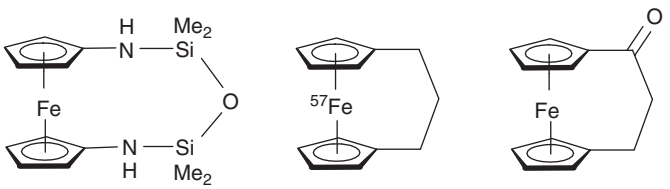

170 **171** **172**

This chapter terminates with the description of a series of tetraaza[4.4]ferrocenophanes, **173a–e**, carrying zero, two, or four methyl groups at various bridge positions.[120] NMR spectroscopy was used to establish free rotation of the –CH = N–N = C(R)– bridging chains (R = H, Me) and rigidity of the –C(Me) = N–N = C(Me)– chains in these macrocycles. It was found that the atom pairs C/H-2 and C/H-5 in the cp rings were chemically nonequivalent in **173b** and **173c** and remained so up to 430 K (500 MHz, DMSO-d_6). The same was true for the pairs C/H-3 and C/H-4. Thus, **173b** and **173c** possess a very rigid framework. Rotation of the four-membered chains is not possible because one **(173c)** or two **(173b)** methyl groups would have to pass through the interior of the macrocyclic

ring. By way of contrast, **173a**, **173d**, and **173e** are very flexible. The atom pairs C/H-2 and C/H-5 and also C/H-3 and C/H-4 are chemically equivalent at room temperature and remain so down to 210 K (500 MHz, $CDCl_3$). Here the movement of the bridges is unhindered because conformers can be interconverted without a methyl group having to pass through the interior of the macrocycle. All ^1H and ^{13}C NMR spectra of **173a–f** were assigned by 2D H,H- and H,C-correlation methods.

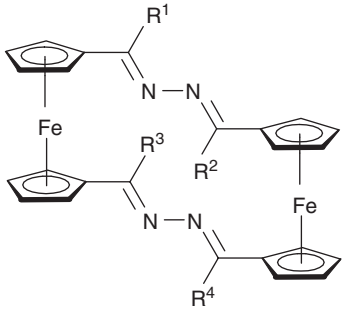

173	R^1	R^2	R^3	R^4
a	H	H	H	H
b	Me	Me	Me	Me
c	H	H	Me	Me
d	H	Me	Me	H
e	Me	H	Me	H

10. CONCLUSION

The author hopes to have shown in the present chapter that cyclophanes continue to be an exciting object of NMR investigations in spite of the fact that this theme has already enjoyed substantial popularity for the past several decades. The increase over the years of magnetic field strengths, the ever-improving performance of NMR spectrometers, and the multitude of available 1D and 2D NMR experiments have made it possible to study cyclophane molecular structures and dynamics in much more detail than before. The enormous variability of cyclophane structures will ensure that NMR studies of this class of compounds will not lose their attraction in the foreseeable future.

REFERENCES

1. B. H. Smith, *Bridged Aromatic Compounds*, Academic Press, New York, 1964.
2. P. M. Keehn and S. M. Rosenfeld, eds., *Cyclophanes*, Vols. 1 and 2, Academic Press, New York, 1983.
3. R. H. Mitchell, Nuclear magnetic resonance properties and conformational behavior of cyclophanes, in: *Cyclophanes*, P. M. Keehn and S. M. Rosenfeld, eds., Vol. 1, Academic Press, New York, 1983, pp. 239–310.
4. S. M. Rosenfeld and K. A. Choe, [*n*]Cyclophanes, in: *Cyclophanes*, P. M. Keehn and S. M. Rosenfeld, eds., Vol. 1, Academic Press, New York, 1983, pp. 311–357.
5. W. W. Paudler and M. D. Bezoari, Synthesis and properties of heterophanes, in: *Cyclophanes*, P. M. Keehn and S. M. Rosenfeld, eds., Vol. 2, Academic Press, New York, 1983, pp. 359–441.
6. S. Itô, Y. Fujise and Y. Fukazawa, Nonbenzenoid cyclophanes, in: *Cyclophanes*, P. M. Keehn and S. M. Rosenfeld, eds., Vol. 2, Academic Press, New York, 1983, pp. 485–520.

7. S. Misumi, Multilayered cyclophanes, in: *Cyclophanes*, P. M. Keehn and S. M. Rosenfeld, eds., Vol. 2, Academic Press, New York, 1983, pp. 573–628.
8. L. Ernst, *Prog. NMR Spectrosc.*, 2000, **37**, 47–190.
9. L. Ernst and K. Ibrom, NMR spectra of cyclophanes, in: *Modern Cyclophane Chemistry*, R. Gleiter and H. Hopf, eds., Wiley-VCH, Weinheim, 2004, pp. 381–414.
10. R. H. Mitchell, R. Blunden, G. Hollett, S. Bandyopadhyay, R. V. Williams and B. Twamley, *J. Org. Chem.*, 2005, **70**, 675–680.
11. M. Nitta, T. Sakakida, H. Miyabara, H. Yamamoto and S.-I. Naya, *Org. Biomol. Chem.*, 2005, **3**, 638–644.
12. N. Kanomata and M. Nitta, *Tetrahedron Lett.*, 1988, **29**, 5957–5960.
13. N. Kanomata and M. Nitta, *J. Chem. Soc., Perkin Trans.*, 1990, **1**, 1119–1126.
14. I. Aprahamian, G. J. Bodwell, J. J. Fleming, G. P. Manning, M. R. Mannion, T. Sheradsky, R. J. Vermeij and M. Rabinovitz, *J. Am. Chem. Soc.*, 2003, **125**, 1720–1721.
15. I. Aprahamian, G. J. Bodwell, J. J. Fleming, G. P. Manning, M. R. Mannion, T. Sheradsky, R. J. Vermeij and M. Rabinovitz, *Angew. Chem.*, 2003, **115**, 2651–2654; *Angew. Chem. Int. Ed.*, **42**, 2547–2550.
16. I. Aprahamian, G. J. Bodwell, J. J. Fleming, G. P. Manning, M. R. Mannion, B. L. Merner, T. Sheradsky, R. J. Vermeij and M. Rabinovitz, *J. Am. Chem. Soc.*, 2004, **126**, 6765–6775.
17. G. Bringmann, T. A. M. Gulder, K. Maksimenka, D. Kuckling and W. Tochtermann, *Tetrahedron*, 2005, **61**, 7241–7246.
18. M. Ashram, D. O. Miller, J. N. Bridson and P. E. Georghiou, *J. Org. Chem.*, 1997, **62**, 6476–6484.
19. N. L. Allinger, B. J. Gorden, S.-E. Hu and R. A. Ford, *J. Org. Chem.*, 1967, **32**, 2272–2278.
20. R. H. Mitchell, T. R. Ward, Y. S. Chen, Y. Wang, S. A. Weerawarna, P. W. Dibble, M. J. Marsella, A. Almutairi and Z. Q. Wang, *J. Am. Chem. Soc.*, 2003, **125**, 2974–2988.
21. R. H. Mitchell, W. Fan, D. Y. K. Lau and D. J. Berg, *J. Org. Chem.*, 2004, **69**, 549–554.
22. Y. Ting and Y.-H. Lai, *J. Am. Chem. Soc.*, 2004, **126**, 909–914.
23. H. Hopf, A. A. Aly, V. N. Swaminathan, L. Ernst, I. Dix and P. G. Jones, *Eur. J. Org. Chem.*, 2005, 68–71.
24. M. L. Birsa, P. G. Jones and H. Hopf, *Eur. J. Org. Chem.*, 2005, 3263–3270.
25. A. J. Roche, A. A. Marchione and S. A. Rabinowitz, *Magn. Reson. Chem.*, 2005, **43**, 1016–1022.
26. A. J. Roche and B. Canturk, *J. Fluorine Chem.*, 2005, **126**, 483–490.
27. Y. Zhai, I. Ghiviriga, M. A. Battiste and W. R. Dolbier Jr., *Synthesis*, 2004, 2747–2750.
28. D. C. Braddock, I. D. MacGilp and B. G. Perry, *Adv. Synth. Catal.*, 2004, **346**, 1117–1130.
29. M. Maekawa, N. Hashimoto, K. Sugimoto, T. Kuroda-Sowa, Y. Suenaga and M. Munakata, *Inorg. Chim. Acta*, 2003, **344**, 143–157.
30. K. Ibrom, G. Kohn (né Wentzel), K.-U. Boeckmann, R. Kraft, P. Holba-Schulz and L. Ernst, *Org. Lett.*, 2000, **2**, 4111–4113.
31. P. E. Hansen, *Annu. Rep. NMR Spectrosc.*, 1983, **15**, 105–234.
32. P. E. Hansen, *Prog. NMR Spectrosc.*, 1988, **20**, 207–255.
33. T. Dziembowska, P. E. Hansen and Z. Rozwadowski, *Prog. NMR Spectrosc.*, 2004, **45**, 1–29.
34. L. Minuti, A. Taticchi, A. Marrocchi, A. Broggi and E. Gács-Baitz, *Polycycl. Aromat. Comp.*, 2003, **23**, 483–493.
35. L. Minuti, A. Taticchi, D. Lanari, A. Marrocchi and E. Gács-Baitz, *Tetrahedron: Asymmetry*, 2003, **14**, 2775–2779.
36. A. Taticchi, L. Minuti, D. Lanari, A. Marrocchi, I. Tesei and E. Gács-Baitz, *Tetrahedron*, 2004, **60**, 11759–11764.
37. L. Minuti, A. Taticchi, A. Marrocchi, D. Lanari, E. Gács-Baitz and A. Gomory, *Tetrahedron Lett.*, 2005, **46**, 949–950.
38. L. Minuti, A. Taticchi, A. Marrocchi and E. Gács-Baitz, *Polycycl. Aromat. Comp.*, 2005, **25**, 13–22.
39. L. Minuti, A. Marrocchi, I. Tesei and E. Gács-Baitz, *Tetrahedron Lett.*, 2005, **46**, 8789–8792.
40. L. Minuti, A. Taticchi, D. Lanari, A. Marrocchi and E. Gács-Baitz, *Tetrahedron Asymmetry*, 2003, **14**, 2387–2392.
41. E. Gács-Baitz, O. Egyed, A. Taticchi, L. Minuti and A. Marrocchi, *Struct. Chem.*, 2005, **16**, 581–585.

42. O. Egyed, A. Taticchi, L. Minuti and E. Gács-Baitz, *Struct. Chem.*, 2004, **15**, 247–252.
43. A. Taticchi, personal communication, February 2006.
44. A. Renault, C. Cohen-Addad, J. Lajzerowicz-Bonneteau, J.-P. Dutasta and M. J. Crisp, *Acta Crystallogr.*, 1987, **43B**, 480–488.
45. K. Tani, K. Matsumura, E. Togo, K. Hori, Y. Tohda, H. Takemura, H. Ohkita, S. Ito and M. Yamamoto, *Chem. Lett.*, 2003, **32**, 910–911.
46. K. Tani, K. Matsumura, K. Hori, Y. Tohda, H. Takemura, H. Ohkita, S. Ito and M. Yamamoto, *Chem. Lett.*, 2002, 934–935.
47. A. Tsuge, H. Nishimoto, T. Moriguchi and K. Sakata, *Chem. Lett.*, 2003, **32**, 776–777.
48. K. Matsumoto, H. Minami, T. Kawase and M. Oda, *Org. Biomol. Chem.*, 2004, **2**, 2323–2326.
49. M.-K. Leung, M. B. Viswanath, P. -T. Chou, S. -C. Pu, H. -C. Lin and B. -Y. Jin, *J. Org. Chem.*, 2005, **70**, 3560–3568.
50. H. Hinrichs, A. K. Fischer, P. G. Jones, H. Hopf and M. M. Haley, *Org. Lett.*, 2005, **7**, 3793–3795.
51. G. Ricci, R. Ruzziconi and E. Giorgio, *J. Org. Chem.*, 2005, **70**, 1011–1018.
52. R. J. Vermeij, *Ph.D. Thesis*, Memorial University of Newfoundland, St. John's/NL, 2001, Chapter 2, 66–136.
53. S. H. Mashraqui, S. Kumar and K. R. Nivalkar, *J. Chem. Res. Synop.*, 2003, 225–227.
54. A. Moores, C. Defieber, N. Mézailles, N. Maigrot, L. Ricard and P. Le Floch, *New J. Chem.*, 2003, **27**, 994–999.
55. J. Jiang and Y.-H. Lai, *J. Am. Chem. Soc.*, 2003, **125**, 14296–14297.
56. H. Takemura, M. Kotoku, M. Yasutake and T. Shinmyozu, *Eur. J. Org. Chem.*, 2004, 2019–2024.
57. A. Tsuge, W. Iwasaki, T. Moriguchi and K. Sakata, *Chem. Lett.*, 2004, **33**, 756–757.
58. A. Tsuge, M. Otsuka, T. Moriguchi and K. Sakata, *Org. Biomol. Chem.*, 2005, **3**, 3590–3593.
59. T. Yamato, K. Noda and K. Tanaka, *J. Chem. Res. Miniprint*, 2002, 256–270.
60. P. Paetzold, U. Welling-Osterloh and U. Englert, *Z. Anorg. Allg. Chem.*, 2004, **630**, 2569–2570.
61. L. Ma, K. F. Mok and Y.-H. Lai, *Tetrahedron Lett.*, 2003, **44**, 3527–3530.
62. Y. Nakamura, T. Yamazaki and J. Nishimura, *Org. Lett.*, 2005, **7**, 3259–3262.
63. T. Yamato, S. Miyamoto, T. Hironaka and Y. Miura, *Org. Lett.*, 2005, **7**, 3–6.
64. S. H. Mashraqui and S. S. Lele, *Indian J. Chem.*, 2004, **43B**, 127–131.
65. H. Yoshida, K. Hiratani, T. Ogihara, Y. Kobayashi, K. Kinbara and K. Saigo, *J. Org. Chem.*, 2003, **68**, 5812–5818.
66. S. Bartlett and A. Nelson, *Chem. Commun.*, 2004, 1112–1113.
67. S. Barrett, S. Bartlett, A. Bolt, A. Ironmonger, C. Joce, A. Nelson and T. Woodhall, *Chem. Eur. J.*, 2005, **11**, 6277–6285.
68. C. Mateo, C. Pérez-Melero, R. Peláez and M. Medarde, *J. Org. Chem.*, 2005, **70**, 6544–6547.
69. C. Mateo, C. Pérez-Melero, R. Peláez and M. Medarde, *Tetrahedron Lett.*, 2005, **46**, 7055–7057.
70. Y. Tanoue, K. Sakata, M. Hashimoto, M. Hamada, N. Kai and T. Nagai, *ITE Lett. Batteries, New Technol. Med.*, 2003, **4**, 802–805.
71. F. R. Cibin, N. Di Bello, G. Doddi, V. Fares, P. Mencarelli and E. Ullucci, *Tetrahedron*, 2003, **59**, 9971–9978.
72. M. Balog, I. Grosu, G. Plé, Y. Ramondenc, E. Condamine and R. A. Varga, *J. Org. Chem.*, 2004, **69**, 1337–1345.
73. N. G. Lukyanenko, T. I. Kirichenko, A. Y. Lyapunov, A. V. Mazepa, Y. A. Simonov, M. S. Fonari and M. M. Botoshansky, *Chem. Eur. J.*, 2005, **11**, 262–270.
74. T. Sakai, T. Satou, T. Kaikawa, K. Takimiya, T. Otsubo and Y. Aso, *J. Am. Chem. Soc.*, 2005, **127**, 8082–8089.
75. A. Conejo-García, J. Campos, C. Eder, A. Entrena, M. A. Gallo and A. Espinosa, *J. Org. Chem.*, 2005, **70**, 5748–5751.
76. J. Campos Rosa, D. Galanakis and C. R. Ganellin, *Magn. Reson. Chem.*, 1998, **36**, 951–955.
77. J. -W. Xu, T.-T. Lin and Y. -H. Lai, *Tetrahedron*, 2005, **61**, 2431–2440.
78. J. -W. Xu, W.-L. Wang and Y. -H. Lai, *Tetrahedron*, 2005, **61**, 9248–9256.
79. H. Meier and E. Karpouk, *Tetrahedron Lett.*, 2004, **45**, 4477–4480.

80. W. R. Dolbier, Y.-A. Zhai, M. A. Battiste, K. A. Abboud and I. Ghiviriga, *J. Org. Chem.*, 2005, **70**, 10336–10341.
81. T. Brotin and J.-P. Dutasta, *Eur. J. Org. Chem.*, 2003, 973–984.
82. K. Bartik, M. Luhmer, J.-P. Dutasta, A. Collet and J. Reisse, *J. Am. Chem. Soc.*, 1998, **120**, 784–791.
83. H. Desvaux, J. G. Huber, T. Brotin, J.-P. Dutasta and P. Berthault, *Chem. Phys. Chem.*, 2003, 384–387.
84. G. Navon, Y.-Q. Song, T. Rööm, S. Appelt, R. E. Taylor and A. Pines, *Science*, 1996, **271**, 1848–1851.
85. J. G. Huber, L. Dubois, H. Desvaux, J. P. Dutasta, T. Brotin and P. Berthault, *J. Phys. Chem. A*, 2004, **108**, 9608–9615.
86. M. Marjanska, B. M. Goodson, F. Castiglione and A. Pines, *J. Phys. Chem. B*, 2003, **107**, 12558–12561.
87. Z. Tošner, O. Petrov, S. V. Dvinskikh, J. Kowalewski and D. Sandström, *Chem. Phys. Lett.*, 2004, **388**, 208–211.
88. O. Petrov, Z. Tošner, I. Csöregh, J. Kowalewski and D. Sandström, *J. Phys. Chem. A*, 2005, **109**, 4442–4451.
89. J. Crassous and S. Hediger, *J. Phys. Chem. A*, 2003, **107**, 10233–10240.
90. Q. Song, D. M. Ho and R. A. Pascal Jr., *J. Am. Chem. Soc.*, 2005, **127**, 11246–11247.
91. G. A. Consiglio, S. Failla and P. Finocchiaro, *J. Phys. Org. Chem.*, 2004, **17**, 760–768.
92. S. H. Mashraqui and S. Kumar, *J. Chem. Res. Synop.*, 2003, 351–353.
93. S. H. Mashraqui, S. Kumar and E. T. H. Dâu, *J. Mol. Struct.*, 2004, **697**, 221–230.
94. K. Utsumi, T. Kawase and M. Oda, *Chem. Lett.*, 2003, **32**, 412–413.
95. S. Odermatt, J. L. Alonso-Gómez, P. Seiler, M. M. Cid and F. Diederich, *Angew. Chem.*, 2005, **117**, 5203–5207; *Angew. Chem. Int. Ed.*, **44**, 5074–5078.
96. A. N. Vedernikov, J. C. Huffman and K. G. Caulton, *Inorg. Chem.*, 2002, **41**, 6867–6874.
97. A. Conejo-García, J. M. Campos, A. Entrena, R. M. Sánchez-Martín, M. Á. Gallo and A. Espinosa, *J. Org. Chem.*, 2003, **68**, 8697–8699.
98. A. Scarso, A. Shivanyuk and J. Rebek Jr., *J. Am. Chem. Soc.*, 2003, **125**, 13981–13983.
99. A. Scarso, H. Onagi and J. Rebek Jr., *J. Am. Chem. Soc.*, 2004, **126**, 12728–12729.
100. M. V. Baker, M. J. Bosnich, D. H. Brown, L. T. Byrne, V. J. Hesler, B. W. Skelton, A. H. White and C. C. Williams, *J. Org. Chem.*, 2004, **69**, 7640–7652.
101. P. Finocchiaro, S. Failla and G. Consiglio, *Russ. Chem. Bull., Int. Ed.*, 2005, **54**, 1355–1372.
102. J. A. Schachner, C. L. Lund, J. W. Quail and J. Müller, *Organometallics*, 2005, **24**, 785–787.
103. J. A. Schachner, C. L. Lund, J. W. Quail and J. Müller, *Organometallics*, 2005, **24**, 4483–4488.
104. Y. Hatanaka, S. Okada, T. Minami, M. Goto and K. Shimada, *Organometallics*, 2005, **24**, 1053–1055.
105. S. C. Bourke, F. Jäkle, E. Vejzovic, K.-C. Lam, A. L. Rheingold, A. J. Lough and I. Manners, *Chem. Eur. J.*, 2003, **9**, 3042–3054.
106. U. Vogel, A. J. Lough and I. Manners, *Angew. Chem.*, 2004, **116**, 3383–3387; *Angew. Chem. Int. Ed.*, **43**, 3321–3325.
107. M. Tanabe, S. C. Bourke, D. E. Herbert, A. J. Lough and I. Manners, *Angew. Chem.*, 2005, **117**, 6036–6040; *Angew. Chem. Int. Ed.*, **44**, 5886–5890.
108. B. Wrackmeyer, A. Ayazi, W. Milius and M. Herberhold, *J. Organomet. Chem.*, 2003, **682**, 180–187.
109. M. Herberhold, U. Steffl, W. Milius and B. Wrackmeyer, *Angew. Chem.*, 1997, **109**, 1545–1546; *Angew. Chem. Int. Ed.*, **36**, 1508–1510.
110. M. Herberhold, U. Steffl, W. Milius and B. Wrackmeyer, *Chem. Eur. J.*, 1998, **4**, 1027–1032.
111. B. Wrackmeyer, W. Milius, H. E. Maisel, H. Vollrath and M. Herberhold, *Z. Anorg. Allg. Chem.*, 2003, **629**, 1169–1174.
112. B. Wrackmeyer, H. E. Maisel, W. Milius and M. Herberhold, *J. Organomet. Chem.*, 2003, **680**, 271–280.
113. B. Wrackmeyer, E. V. Klimkina and W. Milius, *Inorg. Chem. Commun.*, 2004, **7**, 884–888.

114. B. Wrackmeyer, E. V. Klimkina, H. E. Maisel, W. Milius and M. Herberhold, *Inorg. Chim. Acta*, 2004, **357**, 1703–1710.
115. B. Wrackmeyer, E. V. Klimkina, W. Milius, O. L. Tok and M. Herberhold, *Inorg. Chim. Acta*, 2005, **358**, 1420–1428.
116. B. Wrackmeyer, E. V. Klimkina and W. Milius, *Inorg. Chem. Commun.*, 2004, **7**, 412–416.
117. B. Wrackmeyer, E. V. Klimkina and W. Milius, *Struct. Chem.*, 2004, **15**, 333–337.
118. B. Wrackmeyer, O. L. Tok and A. A. Koridze, *Magn. Reson. Chem.*, 2004, **42**, 750–755.
119. B. Wrackmeyer, O. L. Tok, A. Ayazi, H. E. Maisel and M. Herberhold, *Magn. Reson. Chem.*, 2004, **42**, 827–830.
120. P. Sohár, A. Csámpai, Á. Abrán, G. Túrós, E. Vass, V. Kudar, K. Ujszászy and B. Fábián, *Eur. J. Org. Chem.*, 2005, 1659–1664.

Applications of Solid-State ^{31}P NMR Spectroscopy

A. IUGA*, C. ADER, C. GRÖGER AND E. BRUNNER

Institut für Biophysik und Physikalische Biochemie, Universität Regensburg, D-93040 Regensburg, Germany

Solid-state ^{31}P NMR spectroscopy has meanwhile found an overwhelming variety of applications. Phosphorous is an important chemical element in biology as well as materials science. Numerous proteins occur in the phosphorylated state. Nucleic acids and phospholipids contain phosphate groups as well. Phosphorylation/dephosphorylation reactions play a crucial role in many biological processes. Furthermore, phosphorous compounds such as phosphate glasses, porous aluminophosphates, phosphorous-containing semiconductors, and many others are extremely important and interesting materials. During the past years, solid-state NMR spectroscopy has become a very valuable analytical tool in biology as well as materials science due to its remarkable methodical and technical progresses. In particular, the invention of magic angle spinning devices with sample spinning rates

*Present address. University of Lethbridge, Canada.

ANNUAL REPORTS ON NMR SPECTROSCOPY
VOLUME 60 ISSN 0066 4103
DOI 10.1016/S0066-4103(06)60004-5

up to 70 kHz, the development of advanced spin polarization transfer and decoupling techniques as well as the commercial availability of superconducting wide-bore magnets with magnetic fields up to ca. 20 T were remarkable breakthroughs. Many multidimensional NMR techniques which were limited to liquid-state NMR spectroscopy in former times can now be applied in solid-state NMR spectroscopy as well. The aim of the present review is to discuss and summarize recent methodical developments and applications of solid-state ^{31}P NMR spectroscopy.

1. INTRODUCTION

Solid-state ^{31}P NMR spectroscopy has found an overwhelming variety of applications. The reasons for this success are obvious. Phosphorous is an important chemical element in biology as well as materials science. Numerous proteins occur in the phosphorylated state. Nucleic acids and phospholipids contain phosphate groups as well. Phosphorylation/dephosphorylation reactions play a crucial role in many biological processes. Furthermore, phosphorous compounds such as phosphate glasses, porous aluminophosphates, phosphorous-containing semiconductors, and many others are extremely important and interesting materials.

The phosphorous isotope ^{31}P occurs with a natural abundance of 100%. It exhibits a nuclear spin $I = \frac{1}{2}$ and a relatively high magnetogyric ratio of $\gamma_I = 1.083941 \times 10^8 \,\mathrm{rad\,s^{-1}\,T^{-1}}$. These properties make phosphorous favorableand convenient from the NMR point of view.

During the past years, solid-state NMR spectroscopy has become a very valuable analytical tool in biology as well as materials science due to its remarkable methodical and technical progresses. In particular, the invention of magic angle spinning (MAS) devices with sample spinning rates up to 70 kHz, the development of advanced spin-polarization transfer and decoupling techniques as well as the commercial availability of superconducting wide-bore magnets with magnetic fields, B_0, up to ca. 20 T were remarkable breakthroughs. Many multidimensional NMR techniques which were limited to liquid-state NMR spectroscopy in former times can now be applied in solid-state NMR spectroscopy as well. The aim of the present review is to discuss and summarize recent methodical developments and applications of solid-state ^{31}P NMR spectroscopy. Since the number of useful and important applications is huge, we have to limit our considerations to selected examples illustrating some interesting trends. In particular, new biological applications will be highlighted. Materials science aspects will also be discussed. However, many more applications of solid-state ^{31}P NMR spectroscopy can be found in the literature apart from the papers discussed here.

2. METHODICAL ASPECTS OF SOLID-STATE ^{31}P NMR SPECTROSCOPY

The NMR spectra of static solids typically exhibit relatively broad signals without spectral resolution, i.e., very limited structural information. The width of

solid-state NMR signals arises from the so-called internal magnetic interactions. For ^{31}P, the line width is mainly determined by the simultaneous influence of the chemical shift anisotropy (CSA) and magnetic dipole–dipole interactions with neighboring spins (through-space interactions). For phosphate-containing compounds such as numerous biomolecules, the heteronuclear ^{31}P–^{1}H magnetic dipole–dipole interaction strongly exceeds the homonuclear ^{31}P–^{31}P magnetic dipole–dipole interaction in general. Indirect spin–spin couplings (through-bond and *J*-couplings) are usually several orders of magnitude smaller than the broadening associated with the aforementioned anisotropic interactions. Therefore, CSA and heteronuclear ^{31}P–^{1}H magnetic dipole–dipole interaction are the dominating line-broadening mechanisms governing the solid-state ^{31}P NMR signals of phosphate-containing compounds (see Sections 2.1.1 and 2.1.2). To evaluate the influence of an internal magnetic interaction upon the line width of a solid-state NMR signal, the so-called second moment, M_2, is usually introduced.[1] The second moment in units of the angular frequency (ω) is defined by

$$M_2 = 4\pi^2 \int (\nu - \nu_0)^2 f(\nu) \mathrm{d}\nu \tag{1}$$

with respect to the center of gravity, ν_0, of a signal. Here, $f(\nu)$ denotes the line shape function of the considered signal and ν the frequency. It should be noted that the center of gravity of a ^{31}P NMR signal is given by $\nu_0 = \gamma_I B_0(1-\sigma)2\pi$ where σ denotes the isotropic shielding constant. The isotropic shielding constant determines the so-called isotropic chemical shift: $\delta = \delta_{iso} = \sigma_{ref} - \sigma$. Here, σ_{ref} is the isotropic shielding constant of a reference compound. ^{31}P NMR spectra are usually referenced relative to the signal of liquid H_3PO_4 (0 ppm).

The second moment, M_2, can be written as the sum of the contributions of the different line-broadening interactions present in the sample.[1] In order to obtain highly resolved spectra, line-narrowing techniques such as MAS (see Section 2.2) have to be applied in combination with efficient heteronuclear ^{1}H decoupling (see Section 2.3). In Section 2.4, polarization transfer by cross-polarization (CP) is discussed. This can be used for signal enhancement and/or to extract information about spatial proximities between neighboring spins, e.g., ^{31}P and ^{1}H. Several important techniques for the measurement of internuclear distances are introduced in Section 2.5 with respect to solid-state ^{31}P NMR. Multiple-quantum (MQ) experiments (see Section 2.6) are nowadays frequently applied also in solid-state ^{31}P NMR spectroscopy. In special cases, the desired information about the samples can be extracted simply by the analysis of one-dimensional (1D) experiments. However, samples with more complex spectra usually require the application of multidimensional experiments[2] which can provide through-space or through-bond correlations of spins with homonuclear or heteronuclear couplings. Some of the corresponding two-dimensional (2D) experiments are described in Section 2.7.

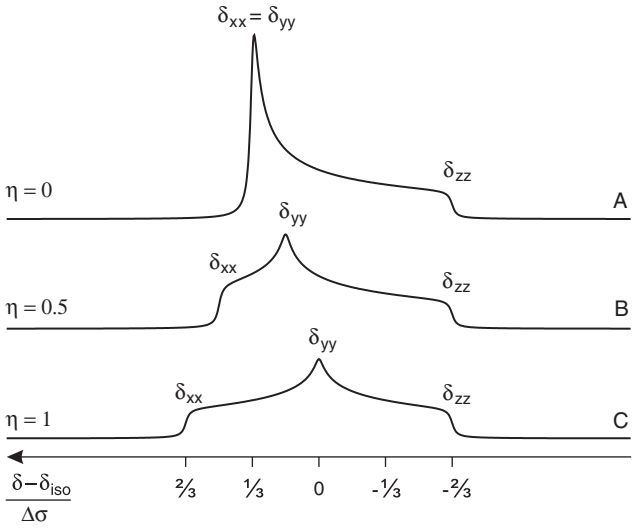

Fig. 1. Calculated powder line shape of an isolated ^{31}P spin for $\eta = 0$ (A), $\eta = 0.5$ (B), and $\eta = 1$ (C). Note that the SIMPSON software package[3] was used for all line shape calculations described in this chapter.

2.1. Relevant line-broadening mechanisms and resulting line shapes

2.1.1. *Chemical shift anisotropy (CSA)*

The spectrum of a single static ^{31}P spin in a powder[†] sample is usually dominated by CSA. In general, the chemical shift is spatially anisotropic and must be described by a tensor with the three principal values δ_{xx}, δ_{yy}, and δ_{zz} in its so-called principal axis system. The isotropic value of this tensor is given by $\delta = \delta_{iso} = \frac{1}{3}(\delta_{xx} + \delta_{yy} + \delta_{zz})$. The principal axes are denoted such that the convention $|\delta_{zz}–\delta_{iso}| > |\delta_{xx}–\delta_{iso}| > |\delta_{yy}–\delta_{iso}|$ is fulfilled. The chemical shift anisotropy can be described by the so-called anisotropy parameter, $\Delta\sigma$

$$\Delta\sigma = \frac{1}{2}(\delta_{xx} + \delta_{yy}) - \delta_{zz} \tag{2}$$

and the asymmetry parameter, η:

$$\eta = \frac{3}{2}\frac{\delta_{xx} - \delta_{yy}}{\Delta\sigma} \tag{3}$$

The resulting line shapes are shown in Fig. 1. Fig. 1A corresponds to an axially symmetric shielding tensor: $\delta_{xx} = \delta_{yy} \neq \delta_{zz}$ (i.e., $\eta = 0$). If no axial symmetry is present in the electronic environment, i.e., for $\delta_{xx} \neq \delta_{yy} \neq \delta_{zz}$, the line shape changes characteristically (see Fig. 1B and C).

[†]Powder means that the crystallites/particles of the sample exhibit random orientation. If not stated else, the present paper always deals with powder samples.

Table 1. Characteristic ranges of the isotropic chemical shift, δ, the chemical shift anisotropy, $\Delta\sigma$, and the asymmetry parameter, η, for various classes of phosphates[4–8]

	δ/ppm	$\Delta\sigma$/ppm	η
Monophosphates Q^0	−30 … 12	15 … 60	0 … 1
Diphosphates Q^1	−33 … 4	−140 … −80	0 … 0.8
Polyphosphates Q^2	−53 … −18	160 … 250	0.3 … 0.8
Monohydrogen monophosphates $Q^0(H^1)$	−7 … 6	−105 … −75	0.1 … 0.6
Dihydrogen monophosphates $Q^0(H^2)$	−6 … 4	33 … 120	0 … 0.7
Dihydrogen diphosphates $Q^1(H^1)$	−20 … −8	110 … 180	0.8 … 1

Note: The index m in the notation $[Q(H^m)]$ indicates the number of P–OH or hydrogen bonds per PO_4 tetrahedron.

The CSA contribution to the second moment of a signal is given by

$$M_2^{\mathrm{CSA}} = \frac{4}{45}\gamma_I^2 B_0^2 \Delta\sigma^2 \left(1 + \frac{1}{3}\eta^2\right) \tag{4}$$

The NMR spectroscopic parameters of several unprotonated phosphates in inorganic materials are known.[4] Phosphate structures can be characterized by the so-called Q^n group classification (see Section 4.1). The Q^n groups are basic structural units (PO_4 tetrahedra), where n denotes the number of other PO_4 units attached to the considered unit. The ^{31}P chemical shift anisotropy was shown,[5–8] to depend strongly on the number n (see Table 1). Protonated phosphates (i.e., phosphates with P–OH or P–O involved in hydrogen bonds) exhibit significantly different ^{31}P chemical shift anisotropies than unprotonated phosphates (see also Table 1).

For inorganic POX_3 compounds (X = F, Cl, Br, Me) and some inorganic compounds containing PO_4 tetrahedra, Grimmer[9] found a relationship between the chemical shift anisotropy and the P–O bond length given by:

$$\frac{\Delta\sigma}{\mathrm{ppm}} = A\left(\frac{r_{\mathrm{P-O}}}{\mathrm{\AA}}\right) + B \tag{5}$$

where $A = -1585$ and $B = 2553$ were determined empirically. Eq. (5) is based on the idea that a decrease in bond length indicates an increasing π-bond character[10] leading to an increase in the chemical shift anisotropy.

2.1.2. *Magnetic dipole–dipole interaction*

^{31}P nuclei often interact with neighboring spins. On one hand, they may be coupled to other ^{31}P spins (homonuclear magnetic dipole–dipole interaction). On the other, ^{31}P spins often interact with so-called heteronuclei such as ^{1}H, ^{17}O, and others (heteronuclear magnetic dipole–dipole interaction).

Homonuclear magnetic dipole–dipole interaction. The homonuclear magnetic dipole–dipole interaction[1] is a homogeneous line broadening (except for isolated spin pairs or linear chains of spins). Its contribution to the second moment of a signal,

M_2^{II}, is given by the following equation

$$M_2^{\mathrm{II}} = \frac{3}{5}\left(\frac{\mu_0}{4\pi}\right)^2 \gamma_{\mathrm{I}}^4 \hbar^2 I(I+1) \frac{1}{N_{\mathrm{I}}} \sum_{i \neq j}^{N_{\mathrm{I}}} r_{ij}^{-6} \tag{6}$$

μ_0 is the permeability of vacuum and I the spin quantum number of the considered nucleus ($I = \frac{1}{2}$ for ^{31}P). r_{ij} the internuclear distance between the spins numbered by i and j, N_I denotes the number of spins I, and $\hbar$ is the Planck constant divided by 2π. For an isolated pair of ^{31}P nuclei, Eq. (6) simplifies to

$$M_2^{\mathrm{II}} = \frac{9}{20}\pi^2 D^2 \tag{7}$$

where D denotes the so-called dipolar coupling constant given by

$$D = \frac{1}{\pi}\left(\frac{\mu_0}{4\pi}\right)\gamma_{\mathrm{I}}^2 \hbar r^{-3} \tag{8}$$

The dipolar coupling constant strongly depends on the internuclear distance, r. For a diphosphate, this distance amounts to approximately 2.8 Å corresponding to a dipolar coupling constant, D, of ca. 900 Hz. The length of a ^{31}P–^{31}P bond amounts to ca. 2.2 Å giving rise to a dipolar coupling constant of 1.8 kHz. That means, characteristic ^{31}P–^{31}P dipolar coupling constants are of the order of 1 kHz. This is small compared with the sample spinning rates typically applied in recent experiments (cf. Section 2.2).

Heteronuclear magnetic dipole–dipole interaction. The heteronuclear magnetic dipole–dipole interaction[1] is an inhomogeneous line broadening. Magnetic dipole–dipole interaction between two isolated spins results in a characteristic doublet splitting (Pake doublet[11]). The heteronuclear dipolar coupling constant, D, which determines the size of this splitting for I–S spin pairs follows from Eq. (8) replacing γ_{I}^2 by the product of the magnetogyric ratios, $\gamma_{\mathrm{I}} \times \gamma_{\mathrm{S}}$, of I (^{31}P) and S (^{1}H), respectively. In most cases, however, ^{31}P nuclei are coupled to more than one neighboring ^{1}H spin. It is then useful to define the second moment contribution of the heteronuclear magnetic dipole–dipole interaction given by

$$M_2^{\mathrm{IS}} = \frac{4}{15}\left(\frac{\mu_0}{4\pi}\right)^2 \gamma_{\mathrm{I}}^2 \gamma_{\mathrm{S}}^2 \hbar^2 I(I+1) \frac{1}{N_{\mathrm{I}}} \sum_{i=1}^{N_{\mathrm{I}}} \sum_{j=1}^{N_{\mathrm{S}}} r_{ij}^{-6} \tag{9}$$

N_{S} denotes the number of ^{1}H nuclei coupled to a ^{31}P spin.

2.2. Magic angle spinning

The resolution and sensitivity of the NMR spectra of solid samples may be improved significantly by MAS, i.e., rapid rotation of the sample around an axis tilted by the "magic angle" of $\theta_m = \arccos(\sqrt{1/3}) = 54.74^\circ$ with respect to B_0.[12,13] This MAS of the sample causes the orientation-dependent anisotropic spin interactions such as chemical shift anisotropy and magnetic dipole–dipole interaction to become time-dependent.[14] The secular parts of these interactions are averaged out

completely if the sample spinning rate, ν_r, is large compared to the static line width (fast spinning limit). The ^{31}P chemical shift anisotropy of phosphate groups is of the order of 100–200 ppm. This corresponds to 12–24 kHz at 7.05 T (300 MHz ^{1}H resonance frequency) and to 30–60 kHz at 17.62 T (750 MHz ^{1}H resonance frequency). It is, therefore, hardly possible to fulfill the aforementioned fast spinning condition. Since the MAS-NMR signal is periodic with $t_r = 1/\nu_r$, Fourier transformation yields a spectrum with intensities only at the resonance frequency, ν_0, plus integer multiples of the sample spinning rate $n \times \nu_r$ ($n = 0, \pm 1, \pm 2, \ldots$). Fig. 2 represents the simulated spectra of a powder showing the effect of MAS upon the CSA-dominated line of a ^{31}P nucleus. For purely inhomogeneous internal magnetic interactions such as CSA and/or heteronuclear magnetic dipole–dipole interaction, the central line ($n = 0$) as well as the spinning sidebands ($n \neq 0$) are narrow even if the sample spinning rate is low compared to the line width. If, however, homogeneous internal magnetic interactions such as the homonuclear magnetic dipole–dipole interaction are present in addition, the situation changes. Central line and spinning sidebands do then exhibit a broadening which is a function of the sample spinning rate.[14–16] For phosphorous, the homonuclear magnetic dipole–dipole interaction among the ^{31}P nuclei is small compared to the sample spinning rate (see above). The homonuclear magnetic dipole–dipole interaction among ^{1}H nuclei, however, is large and the so-called residual line width[15] of the central line can then be written as

$$\Delta\nu_{1/2}^{\mathrm{MAS}} \approx C \frac{\sqrt{M_2^{IS} M_2^{SS}}}{\nu_r} \tag{10}$$

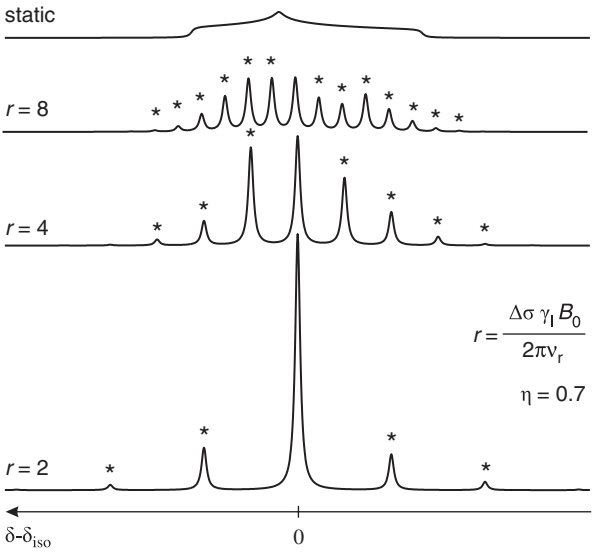

Fig. 2. Calculated ^{31}P MAS NMR spectra for a CSA-broadened signal ($\eta = 0.7$) for various ratios $(\Delta\delta \cdot \gamma_I \cdot B_0)/2\pi\gamma_r$. A central line and so-called spinning sidebands occur which are separated by multiples of the sample spinning rate. Spinning side bands are marked with asterisks.

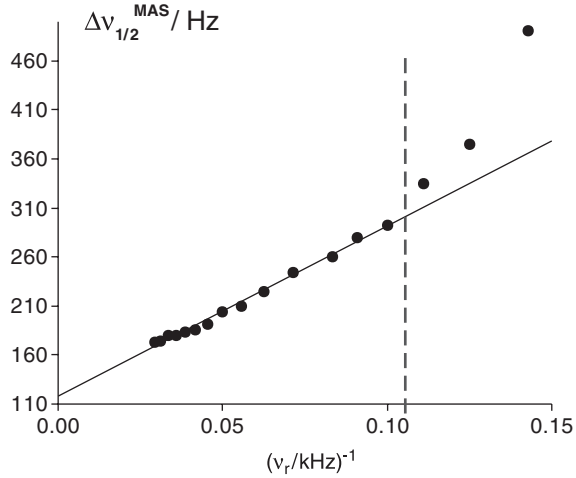

Fig. 3. Residual line width of the central line of the $^{31}P\{^1H\}$ CP MAS NMR signal of *O*-phospho-L-threonine measured at $B_0 = 7.05\,T$ ($T = 302\,K$) plotted as a function of the inverse sample spinning rate ν_r^{-1} (in kHz^{-1}).

M_2^{SS} is the second moment due to the homonuclear magnetic dipole–dipole interaction among the ^1H nuclei which can easily be obtained from Eq. (7) replacing I (^{31}P) by S (^1H). The coefficient C depends on the spatial arrangement of the spins. For three spins (two ^1H spins and one ^{31}P) at the corners of an equilateral triangle,[15] it amounts to 0.018. In complete agreement with this prediction, a linear correlation between $\Delta\nu_{1/2}^{MAS}$ and the inverse sample spinning rate is found for the ^{31}P MAS NMR signal of crystalline *O*-phospho-L-threonine (see Fig. 3). Significant deviations from this linear interdependence are found for sample spinning rates below 10 kHz, i.e. for $(1000\,Hz/\nu_r) > 0.1$. The reason for this deviation is that Eq. (10) was derived[15,16] under the assumption that the so-called Magnus expansion of the Hamiltonian can be limited to the first-order term which is not true for low sample spinning rates. The line-broadening effect described in Eq. (10) can, in principle, be removed either by further increasing the sample spinning rate or by switching off the heteronuclear ^{31}P–^1H magnetic dipole–dipole interaction, i.e., by heteronuclear decoupling. It should be noted within this context that the highest sample spinning rate so far obtained amounts to ca. 70 kHz.[17] Commercial MAS devices are offered with sample spinning rates up to ca. 35 kHz.

2.3. Heteronuclear ^1H decoupling and rotational resonance

Heteronuclear decoupling[18] has to be applied usually when observing ^{31}P spins (I) in compounds with high concentration of ^1H (S). Nowadays, one of the most frequently used decoupling sequences is two-pulse phase-modulated (TPPM) decoupling.[19] In general, the efficiency of the ^1H decoupling raises with increasing decoupling field strengths, B_1. Note that the decoupling field strength

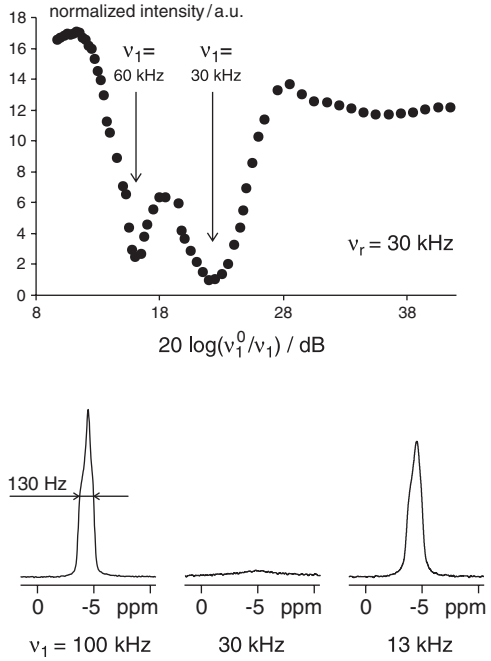

Fig. 4. Intensity of the $^{31}P\{^1H\}$ CP MAS NMR signal (peak maximum) of *O*-phospho-L-threonine in arbitrary units (a.u.) measured at $B_0 = 7.05\,T$ ($T = 302\,K$) as a function of the damping of the decoupling field strength ν_1 (in frequency units). $\nu_1^0 = 180\,kHz$ corresponds to the maximum decoupling field strength obtained at 6 dB damping. The pronounced influence of rotational resonance upon the line width is demonstrated in the spectra at the bottom.

is often given in frequency units according to the following definition: $\nu_1 = \gamma_S \times B_1/(2\pi)$. Nowadays, maximum decoupling fields corresponding to ca. 100–200 kHz are usually obtained on commercial NMR spectrometers for high power ^1H decoupling. It is important to mention that heteronuclear decoupling sequences may destructively interfere with MAS. If the decoupling field strength corresponds to integer multiples of the sample spinning rate, ν_r, i.e., for $\nu_1 = n \times \nu_r$ ($n = 1, 2, \ldots$), rotational resonance (RR[20]) takes place. Considerable broadening of the MAS NMR signals may then occur. This broadening is accompanied by a corresponding decrease of the signal-to-noise ratio since the area underneath a signal is constant. This effect, in particular the pronounced $n = 1$ and $n = 2$ rotational resonances, are demonstrated in Fig. 4 for *O*-phospho-L-threonine. One can conclude from this figure that the maximum resolution and signal-to-noise ratio is obtained either for relatively high decoupling field strengths (here, beyond 100 kHz) or for a decoupling power well below the $n = 1$ rotational resonance condition. In other words, the increasingly high sample spinning rates obtained on advanced MAS devices make low-power decoupling techniques more and more attractive. In any case, an optimization of the decoupling field strength

at the given sample spinning rate is crucial in order to obtain the maximum possible resolution and signal-to-noise ratio. It should, furthermore, be noted that rotational resonance phenomena can be used to determine internuclear distances (see Section 2.5).

2.4. Cross-polarization

For solid-state NMR spectroscopy of dilute spins, MAS is usually combined with CP.[21–24] This results in a sensitivity enhancement as a consequence of the transfer of polarization from abundant nuclei with a high gyromagnetic ratio (S), usually ^{1}H, to dilute spins (I, here: ^{31}P) via mutual flip-flop. The S spins serving as the source of polarization (^{1}H) are excited by a $\pi/2$ pulse followed by a contact time, τ_P. Both spins are locked by simultaneous resonance radio frequency (rf) irradiation during the contact period. The precession frequencies of the ^{1}H and ^{31}P spins in their respective rotating frames are then given by:

$$\begin{aligned} \omega_{1H} &= \gamma_H B_{1H} \\ \omega_{1P} &= \gamma_P B_{1P} \end{aligned} \tag{11}$$

By properly adjusting the ratio B_{1H}/B_{1P} of the rf field strengths applied to ^{1}H (B_{1H}) and ^{31}P (B_{1P}), the rotating frame Zeeman splitting of ^{1}H and ^{31}P spins can be matched. This matching condition:

$$\gamma_H B_{1H} = \gamma_P B_{1P} \tag{12}$$

is known as the Hartmann–Hahn[21] condition. For ^{31}P{^{1}H} CP, the Hartmann–Hahn condition requires $B_{1P} = 2.47 \times B_{1H}$ since $\gamma_H = 2.47 \times \gamma_P$.

The sensitivity enhancement for a ^{31}P{^{1}H} CP experiment cannot exceed γ_H/γ_P. The signal intensity, I_{CP}, observed for a CP experiment depends on the contact time, τ_P, in a characteristic manner:[25]

$$I_{CP}(\tau_P) \propto \left(1 - \frac{T_{CP}}{T_{1\rho}^{H}}\right)^{-1} \left(\exp\left\{-\frac{\tau_P}{T_{1\rho}^{H}}\right\} - \exp\left\{-\frac{\tau_P}{T_{CP}}\right\}\right) \tag{13}$$

T_{CP} denotes the CP buildup time constant which is inversely proportional to M_2^{IS} and $T_{1\rho}^{H}$ is the longitudinal relaxation time of the ^{1}H nuclei under spin-locking conditions. Note that Eq. (13) only holds if $T_{1\rho}^{H}$ is much shorter than $T_{1\rho}^{P}$ for ^{31}P; a condition which is fulfilled in most cases. A characteristic CP buildup curve is shown in Fig. 5 for the ^{31}P{^{1}H} CP MAS NMR signal of *O*-phospho-L-threonine. Since the polarization source used in ^{31}P{^{1}H} CP MAS NMR experiments is the ^{1}H spin bath, the repetition rate of the experiment is dictated by the longitudinal relaxation time T_1 of the ^{1}H nuclei which is usually much shorter than that of ^{31}P.

In particular, when the sample spinning rate exceeds both ^{1}H–^{1}H and ^{1}H–^{31}P dipolar coupling constants, the Hartmann–Hahn condition splits into a series of

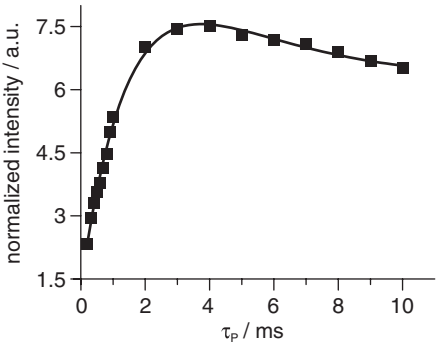

Fig. 5. Cross-polarization buildup curve measured for *O*-phospho-L-threonine using a conventional RAMP-CP experiment at $B_0 = 7.05\,\mathrm{T}$, ($T = 302\,\mathrm{K}$). The following time constants could be determined by fitting the experimental data using Eq. (13): $T_{CP} = 150\,\mu\mathrm{s}$; $T_{1\rho} = 27\,\mathrm{ms}$.[26]

matching sidebands determined by:

$$\Delta = \omega_{1H} - \omega_{1P} = 2\pi \times n \times \nu_r \tag{14}$$

An efficient CP is obtained only for $n = \pm 1$ or ± 2. This behavior poses problems in adjusting and maintaining an optimum Hartmann–Hahn matching. The problem can be circumvented by a variation of the phase and/or the amplitude of the rf fields applied during τ_P. Several methods[27–30] have meanwhile been proposed. One of the most frequently used techniques is the so-called ramped-amplitude CP MAS NMR experiment (RAMP-CP[28]) which delivers a broad matching profile rather than the separated matching sidebands (Eq. (14)). Instead of adjusting both, B_{1H} and B_{1P} to the constant values defined by the Hartmann–Hahn-matching condition, one of the two field strengths is varied (''ramped'') such that the ramped field passes through the matching condition. A very efficient technique is the so-called adiabatic passage Hartmann–Hahn CP (APHH-CP) experiment[29,30] which relies on a tangential amplitude profile that depends on the strengths of the magnetic dipole–dipole interactions as well as the sample spinning rate. Another interesting variant is the so-called Lee–Goldburg CP experiment with frequency modulation (LG-FMCP).[31] During the contact time, the ^{1}H magnetization (S spins) is spin-locked along the magic angle by a LG sequence (cf. Section 2.7.1) and the irradiation offset of the spins to be polarized (I spins) is modulated. The advantage of this method is a considerable lengthening of $T_{1\rho}$ of the ^{1}H nuclei as well as a shortening of T_{CP}. With respect to applications in multidimensional HETCOR experiments, the LG-CP experiment should be preferred if ^{1}H spin diffusion is to be minimized.

Fig. 6 demonstrates the stepwise improvement in sensitivity and resolution obtained for the ^{31}P NMR signal of *O*-phospho-L-tyrosine by combining CP with MAS and heteronuclear decoupling techniques.

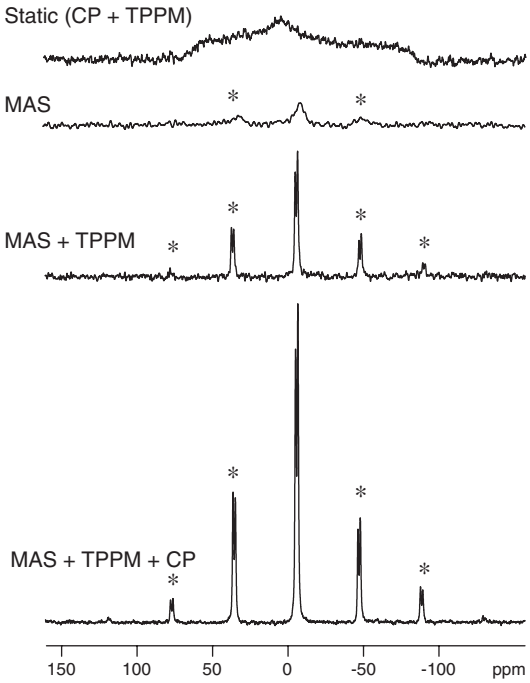

Fig. 6. Experimental solid-state ^{31}P NMR spectra of *O*-phospho-L-tyrosine measured at $B_0 = 7.05\,\mathrm{T}$ ($T = 302\,\mathrm{K}$). From top to bottom: Static spectrum measured using CP and heteronuclear TPPM decoupling; MAS NMR spectrum acquired without CP and heteronuclear decoupling; MAS NMR spectrum measured without CP but under heteronuclear TPPM decoupling; MAS NMR spectrum acquired with CP and heteronuclear TPPM decoupling ($\nu_r = 5\,\mathrm{kHz}$, 16 scans). ∗ denotes spinning sidebands.

2.5. Internuclear distance measurements

Solid-state NMR spectroscopy is capable of measuring internuclear distances. This makes solid-state NMR particularly important for amorphous or disordered systems where diffraction methods often fail. The measurement of internuclear distances in solid-state NMR spectroscopy is commonly based on the exploitation of the magnetic dipole–dipole interaction. A variety of methods has meanwhile been developed. Several techniques of special importance with respect to solid-state ^{31}P NMR spectroscopy will be discussed below. In the simplest case, line shape analysis allows the extraction of the dipolar coupling constant. Usually, the line shape is governed by the superimposition of various interactions (see above). It is then necessary to selectively determine the magnetic dipole–dipole interaction of interest. In the absence of MAS, the so-called SEDOR (spin echo double resonance) technique can be applied.[32,33] This double resonance method allows the measurement of the heteronuclear magnetic dipole–dipole interaction between spins I and S. A conventional Hahn echo[34] experiment is carried out in one of the two frequency

channels (e.g., I) with a time delay, τ, between the $\pi/2$ and the π pulse. Echo formation at the time 2τ can be perturbed by the application of a π pulse in the other frequency channel (S). The observed echo intensity $I(t_1)$ depends on the time t_1 ($0 \leqslant t_1 \leqslant \tau$) at which the latter π pulse is applied. The so-called SEDOR fraction, $S_F = 1 - I(t_1)/I(0)$, is usually measured as a function of t_1. For an isolated I–S spin pair, $I(t_1)$ is given by the expression

$$I(t_1) \propto \int_0^{\pi} \cos\{\omega(D,\theta)t_1\} \sin\ \theta \mathrm{d}\theta \tag{15}$$

with

$$\omega(D,\theta) = \pi D\left(3\cos^2\theta - 1\right) \tag{16}$$

where θ denotes the angle between the internuclear vector and B_0. An analysis of the SEDOR fraction then directly allows to measure the internuclear I–S distance in the isolated spin pair. There are, however, two major problems with this technique: (i) The analysis of the SEDOR fraction becomes complicated if more than two spins I and S are coupled to each other (multi-spin systems, see Section 4.1). (ii) If there are different types of I spins with different chemical shifts, SEDOR experiments usually do not allow to resolve the corresponding signals. The internuclear distances obtained from SEDOR experiments do then only represent average values. The application of the so-called REDOR (rotational echo double resonance) experiment[35,36] should be preferred in such cases (see Fig. 7). Owing to the application of MAS, spectral resolution is obtained for the I spins. The heteronuclear magnetic dipole–dipole interaction – which would be suppressed by pure MAS – is reintroduced by the application of rotor-synchronized trains of π pulses in the S channel (see Fig. 7). In analogy to the SEDOR fraction described above, one can define a corresponding REDOR fraction, R_F, which is also determined by the heteronuclear magnetic dipole–dipole interaction among the I and S spins as follows

$$R_F(nt_r) = 1 - \frac{1}{4\pi}\int_0^{2\pi} \mathrm{d}\alpha \int_0^{\pi} \mathrm{d}\beta \sin\ \beta \cos(n\Delta\Phi) \tag{17}$$

with

$$\Delta\Phi = \pm 2\sqrt{2} \sin\ 2\beta\ \sin(\omega_r t_1 + \alpha) D t_r \tag{18}$$

Here, n denotes the number of rotor cycles, $t_r = 2\pi/\omega_r$ is the rotor period, and the angles α and β denote the polar angles of the I–S internuclear vector with respect to a rotor-fixed coordinate system with the z-axis directed along the symmetry axis of the MAS rotor. t_1 is the delay between the $\pi/2$ pulse in the I channel and the first π pulse in the S channel which was set to $t_r/2$ in Fig. 7. In analogy to the SEDOR technique, however, the interpretation of the REDOR fraction becomes complicated in multi-spin systems.[37]

In the case of homonuclear ^{31}P–^{31}P spin pairs, rotational resonance can be applied to measure the internuclear distance. Rotational resonance phenomena can be observed in homonuclear pairs of ^{31}P spins with different isotropic chemical shift if the following condition is fulfilled: $\Delta\nu_{iso} = n \times \nu_r$ ($n = 1, 2, 3, \ldots$) where $\Delta\nu_{iso}$ denotes the frequency difference between the two considered signals.[38–40]

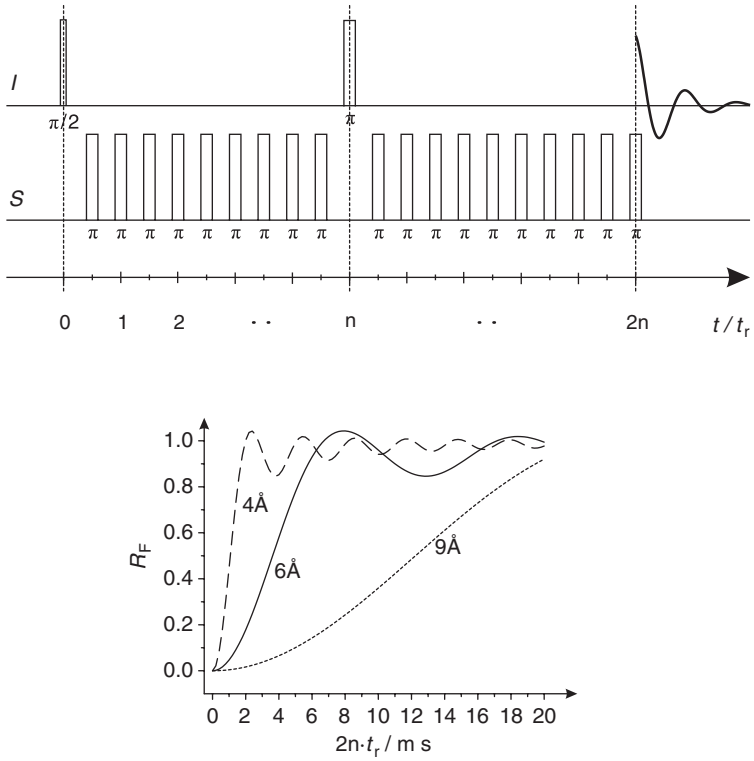

Fig. 7. Top: REDOR pulse sequence. Bottom: Calculated REDOR fractions R_F for the example of isolated ^{31}P–^{19}F spin pairs at a sample spinning rate of 10 kHz for different internuclear distances.

A comprehensive treatment of rotational resonance in homonuclear spin pairs is given by Levitt *et al.*[41] If the sample spinning rate is set properly (e.g., such that $n = 1$), a characteristic line broadening is observed which depends on the homonuclear ^{31}P–^{31}P magnetic dipole–dipole interaction. A characteristic example[42] is shown in Fig. 8. Numerical line shape analysis then allows the determination of the internuclear distance as is demonstrated in this figure.

2.6. Multiple-quantum NMR spectroscopy

For isolated spin$-\frac{1}{2}$ nuclei, single-quantum (SQ) coherences can be excited only. In contrast, MQ coherences appear in multi-spin systems due to the presence of couplings.[43,44] They can be used, e.g., in order to detect connectivities between the nuclei involved into the coupling network. Furthermore, the cluster size of spin systems can be determined by MQ coherence excitation (spin counting).[43,45] The distribution and clustering of spins can be probed evaluating the time dependence of the excitation. Furthermore, MQ techniques can be applied to simplify the

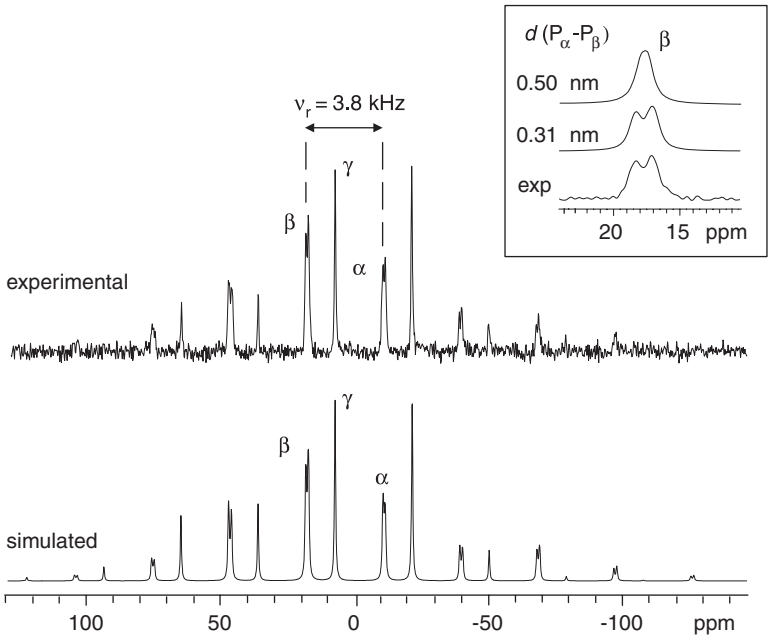

Fig. 8. $^{31}P\{^{1}H\}$ CP MAS NMR rotational resonance spectrum of the crystalline protein **Ras(wt)** · $\mathbf{Mg^{2+}}$ · $\mathbf{GppCH_{2p}}$[42] measured at $B_0 = 7.05$ T and $T = 303$ K ($GppCH_2p$: a guanosine triphosphate (GTP)-analog where the bridging oxygen between the phosphorous atoms P_β and P_γ is replaced by a CH_2 group). The $n = 1$ rotational resonance condition is fulfilled for the signals at –12.8 and 18.8 ppm as indicated. The spectrum simulated for a P_α–P_β distance $d(P_\alpha$–$P_\beta) = 0.31$ nm is shown at the bottom. The inlet exhibits the signal at 18.8 ppm simulated for $d(P_\alpha$–$P_\beta) = 0.50$ nm and 0.31 nm (top and middle) as well as the experimental spectrum (bottom).

spectra of multi-spin systems (MQ filtering)[46,47] and to uncover connectivities between nuclei which are hardly detectable in ''conventional'' experiments.

J-couplings are routinely exploited to excite MQ coherences in liquid-state NMR. In contrast, MQ experiments in solid-state NMR spectroscopy more often rely on the magnetic dipole–dipolar interaction. In general, MQ excitation is achieved by the application of a series of radio frequency pulses which together with the couplings result in an excitation of the desired coherences. Owing to the fact that MQ coherences cannot be detected directly, MQ coherences have to be converted into observable SQ coherences. This is most suitably accomplished in 2D NMR experiments (see also Section 2.7). First, MQ coherences have to be excited by a proper pulse sequence. Afterwards, the system is allowed to evolve during an evolution time, t_1. Subsequently, the MQ coherences have to be converted into SQ coherences by pulses or pulse sequences similar to that of the excitation. Finally, these SQ coherences can be detected during a second evolution period, t_2. The various MQ coherences do not all appear at once, because the order of MQ excitation depends on the strength of the couplings and the excitation time. Therefore, the order of MQ

excitation can be chosen by the duration of the excitation. Finally, different coherence orders can be distinguished and selected due to their different behavior under phase shifts of the pulses in the 2D pulse sequence.[48]

2.7. Multidimensional correlation spectroscopy

Multidimensional correlation spectroscopy is routinely applied in liquid-state NMR spectroscopy.[49,50] Scalar couplings (*J*-couplings) or nuclear Overhauser effect[51] (NOE) contacts are normally used[49,50] to correlate different spins in liquid-state NMR spectroscopy. In contrast, many techniques in solid-state NMR make use of dipolar couplings in order to transfer spin polarization between adjacent spins. Correlation spectra provide information which is normally inaccessible in 1D experiments. Furthermore, multidimensional experiments often allow to resolve signals which are overlapping in the 1D spectrum.

2.7.1. *Through-space correlations*

^{1}H-driven spin diffusion. Spin diffusion is induced by the magnetic dipole–dipole interaction and leads to a transfer of magnetization between neighboring spins. The transition rate W for spin diffusion processes between two adjacent ^{31}P nuclei, A and B, with a frequency difference, $\Delta\nu_{iso}$, due to their different isotropic chemical shifts is given[52] by:

$$W \propto g_0^{AB}(\Delta\nu_{iso})D^2 \tag{19}$$

where D is the ^{31}P–^{31}P dipolar coupling constant (see Eq. (8)). g_0^{AB} is the line shape function for the zero quantum transition (flip–flop processes). The width of the latter function is determined by the average ^{1}H–^{31}P dipolar coupling constant. Therefore, spin diffusion effectively takes place if $\Delta\nu_{iso}$ is small compared to the average ^{1}H–^{31}P dipolar coupling constant. Under ^{1}H decoupling, magnetization transfer only takes place for sites with $\Delta\nu_{iso} = 0$. Without ^{1}H decoupling, ^{1}H–^{31}P dipolar couplings are large enough at least for ^{1}H-rich compounds such as biomolecules to make ^{31}P spin diffusion possible. In other words, the ^{1}H nuclei drive the ^{31}P spin diffusion. Note that this ^{1}H-driven (proton-driven) spin diffusion does not involve a transfer of magnetization via the ^{1}H nuclei. The transfer occurs through-space from ^{31}P to ^{31}P. Owing to the D^2-dependence of the transition rate, spatial proximities can sensitively be determined via spin diffusion experiments. That means, spin diffusion experiments can be considered to be the solid-state NMR spectroscopic analog of the famous NOESY (nuclear Overhauser effect spectroscopy) experiment[53] which is of crucial importance in biomolecular liquid-state NMR spectroscopy.

2D NMR spectroscopy is a valuable method for the study of spin diffusion. The pulse sequence for the 2D ^{1}H-driven spin diffusion experiment was originally introduced by Szeverenyi *et al.*[54] (see Fig. 9, top). It creates a transverse ^{31}P magnetization via CP. After this, the spins are allowed to precess during the evolution time, t_1. During that time, ^{31}P is under the influence of the Zeeman interaction (including the ^{31}P chemical shift Hamiltonian). ^{1}H decoupling and MAS are applied.

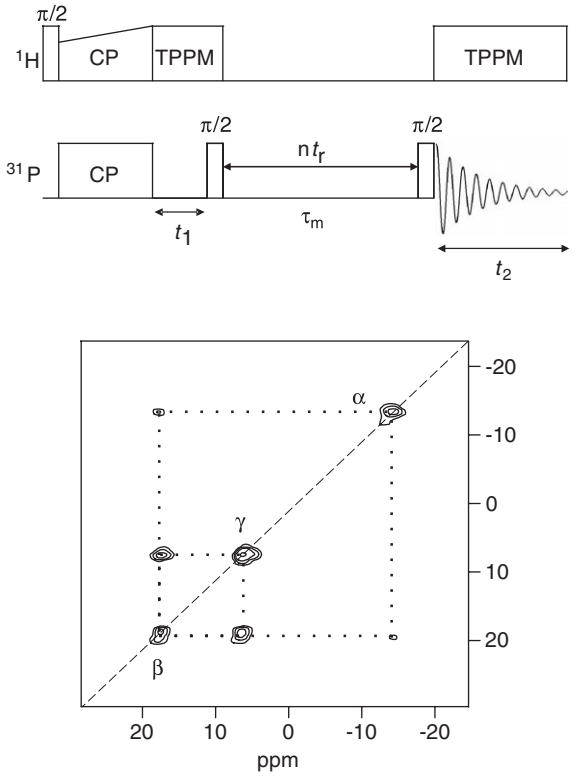

Fig. 9. Top: Pulse sequence for the 2D ^{1}H-driven ^{31}P–^{31}P spin diffusion experiment.[54] Bottom: ^{1}H-driven ^{31}P–^{31}P spin diffusion spectrum of microcrystals of the protein **Ras(wt)** · $\mathbf{Mg^{2+}}$ · $\mathbf{GppCH_{2p}}$ measured at $B_0 = 7.05$ T and $T = 303$ K.

Identical conditions are present during the detection period, t_2. At the end of t_1, a $\pi/2$ pulse in the ^{31}P channel converts the transverse magnetization back into longitudinal magnetization. The mixing period, τ_m, between t_1 and t_2 is an interval allowing for longitudinal magnetization transfer among the ^{31}P spins either by spin diffusion or chemical exchange. In the latter case, the experiment is called EXSY[53] (exchange spectroscopy). The second $\pi/2$ pulse switches the magnetization back to the transverse plane before acquisition (t_2). The measured 2D NMR spectrum represents the spin exchange pathways between spins with different chemical shifts. Any spin diffusion process that correlates spins with different resonance frequencies results in corresponding off-diagonal peaks (cross-peaks) in the 2D spectrum (see Fig. 9, bottom). In order to suppress artifact cross-peaks resulting from the reorientation of the rotor, the mixing time must be set to an integer multiple of the rotor period, t_r.[55]

HETCOR experiments. Heteronuclear correlation spectroscopy (HETCOR) allows the detection of spatial proximities between unlike spins. Heteronuclear correlation experiments such as ^{1}H–^{13}C or ^{1}H–^{15}N correlation experiments are the

basis of modern biomolecular NMR spectroscopy.[50] HETCOR relies on heteronuclear polarization transfer techniques. In liquid state, heteronuclear polarization transfer is usually accomplished by making use of scalar couplings. In solid-state NMR spectroscopy, CP is often applied which relies on the heteronuclear magnetic dipole–dipole interaction (see Section 2.4). ^{31}P–^{1}H HETCOR is complicated by the strong homonuclear ^{1}H–^{1}H magnetic dipole–dipole interactions giving rise to a relatively poor spectral resolution in ^{1}H dimension. Therefore, the ^{1}H dimension is usually chosen to be the indirect dimension in a 2D spectrum (t_1 evolution), while the well-resolved ^{31}P MAS NMR spectrum is directly detected during t_2. A variety of multiple pulse sequences, including WAHUHA,[56] MREV-8,[57,58] BR-24,[59] DUMBO,[60] FSLG,[61] and PMLG,[62] can then be applied during the evolution time, t_1, in order to suppress the influence of the homonuclear magnetic dipole–dipole interaction as complete as possible. Nowadays, phase-modulated Lee–Goldburg[62] (PMLG) decoupling is one of the most popular homonuclear decoupling sequences.[63–69] In PMLG experiments, line narrowing is accomplished by a series of pulses with special phases. The pulse sequence for a corresponding HETCOR experiment[70] is shown in Fig. 10 (top). It starts with a magic angle excitation pulse

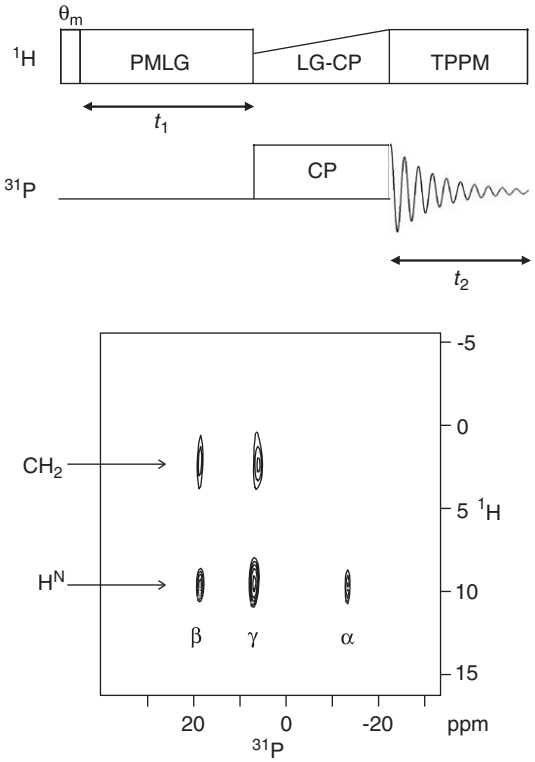

Fig. 10. Top: Pulse sequence for the 2D PMLG decoupled ^{1}H–^{31}P LG–CP HETCOR experiment.[70] Bottom: 2D PMLG decoupled ^{1}H–^{31}P LG-CP HETCOR spectrum of **Ras(wt)** · $\mathbf{Mg^{2+}}$ · $\mathbf{GppCH_{2p}}$ measured at $B_0 = 7.05$ T and $T = 303$ K.

($\theta_m = 54.74°$) that puts the ^{1}H magnetization along the magic angle with respect to B_0. After ^{1}H excitation, the protons are allowed to evolve (t_1) under PMLG irradiation. Afterwards, Lee–Goldburg CP (LG-CP) is applied to transfer the magnetization from ^{1}H to ^{31}P. The ^{31}P signal is then detected under TPPM decoupling of the ^{1}H nuclei. A typical 2D ^{31}P–^{1}H HETCOR spectrum (GppCH$_2$p bound to the protein Ras[42]) is shown in Fig. 10 (bottom).

2.7.2. *Through-bond correlations*

Although through-bond couplings (*J*-couplings) are small compared to the above-described internal magnetic interactions in solids, a number of solid-state NMR spectroscopic experiments exploits the *J*-couplings in order to establish correlations between spins. One example is the incredible natural abundance double quantum (DQ) transfer experiment (INADEQUATE[71–73]). It was demonstrated that a variant of this experiment, the so-called refocused INADEQUATE,[74] allows an unambiguous detection of the oxygen mediated ^{31}P–^{31}P *J*-couplings in crystalline and disordered phosphates.[75,76] The refocused INADEQUATE pulse sequence is shown in Fig. 11 (top). After CP, the ^{31}P magnetization evolves during the delay, 2τ, under the isotropic homonuclear *J*-coupling Hamiltonian. The ^{31}P–^{31}P homonuclear dipolar

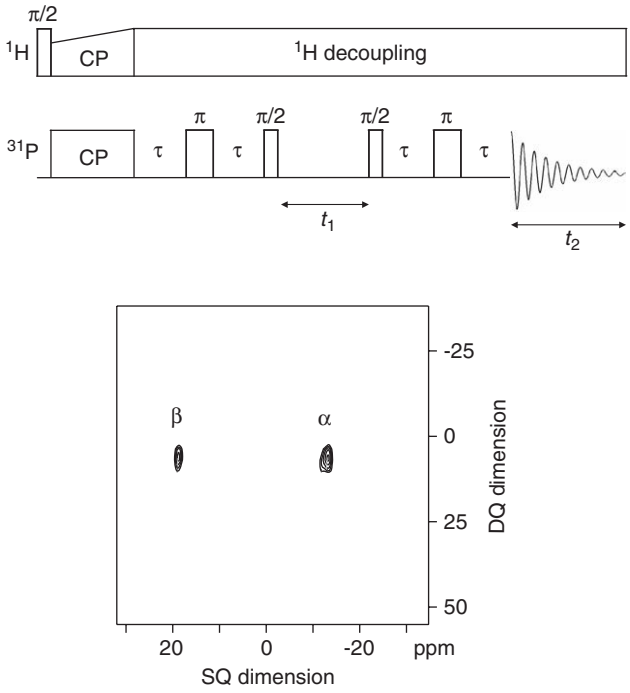

Fig. 11. Top: Pulse sequence for the refocused INADEQUATE experiment.[74] Bottom: Refocused INADEQUATE spectrum of **Ras(wt)·Mg^{2+}·GppCH$_{2p}$** measured at $B_0 = 7.05$ T and $T = 303$ K.

coupling ($D = 1.8$ kHz for a ^{31}P–^{31}P distance of 2.2 Å) is removed by fast MAS, while the chemical shift interaction is refocused by the π pulse. The DQ coherence created by the first $\pi/2$ pulse evolves during t_1 at the sum of the (SQ) frequencies of the two spins (A and B), $\nu_{DQ} = \nu^{A}_{SQ} + \nu^{B}_{SQ}$. The last $\pi/2$ pulse reconverts the DQ coherence into an anti-phase SQ coherence. This anti-phase component is converted back during the second $\tau-\pi-\tau$ delay into an in-phase signal before detection. In the refocused INADEQUATE SQ–DQ experiment, the signals of the two coupled ^{31}P atoms will occur at their common DQ frequency ν_{DQ} (see above) in indirect dimension and will be correlated with the SQ frequencies ν^{A}_{SQ} and ν^{B}_{SQ} of each individual signal in direct dimension. The maximum transfer of magnetization into DQ coherence occurs for $\tau = 1/(4J_{P-P})$. No transfer is observed for $\tau = 1/(2J_{P-P})$. Fig. 11 (bottom) shows the solid-state INADEQUATE spectrum of the same sample as studied in Figs. 9 and 10. A pair of cross-peaks is observed for the J-coupled P_α–P_β spin pair ($J = 26$ Hz) at the expected position. However, no cross-peaks are observed for the P_β–P_γ pair since the J-coupling constant is much smaller (less than 9 Hz).

Another very interesting experiment based on the exploitation of through-bond couplings is the so-called TOBSY (total through-bond correlation spectroscopy) experiment[77] shown in Fig. 12. This experiment relies on mixing sequences which are capable of suppressing homo- and heteronuclear magnetic dipole–dipole interactions as well as chemical shifts simultaneously, while the isotropic J-coupling must be retained. After CP, on resonance ^{1}H decoupling is applied during evolution period, t_1. During the mixing time, τ_{mix}, the homonuclear and heteronuclear magnetic dipole–dipole interactions as well as the chemical shift interaction are suppressed such that polarization transfer is mediated by J-couplings. Owing to long mixing times needed to determine small J-coupling constants, LG decoupling is applied to eliminate ^{1}H–^{1}H interactions, while ^{1}H–^{31}P interactions are removed by a combination of MAS with composite pulses.[78] During the detection period, t_2, on resonance ^{1}H decoupling is used. A 2D TOBSY experiment shows cross-peaks between signals of J-coupled spins. The intensity of the cross-peaks as a function of mixing time shows an oscillatory time dependence. The observed oscillation frequency determines the

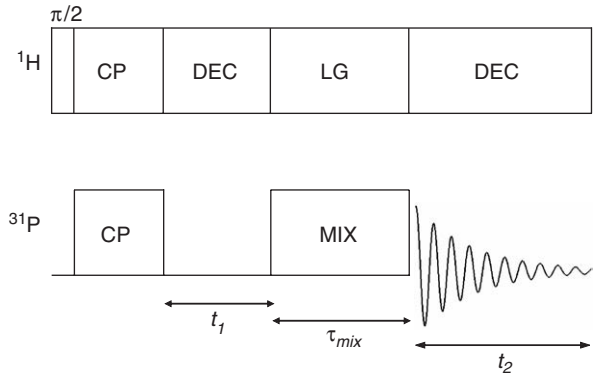

Fig. 12. Pulse sequence for the TOBSY experiment.[77]

size of *J*-coupling.[79,80] An interesting modification of the TOBSY experiment, the so-called R-TOBSY was introduced by Chan and Brunklaus.[81]

3. BIOLOGICAL APPLICATIONS OF SOLID-STATE ^{31}P NMR SPECTROSCOPY

Solid-state NMR spectroscopy is increasingly important in structural biology for several reasons. X-ray diffraction, the "classical" method in structural biology of crystalline samples fails if the samples are amorphous. This is, for example, the case for fibril-forming peptides/proteins as well as for membrane proteins which usually have to be embedded into a lipid matrix in order to mimic their native environment. Furthermore, solid-state NMR spectroscopy is capable of delivering important additional information even in the case of crystalline samples, e.g., if the molecules exhibit an internal mobility making certain parts of the molecule "invisible" for diffraction techniques. Applications of solid-state ^{31}P NMR spectroscopy to biological samples will be discussed in the present section.

3.1. Proteins and peptides

Phosphorylation, especially of serine, threonine, and tyrosine residues belongs to the most common post-translational modifications observed on peptides and proteins in nature.[82] Characteristic solid-state ^{31}P NMR spectroscopic parameters for crystalline amino acids (*O*-phospho-L-serine, *O*-phospho-L-threonine, and *O*-phospho-L-tyrosine[26,83,84]) are summarized in Table 2. Phosphorylation of silaffins, a novel class of peptides involved in the formation of the highly siliceous and regularly structured cell walls of diatoms, was shown to be responsible for their ability to phase-separate and to precipitate silica.[85] Guanine nucleotide-binding proteins (heterotrimeric G proteins and proteins of the Ras-superfamily) – molecules responsible for signal transduction between transmembrane receptors and cellular effectors – switch between their active and inactive state by binding to GTP and GDP, respectively.[86]

For these reasons, ^{31}P NMR spectroscopy currently gains increasing interest in protein NMR spectroscopy. Numerous liquid-state ^{31}P NMR spectroscopic studies were meanwhile carried out on members of the Ras-superfamily such as Ras and Ran complexed with GTP analogs like GppCH$_2$p and GppNHp.[87–89] Liquid-state ^{31}P NMR spectroscopy was also used to investigate the self-aggregation of silaffins.[85] This method, however, suffers from two major drawbacks: large longitudinal relaxation times, T_1, and considerable line broadening resulting from relaxation by chemical shift anisotropy especially at high magnetic fields, B_0. Characteristic T_1-values of 2–30 s occur for phosphate groups or nucleotides bound to proteins and peptides in solution. The repetition time applicable in liquid-state ^{31}P NMR-experiments can, therefore, be of the order of minutes which results in very long acquisition times limiting the sensitivity. At external magnetic fields

Table 2. NMR parameters of phosphorylated amino acids in solid-state.[26] T_1^P and T_1^H denote the longitudinal relaxation times of ^{31}P and ^{1}H, respectively. $T_{1\rho}^H$ and T_{CP} were determined from the CP buildup curve, i.e., the dependence of the intensity, I_{CP}, of the $^{31}P\{^{1}H\}$ CP MAS NMR signal upon the contact time (see Eq. (13)). τ_{max} is the contact time where the intensity I_{CP} of the CP signal is maximum. Note that the chemical shift anisotropy and asymmetry parameter given for *O*-phospho-L-serine excellently agree with earlier static ^{31}P NMR measurements carried out by Kohler and Klein[84].

Compound	δ/ppm ($\pm$0.1 ppm)	$\Delta\sigma$/ppm ($\pm$3 ppm)	η ($\pm$0·1)	T_1^P/s ($\pm$5%)	T_1^H/ms ($\pm$5%)	$T_{1\rho}^H$/ms ($\pm$10%)	T_{CP}/μs ($\pm$10%)	τ_{Max}/ms ($\pm$10%)
P-ser	0.3	86	0.9	64	148	57	250	4
P-thr	–4.5	105	0.8	25	70	27	150	4
P-Tyr								
(peak 1)	–5.1	117	0.7	16	35	12	75	3
(Peak 2)	–6.6	124	0.6	19	45	12	75	3

$B_0 \geqslant 5$ T, transverse ^{31}P relaxation is governed by chemical shift anisotropy.[90] The correlation time, τ_C, for molecular reorientation is higher than 5 ns for proteins with a molecular weight exceeding 10 kDa dissolved in water at room temperature. CSA relaxation rates, R_2^{CSA} beyond 30 s^{-1} follow for $\Delta\sigma = 150$ ppm and $\eta = 0.5$, the average values observed[42] for the ^{31}P NMR signals of **Ras(wt)·Mg^{2+}·GppNH$_P$** ($M = 19$ kDa), and at a ^{31}P resonance frequency of 202.46 MHz ($B_0 = 11.75$ T). This corresponds to a contribution to the line width (full width at half maximum) exceeding 10 Hz. It rapidly increases at higher field strengths since R_2^{CSA} is proportional to $(\Delta\sigma \times B_0)^2$. In other words, the liquid-state ^{31}P NMR spectra exhibit a decreasing spectral resolution at further increasing B_0. It is, therefore, not reasonable to apply very high magnetic fields in such cases.

Therefore, solid-state ^{31}P NMR may be advantageous even for soluble proteins. On one hand, the application of the ^{31}P{^{1}H} CP technique results in a much shorter repetition time for the experiments since the ^{1}H nuclei serving as the source of magnetization exhibit much shorter longitudinal relaxation times than ^{31}P. On the other, well-prepared samples are nowadays capable of delivering highly resolved solid-state ^{31}P NMR spectra of similar resolution as liquid-state NMR spectroscopy. In general, proteins or peptides can be studied by solid-state NMR spectroscopic techniques either in the crystalline or in the amorphous state. Fig. 13 shows the ^{31}P{^{1}H} CP MAS NMR spectrum of crystalline **Ras(wt)·Mg^{2+}·GppNH$_p$** measured at 273 K (top). For comparison, the liquid-state ^{31}P NMR spectrum of the same sample measured at 273 K is shown at the bottom. The inlet exhibits a microscopic image of characteristic microcrystallites used for the solid-state NMR measurements. Note, that the resolution of both spectra is sufficient to resolve the splitting of the γ-phosphate group-signal into two lines characteristic for the two conformational states (1) and (2) of the Ras protein acting as a molecular switch (see above). Although the amount of sample and measurement time was the same for both spectra, the signal-to-noise ratio of the solid-state NMR spectrum is better than that of the liquid-state NMR spectrum. This is due to the shorter repetition time and sensitivity gain in the ^{31}P{^{1}H} CP MAS NMR experiment compared to the liquid-state ^{31}P NMR spectrum using direct ^{31}P excitation.

Solid-state ^{31}P NMR in combination with ^{13}C NMR spectroscopy was used to study the influence of phosphorylation upon the structure of keratin from bovine hoof.[91]

3.2. Biominerals

Biomineralization, i.e., the process of formation and patterning of inorganic materials by living organisms currently gains enormous interest. On the one hand, the understanding of these genetically controlled processes is of fundamental biological interest. On the other, the knowledge of the biochemical and biophysical principles steering these processes would greatly enhance the possibilities of inorganic synthesis. Indeed, so-called biomimetic materials synthesis has meanwhile become a rapidly growing research area. Interestingly, phosphate groups and phosphorylated

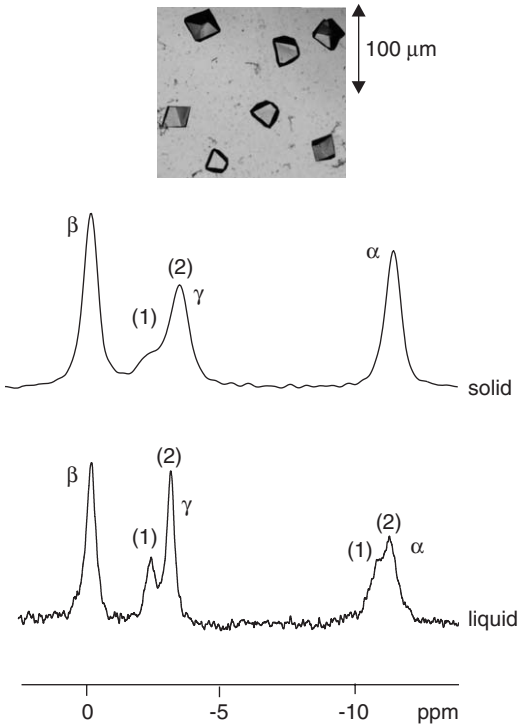

Fig. 13. Top: $^{31}P\{^{1}H\}$ CP MAS NMR spectrum of crystalline **Ras(wt)** · $\mathbf{Mg^{2+}}$ · $\mathbf{GppNH_p}$ measured at $B_0 = 7.05\,T$ and $T = 273\,K$.[42] Bottom: Liquid-state ^{31}P NMR spectrum of the same sample measured at $B_0 = 11.75\,T$ and at $T = 273\,K$.[42]

proteins seem to be of special importance in biomineralization as can be seen from the following two examples.

The highly siliceous cell walls of diatoms are probably the most outstanding examples for nanostructured materials in nature. This makes diatoms particularly interesting model organisms for the study of biomineralization. The regularly structured cell walls of diatoms are made up of a composite material containing silica as well as certain biomolecules. Two different classes of biomolecules, namely the highly phosphorylated silaffins[85] as well as long-chain polyamines were found to play an important role in the biomineralization process. On the basis of electron microscopic studies, Sumper[92] has suggested a model for diatom cell wall formation. This model is mainly based on the assumption that phase separation processes taking place in the so-called silica deposition vesicle are responsible for silica nanopatterning. Meanwhile, it could be shown[85,93,94] by NMR spectroscopy and dynamic light scattering that the self-aggregation and microscopic phase separation of silaffins and polyamines is indeed of central importance for the precipitation and nanopatterning of silica during diatom cell wall formation. The zwitterionic silaffins self-assemble provided they are in their native, phosphorylated form. The parameters tuning the size of the supramolecular aggregates of long-chain polyamines are

pH and inorganic phosphate concentration.[93,94] Recently, we could show by solid-state ^{31}P NMR spectroscopy that inorganic phosphate as well as phosphate bound to silaffins is indeed incorporated into the cell walls of diatoms[95] (see Fig. 14). This observation does not only confirm the aforementioned phase separation model. It is also interesting with respect to the phosphate-storing function of marine sediments. Solid-state ^{31}P NMR spectroscopic studies[96] have shown that phosphorous is enriched and stored in marine sediments preferentially in the form of phosphate esters

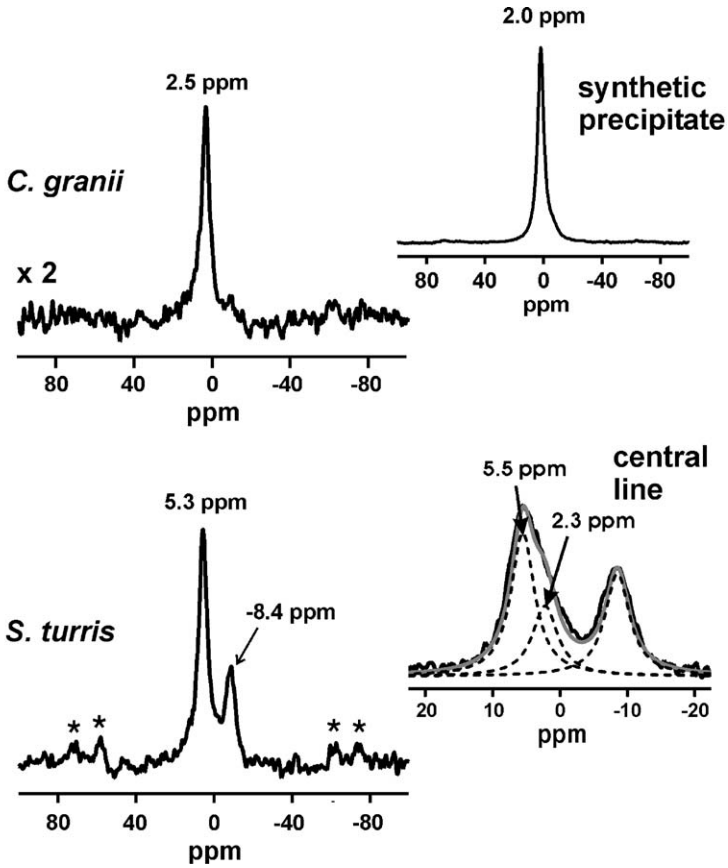

Fig. 14. Left: ^{31}P MAS NMR spectra of cell walls from *Coscinodiscus granii* (top) and *Stephanopyxis turris* (bottom). * denotes spinning sidebands. Right: ^{31}P MAS NMR spectrum of a synthetic silica precipitate (top) and central line of the ^{31}P MAS NMR spectrum of *S. turris* cell walls (bottom, solid black line). It is demonstrated that the latter spectrum must be decomposed into three components (dashed black lines) due to the asymmetry of the line at 5.3 ppm. The sum of the three components (solid gray line) agrees well with the experimental data. *C. granii* exhibits only one signal due to inorganic phosphate since the cell walls of this species do not contain phosphorylated silaffins. In contrast, *S. turris* cell walls contain phosphorylated silaffins in addition to polyamines. The ''shoulder'' at 2.3 ppm in *S. turris* is assigned to inorganic phosphate interacting with polyamines, the other signals are due to phosphorylated silaffins.

and phosphonates. Diatom cell walls are sedimented in huge amounts and the phosphate groups embedded into diatom cell walls may, therefore, contribute significantly to the phosphate contained in the marine sediments.

In analogy to silica biomineralization in diatoms, phosphorylated proteins are also found in the organic matrix of bones. These proteins are assumed to be involved in the nucleation and growth of bone minerals.[97–100] Solid-state ^{31}P NMR spectroscopy is, therefore, a valuable tool to study the biomineralization process of bones. The chemical structure of human bones was characterized by $^{31}P\{^{1}H\}$ CP MAS NMR and ^{1}H–^{31}P HETCOR spectroscopy.[101] Wu *et al.*[102] have studied the role of phosphorylated proteins in bone formation of chicken embryos. In particular, the presence and function of calcium–phosphoryl complexes in the very early stage of bone formation could be elucidated by spinning sideband analysis of the ^{31}P MAS NMR spectra. Furthermore, measurements of the ^{31}P NMR chemical shift anisotropy as a function of the age of the chicken embryos interestingly showed a continuous decrease of the so-called total span $\Delta = |\delta_{zz}–\delta_{xx}|$of the chemical shift tensor (measured in ppm) with increasing time t (in days) following an exponential law: $\Delta = A\exp\{–Bt\} + C$ with the empirical parameters: $A = 504 \pm 87$ ppm; $B = -0.22 \pm 0.12$ day^{-1}; and $C = 50 \pm 23$ ppm. This behavior could be interpreted as follows. In the early stage of the embryos (ca. 8 days), ^{31}P mainly occurs in the phosphorylated proteins where Δ amounts to ca. 130–150 ppm. With increasing time, however, apatite is formed as a constituent of mature bones. Apatite, however, exhibits a relatively low Δ-value of ca. 40 ppm. That means, ^{31}P MAS NMR spectroscopy could be established as a tool to determine the degree of bone maturity.[102]

3.3. Phospholipids

^{31}P NMR spectroscopy has been used extensively to study phospholipids, biomembranes, and related compounds over the past three decades.[103–127] The reason for this success is simple. Since phospholipids exhibit a phosphate moiety in their polar headgroups, ^{31}P NMR spectroscopy can be used to probe the orientation of the lipid bilayers as well as the mobility and conformational state of the individual lipid molecules. It is, therefore, of crucial importance to know the principal elements and the orientation of the principal axis system of the chemical shift anisotropy tensor with respect to the lipid molecule in order to quantitatively interpret such experiments. The chemical shift anisotropy tensor of several phospholipids, lipid-analogs, as well as certain model compounds[109–111] could be determined (see also Table 3). In general, phospholipids exhibit relatively asymmetric chemical shift anisotropy tensors as it was already observed for phosphorylated amino acids (cf. Table 2). For example, an asymmetry parameter $\eta = 0.9$ could be observed for 1-hexadecyl-2-deoxyglycerophosphoric acid monohydrate.[110] If incorporated into aggregates such as lipid bilayers or micelles, the lipid molecules are restricted in their mobility.[106,107] This leads to motional averaging, i.e., the original chemical shift anisotropy tensor has to be replaced by a motionally averaged tensor.[106,128] In bilayers, the lipid molecules undergo a rapid rotation around the bilayer normal

Table 3. Principal values (δ_{xx}, δ_{yy}, δ_{zz}) of the CSA tensor, chemical shift anisotropy ($\Delta\sigma$) and asymmetry parameter (η) for selected phospholipids and related compounds as determined by single crystal ^{31}P NMR spectroscopy or line shape analysis of ^{31}P NMR powder spectra (see Section 2.1.1).

Compound	δ_{xx}/ppm	δ_{yy}/ppm	δ_{zz}/ppm	$\Delta\sigma$/ppm	η
BDEP[111]	79	19	−113	132	0.68
HPA[110]	53	2	−58	84	0.91
DPE[109]	85	14	−87	122	0.87
DMPC (anhydr)[111]	98	34	−134	166	0.58
DMPC · H_2O[111]	81	22	−110	140	0.63

Abbreviations: BDEP, bariumdiethylphosphate; HPA, 1-hexadecyl 2-deoxyglycerophosphoric acid monohydrate; DPE, dipalmitoylphosphatidylethanolamine; DMPC, dimyristoylphosphatidylcholine.
Note: The orientation of the principal axis systems of the CSA tensors with respect to the molecules is given in the cited references[109–111] for BDEP, HPA, and DPE.

(director). The motionally averaged CSA tensor does, therefore, become axially symmetric with the principal elements $\delta_{||}$ (parallel to the director axis) and $\delta_{\perp}$ (perpendicular to the director axis):

$$\delta_{||} = \delta_{xx}\langle\cos^2\theta_1\rangle + \delta_{yy}\langle\cos^2\theta_2\rangle + \delta_{zz}\langle\cos^2\theta_3\rangle \tag{20}$$

$$\delta_{\perp} = \frac{1}{2}(\delta_{xx} + \delta_{yy} + \delta_{zz} - \delta_{||}) \tag{21}$$

where θ_i ($i = 1, 2, 3$) denote the angles between the ith principal axis of the CSA tensor and the bilayer normal.[106] Note, that the cosine functions in Eq. (20) have to be averaged as indicated by the brackets if the molecules exhibit other motions apart from the aforementioned rapid rotation around the bilayer director (dynamic disorder). Lipid bilayers in aqueous solutions can be oriented in the external magnetic field. In so-called L_α-phases, lipid bilayers are oriented such that their normal is perpendicular to the external magnetic field, B_0. For perfectly ordered samples, the individual lipid molecules do then have an identical orientation of their rotation axes with respect to the external magnetic field. In other words, such samples can no longer be considered as "powders" (cf. Section 2.1.1) from the NMR spectroscopic point of view. For this scenario,[106] only one single signal is observed at a chemical shift given by $\delta_{\perp}$ (see Eq. (21)). In other words, ^{31}P NMR spectroscopy, for example, allows the evaluation of the degree of alignment of a phospholipid sample as well as the determination of so-called order parameters.[106] This technique could, e.g., be used by Sanders and Schwonek[112] in order to detect the formation and magnetic alignment of so-called phospholipid bicelles, disk-shaped aggregates which occur in binary mixtures of phospholipids of different chain length.

On the basis of these principles, ^{31}P NMR spectroscopy was used in numerous studies to determine the structure, order, and mobility of phospholipid membranes.[103–108] As an example of special methodical interest, motionally averaged dipolar couplings in phosphocholine could be measured by 2D NMR

experiments.[113] Furthermore, 2D ^{31}P exchange NMR spectroscopy was applied to study model membranes and biological systems.[114] Molecular insight into the electrostatic membrane surface potential could be obtained from ^{31}P MAS NMR spectroscopic studies of phospolipids.[115] Systematic changes of both, the isotropic ^{31}P NMR chemical shifts as well as the chemical shift anisotropy were found if the membrane potential varies.[115] ^{31}P NMR spectroscopy is frequently applied to characterize the reconstitution of membrane proteins or peptides into phospholipid membranes.[116–124] The binding of tetraphenylphosphonium to the ion-coupled multidrug transport protein EmrE reconstituted into DMPC bilayers was recently studied by ^{31}P{^{1}H} CP MAS NMR spectroscopy.[123] Glaubitz and Watts[125] have introduced the so-called magic angle-oriented sample spinning (MAOSS) technique. Lipid membranes are deposited on glass disks which are packed into a MAS rotor such that the membrane director is aligned parallel to the rotor axis. Proteins can be reconstituted into the oriented lipid membranes. This combination of sample orientation with MAS results in highly resolved spectra making membrane proteins accessible to solid-state NMR spectroscopic investigations. ^{31}P NMR can be used in MAOSS experiments, e.g., in order to characterize the state of the lipid membranes.[125] Finally, the reader is referred to a number of review articles[106,107,126,127] describing the use of solid-state ^{31}P NMR spectroscopy to characterize phospholipid membranes in much more detail.

3.4. Nucleic acids

Liquid-state ^{31}P NMR spectroscopy has been used for a long time to study nucleic acids such as DNA and RNA[129,130] and numerous subsequent publications. Terao *et al.*[131] were the first to measure the principal values of the CSA tensors for several nucleic acids. For salmon DNA, a chemical shift anisotropy of 163 ppm and an asymmetry parameter $\eta = 0.55$ were determined.[131] Almost identical values could be measured in later experiments for calf thymus DNA ($\Delta\sigma = 164$ ppm, $\eta = 0.55$).[132] On the basis of the knowledge of the chemical shift anisotropies, the geometry of DNA double helices in oriented DNA fibers could be investigated.[133,134] Conformational transitions of the phosphodiester backbone in DNA fibers were studied by the so-called sync-2D-MAS experiment[135,136] allowing the determination of the orientation distribution functions of the ^{31}P CSA tensors.

Drobny *et al.*[137–140] have developed a very interesting method to measure long-range distances in the phosphodiester backbone of solid nucleic acids. This method is based on ^{31}P–^{19}F REDOR measurements (cf. Section 2.5) and requires the introduction of special labels, namely phosphorothioate groups as unique ^{31}P labels and nucleotides containing ^{19}F spins such as –CF_3-groups. It is possible to measure ^{31}P–^{19}F distances up to 1.3–1.4 nm by this method.[140] It could meanwhile be applied, e.g., to study protein or peptide binding-induced structural changes of RNA and DNA[138,139] as well as to study proteins.[141]

Finally, it should be noted that solid-state ^{31}P NMR spectroscopy could also be used to study several viruses.[142,143] Line shape and relaxation analysis allowed to

determine the motional and conformational state of the RNA or DNA molecules incorporated into the viruses.

4. SOLID-STATE ^{31}P NMR SPECTROSCOPY IN MATERIALS SCIENCE

During the past decades, solid-state ^{31}P NMR spectroscopy has found numerous applications in materials science. Prominent examples are glasses as well as crystalline, microporous aluminophosphates acting as molecular sieves. Materials science applications of solid-state ^{31}P NMR spectroscopy will be discussed in the present chapter especially with respect to these two classes of substances.

4.1. Phosphate- and phosphate-containing glasses

4.1.1. *Network structure of phosphate glasses*

The P–O bonds are the strongest chemical bonds in most of the vitreous phosphate compounds which allow the description of phosphate glass structures by phosphate tetrahedra interconnected via P–O–P bonds.[144–146] These units are referred to as network builders. The incorporation of oxides (network modifiers) such as alkali or alkaline earth oxides causes a depolymerization of the phosphate network, i.e., a break of P–O–P bridges.[147] Depending on the [network modifier]:[network builder] ratio, four different types of phosphate units (Q^n) occur which are distinguished by the number n ($0 \leqslant n \leqslant 3$) of P–O–P bridging oxygen (BO) atoms (see Section 2.1.1). The isotropic ^{31}P NMR chemical shift is characteristic for the different Q^n units. ^{31}P MAS NMR spectroscopy is, therefore, capable of resolving and distinguishing the different Q^n sites.[144–146] Furthermore, ^{31}P NMR spectra of phosphate glasses may exhibit large chemical shift anisotropies depending on n (see Table 1). The different Q^n units can, therefore, also be identified by an analysis of the spinning sideband pattern or the static powder spectrum which reflects the geometry of the phosphate tetrahedra.

4.1.2. *1D NMR spectroscopy and the influence of network modifiers*

The short-range structure as well as the depolymerization of the phosphate network can be qualitatively analyzed by ^{31}P MAS NMR spectroscopy. For binary glasses like magnesium-,[148] cesium-,[149] sodium-,[150] lithium-[151] or other rare earth-phosphate glasses,[152] the spectra show a decreasing number of Q^3 accompanied by an increasing number of Q^2 sites if network modifiers are added. At further increasing network modifier concentrations, Q^1 units are formed more and more. These NMR spectroscopic observations agree very well with the so-called depolymerization model.[147] Changes in the isotropic chemical shift and line width indicate a change and redistribution of the local structure of the phosphate tetrahedra during the depolymerization process.[153,154] Moreover, a CSA analysis of magnesium phosphate glasses[148] together with the results of other NMR studies suggest a structural change from phosphate rings to phosphate chains for MgO/P_2O_5 ratios close to 1.

It should be noted that H_2O acts as an additional network modifier. The hygroscopic nature of binary phosphate glasses can, therefore, complicate the quantification of the depolymerization state as a function of network modifier content which could be shown by $^{31}P\{^{1}H\}$ CP MAS NMR studies.[145,155]

4.1.3. *2D NMR spectroscopy and medium range order*

Despite the aforementioned successful applications of 1D MAS NMR experiments for the structural analysis of phosphate-containing glasses, these methods often fail for more complicated spectra. In particular, the connectivities between the various Q^n units cannot be determined. In order to overcome this limitation, modern 2D NMR techniques have to be applied. Jäger *et al.*[156] have used the 2D radio frequency-driven recoupling (RFDR) technique[157] to extract direct information about the connectivities of the various Q^n units. The principle of this experiment is similar to that described in Section 2.7.1. In contrast to the ^{1}H-driven spin-diffusion experiment, however, a pulse sequence is applied to the ^{31}P nuclei during the mixing time, τ_m, in RFDR experiments. This pulse sequence restores the ^{31}P–^{31}P magnetic dipole–dipole interaction, which would be suppressed by fast MAS alone. Therefore, spin diffusion processes can occur. Olsen *et al.*[158] applied this technique to silver iodide – silver phosphate glasses. However, the RFDR experiment suffers from a number of limitations. In particular, transferred spin diffusion via third interaction partners may complicate the interpretation of RFDR spectra.

A more selective approach which can overcome the limitations of the RFDR experiment is the DQ 2D experiment which could be applied to crystalline phosphates by Feike *et al.*[159] Subsequently, this experiment was used to investigate phosphate glasses.[148,160–162] The basic concept is explained in Section 2.6. Fig. 15 demonstrates the application of the DQ 2D experiment to phosphate glasses. Owing to the DQ excitation at the beginning of the experiment, signals caused by dipolarly coupled Q^n units exclusively appear in the spectrum. The different sites can be identified easily from their isotropic chemical shift in the SQ dimension. Information about connectivities is found in the DQ dimension. DQ signals occur at the sum frequency of the coupled spins. As long as the distances between the chemically interconnected sites are shorter than the distances to other groups in the neighborhood, short excitation times ensure the exclusive detection of interconnected sites. This is, however, not always the case, as it was demonstrated by Fayon *et al.*[75] for the crystalline phosphate $Zn_2P_2O_7$. Here, the 2D DQ spectrum exhibits many dipolarly coupled spin pairs which are not directly chemically bound. Therefore, other approaches based on the exploitation of through-bond couplings have to be applied in such cases. The INADEQUATE[163] experiment which is explained in Section 2.7.2 as well as spin-locking techniques[164] are two methods making use of the *J*-couplings in phosphate glasses. Furthermore, a triple-quantum method[165] based on *J*-couplings could be applied to lead-phosphate glasses. It provides an improved description of the connectivities and chain length distributions of the phosphate network.

Owing to the improved resolution in 2D DQ NMR experiments, the spectra revealed that Q^n groups having an equal coordination number n but different

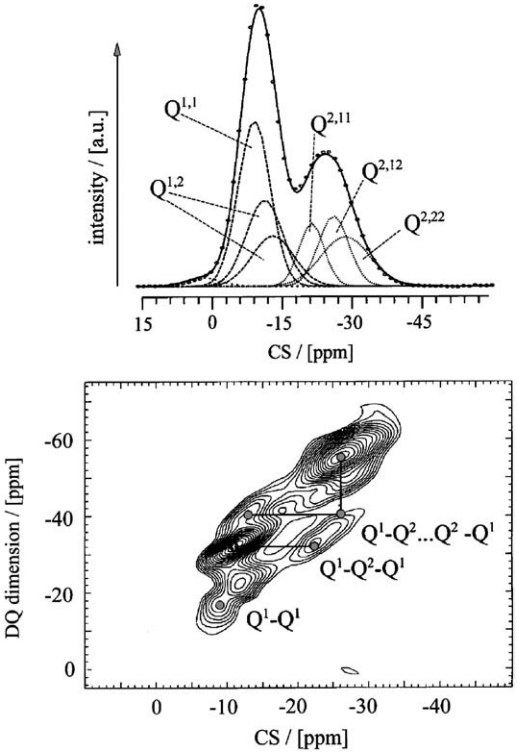

Fig. 15. Top: Gaussian line shape fit of ^{31}P MAS NMR spectrum using the corresponding isotropic chemical shifts obtained from the DQ spectrum below. Bottom: DQ spectrum of a binary calcium phosphate glass.[162] Peaks at the double-quantum diagonal ($\omega_1 = 2\omega_2$) and off-diagonal signals give a direct verification of pair connectivity between the different Q^i units. Reproduced from Jäger *et al.*[162] by permission from Elsevier Science B.V.

neighboring units $Q^{n'}$ exhibit small differences in their isotropic chemical shifts. Witter *et al.*,[161] suggested a new notation $Q^{n,jkl}$ extending the commonly used Q^n notation by the additional superscripts *j, k, l*. These superscripts define the type of the three adjacent $Q^{n'}$ units. It is, however, difficult to quantify the DQ signal intensities, since the DQ excitation depends on a number of parameters, e.g., on the mutual orientation of CSA and dipolar tensors. Nevertheless, the very accurate isotropic chemical shifts obtained from the 2D DQ NMR spectra can be taken as a starting point in order to interpret and simulate the corresponding 1D MAS spectra (see Fig. 15), enabling a quantitative determination, e.g., of chain-length statistics and the presence of ring structures.

4.1.4. *Distribution of network builders and modifiers: Dipolar NMR spectroscopy*

As already mentioned in Section 2.5, internuclear distances can be measured by the exploitation of the magnetic dipole–dipole interaction. The corresponding coupling

networks are relatively complex in phosphate-glasses due to the superposition of multi-spin interactions. It is, therefore, more suitable to quantify these interactions in terms of the second moment (Section 2.1.2).

Spin-echo spectroscopy is a powerful tool to obtain quantitative information about dipolar couplings in multi-spin systems.[144,166] One approach, developed for the non-spinning case, is the Hahn echo experiment, $\pi/2{-}t_1{-}\pi{-}t_1$. It eliminates all interactions that are linear in I_z, including both the heteronuclear magnetic dipole–dipole interaction and the chemical shift anisotropy. As a result, the normalized echo decay $E(2t_1)/E(0)$ as a function of evolution time $2t_1$ is only affected by homonuclear interactions which are bilinear in I_z. For multi-spin systems, the echo decay can be approximated by a Gaussian in the static case (i.e., without MAS):

$$\frac{E(2t_1)}{E(0)} = \exp\left(-\frac{M_2^{\mathrm{II}}}{2}(2t_1)^2\right) \tag{22}$$

This directly allows the determination of the homonuclear second moment, M_2^{II}, and delivers, therefore, distance information.[167]

Static spin-echo decay spectroscopy can also be applied to measure distances between unlike spins I and S. The corresponding experiment (SEDOR, see Section 2.5) is used by Eckert *et al.*[166] in a somewhat modified fashion: A Hahn echo experiment $\pi/2{-}t_1{-}\pi{-}t_1$ (see above) is carried out in the I channel. A π-pulse is applied to the S spins synchronously with that to the I spins at t_1. It is, however, difficult to quantitatively interpret the SEDOR-fraction in multi-spin systems (see Section 2.5, Eqs. (15) and (16)). Nevertheless, the spin-echo decay can be approximated by a Gaussian function for a multi-spin system[166,169]

$$S_F = 1 - \frac{I(2t_1)}{I(0)} = 1 - \frac{E(2t_1)}{E(0)}\exp\left(-\frac{M_2^{IS}}{2}(2t_1)^2\right) \tag{23}$$

$E(2t_1)/E(0)$ is the normalized echo decay in the absence of the π-pulse in the S channel which is determined by the homonuclear magnetic dipole–dipole interaction among the I spins (see Eq. (22)).

Lathrop *et al.*[167–169] used these techniques to study the structure and distribution of P–P and P–Se units in non-oxidic phosphorous-selenium glasses. The simulation of three different distribution models for ^{31}P nuclei (uniform-, clustered-, and random-distributed) and the comparison with experimental echo decay functions indicate the preferred formation of P–Se rather then P–P bonds.[167] Furthermore, the presence of three- and four-coordinated phosphorous sites could be detected and quantified. The different phosphorous/selenium structural units and their distribution in the glassy system could be determined.[168,169] These studies were meanwhile also extended to other phosphorous chalcogenide glasses.[170]

A great disadvantage of the described static techniques is the lack of spectral resolution. This can in general be overcome by the application of MAS, i.e., by REDOR techniques. REDOR (see Section 2.5) is one of the most powerful approaches to quantify the strength of heteronuclear magnetic dipole–dipole interactions under MAS conditions. Similar to SEDOR, this technique faces a number of complications if applied to multi-spin systems like phosphate glasses. The analysis of

the oscillatory part of the REDOR curve is in general the basis for the calculation of the dipolar coupling constant and the determination of bond geometries.[171] However, this analysis can only be performed in the case of small and truly isolated spin clusters. Complex coupling networks lead to a superimposition and, hence, a damping of the oscillations which makes the evaluation of longer REDOR evolution times, nt_r, impossible.[171] Furthermore, dipolar couplings to quadrupolar nuclei which often occur as network modifier cations, can also affect the efficiency of REDOR.[172] Both complications can be overcome by limiting the analysis of the REDOR curve to its initial part ($0 \leqslant R_F(nt_r) \leqslant 0.2$, cf. Eq. (17)). Within this short evolution time limit, the REDOR curve can be described in terms of the second moment.[171–173] An exact theoretical treatment of this subject is beyond the scope of this paper and the reader is referred to the comprehensive review given by Eckert *et al.*[166]

In the following, some recent applications of the REDOR technique to phosphate and other phosphorous-containing glasses will be discussed. Van Wüllen *et al.*[174] have studied lithium phosphate glasses which exhibit an unexpected minimum in the glass transition temperature at alkali concentrations near 20–25 mol%. ^{6,7}Li and ^{31}P MAS NMR together with 2D RFDR spectroscopy could not confirm the existence of unexpectedly abrupt changes of the local phosphorous coordination within the critical concentration range which would explain this phenomenon.[150,151] In contrast, ^{31}P$\{^{7}$Li$\}$ REDOR experiments indicate a pronounced change of the interaction between the phosphorous Q^n units and the modifier cation Li^+. The data suggest that the average number of lithium atoms surrounding a phosphorous site increases rapidly near 20–25 mol% LiO_2. The phosphate chains do then become cross-linked by Li^+ cations. REDOR has also been adopted to obtain information about the relative orientations of chemical shift and heteronuclear dipolar tensors by the analysis of the sideband distribution of the REDOR spectrum.[175] Zeyer *et al.*[176] showed that the relative orientation of the quadrupolar and dipolar tensors of ^{17}O–^{31}P spin pairs in sodium phosphate glasses can be determined by the analysis of the ^{17}O quadrupolar pattern as a function of the ^{17}O$\{^{31}$P$\}$ REDOR decay time. That means, distance and tensor orientation information can be obtained simultaneously. Strojek *et al.*[172] performed REDOR experiments on glassy sodium phosphates which showed that the ^{31}P–^{23}Na dipolar interaction is differently strong for the various Q^n sites. The ^{31}P–^{23}Na dipolar interaction raises with increasing charge of the phosphate moiety (Fig. 16). However, even the neutral Q^3 site displays ^{31}P–^{23}Na dipolar couplings of significant strength which suggests that the double-bound non-bridging oxygens (NBOs) participate in the Na^+ coordination although no charge compensation is necessary for these sites. Furthermore, the REDOR experiments exclude clustering or phase separation of the cations; effects which were shown previously for other glassy systems.[177] REDOR measurements were also used to identify and quantify network former – network modifier distributions in borophosphate glasses.[178,179]

In order to handle the complications which arise due to the presence of quadrupolar nuclei, alternative techniques such as transfer of populations with double resonance (TRAPDOR)[180] and rotational echo adiabatic passage double resonance (REAPDOR)[181] were designed and successfully applied to phosphate glasses.[182–184]

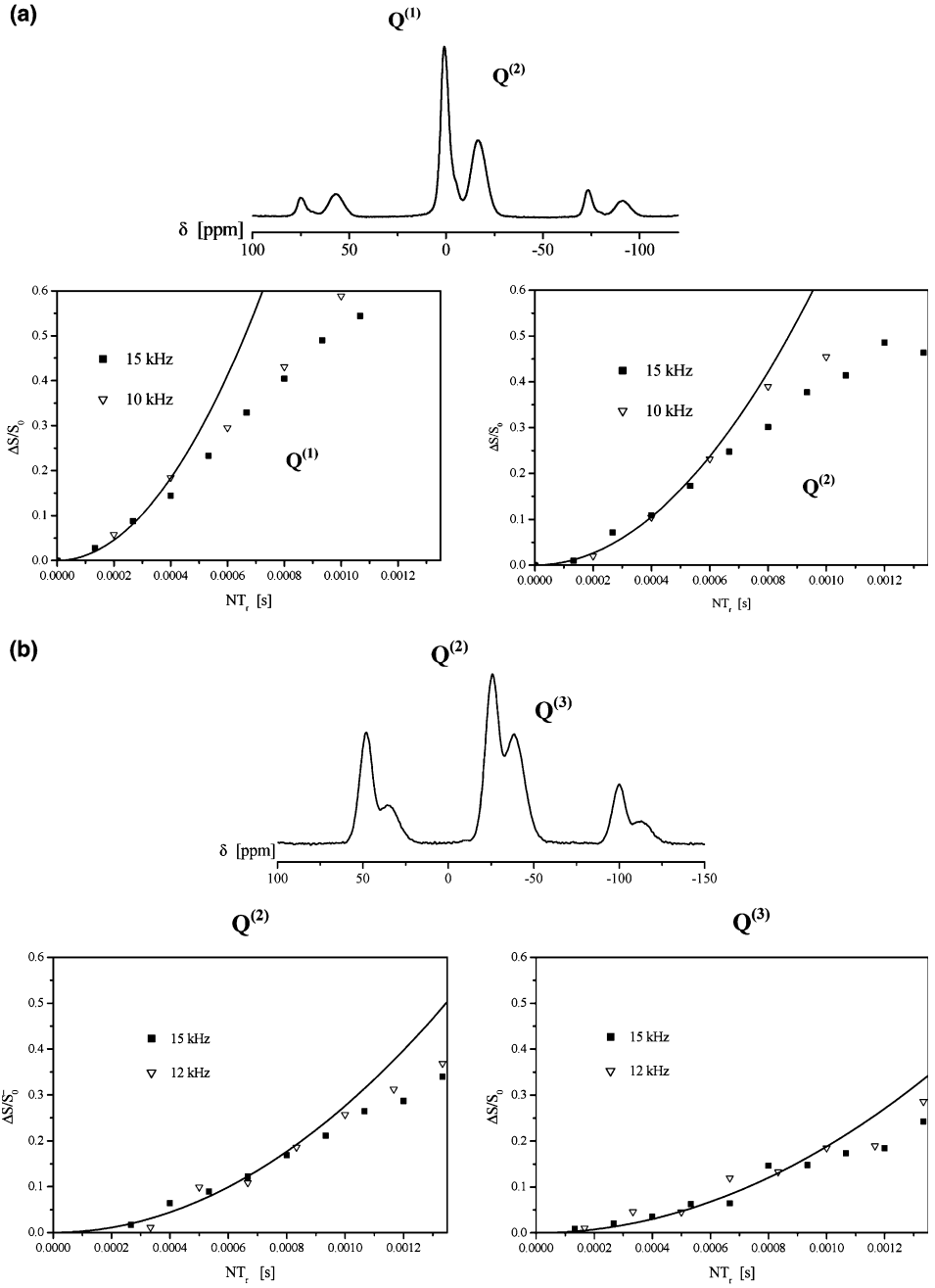

Fig. 16. ^{31}P MAS NMR spectra for two sodium phosphate glasses[172] $x[Na_2O](x–1)[P_2O_5]$ with (a) $x = 0.6$ and (b) $x = 0.35$. The analysis of the site-resolved $^{31}P\{^{23}Na\}$ REDOR curves reveals different second moments for the different Q^n units. Reproduced from Bertmer and Eckert[172] with permission from the American Chemical Society.

As explained in Section 2.4, the CP experiment allows to detect and exploit heteronuclear magnetic dipole–dipole interactions. As shown by the results of variable contact time $^{31}P\{^{23}Na\}$ CP MAS experiments, Mueller *et al.*[185,186] suggested a change of the alkali–cation coordination of the Q^2 unit: as for low cation concentration, the two NBOs of the Q^2 unit are linked to only one single cation. For higher alkali content, both NBOs at a Q^2 unit are able to coordinate with different alkali cations.

4.2. Molecular sieves: Aluminophosphates and related compounds

Aluminophosphates ($AlPO_4$s) and related compounds are capable of forming zeolite-like microporous framework structures with molecular sieve properties.[187,188] They exhibit a crystalline structure, in the case of pure $AlPO_4$s with alternating AlO_4 and PO_4 tetrahedra. The P/Al ratio is then 1 and the system is neutral, i.e., no charge-balancing ions are necessary. It is also possible to incorporate silicon (SAPOs) or certain metal atoms (MeAPOs) into the framework. The P/Al ratio may then be different from 1. Moreover, gallophosphates such as cloverite do also exhibit zeolite-like structures.

Owing to the crystalline structure of these materials, X-ray diffraction is the first choice to probe the long-range order of $AlPO_4$s and related compounds. On the other hand, solid-state NMR spectroscopy is a powerful tool to reveal the medium- and short-range structure of the Al–O–P or Ga–O–P framework. In particular, connectivities among the framework builders, e.g., ^{27}Al and ^{31}P as well as interactions with organic template molecules or adsorbed water can be studied by solid-state NMR spectroscopy.

First solid-state ^{31}P NMR investigations of $AlPO_4$s were carried out by Blackwell and Patton.[189] In the mean time, solid-state NMR spectroscopy was applied to an overwhelming variety of different $AlPO_4$ compounds and related materials.[146,190–216] Selected recent applications will be discussed especially with respect to advanced solid-state NMR methods established for the investigation of crystalline $AlPO_4$s. For more details, the reader is referred to earlier review articles.[217,218]

4.2.1. *Application of 1D NMR spectroscopy and the influence of the hydration state*

The ^{31}P NMR signals of PO_4 tetrahedra in crystalline $AlPO_4$s typically occur at isotropic chemical shifts, δ, between ca. –20 and –35 ppm. The isotropic ^{31}P chemical shift of several $AlPO_4$ polymorphs was found[219] to be linearly correlated with the average Al–O–P angle, θ. The slope $d\delta/d\theta$ of the regression line amounts to ca. –0.6 ppm/deg. Interestingly, the same behavior with an identical slope was also found for the isotropic ^{27}Al chemical shift of tetrahedral Al in $AlPO_4$s.[219]

It could, furthermore, be shown that the incorporation of metal ions such as Mg also influences the isotropic ^{31}P NMR chemical shift.[193] Isotropic chemical shifts of –14.0 ppm (P(1Al, 3Mg)), −21.1 ppm (P(2Al, 2Mg)), –28.0 ppm (P(3Al, 1Mg)), and –34.9 ppm (P(4Al)) could be observed for the various (Al, Mg) environments of the material. That means, replacement of one Al atom in the neighborhood of a P atom by Mg results in a chemical shift change of ca. −7 ppm. In gallophosphates such as

cloverite, the PO_4 tetrahedra are surrounded by four gallium atoms. The signals due to the different crystallographic positions for phosphorous in cloverite occur at isotropic ^{31}P NMR chemical shifts between −2 and −11 ppm.[196–198]

Several groups have performed dehydration and rehydration studies on as-synthesized, calcined, and rehydrated $AlPO_4$s and detected pronounced changes of the local structure caused by the hydration/dehydration processes.[194,195,208–210,215] For example, Zibrowius *et al.*[195] studied the dependence of the ^{31}P NMR signals of $AlPO_4$-14 on the hydration state. Caldarelli *et al.*[208] examined the structure of as-synthesized, calcined, and rehydrated samples of $AlPO_4$-41 using ^{27}Al and ^{31}P MAS NMR techniques. The ^{31}P MAS NMR spectrum of the as-synthesized $AlPO_4$-41 exhibits six signals which can be fully assigned to the various positions in the framework. While calcination does not significantly modify the X-ray pattern, the ^{31}P NMR spectrum of the calcined, dehydrated $AlPO_4$-41 shows only one single broad resonance at –31.5 ppm. Rehydration of the calcined sample changes the X-ray pattern indicating a modification of the unit cell, in particular of the crystallographic b axis and the angle γ. The ^{31}P MAS NMR spectra of the aluminophosphate VPI-5 also exhibit a pronounced dependence on the hydration state. The ^{31}P MAS NMR spectra of hydrated VPI-5 consist of three well-resolved signals at –23.3 ppm, −27.2 ppm, and −33.1 ppm.[192,202] In contrast, the dehydrated samples only exhibit two signals at ca. −27 ppm and −32 ppm.

4.2.2. *Application of double resonance and 2D NMR techniques*

The feasibility of various double resonance and 2D NMR techniques to study $ALPO_4$s could be demonstrated.[199–207] The use of CP, HETCOR, REDOR (see Sections 2.4 and 2.5) and the so-called transferred-echo double-resonance (TEDOR[220]) technique to explore dipolar couplings between quadrupolar (^{27}Al) and spin-1/2 nuclei (^{31}P) could be established. These methods allow the measurement of interatomic distances and to extract connectivity information in $AlPO_4$s.

Polarization transfer from quadrupolar nuclei to spin-1/2 nuclei is particularly helpful because quadrupolar nuclei usually have very short longitudinal relaxation times. It is, therefore, possible to measure spectra of spin-1/2 nuclei with long T_1 in a relatively short time using such CP techniques.[200] Moreover, this polarization transfer is required for HETCOR experiments (see below).

A 2D extension of TEDOR could be developed which directly maps connectivities between distinct ^{27}Al and ^{31}P sites in a 2D correlation spectrum.[199] The framework structure of VPI-5,[199–201] $ALPO_4$-8,[201] as well as the silicon-containing compound SAPO-37[203] could be studied by using these techniques. An increased efficiency of the coherence transfer from octahedral ^{27}Al to ^{31}P could be observed for $AlPO_4$-5 if H_2O was replaced by D_2O. This observation suggests that the presence of an abundant third spin (^1H) perturbs the ^{27}Al–^{31}P coherence transfer.[204] All ^{27}Al and ^{31}P resonances in as-synthesized $AlPO_4$-14 could be assigned by the application of a 2D INEPT (insensitive nuclei enhanced by polarization transfer[221,50]) experiment.[205] The described techniques were also applied to $AlPO_4$-14A, which exhibits some unique structural features, as it does not possess a strictly alternating

framework of AlO_4 and PO_4 tetrahedra.[206] Moreover, 2D dipolar-based $^{31}P\{^1H\}$ CP and $^{27}Al\{^1H\}$ TEDOR experiments allowed to determine the location and orientation of the template molecules within the Al–O–P framework.

HETCOR experiments based on CP are a powerful tool to verify connectivities in inorganic solids. However, if quadrupolar nuclei are involved as in the Al–O–P framework of $AlPO_4$s, the HETCOR spectra are poorly resolved in the dimension of the quadrupolar nucleus because the second-order quadrupolar interaction is not fully suppressed by MAS. Fernandez *et al.*[213] developed a new HETCOR experiment (referred to as MQHETCOR) using MQ MAS to produce an isotropic echo in the indirect dimension that is not affected by second-order quadrupolar broadening. The magnetization is then transferred via CP or an INEPT-like sequence[216] to the spin-1/2 nuclei, resulting in an improved resolution for the quadrupolar nuclei. This method was applied to VPI-5, $ALPO_4$-40, and $ALPO_4$-14. The MQHETCOR spectrum of VPI-5 reveals two resonances for the tetrahedral ^{27}Al, which are not resolved in the conventional HETCOR experiment. A further enhancement of resolution in ^{31}P dimension can be achieved by the application of double resonance decoupling. A corresponding improvement in resolution could be demonstrated by Delevoye *et al.*[214] for $AlPO_4$-14 (see Fig. 17) and $AlPO_4$-40. In combination with the ordinary ^{1}H high-power decoupling, additional ^{27}Al decoupling yields a reduction of the line width of the ^{31}P signals by a factor of 2.5.

4.2.3. *Investigation of the crystallization process of $AlPO_4$ molecular sieves*

^{31}P MAS NMR and $^{27}Al/^{31}P$ double resonance solid-state NMR techniques could also be used to characterize the crystallization process. In particular, the intermediate phases formed during the crystallization process of molecular sieves VPI-5,[222] SAPO-44,[222] $AlPO_4$-11,[223] and $AlPO_4$-18[224] could be studied. Huang and Machado[222] applied $^{31}P\{^{27}Al\}$ CP techniques to map the P–O–Al connectivities during the crystallization process of $AlPO_4$s. The 1D ^{31}P MAS-NMR spectrum of the initial gel in VPI-5-synthesis exhibits a broad signal at a chemical shift of –12 ppm which was assigned to amorphous phosphate species. The 1D $^{31}P\{^{27}Al\}$ CP NMR as well as 2D $^{31}P\{^{27}Al\}$ HECTOR spectra confirmed the existence of the signal at –12 ppm and revealed that some of the P atoms are already connected to Al atoms even in the gel phase. After 1 h of heat treatment, the 1D $^{27}Al\{^{31}P\}$ CP spectrum displays two signals indicating that the phosphorous is now connected to tetrahedral as well as octahedral Al sites. After heating the initial gel for three hours, the ^{31}P MAS NMR spectrum contains three sharp signals superimposed to a very broad resonance. The three peaks could be assigned to the three nonequivalent P sites of VPI-5. The 2D $^{31}P\{^{27}Al\}$ HETCOR spectrum shows that all three P sites are connected to both tetrahedral and octahedral Al sites, suggesting that VPI-5 begins to crystallize from the gel.

In contrast to VPI-5, the ^{31}P MAS NMR spectrum of the starting mixture of $AlPO_4$-18 already contains three narrow signals suggesting the existence of an ordered phase.[224] After 1 h of heat treatment, the ^{31}P MAS NMR spectrum exhibits only one broad signal indicating the amorphous state of the mixture. Further

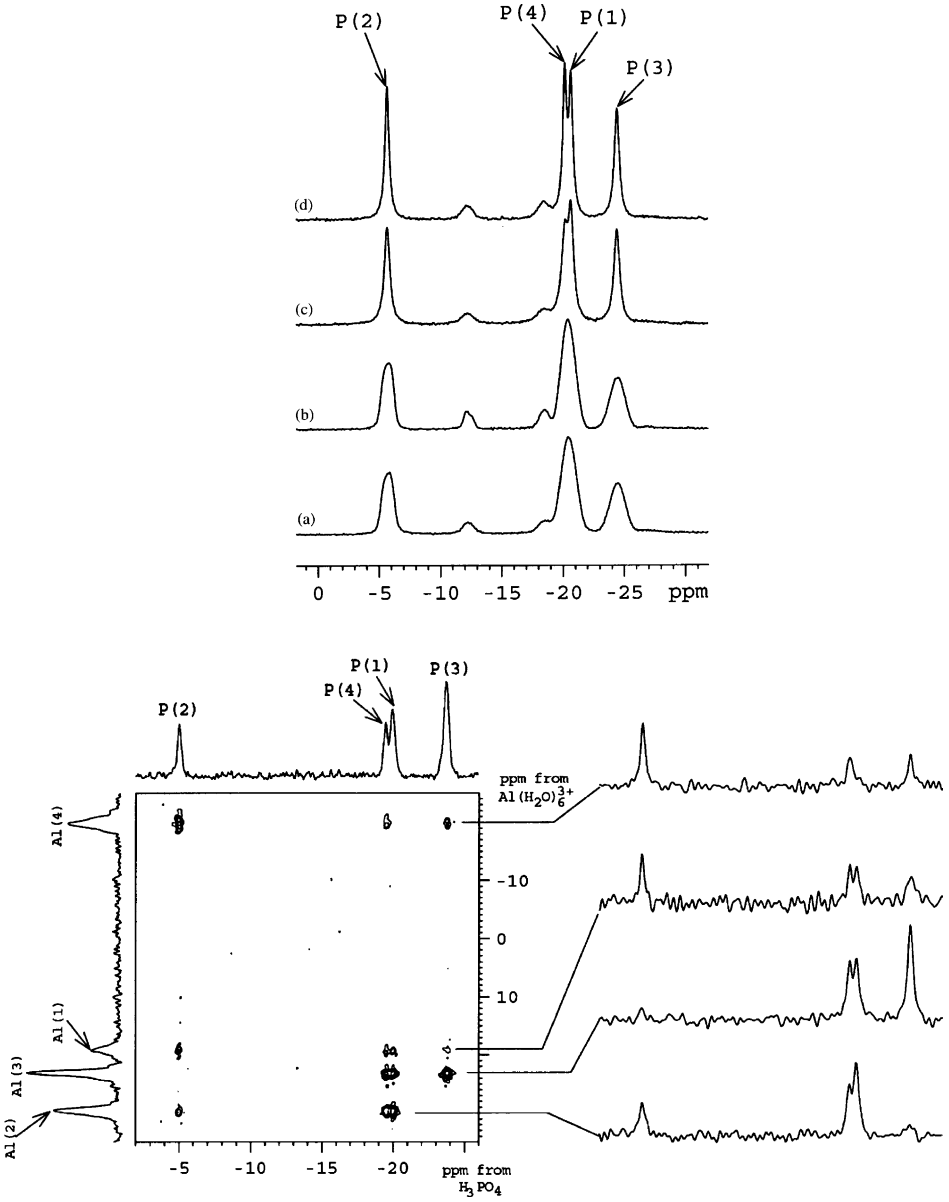

Fig. 17. Top: ^{31}P MAS NMR spectrum of $AlPO_4$-14[214] (a) no decoupling, (b) with ^{1}H high-power decoupling, (c) with ^{27}Al low-power decoupling, and (d) with ^{1}H/ ^{27}Al double-resonance decoupling. Bottom: 2D ^{27}Al-^{31}P MQHETCOR spectrum of $AlPO_4$-14[214] with ^{1}H/ ^{27}Al double-resonance decoupling. Reproduced from Delevoye *et al.*[214] with permission from Elsevier Science B.V.

heating results in a partial transformation of the mixture into crystalline $AlPO_4$-5, and finally the formation of $AlPO_4$-18. Both observations could be confirmed by the presence of characteristic signals in the ^{31}P and ^{27}Al MAS NMR spectra. The crystallization process of $AlPO_4$-11 was also analyzed using various ^{27}Al/^{31}P double resonance techniques, such as CP, TRAPDOR, and REDOR.[223]

4.3. Other materials

Other materials such as phosphorous-containing molecular cage compounds and their adducts recently find increasing interest due to their ion-conducting properties.[225] Some of the examples are the copper(I) halides of phosphorous-based clusters and networks such as $(CuI)P_4Se_4$, $(CuI)_3P_4S_4$ and others.[226,227] Since some of the ^{31}P nuclei are directly bound to ^{63}Cu or ^{65}Cu in these compounds, their line shape under MAS is dominated by *J*-coupling to ^{63}Cu or ^{65}Cu ($S = 3/2$). For example, Fig. 18 shows the 2D ^{31}P R-TOBSY spectrum of $(CuI)_3P_4S_4$.[227] As can be seen, the two signals at ca. 145 ppm (P1) and 117 ppm (P2) exhibit a well-resolved quartet splitting caused by the *J*-coupling to neighboring ^{63}Cu or ^{65}Cu nuclei corresponding to an isotropic *J*-coupling constant of ca 1230 Hz. It should be noted within this context that an ^{31}P–^{115}In *J*-coupling constant of 350 Hz could be found

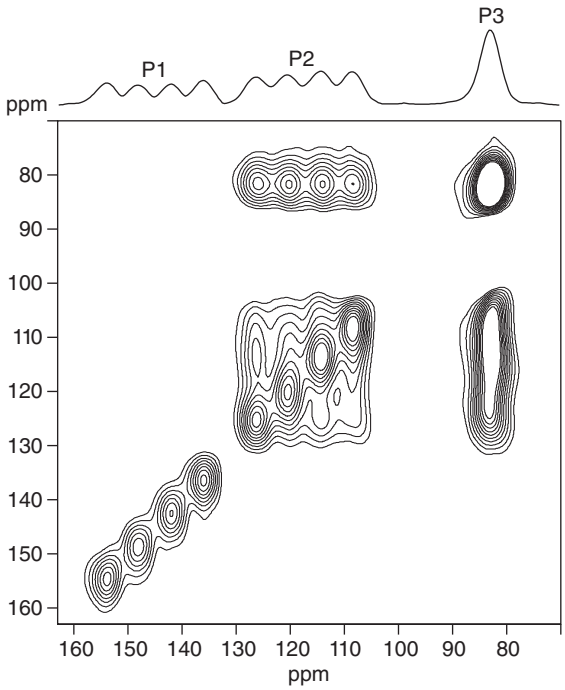

Fig. 18. ^{31}P R-TOBSY spectrum of $(CuI)_3P_4S_4$ measured under the following experimental conditions: $\nu_r = 25$ kHz, $B_0 = 11.7$ T, mixing time = 4.8 ms. Reproduced from Brunklaus *et al.*[227] with permission from the PCCP owner societies.

for InP.[228,229] As can be further seen from the spectrum in Fig. 18, direct bonding between the phosphorous sites P2 and P3 results in corresponding ^{1}J-coupling and, therefore, in cross-peaks in the R-TOBSY spectrum for a mixing time of 4.8 ms.

Finally, it should be mentioned that solid-state ^{31}P NMR spectroscopy could also be used to study phosphorous nanorods[230] and 1D polymers[231]containing phosphorous.

ACKNOWLEDGMENTS

The authors gratefully acknowledge financial support from the Deutsche Forschungsgemeinschaft (Project no. Br 1278/9-1,2). Thanks are further due to Prof. Dr. Dr. H.R. Kalbitzer and Dr. M. Spoerner for helpful discussions and to Ms I. Cuno for carefully proofreading the manuscript.

REFERENCES

1 A. Abragam, *Principles of Nuclear Magnetism*, Oxford University Press, Oxford, 1961.
2 R. R. Ernst, G. Bodenhausen and A. Wokaun, *Principles of Nuclear Magnetic Resonance in One and Two Dimensions*, Oxford University Press, Oxford, 1987.
3. M. Bak, J. T. Rasmussen and N. C. Nielsen, *J. Magn. Reson.*, 2000, **147**, 296–330.
4. P. Hartmann, J. Vogel and B. Schnabel, *J. Magn. Reson. A*, 1994, **111**, 110–114.
5. A. R. Grimmer and U. Haubenreisser, *Chem. Phys. Lett.*, 1983, **99**, 487–490.
6. T. M. Duncan and C. D. Douglas, *Chem. Phys.*, 1984, **87**, 339–349.
7. S. Un and M. P. Klein, *J. Am. Chem. Soc.*, 1989, **111**, 5119–5124.
8. A. R. Grimmer, D. Müller, G. Gözet and R. Kniep, *Fresenius J. Anal. Chem.*, 1997, **357**, 485–488.
9. A. R. Grimmer, *Spectrochim. Acta A*, 1978, **34**, 941.
10. J. R. van Wazer, *J. Am. Chem. Soc.*, 1956, **78**, 5709–5715.
11. G. E. Pake, *J. Chem. Phys.*, 1948, **16**, 327–336.
12. E. R. Andrew, A. Bradbury and R. G. Eades, *Nature*, 1958, **182**, 1659.
13. I. J. Lowe, *Phys. Rev. Lett.*, 1959, **2**, 258–287.
14. M. M. Maricq and J. S. Waugh, *J. Chem. Phys.*, 1979, **70**, 3300–3316.
15. E. Brunner, D. Freude, B. C. Gerstein and H. Pfeifer, *J. Magn. Reson.*, 1990, **90**, 90–99.
16. E. Brunner, D. Fenzke, D. Freude and H. Pfeifer, *Chem. Phys. Lett.*, 1990, **169**, 591–594.
17. A. Samoson, T. Tuherm, J. Past, A. Reinhold, T. Anupõld and I. Heinmaa, *Top. Curr. Chem.*, 2005, **246**, 15–31.
18. M. Ernst, *J. Magn. Reson.*, 2003, **162**, 1–34.
19. A. E. Bennett, C. M. Rienstra, M. Auger, K. V. Lakshmi and R. G. Griffin, *J. Chem. Phys.*, 1995, **103**, 6951–6958.
20. D. Raleigh, M. H. Levitt and R. G. Griffin, *Chem. Phys. Lett.*, 1988, **146**, 71–76.
21. S. R. Hartmann and E. L. Hahn, *Phys. Rev.*, 1962, **128**, 2042–2053.
22. A. Pines, J. S. Waugh and M. G. Gibby, *J. Chem. Phys.*, 1972, **56**, 1776–1777.
23. A. Pines, M. G. Gibby and J. S. Waugh, *J. Chem. Phys.*, 1973, **59**, 569–590.
24. J. Schaefer and E. O. Stejskal, *J. Am. Chem. Soc.*, 1976, **98**, 1031–1032.
25. M. Mehring, *Principles of High-Resolution NMR in Solids*, Springer, Berlin, 1983.
26. A. Iuga and E. Brunner, *Magn. Reson. Chem.*, 2004, **42**, 369–372.
27. O. B. Peersen, X. Wu, I. Kustanovich and S. O. Smith, *J. Magn. Reson. A*, 1993, **104**, 334–339.
28. G. Metz, X. Wu and S. O. Smith, *J. Magn. Reson. A*, 1994, **110**, 219–227.

29. S. Hediger, B. H. Meier, N. D. Kurur, G. Bodenhausen and R. R. Ernst, *Chem. Phys. Lett.*, 1994, **223**, 283–288.
30. S. Hediger, B. H. Meier and R. R. Ernst, *Chem. Phys. Lett.*, 1995, **240**, 449–456.
31. R. Fu, J. Hu and T. A. Cross, *J. Magn. Reson.*, 2004, **168**, 8–17.
32. D. E. Kaplan and E. L. Hahn, *J. Phys. Radium*, 1958, **19**, 821–825.
33. C. P. Slichter, *Principles of Magnetic Resonance*, 2nd edition, Springer, Berlin, 1978.
34. E. L. Hahn, *Phys. Rev.*, 1950, **80**, 580–594.
35. T. Gullion and J. Schaefer, *J. Magn. Reson.*, 1989, **81**, 196–200.
36. T. Gullion and J. Schaefer, *Adv. Magn. Reson.*, 1989, **13**, 57–83.
37. J. M. Goetz and J. Schaefer, *J. Magn. Reson.*, 1997, **127**, 147–154.
38. E. R. Andrew, A. Bradbury, R. G. Eades and V. T. Wynn, *Phys. Lett.*, 1963, **4**, 99–100.
39. D. P. Raleigh, G. S. Harbison, T. G. Neiss, J. E. Roberts and R. G. Griffin, *Chem. Phys. Lett.*, 1987, **138**, 285–290.
40. B. H. Meier and W. Earl, *J. Am. Chem. Soc.*, 1987, **109**, 7937–7942.
41. M. H. Levitt, D. P. Raleigh, F. Creuzet and R. G. Griffin, *J. Chem. Phys.*, 1990, **92**, 6347–6364.
42. A. Iuga, M. Spoerner, H. R. Kalbitzer and E. Brunner, *J. Mol. Biol.*, 2004, **342**, 1033–1040.
43. J. Baum, M. Munowitz, A. N. Garroway and A. Pines, *J. Chem. Phys.*, 1985, **83**, 2015–2025.
44. M. Munowitz and A. Pines, *Science*, 1986, **233**, 525–531.
45. C. E. Hughes, *Prog. Nucl. Magn. Reson. Spectrosc.*, 2004, **45**, 301–313.
46. R. Tycko and G. Dabbagh, *J. Am. Chem. Soc.*, 1991, **113**, 9444–9448.
47. D. Sakellariou, A. Lesage and L. Emsley, *J. Magn. Reson.*, 2001, **151**, 40–47.
48. D. N. Shykind, J. Baum, S. -B. Liu, A. Pines and A. N. Garroway, *J. Magn. Reson.*, 1988, **76**, 149–154.
49. K. Wüthrich, *NMR of Proteins and Nucleic Acids*, Wiley, New York, 1986.
50. J. Cavanagh, W. J. Fairbrother, A. G. Palmer III. and N. J. Skelton, *Protein NMR Spectroscopy*, Academic Press, San Diego, 1996.
51. A. W. Overhauser, *Phys. Rev.*, 1955, **92**, 411–415.
52. D. Suter and R. R. Ernst, *Phys. Rev. B*, 1985, **32**, 5608–5627.
53. J. Jeener, B. H. Meier, P. Bachmann and R. R. Ernst, *J. Chem. Phys.*, 1979, **71**, 4546–4553.
54. N. M. Szeverenyi, M. J. Sullivan and G. E. Maciel, *J. Magn. Reson.*, 1982, **47**, 462–475.
55. K. Schmidt-Rohr and H. W. Spiess, *Multidimensional Solid-State NMR and Polymers*, Academic Press Inc, San Diego, 1994.
56. J. S. Waugh, L. M. Huber and U. Haeberlen, *Phys. Rev. Lett.*, 1968, **20**, 180–182.
57. P. J. Mansfield, *J. Phys. C.*, 1971, **4**, 1444–1452.
58. W. -K. Rhim, D. D. Elleman and R. W. Vaughan, *J. Chem. Phys.*, 1973, **59**, 3740–3749.
59. D. P. Burum and W. -K. Rhim, *J. Chem. Phys.*, 1979, **71**, 944–956.
60. D. Sakellariou, A. Lesage, P. Hodgkinson and L. Emsley, *Chem Phys. Lett.*, 2000, **319**, 253–260.
61. A. Bielecki, A. C. Kolbert and M. H. Levitt, *Chem. Phys. Lett.*, 1989, **155**, 341–346.
62. E. Vinogradov, P. K. Madhu and S. Vega, *Chem. Phys. Lett.*, 1999, **314**, 443–450.
63. P. Sozzani, A. Comotti, S. Bracco and R. Simonutti, *Angew. Chem. Int. Ed.*, 2004, **43**, 2792–2797.
64. D. Huster, L. Xiao and M. Hong, *Biochemistry*, 2001, **40**, 7662–7674.
65. Alia, J. Matysik, I. de Boer, P. Gast, H. J. van Gorkom and H. J. M. de Groot, *J. Biomol. NMR*, 2004, **28**, 157–164.
66. J. D. Walls, M. Marjanska, D. Sakellariou, F. Castiglione and A. Pines, *Chem. Phys. Lett.*, 2002, **357**, 241–248.
67. E. Vinogradov, P. K. Madhu and S. Vega, *Chem. Phys. Lett.*, 2002, **354**, 193–202.
68. A. Goldbourt, E. Vinogradov, G. Goobes and S. Vega, *J. Magn. Reson.*, 2004, **169**, 342–350.
69. B. Alonso and F. Fayon, *J. Sol-Gel Sci. Technol.*, 2003, **26**, 95–98.
70. B. -J. Van Rossum, C. P de Groot, V. Ladizhansky, S. Vega and H. J. M. de Groot, *J. Am. Chem. Soc.*, 2000, **122**, 3465–3472.
71. A. Bax, R. Freeman and S. P. Kempsell, *J. Am. Chem. Soc.*, 1980, **102**, 4849–4851.
72. M. H. Levitt and R. R. Ernst, *Mol. Phys.*, 1983, **50**, 1109–1124.
73. A. Lesage, M. Auger, S. Caldarelli and L. Emsley, *J. Am. Chem. Soc.*, 1997, **119**, 7867–7868.

74. A. Lesage, M. Bardet and L. Emsley, *J. Am. Chem. Soc.*, 1999, **121**, 10987–10993.
75. F. Fayon, G. Le Saout, L. Emsley and D. Massiot, *Chem. Commun.,* 2002, 1702–1703.
76. F. Fayon, I. J. King, R. K. Harris, R. K. B. Gover, J. S. O. Evans and D. Massiot, *Chem. Mater.*, 2003, **15**, 2234–2239.
77. M. Baldus and B. H. Meier, *J. Magn. Reson. A*, 1996, **121**, 65–69.
78. A. J. Shaka, J. Keeler and R. Freeman, *J. Magn. Reson.*, 1983, **53**, 313–340.
79. M. Baldus, R. Iuliucci and B. H. Meier, *J. Am. Chem. Soc.*, 1997, **119**, 1121–1124.
80. E. Hardy, R. Verel and B. H. Meier, *J. Magn. Reson.*, 2001, **148**, 459–464.
81. J. C. C. Chan and G. Brunklaus, *Chem. Phys. Lett.*, 2001, **349**, 104–112.
82. D. Voet and J. G. Voet, *Biochemistry*, 3rd edition, John Wiley & Sons Inc., New York, 2004.
83. M. J. Potrzebowski, X. Assfeld, K. Ganicz, S. Olejniczak, A. Cartier, C. Gardiennet and P. Tekely, *J. Am. Chem. Soc.*, 2003, **125**, 4223–4232.
84. S. J. Kohler and M. P. Klein, *J. Am. Chem. Soc.*, 1977, **99**, 8290–8293.
85. N. Kröger, S. Lorenz, E. Brunner and M. Sumper, *Science*, 2002, **298**, 584–586.
86. A. Wittinghofer and H. Waldmann, *Angew. Chem. Int. Ed.*, 2000, **39**, 4192–4214.
87. M. Geyer, R. Assheuer, C. Klebe, J. Kuhlmann, J. Becker, A. Wittinghofer and H. R. Kalbitzer, *Biochemistry*, 1999, **38**, 11250–11260.
88. M. Spoerner, C. Herrmann, I. R. Vetter, H. R. Kalbitzer and A. Wittinghofer, *Proc. Natl. Acad. Sci. USA*, 2001, **98**, 4944–4949.
89. M. Spoerner, A. Nuehs, P. Ganser, C. Herrmann, A. Wittinghofer and H. R. Kalbitzer, *Biochemistry*, 2005, **44**, 2225–2236.
90. M. Brauer and B. D. Sykes, *Methods in Enzymology*, 1984, **107**, 36–81.
91. P. L. Yeagle, J. Frye and B. S. Eckert, *Biochemistry*, 1990, **29**, 1508–1514.
92. M. Sumper, *Science*, 2002, **295**, 2430–2433.
93. M. Sumper, S. Lorenz and E. Brunner, *Angew. Chem. Int. Ed.*, 2003, **42**, 5192–5195.
94. E. Brunner, K. Lutz and M. Sumper, *PCCP*, 2004, **6**, 854–857.
95. K. Lutz, C. Gröger, M. Sumper and E. Brunner, *PCCP*, 2005, **7**, 2812–2815.
96. E. D. Ingall, P. A. Schroeder and R. A. Berner, *Geochim. Cosmochim. Acta*, 1990, **54**, 2617–2620.
97. A. Veis, J. Anesey and S. Mussell, *Biochemistry*, 1967, **6**, 2409–2416.
98. S. L. Lee, T. Glonek and M. J. Glimcher, *Calcif. Tissue Int.*, 1983, **35**, 815–818.
99. M. J. Glimcher, *Anat. Rec.*, 1989, **224**, 139–153.
100. A. George, B. Sabsay, P. A. L. Simonian and A. Veis, *J. Biol. Chem.*, 1993, **268**, 12624–12630.
101. A. Kaflak-Hachulska, A. Samoson and W. Kolodziejski, *Calcif. Tissue Int.*, 2003, **73**, 476–486.
102. Y. Wu, J. L. Ackerman, E. S. Strawich, C. Rey, H. -M. Kim and M. J. Glimcher, *Calcif. Tissue Int.*, 2003, **72**, 610–626.
103. H. -U. Gally, W. Niederberger and J. Seelig, *Biochemistry*, 1975, **14**, 3647–3652.
104. J. Seelig and H. -U. Gally, *Biochemistry*, 1976, **15**, 5199–5204.
105. R. G. Griffin, L. Powers and P. S. Pershan, *Biochemistry*, 1978, **17**, 2718–2722.
106. J. Seelig, *Biochim. Biophys. Acta*, 1978, **515**, 105–140.
107. P. R. Cullis and B. de Kruijff, *Biochim. Biophys. Acta*, 1979, **559**, 399–420.
108. P. G. Scherer and J. Seelig, *Biochemistry*, 1989, **28**, 7720–7728.
109. S. J. Kohler and M. P. Klein, *Biochemistry*, 1976, **15**, 967–973.
110. H. Hauser, C. Radloff, R. R. Ernst, S. Sundell and I. Pascher, *J. Am. Chem. Soc.*, 1988, **110**, 1054–1058.
111. J. Herzfeld, R. G. Griffin and R. A. Haberkorn, *Biochemistry*, 1978, **17**, 2711–2718.
112. C. R. Sanders II and J. P. Schwonek, *Biochemistry*, 1992, **31**, 8898–8905.
113. M. Hong, K. Schmidt-Rohr and D. Nanz, *Biophys. J.*, 1995, **69**, 1939–1950.
114. B. D. Fenske and H. C. Jarrell, *Biophys. J.*, 1991, **59**, 55–69.
115. F. Lindström, P. T. F. Williamson and G. Gröbner, *J. Am. Chem. Soc.*, 2005, **127**, 6610–6616.
116. T. Byström, G. Gröbner and G. Lindblom, *Colloids Surfaces A: Physicochem. Eng. Aspects*, 2003, **228**, 37–42.
117. T. J. Pinheiro and A. Watts, *Biochemistry*, 1994, **33**, 2459–2467.
118. S. L. Grage, S. Afonin, M. Grune and A. S. Ulrich, *Chem. Phys. Lipids*, 2004, **132**, 65–77.

119. R. Mani, A. J. Waring, R. I. Lehrer and M. Hong, *Biochim. Biophys. Acta*, 2005, **1716**, 11–18.
120. A. J. Mason, J. J. Lopez, M. Beyermann and C. Glaubitz, *Biochim. Biophys. Acta*, 2005, **1714**, 1–10.
121. B. Bechinger, *Biochim. Biophys. Acta*, 2005, **1712**, 101–108.
122. A. J. Mason, A. Martinez, C. Glaubitz, O. Danos, A. Kichler and B. Bechinger, *FASEB J.*, 2006, **20**, 320–322.
123. C. Glaubitz, A. Gröger, K. Gottschalk, P. Spooner, A. Watts, S. Schuldiner and H. Kessler, *FEBS Lett.*, 2000, **480**, 127–131.
124. J. C. Clayton, E. Hughes and D. A. Middleton, *Biochemistry*, 2005, **44**, 17016–17026.
125. C. Glaubitz and A. Watts, *J. Magn. Reson.*, 1998, **130**, 305–316.
126. M. Auger, *Biophys. Chem.*, 1997, **68**, 233–241.
127. M. Auger, *Curr. Issues Mol. Biol.*, 2000, **2**, 119–124.
128. M. Mehring, R. G. Griffin and J. S. Waugh, *J. Chem. Phys.*, 1971, **55**, 746–755.
129. S. Hanlon, T. Glonek and A. Chan, *Biochemistry*, 1976, **15**, 3869–3875.
130. A. Yamada, H. Kaneko, K. Akasaka and H. Hatano, *FEBS Lett.*, 1978, **93**, 16–18.
131. T. Terao, S. Matsui and K. Akasaka, *J. Am. Chem. Soc.*, 1977, **99**, 6136–6138.
132. S. J. Opella, W. B. Wise and J. A. DiVerdi, *Biochemistry*, 1981, **20**, 284–290.
133. H. Shindo, T. Fujiwara, H. Akutsu, U. Matsumoto and Y. Kyogoku, *Biochemistry*, 1985, **24**, 887–895.
134. H. Shindo, J. B. Wooten, B. H. Pheiffer and S. B. Zimmerman, *Biochemistry*, 1980, **19**, 518–526.
135. Z. Song, O. N. Antzutkin, Y. K. Lee, S. C. Shekar, A. Rupprecht and M. H. Levitt, *Biophys. J.*, 1997, **73**, 1539–1552.
136. L. van Dam, N. Korolev and L. Nordenskiöld, *Nucleic Acids Res.*, 2002, **30**, 419–428.
137. M. E. Merritt, S. Th. Sigurdsson and G. P. Drobny, *J. Am. Chem. Soc.*, 1999, **121**, 6070–6071.
138. G. L. Olsen, E. A. Louie, G. P. Drobny and S. Th. Sigurdsson, *Nucl. Acids Res.*, 2003, **31**, 5084–5089.
139. G. L. Olsen, T. E. Edwards, P. Deka, G. Varani, S. Th. Sigurdsson and G. P. Drobny, *Nucl. Acids Res.*, 2005, **33**, 3447–3454.
140. E. A. Louie, P. Chirakul, V. Raghunathan, S. Th. Sigurdsson and G. P. Drobny, *J. Magn. Reson.*, 2006, **178**, 11–24.
141. D. R. Studelska, C. A. Klug, D. D. Beusen, L. M. McDowell and J. Schaefer, *J. Am. Chem. Soc.*, 1996, **118**, 5476–5477.
142. J. A. DiVerdi and S. J. Opella, *Biochemistry*, 1981, **20**, 280–284.
143. P. C. M. M. Magusin and M. A. Hemminga, *Biophys. J.*, 1994, **66**, 1197–1208.
144. H. Eckert, *Prog. Nucl. Magn. Reson. Spectrosc.*, 1992, **24**, 159–293.
145. R. J. Kirkpatrick and R. K. Brow, *Solid State Nucl. Magn. Reson.*, 1995, **5**, 9–21.
146. K. J. D. Mackenzie and M. E. Smith, *Multinuclear Solid-State NMR of Inorganic Materials*, Pergamon – Elsevier Science, Amsterdam, 2002.
147. J. R. van Wazer, *Phosphorus and its Compounds*, Wiley, New York, 1966.
148. F. Fayon, D. Massiot, K. Suzuya and D. L. Price, *J. Non-Cryst. Solids*, 2001, **283**, 88–94.
149. C. A. Click, R. K. Brow and T. M. Alam, *J. Non-Cryst. Solids*, 2002, **311**, 294–303.
150. R. K. Brow, R. J. Kirkpatrick and G. L. Turner, *J. Non-Cryst. Solids*, 1990, **116**, 39–45.
151. T. M. Alam and R. K. Brow, *J. Non-Cryst. Solids*, 1998, **223**, 1–20.
152. J. M. Cole, E. R. H. van Eck, G. Mountjoy, R. Anderson, T. Brennan, G. Bushnell-Wye, R. J. Newport and G. A. Saunders, *J. Phys.: Condens. Matter*, 2001, **13**, 4105–4122.
153. P. Losso, B. Schnabel, C. Jager, U. Sternberg, D. Stachel and D. O. Smith, *J. Non-Cryst. Solids*, 1992, **143**, 265–273.
154. G. Engelhardt and D. Michel, *High-Resolution Solid-State NMR of Silicates and Zeolites*, Wiley, Chichester, 1987.
155. R. M. Wenslow and K. T. Mueller, *J. Phys. Chem. B*, 1998, **102**, 9033–9038.
156. C. Jäger, M. Feike, R. Born and H. W. Spiess, *J. Non-Cryst. Solids*, 1994, **180**, 91–95.
157. A. E. Bennet, J. H. Ok, R. G. Griffin and S. Vega, *J. Chem. Phys.*, 1992, **96**, 8624–8627.
158. K. K. Olsen, J. W. Zwanziger, P. Hartmann and C. Jäger, *J. Non-Cryst. Solids*, 1997, **222**, 199–205.
159. M. Feike, R. Graf, I. Schnell, H. W. Spiess and C. Jäger, *J. Am. Chem. Soc.*, 1996, **118**, 9631–9634.

160. M. Feike, C. Jäger and H. W. Spiess, *J. Non-Cryst. Solids*, 1998, **223**, 200–206.
161. R. Witter, P. Hartmann, J. Vogel and C. Jäger, *Solid State Nucl. Magn. Reson.*, 1998, **13**, 189–200.
162. C. Jäger, P. Hartmann, R. Witter and M. Braun, *J. Non-Cryst. Solids*, 2000, **263**, 61–72.
163. F. Fayon, D. Massiot, M. H. Levitt, J. J. Titman, D. H. Gregory, L. Duma, L. Emsley and S. P. Brown, *J. Chem. Phys.*, 2005, **122** 94313 (1–14).
164. P. Hartmann, J. W. Zwanziger and C. Jäger, *Solid State Nucl. Magn. Reson.*, 2000, **16**, 189–197.
165. F. Fayon, C. Roiland, L. Emsley and D. Massiot, *J. Magn. Reson.*, 2006, **179**, 50–58.
166. H. Eckert, S. Elbers, J. D. Epping, M. Janssen, M. Kalwei, W. Strojek and U. Voigt, *Top. Curr. Chem.*, 2005, **246**, 195–233.
167. D. Lathrop and H. Eckert, *J. Am. Chem. Soc.*, 1989, **111**, 3536–3541.
168. D. Lathrop and H. Eckert, *J. Am. Chem. Soc.*, 1990, **112**, 9017–9019.
169. D. Lathrop and H. Eckert, *Phys. Rev. B*, 1991, **43**, 7279–7287.
170. P. F. Mutolo, M. Witschas, G. Regelsky, J. S. A. D. Guenne and H. Eckert, *J. Non-Cryst. Solids*, 1999, **257**, 63–72.
171. M. Bertmer and H. Eckert, *Solid State Nucl. Magn. Reson.*, 1999, **15**, 139–152.
172. W. Strojek, M. Kalwei and H. Eckert, *J. Phys. Chem. B*, 2004, **108**, 7061–7073.
173. J. C. C. Chan and H. Eckert, *J. Magn. Reson.*, 2000, **147**, 170–178.
174. L. van Wüllen, H. Eckert and G. Schwering, *Chem. Mater.*, 2000, **12**, 1840–1846.
175. J. M. Goetz and J. Schaefer, *J. Magn. Reson.*, 1997, **129**, 222–223.
176. M. Zeyer, L. Montagne and C. Jaeger, *Solid State Nucl. Magn. Reson.*, 2003, **23**, 136–144.
177. U. Voigt, H. Lammert, H. Eckert and A. Heuer, *Phys. Rev. B*, 2005, **72** 064207 (1–11).
178. S. Elbers, W. Strojek, L. Koudelka and H. Eckert, *Solid State Nucl. Magn. Reson.*, 2005, **27**, 65–76.
179. M. Zeyer-Dusterer, L. Montagne, G. Palavit and C. Jäger, *Solid State Nucl. Magn. Reson.*, 2005, **27**, 50–64.
180. C. P. Grey, A. P. Eijkelenboom and W. S. Veeman, *Solid State Nucl. Magn. Reson.*, 1995, **4**, 113–120.
181. T. Gullion, *Chem. Phys. Lett.*, 1995, **246**, 325–330.
182. L. Zhang, C. C. de Araujo and H. Eckert, *Chem. Mater.*, 2005, **17**, 3101–3107.
183. D. P. Lang, T. M. Alam and D. N. Bencoe, *Chem. Mater.*, 2001, **13**, 420–428.
184. T. Schaller, C. Y. Rong, M. J. Toplis and H. Cho, *J. Non-Cryst. Solids*, 1999, **248**, 19–27.
185. S. Prabakar, R. M. Wenslow and K. T. Mueller, *J. Non-Cryst. Solids*, 2000, **263**, 82–93.
186. R. M. Wenslow, K. Fiske and K. T. Mueller, *ACS Symp. Ser.*, 1999, **717**, 228–241.
187. M. E. Davis, *Nature*, 2002, **417**, 813–821.
188. C. S. Cundy and P. A. Cox, *Chem. Rev.*, 2003, **103**, 663–701.
189. C. S. Blackwell and R. L. Patton, *J. Phys. Chem.*, 1984, **88**, 6135–6139.
190. D. Müller, E. Jahn, B. Fahlke, G. Ladwig and U. Haubenreisser, *Zeolites*, 1985, **5**, 53–56.
191. C. S. Blackwell and R. L. Patton, *J. Phys. Chem.*, 1988, **92**, 3965–3970.
192. M. E. Davis, C. Montes, P. E. Hathaway, J. P. Arhancet, D. L. Hasha and J. M. Garces, *J. Am. Chem. Soc.*, 1989, **111**, 3919–3924.
193. P. J. Barrie and J. Klinowski, *J. Phys. Chem.*, 1989, **93**, 5972–5974.
194. J. A. Martens, E. Feijen, J. L. Lievens, P. J. Grobet and P. A. Jacobs, *J. Phys. Chem.*, 1991, **95**, 10025–10031.
195. B. Zibrowius, U. Lohse and J. Richter-Mendau, *J. Chem. Soc. Faraday Trans.*, 1991, **87**, 1433–1437.
196. A. Merrouche, J. Patarin, H. Kessler, M. Solard, L. Delmotte, J. L. Guth and J. F. Joly, *Zeolites*, 1992, **12**, 226–232.
197. B. Zibrowius, M. W. Anderson, W. Schmidt, F. -F. Schüth, A. E. Aliev and K. D. M. Harris, *Zeolites*, 1993, **13**, 607–610.
198. H. Meyer zu Altenschildesche, H. -J. Muhr and R. Nesper, *Microp. Mater.*, 1993, **1**, 257–264.
199. C. A. Fyfe, K. T. Mueller, H. Grondey and K. C. Wong-Moon, *Chem. Phys. Lett.*, 1992, **199**, 198–204.
200. C. A. Fyfe, H. Grondey, K. T. Mueller, K. C. Wong-Moon and T. Markus, *J. Am. Chem. Soc.*, 1992, **114**, 5876–5878.

201. C. A. Fyfe, K. T. Mueller, H. Grondey and K. C. Wong-Moon, *J. Chem. Phys.*, 1993, **97**, 13484–13495.
202. E. R. H. van Eck and W. S. Veeman, *J. Am. Chem. Soc.*, 1993, **115**, 1168–1169.
203. C. A. Fyfe, K. C. Wong-Moon, Y. Huang and H. Grondey, *Microp. Materials*, 1995, **5**, 29–37.
204. C. A. Fyfe, K. C. Wong-Moon and Y. Huang, *Zeolites*, 1996, **16**, 50–55.
205. C. A. Fyfe, H. M. zu Altenschildesche, K. C. Wong-Moon, H. Grondey and J. M. Chezeau, *Solid State Nucl. Magn. Reson.*, 1997, **9**, 97–106.
206. D. H. Brouwer, J. M. Chezeau and C. A. Fyfe, *Microp. Mesop. Mater.*, 2006, **88**, 163–169.
207. F. Taulelle, M. Pruski, J. P. Amoureux, D. Lang, A. Bailly, C. Huguenard, M. Haouas, C. Gerardin, T. Loiseau and G. Ferey, *J. Am. Chem. Soc.*, 1999, **121**, 12148–12153.
208. S. Caldarelli, A. Meden and A. Tuel, *J. Phys. Chem. B*, 1999, **103**, 5477–5487.
209. A. Tuel, S. Caldarelli, A. Meden, L. B. McCusker, C. Baerlocher, A. Ristic, N. Rajic, G. Mali and V. Kaucic, *J. Phys. Chem. B*, 2000, **104**, 5697–5705.
210. M. Roux, C. Marichal, J. L. Paillaud, C. Fernandez, C. Baerlocher and J. M. Chezeau, *J. Phys. Chem. B*, 2001, **105**, 9083–9092.
211. R. D. Gougeon, E. B. Brouwer, P. R. Bodart, L. Delmotte, C. Marichal, J. M. Chezeau and R. K. Harris, *J. Phys. Chem. B*, 2001, **105**, 12249–12256.
212. G. Mali, A. Meden, A. Ristic, N. N. Tusar and V. Kaucic, *J. Phys. Chem. B.*, 2002, **106**, 63–69.
213. C. Fernandez, C. Morais, J. Rocha and M. Pruski, *Solid State Nucl. Magn. Reson.*, 2002, **21**, 61–70.
214. L. Delevoye, C. Fernandez, C. M. Morais, J. P. Amoureux, V. Montouillout and J. Rocha, *Solid State Nucl. Magn. Reson.*, 2002, **22**, 501–512.
215. M. Roux, C. Marichal, J. M. Le Meins, C. Baerlocher and J. M. Chezeau, *Microporous Mesoporous Mater*, 2003, **63**, 163–176.
216. J. W. Wiench and M. Pruski, *Solid State Nucl. Magn. Reson.*, 2004, **26**, 51–55.
217. J. Klinowski, *Anal. Chim. Acta*, 1993, **283**, 929–965.
218. M. Hunger and E. Brunner, *Mol. Sieves*, 2004, **4**, 201–293.
219. D. Müller, E. Jahn, G. Ladwig and U. Haubenreisser, *Chem. Phys. Lett*, 1984, **109**, 332–336.
220. A. W. Hing, S. Vega and J. Schaefer, *J. Magn. Reson.*, 1992, **96**, 205–209.
221. G. A. Morris and R. Freeman, *J. Am. Chem. Soc.*, 1979, **101**, 760–762.
222. Y. N. Huang and D. Machado, *Microp. Mesop. Mater.*, 2001, **47**, 195–202.
223. Y. N. Huang, R. Richer and C. W. Kirby, *J. Phys. Chem. B*, 2003, **107**, 1326–1337.
224. Y. N. Huang, B. A. Demko and C. W. Kirby, *Chem. Mater.*, 2003, **15**, 2437–2444.
225. E. Freudenthaler and A. Pfitzner, *Solid State Ionics*, 1997, **101–103**, 1053–1059.
226. S. Reiser, G. Brunklaus, J. H. Hong, J. C. C. Chan, H. Eckert and A. Pfitzner, *Chem. Eur. J.*, 2002, **8**, 4228–4233.
227. G. Brunklaus, J. C. C. Chan, H. Eckert, S. Reiser, T. Nilges and A. Pfitzner, *PCCP*, 2003, **5**, 3768–3776.
228. M. Engelsberg and R. E. Norberg, *Phys. Rev. B*, 1972, **5**, 3395–3406.
229. N. L. Adolphi, M. S. Conradi and W. E. Buhro, *Chem. Solids*, 1992, **53**, 1073–1074.
230. A. Pfitzner, M. F. Bräu, J. Zweck, G. Brunklaus and H. Eckert, *Angew. Chem. Intl. Ed.*, 2004, **43**, 4228–4231.
231. M. Scheer, L. Gregoriades, J. Bai, M. Sierka, G. Brunklaus and H. Eckert, *Chem. Eur. J.*, 2005, **11**, 2163–2169.

Applications of REDOR for Distance Measurements in Biological Solids

STEPHAN L. GRAGE[1] AND ANTHONY WATTS[2]

[1]*Institut für Biologische Grenzflächen, Forschungszentrum Karlsruhe, Hermann-von-Helmholtz-Platz 1, 76344 Eggenstein-Leopoldshafen, Germany*
[2]*Department of Biochemistry, University of Oxford, South Parks Road, Oxford OX1 3QU, UK*

Abstract

Knowledge of structural details at an atomic level is important in understanding the function and molecular properties of biomolecules. In situations where crystallography or solution state NMR methods are not applicable, solid state NMR can provide valuable insight without the limitations imposed by the availability of crystals, solubility or molecular weight. In particular dedicated solid state NMR methods enable the determination of selective internuclear distances at high accuracy. A popular and robust technique is rotational echo double resonance (REDOR), which allows the measurement of distances of heteronuclear spin pairs. This magic angle spinning method uses radiofrequency pulses to prevent the dipole-dipole interaction from being averaged by the sample spinning, leading to a

ANNUAL REPORTS ON NMR SPECTROSCOPY
VOLUME 60 ISSN 0066 4103
DOI 10.1016/S0066-4103(06)60005-7

reduction of the NMR signal which depends on the internuclear distance. Biological systems constitute a major area of application of the REDOR experiment, and are the focus of this review. First, the theoretical background, developments and experimental considerations of REDOR are discussed, regarding in particular applications on biological samples. Then, an overview of the use of REDOR in a wide range of biological applications, such as ligand binding sites of enzymes, fibrilar proteins, membrane active peptides, transmembrane helices, biomaterials like the peptidoglycan of bacterial cell walls or nucleic acids, is presented.

1. INTRODUCTION

Solid-state nuclear magnetic resonance (NMR) has become a valuable alternative in the study of biological macromolecules in situations where the routine methods of X-ray crystallography or NMR in solution are challenged. Both, X-ray crystallography and solution-state NMR are powerful established tools in structural biology, but are also limited in their applicability. X-ray crystallography relies on the availability of high-quality crystals of the studied biomolecules, and solution-state NMR requires sufficient tumbling rates in solution to achieve the necessary high resolution. Thus, systems such as membrane proteins or membrane-bound peptides, high molecular weight enzyme complexes or fibrillar systems are difficult to tackle by X-ray or solution NMR. Solid-state NMR, in contrast, is in principle not confined by these limitations and has found applications in challenging biological systems.

In solid-state NMR, in contrast to solution-state NMR, anisotropic interactions such as dipole–dipole couplings or chemical shift anisotropies are used as a source of structural information. Different to most solution-state NMR applications, anisotropies and dipole–dipole couplings are not or only partially averaged by molecular tumbling. This way, their orientation and distance dependence can be used for the determination of structural parameters such as internuclear distances, however at the expense of line broadening and hence of resolution and sensitivity. To recover the lost high resolution and sensitivity, the averaging effect of tumbling in solution is imitated by sample spinning at the magic angle (magic-angle spinning, MAS). If combined with suitable manipulation of the spins by radiofrequncy (RF) pulses, the averaging caused by MAS can be prevented for certain interactions. By choosing an appropriate rotor synchronized pulse scheme, it is then possible to prevent selectively only the desired interaction from being averaged, while all other interactions are suppressed. Pulse sequences have been introduced this way for the measurement of chemical shift anisotropy, and of dipole–dipole couplings, which are directly related to internuclear distances.

Methods to determine distances from solid-state NMR can be classified into homo- and heteronuclear experiments, depending on the measurement of dipole–dipole couplings of like or unlike isotopes, respectively. The most prominent among heteronuclear techniques is the experiment reviewed here, rotational echo double resonance (REDOR). It has proven in many applications to be a robust and reliable

technique for the measurement of long-range distances of more than 10 Å, at high accuracies even below tenths of Ångstroms. The REDOR experiment has been invented by Terry Gullion and Jacob Schaefer in 1989,[1] and already early on biological applications have been a major focus of this method. In particular, in the laboratory of Jacob Schaefer, challenging biological questions, such as the conformation of bound inhibitors or the structure of biopolymers, have been solved by REDOR distance measurements. Today REDOR belongs to one of the most often used pulse sequences for distance measurements and has reached many biological areas and all classes of biopolymers ranging from antimicrobial peptides and membrane proteins, amyloid fibrils, silk fibres to DNA and the peptidoglycan in cell walls.

In this review, we first give an overview of the theoretical background of the REDOR experiment, followed by experimental considerations and recent methodological developments, which are important in biological applications. Different applications of REDOR distance measurements in biology then constitute the major focus.

2. THEORETICAL BACKGROUND

Dipole–dipole couplings between the magnetic moments of neighbouring spins constitute the basis of distance measurements by solid-state NMR. The strength of the dipolar coupling

$$d_{kl} = \frac{\mu_0}{4\pi}\frac{\gamma_I\gamma_S h}{(2\pi)^2 r_{kl}^3}\frac{1}{2}(3\cos^2\theta_{kl} - 1)$$

depends on the distance and orientation of the internuclear vector. If the orientation is known or all orientations are present as in most "powder" samples, the coupling strength is described by the orientation-independent part of d_{kl}:

$$D_{kl} = \frac{\mu_0}{4\pi}\frac{\gamma_I\gamma_S h}{(2\pi)^2 r_{kl}^3}$$

Since all other factors, the gyromagnetic ratios of the coupling spins γ_I and γ_S are known, the internuclear distance can be deduced directly from the coupling strength. The dipolar coupling can be measured through the evolution of the spin system caused by the underlying dipolar coupling Hamiltonian H_{IS}. For a heteronuclear spin pair, H_{IS} in the high-temperature approximation is given by

$$H_{IS} = -\sum_{k<l} 2\pi d_{kl} 2I_{z,k}S_{z,l}$$

where I and S are the spin operators of the coupling spins, for an ensemble of spins the individual Hamiltonians add to yield the total heteronuclear dipolar Hamiltonian.

One way of determining the dipolar coupling would be to extract the involved frequency splittings from an NMR spectrum, however, this is usually obscured by

the presence of further interactions, such as chemical shift and homonuclear couplings, and the resulting line broadening makes it difficult to measure weak couplings or long distances. Instead, MAS techniques are often used to selectively average contributions from unwanted interactions, and leaving the interaction of interest. By sample spinning, the orientation-dependent factors of NMR interactions, such as the dipolar coupling strength d_{kl}, become time-dependent

$$d_{kl}(t) = D_{kl}\frac{1}{2}\left(\sin^2\beta_{kl}\cos\ 2\left(\alpha_{kl}+\frac{2\pi t}{T_R}\right)-\sqrt{2}\sin\ 2\beta_{kl}\ \cos\left(\alpha_{kl}+\frac{2\pi t}{T_R}\right)\right)$$

If spinning fast enough, only the time averages of the interactions are relevant to the spin system evolution. For the dipolar interaction, this average, which results as the time integral of $d_{kl}(t)$, vanishes over each rotor period and hence the dipolar coupling is not affecting the NMR signal (see Fig. 1). This way, on average, deleterious broadening effects of the anisotropies of NMR interactions are removed, but at the expense of loosing all structural information provided through the dipolar couplings as well. However, besides averaging by sample spinning, radiofrequency (RF) pulses provide another means to influence the contributions to the NMR signal. A π-pulse irradiated at either the *I*- or *S*-spin resonance frequency will invert the I or S spins, respectively, and can hence be used to manipulate the evolution of the spin system. Inverting either I or S spin is equivalent to an evolution under a Hamiltonian H_{IS}, but now with inverted sign ($I>-I$ or $S>-S$). Hence, the average over each rotor period is no longer zero (Fig. 1), and the spin system is experiencing the ''recoupled'' heteronuclear dipolar coupling.

The REDOR experiment uses a series of such π-pulses, spaced every half-rotor cycle of a ''dephasing'' time, to recouple the heteronuclear dipolar interaction (Fig. 4). The signal which is ''dephased'' by the heteronuclear couplings is then

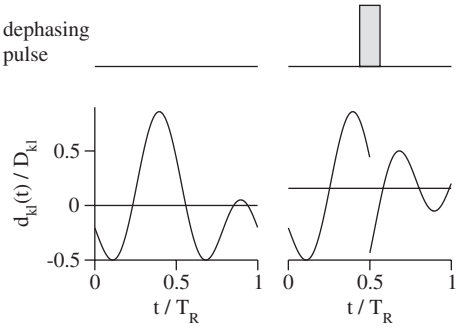

Fig. 1. Because of its orientation dependence, magic-angle sample spinning renders the dipolar coupling time-dependent (left). However, averaged over a full rotor cycle the dipolar interaction vanishes (average denoted with a straight line). With the aid of radiofrequency (RF) pulses effecting one of the two coupled spins, the sign of the dipolar interaction can be inverted (right). This way, MAS is no longer averaging the dipolar coupling to zero, but a finite average (denoted by a straight line) remains.

measured after this period. To separate the influence of the dipolar coupling from the influence of relaxation on the NMR signal, two experiments are usually performed. In one, the dephasing pulses are switched on, and a reduced signal S is obtained, in the second, they are switched off and the full signal S_0 is measured. As relaxation is contributing to both signals equally, the ratio $(S_0-S)/S_0$ is free of these relaxation effects. The signal amplitude results from the acquired phase during evolution under the heteronuclear dipolar interaction H_{IS} for half a rotor period, followed by half a rotor period under $-H_{IS}$, where the inverted sign is due to the RF pulse every half-rotor cycle. As a consequence of this sign change, a non-zero average Hamiltonian H_{IS} and average dipolar coupling d result

$$\overline{H_{IS}} = -\frac{2\pi}{T_R}\sum_{k<l}\left(\int_0^{T_R/2} d_{kl}(t)2I_{z,k}S_{z,l}\,\mathrm{d}t - \int_{T_R/2}^{T_R} d_{kl}(t)2I_{z,k}S_{z,l}\,\mathrm{d}t\right) = -2\pi\sum_{k<l}\overline{d_{kl}}2I_{z,k}S_{z,l}$$

with

$$\overline{d_{kl}} = D_{kl}2\sqrt{2}\sin\ 2\beta_{kl}\sin\ \alpha_{kl}$$

For two spins $I=\frac{1}{2}$ and $S=\frac{1}{2}$ (for spins $>\frac{1}{2}$ see below), the signal $(S_0-S)/S_0$ after N rotor cycles T_R is then

$$\frac{\Delta S}{S_0} = 1 - \sum_{k<l}\frac{1}{4\pi}\int_0^{2\pi}\int_0^{\pi}\cos(NT_R D_{kl}2\sqrt{2}\sin\ 2\beta_{kl}\sin\ \alpha_{kl})\sin\ \beta_{kl}\,\mathrm{d}\alpha_{kl}\,\mathrm{d}\beta_{kl}$$

To determine the dipolar coupling, a series of REDOR experiments with different dephasing times NT_R is performed. This way, a "REDOR-curve" of $(S_0(NT_R)$-$S(NT_R))/S_0(NT_R)$ as a function of dephasing time NT_R is obtained, and the value of the dipolar coupling or corresponding internuclear distance can be evaluated by fitting with theoretical curves. The REDOR-curve depends only on the product of dephasing time and the orientation-independent part of the dipolar coupling D_{kl}. Hence, if considering $(S_0-S)/S_0$ as a function of $D_{kl}NT_R$, a "universal" REDOR-curve is obtained (Fig. 2). Experimental curves can thus be fitted by scaling a single universal function along the ordinate axis, at least in the ideal case of an isolated pair of two spins $\frac{1}{2}$. Deviations from this universal REDOR-curve arise, if e.g. spins other than spin-$\frac{1}{2}$ are involved (see Fig. 2 for the REDOR dephasing caused by spin-1 nuclei), or strong homonuclear couplings have to be considered (see below). An alternative way of determining the dipolar coupling, in particular if the sample consists of spin pairs with different internuclear distances, was presented by Mueller *et al.*[2] With the aid of a REDOR-transform, a spectrum of dipolar couplings can be determined from the time-domain data in a similar fashion as in the Fourier transform.

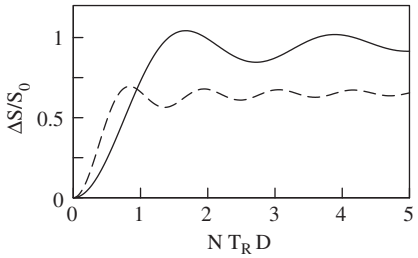

Fig. 2. The dephased signal follows a universal function of the product of the time NT_R, during which RF pulses are applied, and the dipolar coupling constant D. The REDOR curve depends on the spin of the dephasing nucleus. The dephased signal $(S_0\text{-}S)/S_0$ approaches 1 for long dephasing times if the observed spin is coupled to a spin-$\frac{1}{2}$ nucleus (solid line). The dephasing by a spin-1 nucleus is twice as fast and reaches only $\frac{2}{3}$ (dashed line). (Other parameters, such as the pulse sequence or couplings in a spin network also influence the dephasing behaviour.)

3. EXPERIMENTAL CONSIDERATIONS AND METHODOLOGICAL DEVELOPMENTS

3.1. REDOR on biological samples

REDOR has become particularly successful in biological questions which can be addressed by a few, specific distance measurements. This makes REDOR an attractive method in situations where a broad analysis of a large number of constraints is not feasible. Such situations are encountered frequently in biological systems where low amounts of labelled sample material and low signal/noise are mostly the limiting factor. But often, solving an entire structure is not required, and concentrating on an important detail, such as the structure of a binding site of a protein, is enough for a functional understanding. Requiring far viewer increments than in a two-dimensional experiment, and due to its nature as a difference technique, REDOR is a robust technique ideally suited for these situations.

Otherwise, samples, which can be addressed by REDOR, are not restricted in solubility, in size or crystallizability, like in solution-state NMR or crystallography. This way, fibrillar samples, proteins in the form of polycrystalline precipitates, or membrane proteins and membrane-active peptides in the native membrane environment have been investigated.

A limitation for the determination of accurate distances, however, is the molecular mobility inherent to many biological systems, often classified as ''soft matter''. Local motion of labelled side chains or the molecules as a whole can influence the results in several ways. On the one hand, if motions exceed the timescale given by the dipolar interaction frequencies, only averaged distances are accessible. On the other, motions on the time scale of MAS can cause deleterious interference of the two processes and loss in signal.[3–5] Experimentally, the detection of the reduced dipolar couplings in the presence of motion is often challenging or even impossible due to difficulties in maintaining the echo train over the required long dephasing

times. In a number of cases, biological samples are rigid on the relevant time scales, and motional averaging or interference processes do not have to be considered. This way, silk or amyloid fibrils have been the subject of successful REDOR distance measurements. In other cases, such as membrane proteins or membrane-active peptides, molecular mobility has to be considered. One way, which is often pursued in such cases, is the study of frozen samples at temperatures in the range of $-20^{\circ}C$ to $-100^{\circ}C$, where cryoprotectants such as trehalose were often used to preserve structural integrity. Studies of ligands in the binding site of membrane receptors have been performed this way,[6] as well as the interaction of peptide antibiotics with the membrane.[7,8] Keeping the sample in a frozen state often serves a further purpose. In particular, the active state of larger proteins is often only short lived, and freezing can preserve the protein in its functionally relevant state. Furthermore, freezing constitutes a way of trapping intermediate, such as photointermediates of bacteriorhodopsin for NMR studies.[9–11] Nevertheless, freezing always bears the risk of changing the system under study from its natural conditions. In particular for smaller molecules, where dynamical behaviour might be an intrinsic ingredient of their function, immobilization might obscure aspects of the issues addressed by the distance measurement. Also, oligomeric assemblies, e.g. as recently postulated for antimicrobial peptides, might not persist in their biologically relevant form during freezing.

3.2. Orientational information from REDOR

Although REDOR is associated with the measurement of internuclear distances, it has also been employed to obtain orientational constraints. Such information can be inherent in REDOR spectra in several ways. A first possibility to extract relative orientations is through evaluation of the spinning sidebands. If spinning at slow enough rotation speed such that anisotropies of chemical shift or quadrupolar interactions are not entirely averaged, the resulting spinning sidebands will experience different levels of dephasing. As analysed by e.g. O'Connor and Schaefer[12] and Goetz and Schaefer,[13] the differences in dephasing of the individual sidebands depends on the relative orientation of the chemical shift anisotropy or quadrupolar interaction, responsible for the spinning sidebands, and the interconnecting vector of the two coupling nuclei. Intuitively this might be explained as follows. The orientations are contributing to the sidebands in different amounts. Since orientation of chemical shift anisotropy (or quadrupolar interaction) and dipolar vector are related in the molecular context and the dipolar coupling at each point in time is orientation-dependent, the coupling is also effecting the sidebands differently. The relative orientation dependence has been explored to describe the alignment of chemical shift anisotropies in the peptide bond and nucleic acids with respect to their molecular frame.[14–18] Orientational information from spinning sidebands was also complementing distance constraints in various REDOR applications. For example, the relative positioning of peptides in oligomeric assemblies could be described this way,[8] and the possible positions of an ^{19}F-labelled antibiotic with

relative to a CD_3-group incorporated into bacterial cell walls could be further restricted on the basis of the differential dephasing of ^{2}H-spectrum sidebands in $^2H\{^{19}F\}$ REDOR.[19]

Another way orientations are entering REDOR dephasing is through motional averaging. In systems like membrane spanning peptides, molecular motions lead to an averaging of the dipolar interaction tensors. The size of the resulting averaged effective dipolar coupling strength depends then on the averaging geometry. This way, the orientation of peptide backbone segments in Gramicidin A could be related to the axis of the molecular reorientational motions of the peptide around the membrane normal.[20,21]

Apart from techniques employing MAS, another solid-state NMR strategy has been successful with, in particular, membrane proteins and peptides. These systems can be uniaxially oriented with the help of mechanically aligned membrane samples, and segmental orientations become accessible through the orientation dependence of the NMR interactions. By combining MAS with oriented samples in magic angle-oriented sample spinning (MAOSS), the advantages of sample spinning, such as high resolution and sensitivity were combined with the orientational information available from aligned samples.[22] In this fashion REDOR measurements were performed on oriented samples, this way using not only the distance, but also the orientation dependence of the dipolar coupling.[23] Using this approach, the tilt angle of the transmembrane protein phospholamban was determined as a biological application[24] (see Fig. 3).

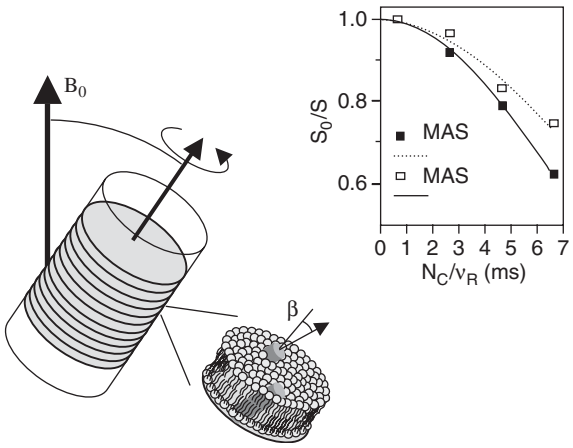

Fig. 3. Spinning oriented samples in magic-oriented sample spinning (MAOSS) provides an opportunity to address the alignment of the internuclear vector with respect to the sample axis. This way, the orientation of biomolecules in aligned membranes can be determined by REDOR measurements, using the orientation dependence of the dipolar interaction. The example REDOR curves compare the different dephasing of an oriented (MAOSS) and powder (MAS) sample of the transmembrane segment of phospholamban in lipid membranes. A peptide tilt angle with respect to the sample normal of 25° was determined here on the basis of $^{13}C\{^{15}N\}$ REDOR under MAOSS. (Figure adapted from Ref. 24.)

3.3. Pulse sequences

The REDOR pulse sequence (Fig. 4) as it was invented by Terry Gullion and Jacob Schaefer in 1989[1] starts with a cross polarization from abundant proton spins to the observed spins, or with a $\pi/2$–pulse excitation irradiated at the resonance frequency of the spin species to be observed (e.g. the I spins). A train of π-pulses at the resonance frequency of the not-observed spins (S spins), placed after every half-rotor period, then causes the interference with the averaging processes of MAS, and "dephases" the observed signal if a I–S dipolar coupling is present. As mentioned above, two data sets are obtained, with and without dephasing pulses, to separate out the contribution of relaxation to the reduction of the signal during the dephasing time. The dephasing pulse in the centre is omitted and replaced by a refocusing π-pulse on the I-spin channel. This additional pulse on the observe channel assures that the isotropic chemical shift is refocused at the end of the dephasing period. In parallel to the pulses on the I and S channel, ^{1}H-decoupling is applied during the dephasing and acquisition time of most biological REDOR experiments to reduce linewidth and enhance signal/noise.

Important in particular for the measurement of large distances, hence small dipolar couplings, is the extension of the REDOR experiment to long dephasing times. To this aim, REDOR pulse sequences have been improved to avoid signal

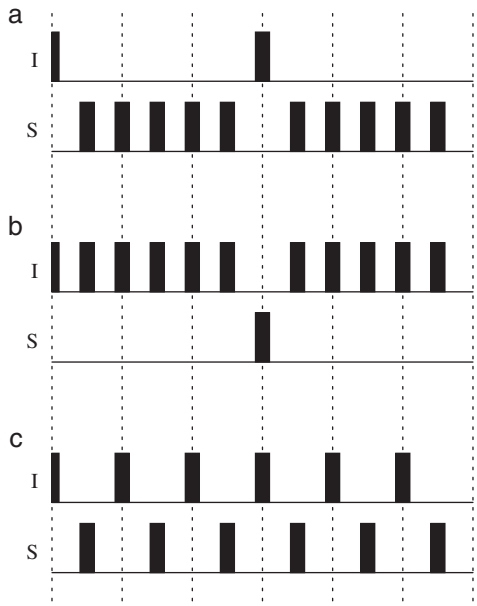

Fig. 4. The REDOR pulse sequence can be implemented in different ways, depending on the experimental requirements imposed by the available hardware or NMR properties of the two involved nuclei. The RF pulses can be distributed mainly on the dephasing channel (a), on the observed channel (b), or in an alternating fashion (c).

loss or incomplete dephasing due to pulse imperfections or resonance offsets effects. In particular in long-pulse trains, an as such small error of a single dephasing pulse can accumulate to a no longer negligible error. Such causes of signal reduction or incomplete dephasing can be kept to a minimum, e.g. using phase cycling. By altering the phase of every pulse of the dephasing pulse train in a particular pattern such as "xy8" or "xy16", the effects of a misadjusted pulse angle cancel each other within a cycle and do not build up.[25] Recently, also replacing the π-pulses by composite pulses as well as EXORCYCLE phase cycling of the single observe refocusing pulse were used to compensate for pulse imperfections.[26] The effect of finite pulse lengths themselves in contrast, which in particular at fast spinning rates can cover a considerable portion of the dephasing pulse train, were found to be not severe.[27,28] Resonance offset presents another potential cause for incomplete dephasing. In particular, large chemical shift anisotropies or quadrupolar interactions often render the original REDOR experiment insufficient. To broaden the frequency bandwidth of the REDOR dephasing, the use of composite pulses or adiabatic inversion pulses as dephasing pulses has proven successful.[26,29–32]

Furthermore, the dephasing pulses are not restricted to the *S* channel, but can be applied on both channels in an alternating fashion, or even almost entirely on the observed channel. It is thus possible to adapt the pulse sequence to sample or hardware-specific circumstances, and for example apply most of the pulses on the channel with the better inversion efficiency.

Since the invention of the REDOR pulse scheme, a large number of derivatives have been derived for the measurement of heteronuclear distances. For example, instead of discrete RF pulses, continuous irradiation with "simultaneous frequency and amplitude modulation" (SFAM) has been used to achieve the dephasing.[33] Following symmetry-based pulse schemes developed by Molcom Levitt, further ways of reintroducing heteronuclear dipolar couplings, termed C-REDOR were introduced.[34] Moreover, REDOR has also been used to transfer coherence in transferred echo double resonance (TEDOR).[35]

3.4. Isotope labels used for distance measurements in biological systems

Although biological materials contain isotopes at high natural abundance, such as ^{1}H, ^{31}P or ^{14}N, most applications of REDOR distance measurements in biological solids rely on selective isotope labelling with rare isotopes. For example, in applications of proteins or peptides, ^{13}C and ^{15}N is the most frequently used heteronuclear pair for REDOR experiments. Both have spin-$\frac{1}{2}$ and can be placed in strategic positions in the peptide backbone without interfering chemically. With a distance range of approximately 5 Å, they cover distances typically encountered in α-helices or β-sheets, and are used for example to evaluate the local secondary structure. This way, ^{13}C–^{15}N distance measurements have become a standard application of REDOR in biology in numerous examples. If present, such as in nucleic acids, but also in phospholipid membrane systems, the 100% natural-abundance nucleus ^{31}P offers an attractive opportunity for distance measurements. Its

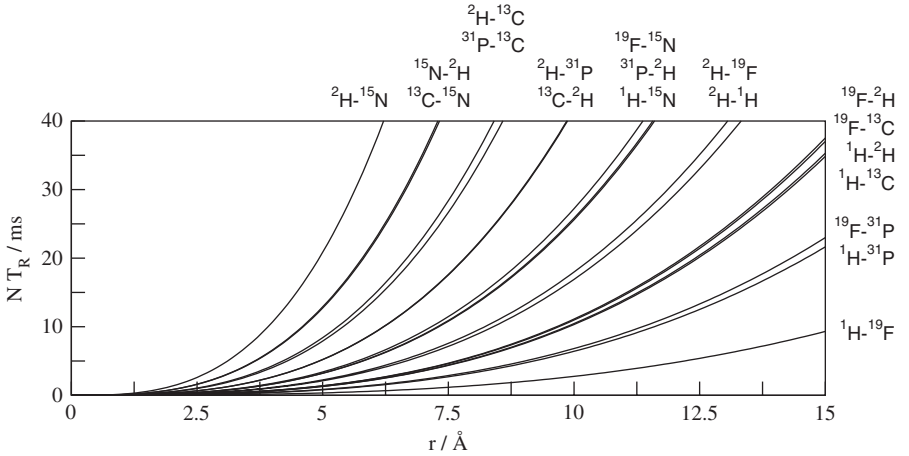

Fig. 5. The distance range accessible in a REDOR experiments depends on the gyromagnetic ratio and spin of the coupled nuclei. (Other parameters, such as coupling of multiple spins, pulse sequence or molecular motions also affect the distance range.) The dephasing time needed to achieve a dephasing $(S_0\text{-}S)/S_0$ of 10% is plotted as a function of the internuclear distance for spin-pairs typically used in biological applications. (For dephasing by ^{2}H the different dephasing of a spin-1 nucleus was assumed. Here, the REDOR signal depends on whether ^{2}H is observed or used as dephasing nucleus. The first nucleus corresponds to the observed spin, and the pairs are ordered from left to right and top to bottom with increasing distance range.)

relatively high gyromagnetic ratio (about 60% larger than e.g. ^{13}C) result in comparatively strong couplings, and have enabled applications such as positioning membrane-active peptides in membranes or drugs in DNA or RNA fragments.[7,8,36–40] Also phosphate derivatives such as nucleotides or phosphorylated metabolites are involved in many biological processes, and are thus often found as enzyme substrates. Here, REDOR experiments involving ^{31}P were often used to characterize ^{31}P containing substrates or inhibitor analogues in their binding sites.[41–50]

The distance ranges accessible with labels typically used in biological solid-state NMR are summarized in Fig. 5.

3.4.1. *^{19}F*

Despite its absence in almost all biological materials, fluorine has been found in frequent use particularly in biological applications of REDOR. Since the fluorine atom is only about 20% larger than hydrogen, it can be introduced into biological molecules as a substitution for hydrogen. Even though its different physicochemical properties, such as a high electronegativity, have to be taken into account, the spectroscopic advantages often outweigh the chemical modification of the molecule under study. Two advantages are benefiting the REDOR experiment here. The gyromagnetic ratio of ^{19}F is only 6% lower than ^{1}H, yielding strong dipolar

couplings and hence a long distance range, and due to 100% natural abundance no background signal has to be considered. This way, distances between ^{31}P and ^{19}F of 13–14 Å were reported in REDOR measurements of nucleic acids.[37,38]

Fluorine has been incorporated in peptides and proteins using fluorine-labelled amino acids in chemical peptide synthesis or even in biosynthesis. Furthermore, ^{19}F-labels have been introduced into the ribose of nucleic acids, such as DNA or RNA. There are also situations where fluorine constitutes an integral part of the studied biological system. In the design of drugs, fluorine is frequently used to adjust the binding and physical properties of pharmaceutical compounds, and this way ^{19}F labels can be placed right at the site of protein activity.[6,19,36,47,51–55]

Often the specialized hardware needed to achieve simultaneous ^{19}F-pulses and ^{1}H decoupling can be demanding due to the proximity of ^{19}F and ^{1}H carrier frequencies. To this aim, a strategy has been presented, which can relax these hardware requirements in suitable situations.[29] With ^{2}H as observed nucleus, often measurements are possible without ^{1}H decoupling and the ^{1}H channel can be tuned to ^{19}F.

3.4.2. *^{1}H*

In principle, ^{1}H should provide an even larger distance range than ^{19}F, and can be an advantageous partner in distance measurements. However, the large abundance in biological materials and homonuclear ^{1}H–^{1}H coupling network which result in low ^{1}H resolution have for a long time limited the use of ^{1}H in REDOR distance measurements. Recently, Mei Hong and Klaus Schmidt-Rohr have presented a way of enabling REDOR experiments with protons. Detecting ^{1}H not directly, but, after cross polarization from ^{1}H to e.g. ^{15}N, via a close label of a dilute spin, a specific ^{1}H was selected. Dephasing of the indirectly detected ^{1}H signal by a further label has allowed the measurement of its distance to the selected ^{1}H. Using this approach, backbone and side chain torsion angles in peptides were determined by measuring ^{15}N-detected distance between the amide ^{1}H and carbonyl ^{13}C, and ^{13}Cβ-detected distance between Hβ and ^{15}N.[56] Recently, even the determination of ^{19}F–^{1}H couplings, thus addressing the theoretically largest distance range possible with REDOR, became possible.[57] ^{1}H–X dipolar interactions were also addressed in the fast MAS techniques employing REDOR principles developed by Kay Saalwächter *et al.*[58–60] Based on the decoupling of the homonuclear ^{1}H dipolar couplings achieved using high-speed MAS at spinning rates larger than ~30 kHz, the characterization of ^{1}H–X local heteronuclear coupling networks, e.g. within methylene or methyl segments became possible with REDOR-like sequences.

3.4.3. *Quadrupolar nuclei*

Spin-$\frac{1}{2}$ nuclei are usually preferred in REDOR measurements, since the large frequency spread associated with the quadrupolar interaction of nuclei with a spin $>\frac{1}{2}$ imposes often a limitation for REDOR experiment with quadrupolar nuclei. However, also quadrupolar nuclei such as ^{2}H or ^{14}N open interesting labelling

strategies in biological samples, as in particular the substitution of ^{1}H by ^{2}H has been established for a long time in organic molecules. Using various types of composite pulses or adiabatic passage, the difficulties imposed by the quadrupolar interaction could be addressed. With techniques such as PM5-REDOR or REAPDOR, distances between e.g. ^{13}C and ^{2}H or ^{15}N and ^{2}H were measured using ^{2}H as the dephasing nucleus.[31,32,61–63] For example, backbone torsion angles in silk were addressed by substituting Hα and determination of its distance to the adjacent carbonyl ^{13}C or Cβ ^{13}C.[63] An interesting application also presents the combined use of ^{15}N–^{2}H and ^{13}C–^{2}H distances for the measurement of torsion angle measurements.[31] The use of deuterium has not been restricted to the dephasing partner in distance measurements. ^{2}H-observed and ^{19}F-dephased REDOR measurements have been employed to study the interaction of an ^{19}F-labelled antibiotic with ^{2}H-labelled cell walls of *Staphylococcus aureus*,[19] and of the conformation of an ^{2}H- and ^{19}F-labelled inhibitor of the gastric H^{+}/K^{+}-ATPase.[29]

Owing to its near 100% natural abundance ^{14}N would as well present an attractive target for REDOR measurements. However, the low distance range and large quadrupolar coupling constant of ^{14}N has led to only few applications of distance measurements with ^{14}N. In particular, the REAPDOR approach has been successful with ^{13}C–^{14}N distance measurements.[62,64,65]

A nucleus with a large potential in biological applications is also ^{17}O. Oxygen has a high abundance in biological molecules, and is involved in structurally important sites such as hydrogen bonds. Distance measurements would thus open up opportunities to probe fundamental structural elements such as the protein secondary structure. The feasibility of ^{17}O distance measurements has been explored in, e.g. ^{13}C–^{17}O REAPDOR experiments.[66]

Noteworthy is that the dephasing by a nucleus with spin $>\frac{1}{2}$ results in a different REDOR dephasing behaviour than for two spin-$\frac{1}{2}$ nuclei.[32] For example, using π-pulses for dephasing of spin-1 nuclei only $\frac{2}{3}$ of the spins contribute to dephasing, and the decay is twice faster than for two spins $\frac{1}{2}$ (see Fig. 2).[67,68]

3.5. Multiple labels

Often labelling schemes in REDOR experiments deviate from the idealized situation of isolated equidistant spin pairs. Multiple spin situations can be unavoidable depending on the label or labelling technique used. If e.g. ^{13}C or ^{15}N labels are introduced uniformly or only amino acid specifically through biosynthesis, or natural abundance ^{31}P in DNA or phospholipids is used, the observed or dephased spin might be coupled to a group of spins rather than to a single spin. In such cases, the analysis of the REDOR data gets often more involved, and homonuclear couplings within the spin can compromise the performance of the REDOR experiment. Using a coupling network, however, can also be beneficial in elucidating molecular structures. For example, the position of a protein ligand in its binding pocket can be pinned down by multiple distance constraints.

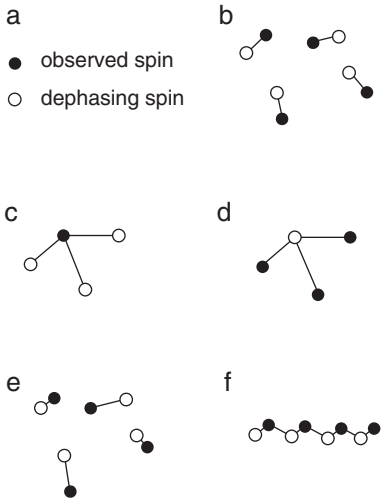

Fig. 6. The coupling network of observed and dephasing spins (a) has to be considered in the interpretation of REDOR results. Isolated, identical spin pairs lead to the ideal REDOR dephasing curve (b). Often, the observed spin is dephased by several spins (c) or a single spin dephases several sites (d). With isolated spin pairs, heterogeneity can lead to a distribution of distances (e). In molecules which are built of repetitive units, the couplings of within each unit might be influenced by couplings between neighbouring units.

Several multiple spin situations can be distinguished (see Fig. 6):[69]

- A single observed spin can be dephased by a group of several spins. This situation was for example encountered in studies of the interaction of antimicrobial peptides with lipid membranes, such as the antibiotic K3. Here, REDOR measurements of the coupling between labels in the peptide and the ^{31}P of the lipid membrane[7,8] were used to locate the peptide in the membrane. Multiple dephasing can also give clues about substrate binding to proteins or DNA. For example, the dephasing by ^{15}N in amino acid side chains was used to locate substrate intermediates bound to 5-enolpyruvylshikimate-3-phosphate (EPSP) synthase.[46–48]
- A single spin can be responsible for the dephasing of several observed spins. This situation was, for example, used in the ^{31}P{^{19}F} REDOR study of ligand binding to a DNA quadruplex.[36]
- The assumption of equidistant spin pairs might not hold if, for example, the sample possesses structural heterogeneity. This situation occurs e.g. if several conformations of a molecule or a residue are present, like peptides which are able to adopt different folds (see, e.g. Ref. 70).
- A further multiple spin situation is encountered if spin pairs are used in the REDOR experiment, which are not isolated and form a coupling network. For example, a chain-like arrangement of spins was found in the study of amyloid fibrils using uniformly ^{13}C- and ^{15}N-labelled glutamine. In the fibrils ^{13}C–^{15}N

couplings between different glutamine side chains are present as well as couplings within the same side chain.[71]

Different issues have to be considered in multi-spin situations. At first, if several spins are responsible for the dephasing of the signal, the resulting REDOR curve is not necessarily a mere sum of the individual dephasing contributions. The way the different spins contribute to the REDOR decay has been discussed in detail by Goetz and Schaefer.[69]

Homonuclear couplings as well as scalar couplings among the observed spins are of particular concern in multiple spin systems, and can compromise a quantitative analysis or cause additional signal decay. In principle, homonuclear couplings should be averaged to zero by MAS. However, commonly used spinning speeds of 5–10 kHz do often not completely remove typical homonuclear dipolar couplings like e.g. the coupling of directly bonded ^{13}C nuclei of ~2 kHz, and scalar couplings which can be of the order of 100 Hz for directly bonded ^{13}C are not affected by MAS at all. Also, homonuclear couplings can be partially reintroduced if the chemical shift separation is close to the spinning frequency. Different approaches have been developed to suppress the influence of homonuclear couplings in REDOR experiments. A straightforward solution is the use of fast MAS (~30 kHz), provided the sample allows fast spinning and the considerably smaller sample amounts are not restricting signal/noise. Another alternative for the suppression of homonuclear couplings within an observed ^{13}C spin cluster has been suggested by Schaefer.[72] Using an MREV8 pulse scheme on the observed ^{13}C channel in combination with the REDOR dephasing pulse train, the ^{13}C couplings could be decoupled during the dephasing time. By using frequency-selective pulses, a "*J*-decoupled" REDOR has been achieved.[73] Here, the central pulse of the observe channel was replaced by a frequency-selective pulse, and this way only one partner of a homonuclear coupling pair is flipped causing then a refocusing of this interaction at the end of the dephasing time.

For the case where weak inter-molecular couplings were obscured by strong intra-molecular couplings, a DSQ–REDOR experiment has been developed in which "double single-quantum" coherences between strongly coupled intra-residue ^{13}C–^{15}N pairs are created and subject to dephasing by a REDOR pulse train, having only the weak ^{13}C–^{15}N inter-residue couplings of interest to evolve.[71]

Interesting multiple spin systems are derivatives of the methyl group, such as CF_3-groups (Fig. 7). Here the fast methyl rotation renders the chemical shifts and dipolar couplings involving the three ^{19}F nuclei identical, and the intra-CF_3-group ^{19}F couplings are no longer influencing the dephasing by the CF_3-group. As discussed in detail by Louie *et al.*[74] or Kim *et al.*,[75] for long distances between the CF_3-group and the observed nucleus, the CF_3-group can then be regarded as a "pseudo-atom" or "super-spin". Owing to the dephasing by three fluorines, stronger signal reduction is achieved equivalent to a nucleus with an increased "effective" gyromagnetic ratio, hence allowing to extend the distance range. For short distances, the relative orientation of the methyl C_3-axis and the interconnecting vector is influencing the amount of dephasing. This dependence is thus to some degree entangling

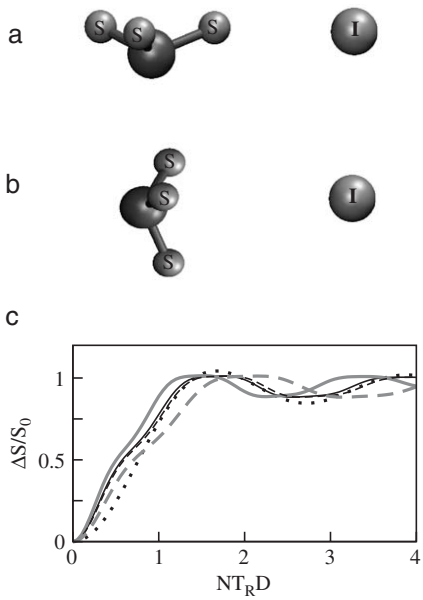

Fig. 7. Trifluoromethyl labels have been used as potent dephasing groups in REDOR experiments, possessing dipolar couplings equivalent to a quasi particle with a gyromagnetic ratio larger than that of a single fluorine. For example, distances between CF_3 groups and ^{31}P in DNA and RNA belong to the largest distances measured by REDOR. Simulated REDOR curves (c) show a stronger dephasing by a methyl group (grey lines for 4 Å distance, black lines for 8 Å distance) than by a single spin placed in the position of the triad centre (dotted line). For small distances, the relative orientation of the observed spin *I* with respect to the *S* spin triad (a, b) has to be taken into account. An equatorial position of the observed spin with respect to the *S* spin plane then results in different dephasing curve (a, dashed lines in c) as a position on the methyl axis (b, solid lines in c). (Molecule segments drawn with VMD.[128])

distance and orientational information derived from the REDOR data. Depending on the nature of the problem addressed, the easier interpretation of the signal reduction by a single ^{19}F or the additional orientation constraints and extended distance range of a CF_3-group might thus be preferable. CF_3-groups were applied in several biological applications, e.g. of fluorine-containing ligands bound to enzymes,[47,76] or of antibiotics targeting the cell wall.[75]

3.6. Background signal

Distance measurements can be severely compromised by background signal, obscuring the signal of interest. The use of one of the most useful labels for REDOR experiments in biology, ^{13}C, is often restricted due to a natural abundance background. In proteins, and in particular in membrane systems, natural abundance ^{13}C can exceed the signal of the actual label, and this way compromise ^{13}C-observed

REDOR experiments. On the other hand, selective labelling at only the desired site might not be possible, e.g. in ^{31}P-observed REDOR of DNA samples the ^{31}P involved in the spin pair of interest but also from all other base units are present in the spectrum. A range of techniques have been developed to select specifically the signal of interest from the background signal. A possibility is to choose or modify the label of interest such that its chemical shift is different from the background signal. For example, the use of both, phosphate and thiolated phosphate derivatives in the synthesis of a DNA quadruplex, allowed the distinction of the phosphothioate ^{31}P signal from the remaining phosphate ^{31}P signal in ^{31}P-observed REDOR experiments on the basis of their different chemical shifts. Often, however, avoiding spectral overlap of the signal from the label of interest and background signal is difficult. In such cases reading out the REDOR signal via a third nucleus provides another route to address the label of interest. This can be done by a magnetization transfer to the third detection nucleus, e.g. via a cross polarization or a TEDOR transfer step following the REDOR pulse sequence.[56] Another interesting way is to use the REDOR experiment itself to select the signal of a particular label of interest. In such a ''double-REDOR'' approach the REDOR experiment used for the actual distance measurement is combined with a second REDOR experiment, in which the observed nucleus is dephased by a nucleus only adjacent to the observed label of interest (Fig. 8). This way of selecting a particular site has been employed frequently for the observation of ^{13}C in the peptide or protein backbone, where the neighbouring amide nitrogen is labelled as ^{15}N ,[42] or to select particular distances in protein ligands.[52,54]

4. BIOLOGICAL APPLICATIONS

4.1. Bound ligands in proteins

Ligands, inhibitors or substrates of enzymes and receptor proteins are probably the most prominent area of application of REDOR distance measurements in biology. Knowledge of the conformation of a bound ligand and its positioning in the binding site not only provides valuable clues of important biochemical processes and reactions, but also is an essential route on the way to rational drug design.[77] Receptor/ligand complexes are often difficult to characterize and REDOR distance measurements can provide an invaluable tool to map out ligand-binding sites. Furthermore, even if the complete protein is not accessible to structural methods or labelling not feasible, by labelling the ligand or substrate a targeted probe can be introduced right into the site of action of a protein or enzyme.

4.1.1. *Synthase enzymes*

Synthase enzymes have been the focus of numerous REDOR distance measurements. To study reaction intermediates, the conformation of inhibitors or the interaction of the substrate with the protein, enzymes were complexed with their

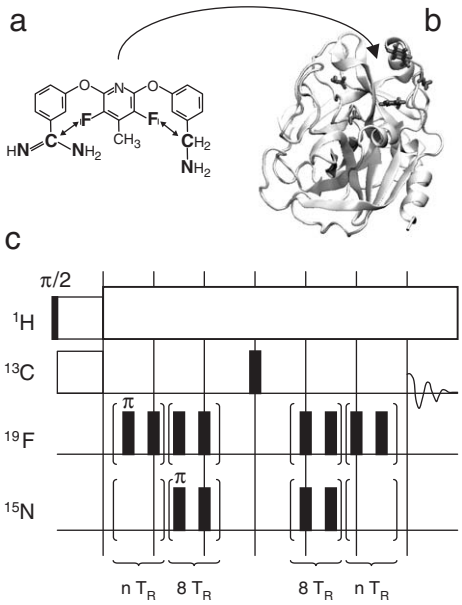

Fig. 8. REDOR can be used to select the signal of e.g. a ^{13}C label from background signal. In the example shown here,[52] the conformation of a bisamidine inhibitor (a) bound to Factor Xa (b, figure produced by VMD[128] from PDB 1MSX) was studied exploring ^{13}C–^{19}F distances. To select the two carbon labels, the dephasing by proximate ^{15}N labels was used in a double REDOR experiment (c). Two dephased ^{13}C spectra are acquired, dephased either by ^{19}F or ^{15}N, where the ^{15}N-dephased spectrum is then taken as the full echo.

ligands and trapped in the bound state. This has been achieved mostly by incubation of the enzymes with their substrates and subsequent supercooling and lyophilization, often in the presence of cryoprotectants.

One of the most studied enzymes is the EPSP synthase (Fig. 9). This enzyme, and the closely related enolpyruvyl transferase,[44] play an important role in the synthesis of aromatic amino acids by plants and microorganisms. It condenses shikimate-3–phosphate (S3P) and phosphoenolpyruvate (PEP) to yield a precursor of amino acids, a reaction which can be inhibited by glyphosate if simultaneously bound with S3P to the synthase. In a number of studies this reaction and its inhibitions were followed and structurally characterized. To get insight into the synthesis, the gradual formation of bonds was monitored using REDOR distance measurements between ^{31}P in S3P and ^{13}C in labelled PEP.[50] The conformation of the two substrates while bound to the enzyme and their interaction with the protein were studied using a shikimate-based bisubstrate, mimicking the interaction intermediate.[47] The molecular basis of inhibition by the plant herbizide glyphosate was the focus of REDOR distance determinations of the inhibitor bound together with S3P to the enzyme. Various labels were used to identify the conformation of the inhibitor complex in the binding pocket, such as ^{31}P, which is naturally occurring in both compounds, and ^{13}C as well ^{15}N labels introduced into the ligands. Besides these

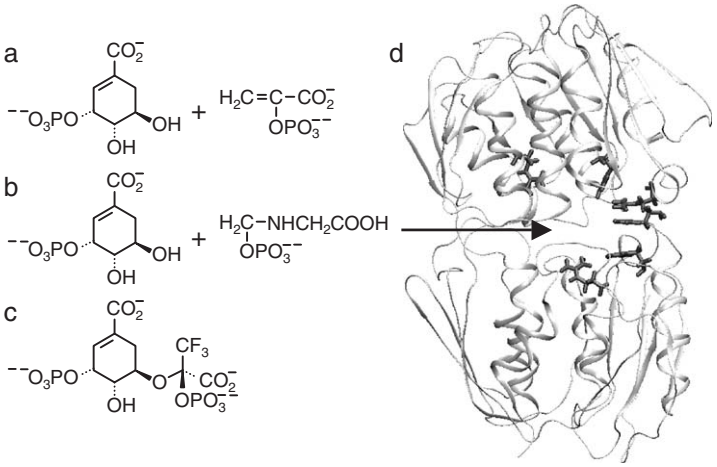

Fig. 9. REDOR distance measurements play an important role in determining the position and conformation of inhibitors or substrates of enzymes in their binding site. A well-studied example is the 5-enolpyruvylshikimate-3-phosphate synthase (EPSP). Its two substrates S3P and PEP (a) the inhibitor glyphosate bound together with S3P (b), as well as a shikimate bisubstrate-based inhibitor (c) were studied in the binding pocket (d) by REDOR measurements. (Figure produced with VMD[128] from PDB 1Q0I.)

intra-ligand distance measurements, the interaction with the protein was characterized by protein–ligand distance measurements to ^{15}N labels in lysine, arginine and histidine side chains in the protein.[43,45–48] In a similar way, the 3-deoxy-D-manno-2-octulosonate-8-phosphate synthase (KDO8PS) was studied, as well making use of the ^{31}P occurring naturally in phosphate-containing substrates.[41,78–81] This enzyme catalyzes the condensation reaction between PEP and D-arabinose 5-phosphate (A5P) to produce KDO8P and inorganic phosphate, and REDOR distance measurements on a phosphonate inhibitor analogue were conducted to get insight into the reaction centre and provide a route to improved inhibitors. As in the EPSP synthase, one aim was to identify proximities of labels in bound inhibitor to ^{15}N of primarily arginine and lysine side chains of labelled synthase protein. Interestingly, contacts to side chains involved in A5P binding could be found, but an involvement of the PEP-binding region in inhibitor binding was not manifested in the solid-state NMR studies. A subsequent study employing frequency-selective REDOR techniques was confirming this interaction pattern, which at first seemed to disagree with solution NMR and X-ray results. Finally, it was concluded that the only remote contacts observed with the latter techniques probably as a consequence of conformational changes upon inhibitor binding are not preserved in the lyophilized samples used for solid-state NMR.[78]

Another interesting enzyme-catalyzed synthesis reaction which was studied by REDOR NMR is the lumazine and riboflavin synthase cycle.[76,82] To shed light on the synthesis intermediates, substrate analogues were introduced, where a CF_3-group prohibits progressing of the catalyzed reaction and the intermediate stays

bound in the reaction centre. $^{15}N\{^{19}F\}$ REDOR measurements then allowed to evaluate distances between the CF_3-label of the ligand and ^{15}N labels in the protein. On the basis of proximities to side chains important in the catalysis, one of two possible epimers was identified as relevant for follow-up reactions. With a molecular weight of 1 MDa, the lumazine enzyme capsid also belongs to one of the largest systems studied by NMR.[76]

Studies of the tryptophan synthase present a further example where REDOR measurements gave insight into enzyme activity on a structural level.[83] For REDOR distance measurement, the protein was selectively labelled with ^{19}F-Phe and ^{13}C-Tyr, and changes in ^{13}C–^{19}F distances upon binding of the serine substrate observed. In addition, ^{13}C-labelled serine was used to monitor protein–ligand interactions.

4.1.2. *Proteases*

Proteases constitute one of the most important classes of enzymes involved in many biological processes, and their reaction mechanisms have become prototype examples for enzymatic catalysis. In the study the reaction mechanism as well as inhibition of proteases also REDOR was used as a tool to provide conformational constraints of reaction intermediates or inhibitors. An early example was the investigation of a phosphonamidate transition-state inhibitor bound to thermolysin by REDOR in 1995.[42] Intensive studies were also done on inhibitors of the human coagulation factor Xa.[52,54,55] With the aid ^{13}C–^{15}N and ^{13}C–^{19}F REDOR distance measurements, the conformation of several amidine-based inhibitors could be revealed and specific ligand–protein interactions could be identified.

4.1.3. *Soluble binding proteins*

Labelling, both the ligand and the protein, the binding sites of the glutamine-binding protein[84,85] or the elongation factor Tu[86] were characterized by REDOR distance measurements. To immobilize the ligand protein complexes for accurate distance measurements, the samples were prepared in solution and subsequently frozen and lyophilized. In the case of the glutamine-binding protein, distances were observed between ^{13}C or ^{15}N labels in the bound glutamine and ^{15}N-, ^{13}C- and ^{19}F-labelled histidine, lysine and tyrosine residues of the binding protein. With the aid of nine distance constraints, the position of glutamine in the binding pocket could be determined at high fidelity. To locate GDP in the elogantion factor Tu,[86] uniformly ^{15}N-labelled protein was used and distances between ^{15}N of the protein and the ^{31}P naturally occurring in the GDP ligand were determined.

4.1.4. *Membrane proteins*

Membrane proteins play an important role in many of the most important biological processes, which are located in biomembranes. They are responsible for transport in and out of cells, signal transduction or energy production and conversion, and constitute around a quarter to a third of most genomes. Moreover,

membrane-bound proteins constitute a major target for pharmaceutical drugs and knowledge of ligand-binding sites in membrane proteins is crucial for drug development. Despite their importance, however, much less is known of membrane protein structure and function than for soluble proteins, which are easier accessible to crystallization and solution-state NMR techniques. Here solid state has proven to provide nonetheless a route to get structural insight into membrane proteins in their membrane environment. In particular, REDOR distance measurements were providing valuable clues of how ligands bind to membrane proteins. Such experiments were performed successfully on ligand protein complexes reconstituted into model membranes or on isolated native membranes. Labelling the ligand provides even a means to introduce NMR labels into systems such as native membranes, which would be difficult to label biosynthetically. Also this way, the label is brought right into the site of action and of possible pharmaceutical interest.

One of the earliest applications of REDOR on a membrane receptor in its membrane-bound state has been the study of the serine receptor of *Escherichia coli*.[87] This 120 kDa membrane protein was ^{13}C-labelled selectively in phenylalanines, and the position of ^{15}N-labelled serine in the binding site was mapped out by ^{15}N–^{13}C REDOR distance measurements. A distance of 4 Å was found, demonstrating the applicability of REDOR experiments to such membrane systems.

An important example of REDOR applications on membrane proteins is bacteriorhodopsin (bR). This membrane protein has been studied intensively as a prototype of the family of 7-*trans*-membrane proteins, which also contains the pharmaceutically highly relevant G-protein-coupled receptors. The function of this proton pump from *Halobacterium salinarium* is the conversion of light energy into a proton gradient across the cell membrane. For this aim, bR carries a covalently linked proteostetic group, the retinal, which uses light-induced isomerizations to transport protons. The structural changes in the retinal itself have been the focus of a number of solid-state NMR studies, but also the interaction between the chromophore and the surrounding residues of the protein is important for the understanding of the function of the proton pump. Here, REDOR distance measurements were helping to provide valuable insight into the role of different residues in the vicinity of the retinal.[10,11] In the first protein application of the SFAM derivative of the REDOR experiment, distances between ^{15}N labels of the tryptophan side chains and ^{13}C labels in positions 14 and 15 of retinal were determined in the dark-adapted state of bR. A moderate change from 4.2 to 3.9 Å in two conformers (15syn and 15anti) was observed. This study was extended to position 20 of the retinal, where ^{13}C–^{15}N distances between the dark- and light-adapted states were compared. The 3 Å distance between the retinal label and Trp182 was found to remain unchanged and no change in hydrogen bonding in this region was manifested. Insight into the function of membrane proteins is often the key to understand disease and development of cures. In many cases, potent drugs are inhibitors blocking membrane proteins in a specific way. The characterization of the conformation of the bound inhibitor and the binding site is then crucial for the design of improved drugs. A prominent example is the renal Na^+/K^+-ATPase, which is involved in heart diseases. Digitalis has gained large clinical importance as

a steroid-based mixture of inhibitors blocking the dephosphorylization of the ATPase. REDOR distance measurements were conducted to study the conformation of inhibitors derived from digitalis, such as analogues of ouabain.[51] The distances between ^{19}F and ^{13}C labels in the inhibitor bound to the protein were used to determine its conformation, and an arrangement with the sugar moiety extending out of the steroid plane was found.

A similar ATP-driven ion pump, the gastric H^+/K^+-ATPase is involved in gastric pH control, and responsible for diseases such as gastritis (Fig. 10). To improve existing inhibitors, the conformation of 2-methyl-3-eyanomethyl-8-phenylmethoxy)imidazo[1,2–a]pyridine analogues was characterized using REDOR distance constraints.[6,88] Again, ^{19}F–^{13}C distances and recently also ^{19}F–^{2}H distances of labels in the ligand were determined and lead to an extended conformation of the inhibitor in its binding site.

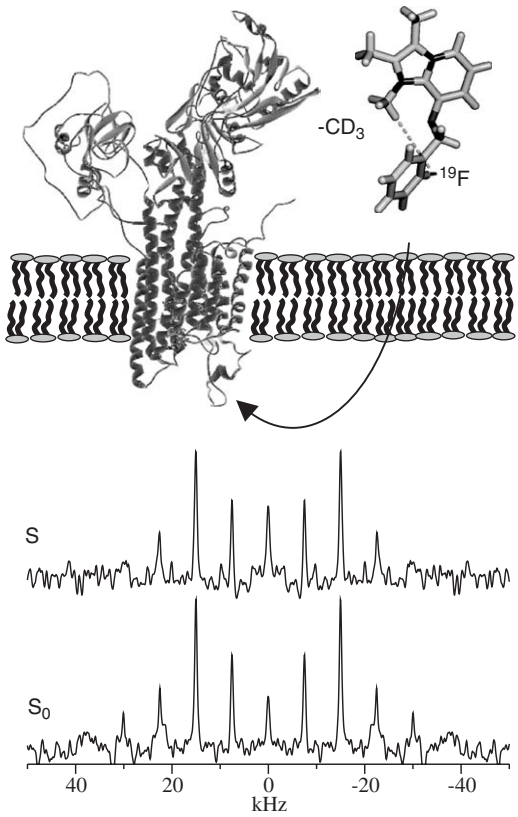

Fig. 10. The conformation of imidazopyridine-based inhibitors of the gastric H^+/K^+-ATPase (shown is a homology model drawn with VMD[128]) in the binding site was studied by $^{13}C\{^{19}F\}$ REDOR,[6] and recently using $^{2}H\{^{19}F\}$ REDOR (b, full echo S_0 and dephased spectrum S for 1.87 ms dephasing time). A distance between the ^{19}F and CD_3-group labels in the inhibitor of ~5 Å was found.

4.2. Fibrillar peptides and proteins

Solid-state NMR has been the tool of choice in structural studies of fibril-forming proteins and peptides. Often, biological fibres do not crystallize well enough for high-resolution X-ray studies, and solution-state NMR is not applicable. Distance measurements by solid-state NMR then provide an opportunity to still gather structural information. This way REDOR has helped to gain insight into fibrous proteins or peptides in several ways. On the one hand, intramolecular distance measurements were used to probe local secondary structure; on the other, intermolecular distances were used to determine the arrangement of building blocks forming fibrils.

4.2.1. *Silk*

The structures of dragline and spider silk have been of interest with the aim of understanding the unique mechanical properties of these biological fibres. Silk from silkworms *Bombyx mori* or *Samia cynthia ricini* has been classified as silk I and silk II, before and after spinning, respectively. Silk II was found to adopt an antiparallel β-sheet structure on the basis of diffraction and solid-state NMR techniques. The structure of silk I, however, has been difficult to obtain because attempts to cause macroscopic alignment as needed for diffraction methods lead to the formation of silk II. With the aid of solid-state NMR and in particular REDOR experiments on silk and model peptides, a structural characterization of silk I became possible[63,89–99](see Fig. 11). It was found to consist of crystalline and semicrystalline regions. The structure of the crystalline region of silk I of *B. mori* was identified as a β-turn type II on the basis of molecular distance constraints obtained by REDOR experiments. To this aim, ^{13}C and ^{15}N labels were introduced for example in the carbonyl of Gly_i and amide nitrogen of Ala_{i+3} to probe the hydrogen-bonding pattern of a β-turn type II repeat. In *S. c. ricini* silk I, the crystalline parts are built of α-helical alanine-rich regions flanked by unusually tight wound helices of several glycines. This structural peculiarity at the α-helix termini was confirmed by REDOR distance measurements across a helix turn.

Apart from silk worms, also spiders have developed silk fibres with remarkable mechanical properties, such as supercontraction upon wetting. The structure of dragline spider silk is generally thought to consist of crystalline alanine-rich regions of β-sheets, which possess different degrees of alignment, and which are embedded in a glycine-rich amorphous matrix. Important for the development of a structural model which is able to explain these features was to understand the role of the well-conserved LGXQ motifs in the silk sequence. Their conformation could be determined by REDOR experiments, which provided evidence for the formation of compact turns by the LGXQ segments.[100,101] These bends allow the silk sequence to fold back, such that alanine-rich segments can stack to form the crystalline β-sheet regions flanked by amorphous glycine-rich parts.

4.2.2. *Amyloid fibrils*

The formation of fibrillar structures is not restricted to large proteins such as silk. More and more examples have been discovered how also small peptides can form

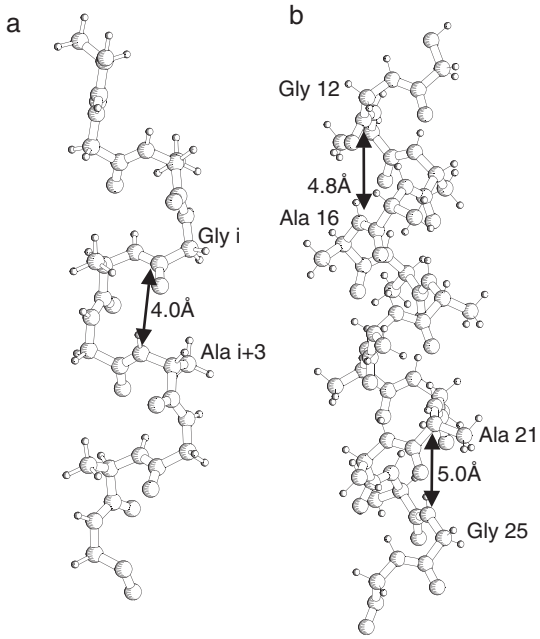

Fig. 11. REDOR was playing an important role in the structure determination of silk. Two major forms of silk were identified with different secondary structure in the ordered regions. After spinning, silk adopts a β-sheet structure known as silk II. The structure of silk I before spinning was more difficult to access. Using solid-state NMR, silk from *B. mori* was found to follow a β-turn type II like structure in the silk I state, which could be verified by REDOR measurements between labels e.g., placed in residues i and $i+3$ (a). A different, helical structure, with unusually tightly wound stretches was observed for silk I of *S. c. ricini*, using REDOR measurements of distances between residues i and $i+4$ (b). (Figures produced with COSMOS.[129,30])

fibrillar supramolecular assemblies. The first and most prominent cases where fibrils built of small peptides and proteins have been encountered were associated with diseases. A well-known example is Alzheimer's disease caused by plaque formation in the brain. The underlying β-amyloid fibrils are formed by a 42 amino acid peptide building block (the Aβ peptide). To identify intermolecular contacts and determine the structure of the fibrillar assembly, various solid-state NMR techniques have been employed. With the aid of REDOR ^{15}N–^{13}C distance measurements, an antiparallel β-sheet arrangement could be determined for the shortest fibril-forming segment, Aβ16-22.[102] REDOR measurements were also contributing to gain insight into the role of the amphipathicity of the fibril-forming peptide in causing parallel or antiparallel β-sheets.[103]

Besides fibrils associated with Alzheimer's disease, further fibril-forming peptides have been studied using the REDOR distance constraints. Examples include the β-sheet fragment from transthyretin,[104] human calcitonin,[105] or the yeast prion protein Ure2p.[71] In the latter case, an interesting fibril assembly could be identified

by REDOR distance measurements. Inter-molecular interactions were obtained between labels in the glutamine side chains, which were found to form a polar zipper stabilizing the parallel β-sheet.

4.3. Membrane-active peptides

Membrane-bound or -associated peptides play an interesting role in many biological processes. Antimicrobial activity, virus fusion or ion transport are examples for peptide-mediated functions occurring in biomembranes. To study peptide function and their behaviour as well as structure in their native membrane environment, solid-state NMR has been used as an important tool. Various issues, such as the localization of peptides with respect to lipids, local structure of peptides while bound to the membrane or inter-molecular contacts in oligomeric peptide assemblies were also addressed by REDOR distance measurements.

Because of their pharmaceutical potential as antibiotic drugs, antimicrobial peptides have long been the major focus of peptide research. One of the first antimicrobial peptides to be studied by solid-state NMR was gramicidin A. Its structure was in fact the first structure determined solely by solid-state NMR. Even though mostly based on orientational constraints, REDOR distance measurements played an important role in getting to a full understanding of gramicidin A in providing some key structural information. In the first REDOR experiments on gramicidin A, however, REDOR measurements of the dipolar coupling were used to derive orientational constraints as well.[20] To this aim, the ^{13}C–^{15}N dipolar coupling of labels in the adjacent residues Gly2 and Ala3 in samples of peptide powder and peptide reconstituted in lipid vesicles were measured. The comparison of the full dipolar coupling of the powder sample and the residual dipolar coupling averaged by the motion of the peptide in the lipid membrane sample then lead to the orientation of the internuclear vector with respect to the axis of molecular motion. A 2D REDOR sequence was used here to relate the sign of the dipolar coupling to the scalar coupling. Based on the results obtained this way, the right-handed 6.3 β-helix could be identified as the correct structure for the antimicrobial ion channel, discarding other possible models.

While the helical structure of the gramicidin ion channel had been well characterized by orientational constraints, details of its dimeric assembly were still lacking. With the aid of intra- as well as inter-molecular SFAM distance measurements, the monomeric structure was confirmed, but also the interface of the head-to-head dimer could be elucidated.[21]

A different arrangement of the two gramicidin monomers was found in ^{13}C–^{15}N SFAM measurements on gramicidin M. This analogue, with the four tryptophans substituted by phenylalanines, was showing inter-molecular contacts in agreement with a dimerization as intertwined helices.

Another classical membrane-active peptide is mellitin. This major ingredient of the bee venom is able to oligomerize to form a pore-like structure, permeabilizing the target membrane. The mellitin monomer possesses a helical structure with a

characteristic bend, which was investigated by solid-state NMR, where methods to determine segmental orientations in the membrane were employed. In addition, REDOR distance measurements between labels at both sides of the hinge of the peptide were able to provide evidence for the bend, and furthermore, were able to clarify to which side the mellitin helix is bent.[106]

Antimicrobial peptides from frog skin and fish constitute further examples of the application of REDOR on membrane-active peptides. Distance measurements obtained from ^{13}C–^{15}N REDOR and ^{13}C chemical shifts, measured using ^{13}C–^{15}N REDOR for signal selection from the background, were used in studies of magainin and pardaxin to probe their secondary structure.[70,107] This way magainin was found to adopt both, α-helical and β-sheet structure while bound to the membrane. Also for pardaxin an α-helical structure was manifested for the C-terminal side. Moreover, the position of magainin in the membrane was addressed using ^{13}C–^{31}P REDOR measurements. A distance of ~6 Å between the ^{13}C label in the peptide and the ^{31}P of the lipid headgroup indicated here a flat alignment on the membrane surface as the most likely localization of the peptide.

The interaction with the membrane was also the focus of studies of the model peptide K3.[7] This peptide is designed to resemble the amphipatic helix of PGLa, a further antimicrobial peptide from frog skin. As for most antimicrobial peptides, several standard models for their membrane-disruptive activity have been proposed, such as the ''carpet'', the ''barrel-stave'' or ''toroidal wormhole'' model. They are distinguished by the localization of the peptide either at the surface of the bilayer, spanning the bilayer to form a pore, or lining a pore formed by lipids. To elucidate the localization of K_3 in the lipid bilayer, several ^{15}N and ^{13}C labels were introduced in peptide, and their proximity to ^{31}P in the lipid headgroup as well as to ^{19}F labels at the end of the lipid tails was determined. The observed couplings between ^{15}N of lysine side chains as well as ^{13}C in the peptide backbone and ^{31}P of the lipid headgroups indicate a contact of the peptide with the head group region of the membrane. ^{13}C–^{19}F couplings, in contrast, indicate interaction of the peptide with the lipid tails. Furthermore, ^{31}P–^{19}F REDOR measurements showed contacts of lipid headgroups and tails in the presence of the peptide. To get further experimental clues on the structure of K3 responsible for its membrane activity, a mixture of ^{19}F- and ^{13}C-labelled K_3 peptide was used in REDOR experiments to validate inter-molecular contacts.[8] Here, two inter-helical distances together with an evaluation of the spinning sideband dephasing in terms of orientational constraints lead to the postulation of the formation of parallel peptide dimers with an intersecting angle of ~20°. Altogether, assuming that the used frozen or lyophilized samples reflect the biological situatuion, the REDOR results favoured a toroidal pore lined by K_3 dimers and monomers (Fig. 12).

Vesicle fusion is another biological process where membrane-active peptides come into play. In particular peptides involved in viral fusion have become of interest as potential drug targets. Again, solid-state NMR and REDOR distance measurements have contributed to understand their structure in the membrane environment. This way, very different structures were found for the fusion peptides of influenza and HIV-1.[108] While influenza fusion peptide adopts an α-helical

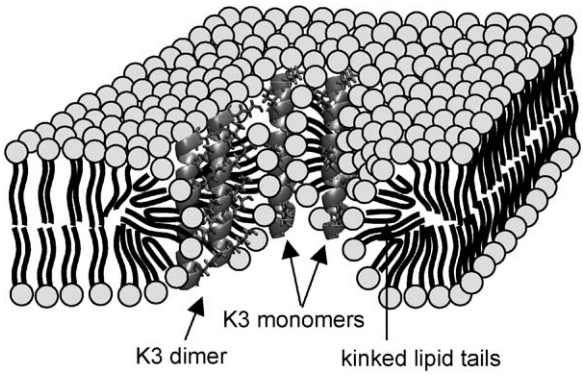

Fig. 12. REDOR and further solid-state NMR experiments on the antimicrobial peptide K3 suggest the formation of a pore in the membrane. With the aid of REDOR distance measurements, a parallel dimer of K3 was postulated and contacts between labels in the peptide and the lipids as well as between lipid headgroups and lipid tails were manifested. On the basis of these results and tilt angle measurements in oriented samples, a model for the antimicrobial activity was developed in which peptide dimers together with monomeric K3 peptide and lipids, line a membrane pore at high peptide : lipid ratios. (Figure in analogy to Ref. 8, molecules drawn with VMD.[128])

structure, the fusion peptide from HIV-1 forms a β-sheet-like conformation. Further studies of the N-terminal end of the HIV-1 fusion peptide gp41 using ^{15}N–^{13}C REDOR distance measurements were targeting inter-molecular contacts.[109] Mixing peptides labelled in the backbone at three consecutive residues with either ^{15}N or ^{13}C, parallel as well as antiparallel β-sheet formations were observed and could be characterized in detail.

4.4. Transmembrane helices of membrane proteins

As discussed above, REDOR has played a prominent role in the elucidation of membrane protein function and the mechanism of membrane-active peptides. The conformation of ligands bound to membrane proteins or the interaction of peptides with lipid bilayers has been the focus of such solid-state NMR studies. Not of lesser importance is the understanding of the basic structural design principles of membrane proteins. To this aim, distance measurements using REDOR have target transmembrane helices as the major building block of membrane proteins. Issues such as structural particularities induced by the membrane environment or helix–helix interactions have been addressed in many examples.

As a prototype of 7TM proteins, the transmembrane helices of bacteriorhodopsin have received attention in several structural solid-state NMR experiments. The dynamics and helix regularity of the transmembrane segment A (residues 6–42), for example was addressed in Ref. 110, where ^{15}N–^{13}C REDOR measurements were used to evaluate helix distortions, and a regular α-helix was found. The role of prolines in transmembrane helices of bacteriorhodopsin was studied by another set of REDOR

experiments by Lansing *et al.*.[111] It had been postulated that the proline residues are of functional importance in the photocycle of the proton pump. However, no change in the X-Pro peptide bond of different photo-intermediates was found, concluding that proline possesses a major structural role in bacteriorhodopsin.

A further membrane spanning protein studied by REDOR distance measurements was phospholamban.[112] This single transmembrane helix protein is involved in the regulation of Ca^{2+} transport and can inhibit the activity of Ca^{2+}-ATPase by binding to this ion pump. Here, distance measurements were able to confirm the α-helical structure of the 52 residue protein in its membrane environment.[112] Furthermore, using REDOR in combination with oriented membrane samples, the orientation dependence of the dipolar coupling was evaluated as well, and a tilt angle of the helix with respect to the membrane normal of $\sim 25^{\circ}$ could be determined.[24] Changes of the helical structure to a more extended structure upon binding to SERCA1 Ca^{2+}-ATPase were observed as well using REDOR distance constraints.[113]

Often oligomers rather than single membrane proteins or peptides are functionally relevant. The contacts and interations between transmembrane helices often are a missing link in understanding the entire structure. REDOR distance measurements then provide a powerful tool to probe such inter-molecular contacts. Such distance measurements were, for example instrumental in validating the oligomeric structure of the H^+ channel from influenza virus.[114] Evaluating distances between ^{15}N and ^{13}C labels in histidine and tryptophan side chains, repectively, revealed inter-helical contacts within a peptide tetramer. Interesting here was the labelling scheme. Both labels were placed in the peptide, however, the observed distance was only possible between side chains of adjacent helices rather than within the same peptide.

Helix–helix contacts became also apparent in the REDOR study of the small membrane protein glycophorin A.[115] The helical membrane spanning protein contains a known seven-residue dimer motif with a threonine as the only polar residue. REDOR measurements were able to confirm inter-helical contacts between the ^{13}C-labelled threonine side chain and ^{15}N-labelled isoleucine. On the basis of the found distance, a detailed model of the dimer could then be derived.

4.5. Complex biomaterials

Solid-state NMR distance measurements like REDOR are especially suited to solve biological questions where the formation of inter-molecular contacts plays a role. The biosynthesis of complex biomaterials often involves interlinking or adhesion to inorganic surfaces, and here REDOR measurements have proven a powerful tool to elucidate structural details. With the aid of REDOR distance measurement, the formation of covalent bonds in the peptidoglycan network of bacterial cell walls, in insect pupal cuticles or mussel adhesive plaques could be characterized this way to give valuable clues of the underlying biochemical processes. Also, insight into the molecular basis of adhesion to inorganic surfaces could be obtained by REDOR distance measurements.

4.5.1. *Bacterial cell walls*

The cell wall peptidoglycan network of *Bacillus subtilis* and *Staphylococcus aureus* has been the focus of a number of REDOR solid-state NMR studies. Understanding the build-up of the cell wall network is of particular importance because it constitutes a major target for antibiotics.

The peptidoglycan network is (Fig. 13) built by glycan fibres with peptide stems attached at every second sugar unit. These peptide stems are then bridged by pentaglycyl links to form the cell wall mesh. The degree of inter-linkage was studied in the first REDOR measurements on cell walls.[116–118] To this aim, ^{13}C- and ^{15}N-labelled amino acids occurring in the peptide stems and glycine bridges were introduced in the metabolism of *B. subtilis* or *S. aureus* cells. With the aid of REDOR distance measurements on whole cells (lyophilized or hydrated and frozen) it was then possible to follow the formation of covalent bonds. This way, a dense network with a degree of ~75% linked peptide stems was found. The influence of antibiotics based on vancomycin on the cell wall formation was studied in subsequent solid-state NMR measurements.[19,53,75,117,119] Here, the localization of the antibiotics in the peptidoglycan network and changes in the interlinkage induced by antibiotics were of interest to understand the antibacterial mechanism. The formation of the peptidoglycan network in the presence of antibiotics was evaluated using REDOR, employing ^{13}C- and ^{15}N-labelling schemes aimed to identify the incorporation of the labelled precursors in cross-link and bridge-link. It could be shown that for

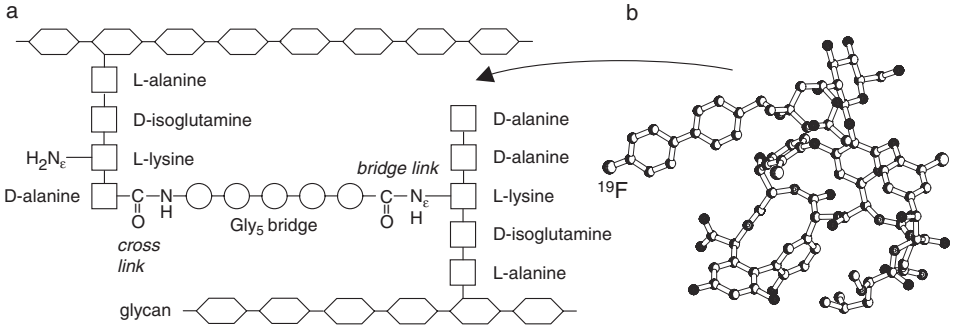

Fig. 13. The synthesis of the peptidoglycan network (a) of bacterial cell walls was the focus of several solid-state and REDOR NMR studies. By following the incorporation of labelled peptidoglycan precursors, insight into the building process of the cell wall was obtained. In addition, REDOR experiments allowed monitoring the formation of covalent bonds within the cell wall network. This way, the influence of the antibiotics such as vancomycin analogues (b: 4-(4-fluorophenyl)benzylvancomycin, drawn with COSMOS[129,130] using PDB 1VAN) on the cell wall synthesis could be characterized. It was found from labelling with 1-^{13}C-glycine and ε-^{15}N-lysine, that vancomycin interferes with the transglycosylase activity leading to a decrease of bridge links, but not effecting cross-link formation. The antibiotics could be localized in the cell wall near the D-Ala-D-Ala end of unlinked stems using REDOR distance measurements between labels in alanine, lysine, and glycine incorporated into the peptidoglycan, and labels such as ^{19}F in the drug compounds.

S. aureus the antibiotic reduces the amount of bridge-links while leaving the amount of cross-links constant. On the basis of this insight into the cell wall metabolism, transglycosylation was identified to be the inhibited cell wall synthesis step, and an interference with transpeptidases could be ruled out as the antibacterial mechanism. To determine the position of cell wall targeting antibiotics, the proximity of ^{19}F-labelled antibiotic to ^{15}N, ^{13}C labels and ^{31}P natural abundance in the peptidoglycan was probed by REDOR measurements. The tested antibiotics were found near the peptide stems, which were not involved in a link. A recent study comparing several analogues could further refine models for binding near the glycyl bridge and the D-Ala-D-Ala end of unlinked stems, and suggested that at this binding site the antibiotic blocks the growth of the glycan chains.[75]

4.5.2. *Insect cuticles*

Another interesting biomaterial which was studied by REDOR in a similar way as peptidoglycan cell walls originates from insects. The pupal cuticle of the tobacco hornworm consists of protein interlinked by catecholamine, and the structural details of its bridging moieties were investigated by probing the formation of covalent bonds. To this aim, ^{13}C- and ^{15}N-labelled precursors for the formation of the catecholamine linkers, β-alanine and dopamine, were introduced into the hornworm metabolism. With the aid of ^{15}N–^{13}C REDOR measurements the incorporation of alanyldopamine built from the labelled precursors could be proven. Furthermore, also ^{15}N–^{13}C dipolar couplings were observed which could only originate from β-alanine and dopamine of two different alanyldopamines in close contact. This way, a cross-linking of the proteins by two catechol units was found.[120] Introducing labelled histidine, the site of attachment of the catechol linkers to the protein was determined as well, resulting altogether in a detailed picture of the biochemistry of pupal cuticle formation.

The formation of a covalently linked protein network also plays an important role in the adhesion of marine organisms like mussels. In a process known as quinine tanning, dihydroxyphenylalanine-mediated bridges are formed to strengthen the adhesive plaques. Evidence for the formation of such linkages could be found by REDOR measurements.[121,122] Introducing ^{13}C-labelled phenol-tyrosine and ^{2}H-labelled tyrosine into the metabolism of mussels grown under different water flow conditions, incorporation of dihydroxyphenylalanine bridges into the adhesive plaques could be verified by ^{13}C{^{2}H} REDOR. Furthermore, an increased amount of cross-linking with increased flow was observed, showing that the observed REDOR contacts are indeed related to the molecular basis of adhesion.

4.5.3. *Hydroxyapatite*

Molecular details of the interaction of biomolecules with inorganic surfaces are only known from very few examples such as the adhesion of marine organism discussed above. The interaction of proteins with hydroxyapatite, the basis of, e.g. bone material, presents another example where REDOR was providing insight in complex biological materials on an atomic level. The surface structure of

hydroxyapatite itself was in the centre of ^{31}P–^{19}F REDOR studies of fluorine-treated hydroxyapatite, the principal inorganic constituent of dental enamel and dentine.[123] The REDOR measurements showed the formation of fluorohydroxyapatite with a surface coverage of less than one unit-cell layer. The interaction of the protein statherin, which plays a role in the regulation of hydroxyapatite biomineralization, with hydroxyapatite surfaces was studied with ^{15}N–^{13}C and ^{31}P–^{15}N REDOR measurements.[124,125] Using several solid-state NMR techniques and probing ^{13}C–^{15}N distances between residues i and $i+4$, the conformation of a peptide fragment from statherin could be determined while bound to hydroxyapatite, and the disordered domain found at the N-terminal end was postulated to be involved in the protein–mineral contact.[125] REDOR experiments between ^{15}N-labelled lysine side chains in statherin and ^{31}P of hydroxyapatite were then providing the first direct evidence for a contact of the protein with the inorganic mineral surface.[124]

4.5.4. *Plant leaves*

An astonishing example of the use of the REDOR experiment to solve open questions in biology presents a recent study of the CO_2 uptake in plants.[126] Molecular details of the binding CO_2 to Rubisco, the enzyme which catalyzes the fixation of CO_2, were already studied by earlier REDOR experiments.[127] This fixation of atmospheric CO_2 in the Calvin cycle constitutes the basis for the synthesis of plant-originating organic material. During this cycle, known as photosynthesis, carbon-rich compounds are built up by consecutive carboxylation. However, in a counter-acting process, part of the synthesized products are oxygenated using atmospheric O_2 to yield smaller compounds. Determining the contribution of this step, referred to as photorespiration, in the photocycle was the aim of the solid-state NMR study. To this aim, soyabean plants were grown in atmosphere enriched with ^{13}C-labelled CO_2, and the ^{13}C content in their leaves was measured in two NMR experiments. In a first experiment, the total $^{13}CO_2$ incorporation, and in a second only the $^{13}CO_2$ involved in the Calvin cycle were measured. Here, a selection of ^{13}C in the Calvin cycle intermediates was possible due to their phosphorylation. Using $^{13}C\{^{31}P\}$ REDOR, only ^{13}C within one or two carbon units distance from ^{31}P contributes to the dephased signal, allowing to quantify the ^{13}C in the phosphorylated photosynthesis intermediates. This way the loss of CO_2 due to photorespiration could be assessed directly for the first time, and was found to be 21%.

4.6. Nucleic acids

Proteins with their wide range of different structures are usually considered as the major biomolecules mediating the function, and thus constitute a main focus of structural biology. However, also the structure of DNA and RNA is important for their function. In particular, similar to proteins, DNA and RNA sequences are of pharmaceutical interest as potential drug targets, and characterization-binding sites

is instrumental for rational drug design. Here, REDOR distance measurements were a valuable tool to monitor changes in RNA or DNA structure upon binding of therapeutic compounds[38,40] or to localize the binding site of drugs.[36,39] In particular, the ^{31}P occurring in the phosphate of DNA or RNA was used frequently together with ^{19}F-labelled drugs or ^{19}F substitution at the 2′ position for ^{31}P{^{19}F} REDOR, which allowed to explore the long distance range of ^{19}F and achieve distance measurements of up to 14 Å.[38] To select a particular ^{31}P resonance, often a phosphate of DNA or RNA was substituted by phosphothioate to shift the ^{31}P resonance.[36,38–40]

The study of the interaction of the pharmaceutical compound distamycin A with DNA is an example where ^{31}P{^{19}F} REDOR was used to characterize structural changes in DNA[38] (see Fig. 14). Here, the width of the minor groove could be measured directly for the first time with spectroscopic techniques. With the aid of ^{19}F introduced at position 2′, and phosphothioate the distance across the minor groove was monitored and a change upon binding of two drug molecules from ~9 to ~14 Å was encountered. A similar strategy was applied in the study of complexes of the HIV transactivation response element RNA with the viral regulatory protein tat. Again 2′F substitutions were introduced into the nucleic acid and distances to phosphothioate labels were followed. A 4 Å distance change upon peptide binding could be determined, and this way peptide–RNA interaction was validated for the first time using solid-state NMR.

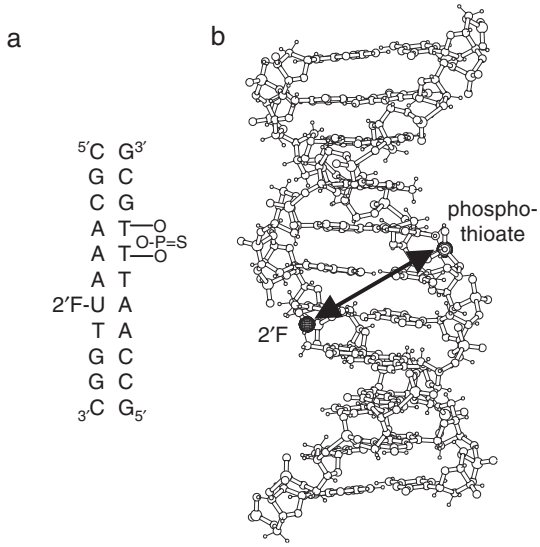

Fig. 14. Among the largest distances obtained in REDOR experiments are ^{31}P–^{19}F distances within DNA or RNA. For example, the changes in the width of the minor groove upon binding of distamycin were measured.[38] A distance of 9.4 Å was determined between the ^{19}F and ^{31}P in labelled 2′F-Uracil and a phosphothioate, which decreased to ~7 Å with bound distamycin at a molar ratio of approximately 1:1, and increased to 13.6 Å with two molecules bound. (Figure produced with COSMOS.[129,130])

The complex of DNA with a repair enzyme was studied by Yu *et al.*[39] The protein uracil DNA glycosylase can remove unwanted uracil utilizing base flipping, and is able to distinguish uracil from thymin despite their structural similarity. To obtain insight into the molecular basis of this recognition, difluorophenyl was incorporated into DNA as a fluorinated isostere of uracil. With the aid of $^{31}P\{^{19}F\}$ REDOR, the stacking geometry could be characterized and identified as an intermediate state of the enzymatic reaction.

DNA G-quadruplexes are an example of DNA of pharmaceutical interest studied by REDOR NMR. Compounds interacting with this DNA structural motif are involved, e.g. in telomere shortening, and play a role in cancer therapy. To study the interaction of this type of drugs with G-quadruplexes, the quadruplex was modelled in vitro by a TAGGGTTA sequence and complexed with a fluorine-containing quinobenzoxazine analogue. $^{31}P\{^{19}F\}$ and $^{13}C\{^{19}F\}$ REDOR was used to relate the ^{19}F label of the bound drug to ^{31}P in DNA phosphate and phosphothioate incorporated into the DNA as well as ^{13}C-labelled thymidine derivatives. This way, a detailed picture of the drug in its binding site could be obtained.[36]

5. CONCLUSIONS

REDOR has grown since its invention into one of the most frequently employed solid-state NMR techniques for the accurate measurement of internuclear distances. Although the elucidations of entire protein structures are usually outside the scope of REDOR, it presents a vital source of structural details. Used with labels placed in key positions, numerous interesting biological questions were addressed and could be solved by solid-state NMR distance measurements. As a heteronuclear method, REDOR has proven a particularly powerful tool in relating the parts of complexes coming together in the course of a biological process. Like shown in the discussed examples, measurements of heteronuclear couplings were able to relate antimicrobial peptides with their lipid bilayer, characterize the interaction of drugs with their protein- or DNA-binding sites, identify labelled educts incorporated in biological materials, evaluate links in protein networks or validate contacts between subunits of oligomeric structures.

REFERENCES

1. T. Gullion and J. Schaefer, *J. Magn. Reson.*, 1989, **81**, 196–200.
2. K. T. Mueller, T. P. Jarvie, D. J. Aurentz and B. W. Roberts, *Chem. Phys. Lett.*, 1995, **242**, 535–542.
3. S. Yamaguchi, K. Shimono, Y. Sudo, S. Tuzi, A. Naito, N. Kamo and H. Saito, *Biophys. J.*, 2004, **86**, 3131–3140.
4. S. Yamaguchi, S. Tuzi, J. U. Bowie and H. Saito, *Biochim. Biophys. Acta-Proteins Proteom.*, 2004, **1698**, 97–105.
5. S. Yamaguchi, S. Tuzi, M. Tanio, A. Naito, J. K. Lanyi, R. Needleman and H. Saito, *J. Biochem.*, 2000, **127**, 861–869.
6. J. A. Watts, A. Watts and D. A. Middleton, *J. Biol. Chem.*, 2001, **276**, 43197–43204.
7. O. Toke, W. L. Maloy, S. J. Kim, J. Blazyk and J. Schaefer, *Biophys. J.*, 2004, **87**, 662–674.

8. O. Toke, R. D. O'Connor, T. K. Weldeghiorghis, W. L. Maloy, R. W. Glaser, A. S. Ulrich and J. Schaefer, *Biophys. J.*, 2004, **87**, 675–687.
9. A. J. Mason, G. J. Turner and C. Glaubitz, *FEBS J*, 2005, **272**, 2152–2164.
10. M. Helmle, H. Patzelt, A. Ockenfels, W. Gartner, D. Oesterhelt and B. Bechinger, Refinement of the geometry of the retinal binding pocket in dark-adapted bacteriorhodopsin by heteronuclear solid-state NMR distance measurements, *Biochemistry*, 2000, **39**, 10066–10071.
11. A. T. Petkova, M. Hatanaka, C. P. Jaroniec, J. G. G. Hu, M. Belenky, M. Verhoeven, J. Lugtenburg, R. G. Griffin and J. Herzfeld, Tryptophan interactions in bacteriorhodopsin: a heteronuclear solid-state NMR study, *Biochemistry*, 2002, **41**, 2429–2437.
12. R. D. O'Connor and J. Schaefer, Relative CSA-dipolar orientation from REDOR sidebands, *J. Magn. Reson.*, 2002, **154**, 46–52.
13. J. M. Goetz and J. Schaefer, Orientational information in solids from REDOR sidebands, *J. Magn. Reson.*, 1997, **129**, 222–223.
14. J. Leppert, B. Heise and R. Ramachandran, ^{15}N chemical shift tensor magnitude and orientation in the molecular frame of uracil determined via MAS NMR, *J. Magn. Reson.*, 2000, **145**, 307–314.
15. J. Leppert, B. Heise and R. Ramachandran, Redor in IS_1S_2 systems, *J. Biomol. NMR*, 2000, **18**, 153–164.
16. J. Leppert, B. Heise and R. Ramachandran, Orientational information from TEDOR spectral sidebands, *Solid State NMR*, 2001, **19**, 1–18.
17. B. Heise, J. Leppert and R. Ramachandran, Characterization of ^{15}N chemical shift tensors via ^{15}N–^{13}C REDOR and ^{15}N–^{1}H dipolar-shift CPMAS NMR spectroscopy, *Solid State NMR*, 2000, **16**, 177–187.
18. B. Heise, J. Leppert, H. Wenschuh, O. Ohlenschlager, M. Gorlach and R. Ramachandran, 2D relayed anisotropy correlation NMR: characterization of the ^{13}C' chemical shift tensor orientation in the peptide plane of the dipeptide AibAib,, *J. Biomol. NMR*, 2001, **19**, 167–179.
19. A. K. Mehta, L. Cegelski, R. D. O'Connor and J. Schaefer, REDOR with a relative full-echo reference,, *J. Magn. Reson.*, 2003, **163**, 182–187.
20. A. W. Hing and J. Schaefer, 2-dimensional rotational-echo double-resonance of Val_1-1-^{13}C Gly_2-^{15}N Ala_3-Gramicidin-a in multilamellar dimyristoylphosphatidylcholine dispersions, *Biochemistry*, 1993, **32**, 7593–7604.
21. R. Q. Fu, M. Cotton and T. A. Cross, Inter- and intramolecular distance measurements by solid-state MAS NMR: determination of gramicidin A channel dimer structure in hydrated phospholipid bilayers, *J. Biomol. NMR*, 2000, **16**, 261–268.
22. C. Glaubitz and A. Watts, Magic angle-oriented sample spinning (MAOSS): a new approach toward biomembrane studies, *J. Magn. Reson.*, 1998, **130**, 305–316.
23. B. J. Gross, J. M. Tanski and A. E. McDermott, Structure determination of aligned systems by solid-state NMR magic angle spinning methods, *J. Magn. Reson.*, 2005, **176**, 223–233.
24. D. A. Middleton, Z. Ahmed, C. Glaubitz and A. Watts, REDOR NMR on a hydrophobic peptide in oriented membranes, *J. Magn. Reson.*, 2000, **147**, 366–370.
25. T. Gullion, D. B. Baker and M. S. Conradi, New, compensated Carr–Purcell sequences, *J. Magn. Reson.*, 1990, **89**, 479–484.
26. N. Sinha, K. Schmidt-Rohr and M. Hong, Compensation for pulse imperfections in rotational-echo double-resonance NMR by composite pulses and EXORCYCLE, *J. Magn. Reson.*, 2004, **168**, 358–365.
27. C. P. Jaroniec, B. A. Tounge, C. M. Rienstra, J. Herzfeld and R. G. Griffin, Recoupling of heteronuclear dipolar interactions with rotational-echo double-resonance at high magic-angle spinning frequencies, *J. Magn. Reson.*, 2000, **146**, 132–139.
28. P. Bertani, J. Raya and M. Hirschinger, F-19/Si-29 rotational-echo double-resonance and heteronuclear spin counting under fast magic-angle spinning in fluoride-containing octadecasil, *Solid State NMR*, 2002, **22**, 188–203.
29. S. L. Grage, J. A. Watts and A. Watts, ^{2}H{^{19}F} REDOR for distance measurements in biological solids using a double resonance spectrometer, *J. Magn. Reson.*, 2004, **166**, 1–10.
30. B. Heise, J. Leppert and R. Ramachandran, REDOR with adiabatic dephasing pulses, *J. Magn. Reson.*, 2000, **146**, 181–187.

31. I. Sack, Y. S. Balazs, S. Rahimipour and S. Vega, Solid-state NMR determination of peptide torsion angles: applications of ^{2}H-dephased REDOR, *J. Am. Chem. Soc.*, 2000, **122**, 12263–12269.
32. T. Gullion, *J. Magn. Reson.*, 2000, **146**, 220–222.
33. R. Q. Fu, S. A. Smith and G. Bodenhausen, *Chem. Phys. Lett.*, 1997, **272**, 361–369.
34. J. C. C. Chan, *Chem. Phys. Lett.*, 2001, **335**, 289–297.
35. S. M. Holl, G. R. Marshall, D. D. Beusen, K. Kociolek, A. S. Redlinski, M. T. Leplawy, R. A. McKay, S. Vega and J. Schaefer, *J. Am. Chem. Soc.*, 1992, **114**, 4830–4833.
36. A. K. Mehta, Y. Shayo, H. Vankayalapati, L. H. Hurley and J. Schaefer, *Biochemistry*, 2004, **43**, 11953–11958.
37. M. E. Merritt, S. T. Sigurdsson and G. P. Drobny, *J. Am. Chem. Soc.*, 1999, **121**, 6070–6071.
38. G. L. Olsen, E. A. Louie, G. P. Drobny and S. T. Sigurdsson, *Nucl. Acids Res.*, 2003, **31**, 5084–5089.
39. L. J. Yu, L. M. McDowell, B. Poliks, D. R. Studelska, C. Y. Cao, G. S. Potter, J. Schaefer, F. H. Song and J. T. Stivers, *Biochemistry*, 2004, **43**, 15429–15438.
40. G. L. Olsen, T. E. Edwards, P. Deka, G. Varani, S. T. Sigurdsson and G. P. Drobny, *Nucl. Acids Res.*, 2005, **33**, 3447–3454.
41. V. Belakhov, E. Dovgolevsky, E. Rabkin, S. Shulami, Y. Shoham and T. Baasov, *Carbohydr. Res.*, 2004, **339**, 385–392.
42. D. D. Beusen, L. M. McDowell, U. Slomczynska and J. Schaefer, *J. Med. Chem.*, 1995, **38**, 2742–2747.
43. A. M. Christensen and J. Schaefer, *Biochemistry*, 1993, **32**, 2868–2873.
44. Y. Li, F. Krekel, C. A. Ramilo, N. Amrhein and J. N. S. Evans, *FEBS Lett.*, 1995, **377**, 208–212.
45. L. M. McDowell, C. A. Klug, D. D. Beusen and J. Schaefer, *Biochemistry*, 1996, **35**, 5395–5403.
46. L. M. McDowell, A. Schmidt, E. R. Cohen, D. R. Studelska and J. Schaefer, *J. Mol. Biol.*, 1996, **256**, 160–171.
47. L. M. McDowell, D. R. Studelska, B. Poliks, R. D. O'Connor and J. Schaefer, *Biochemistry*, 2004, **43**, 6606–6611.
48. L. M. McDowell, B. Poliks, D. R. Studelska, R. D. O'Connor, D. D. Beusen and J. Schaefer, *J. Biomol. NMR*, 2004, **28**, 11–29.
49. D. R. Studelska, C. A. Klug, D. D. Beusen, L. M. McDowell and J. Schaefer, *J. Am. Chem. Soc.*, 1996, **118**, 5476–5477.
50. D. R. Studelska, L. M. McDowell, M. P. Espe, C. A. Klug and J. Schaefer, *Biochemistry*, 1997, **36**, 15555–15560.
51. D. A. Middleton, S. Rankin, M. Esmann and A. Watts, *Proc. Natl. Acad. Sci. U.S.A.*, 2000, **97**, 13602–13607.
52. L. M. McDowell, M. A. McCarrick, D. R. Studelska, R. D. O'Connor, D. R. Light, W. J. Guilford, D. Arnaiz, M. Adler, J. L. Dallas, B. Poliks and J. Schaefer, *J. Med. Chem.*, 2003, **46**, 359–363.
53. S. J. Kim, L. Cegelski, D. R. Studelska, R. D. O'Connor, A. K. Mehta and J. Schaefer, *Biochemistry*, 2002, **41**, 6967–6977.
54. L. M. McDowell, M. A. McCarrick, D. R. Studelska, W. J. Guilford, D. Arnaiz, J. L. Dallas, D. R. Light, M. Whitlow and J. Schaefer, *J. Med. Chem.*, 1999, **42**, 3910–3918.
55. D. R. Studelska, L. M. McDowell, M. Adler, R. D. O'Connor, A. K. Mehta, W. J. Guilford, J. L. Dallas, D. Arnaiz, D. R. Light and J. Schaefer, *Biochemistry*, 2003, **42**, 7942–7949.
56. N. Sinha and M. Hong, *Chem. Phys. Lett.*, 2003, **380**, 742–748.
57. S. Wi, N. Sinha and M. Hong, *J. Am. Chem. Soc.*, 2004, **126**, 12754–12755.
58. K. Saalwächter and K. Schmidt-Rohr, *J. Magn. Reson.*, 2000, **145**, 161–172.
59. K. Saalwächter and H. W. Spiess, *J. Chem. Phys.*, 2001, **114**, 5707–5728.
60. K. Saalwächter and I. Schnell, *Solid State NMR*, 2002, **22**, 154–187.
61. I. Sack, Y. S. Balazs, S. Rahimipour and S. Vega, *J. Magn. Reson.*, 2001, **148**, 104–114.
62. E. Hughes, T. Gullion, A. Goldbourt, S. Vega and A. J. Vega, *J. Magn. Reson.*, 2002, **156**, 230–241.
63. T. Gullion, R. Kishore and T. Asakura, *J. Am. Chem. Soc.*, 2003, **125**, 7510–7511.
64. Y. Ba, H. M. Kao, G. P. Grey, L. Chopin and T. Gullion, *J. Magn. Reson.*, 1998, **133**, 104–114.
65. B. Kesling, E. Hughes and T. Gullion, *Solid State NMR*, 2000, **16**, 1–7.
66. L. Chopin, S. Vega and T. Gullion, *J. Am. Chem. Soc.*, 1998, **120**, 4406–4409.

67. A. Schmidt, T. Kowalewski and J. Schaefer, *Macromolecules*, 1993, **26**, 1729–1733.
68. A. Schmidt, R. A. McKay and J. Schaefer, *J. Magn. Reson.*, 1992, **96**, 644–650.
69. J. M. Goetz and J. Schaefer, *J. Magn. Reson.*, 1997, **127**, 147–154.
70. D. J. Hirsh, J. Hammer, W. L. Maloy, J. Blazyk and J. Schaefer, *Biochemistry*, 1996, **35**, 12733–12741.
71. J. C. C. Chan, N. A. Oyler, W. M. Yau and R. Tycko, Parallel beta-sheets and polar zippers in amyloid fibrils formed by residues 10-39 of the yeast prion protein Ure2p, *Biochemistry*, 2005, **44**, 10669–10680.
72. J. Schaefer, REDOR-determined distances from heterospins to clusters of ^{13}C labels, *J. Magn. Reson.*, 1999, **137**, 272–275.
73. C. P. Jaroniec, B. A. Tounge, J. Herzfeld and R. G. Griffin, Frequency selective heteronuclear dipolar recoupling in rotating solids: accurate ^{13}C–^{15}N distance measurements in uniformly ^{13}C,^{15}N-labeled peptides, *J. Am. Chem. Soc.*, 2001, **123**, 3507–3519.
74. E. A. Louie, P. Chirakul, V. Raghunathan, S. T. Sigurdsson and G. P. Drobny, Using solid-state $^{31}P\{^{19}F\}$ REDOR NMR to measure distances between a trifluoromethyl group and a phosphodiester in nucleic acids, *J. Magn. Reson.*, 2006, **178**, 11–24.
75. S. J. Kim, L. Cegelski, M. Preobrazhenskaya and J. Schaefer, Structures of *Staphylococcus aureus* cell-wall complexes with vancomycin, eremomycin, and chloroeremomycin derivatives by $^{13}C\{^{19}F\}$ and $^{15}N\{^{19}F\}$ rotational-echo double resonance, *Biochemistry*, 2006, **45**, 5235–5250.
76. J. M. Goetz, B. Poliks, D. R. Studelska, M. Fischer, K. Kugelbrey, A. Bacher, M. Cushman and J. Schaefer, Investigation of the binding of fluorolumazines to the 1-MDa capsid of lumazine synthase by $^{15}N\{^{19}F\}$ REDOR NMR, *J. Am. Chem. Soc.*, 1999, **121**, 7500–7508.
77. A. Watts, Solid state NMR in drug design and discovery for membrane embedded targets, *Nat. Rev. Drug Discov.*, 2005, **4**, 555–568.
78. L. Kaustov, S. Kababya, V. Belakhov, T. Baasov, Y. Shoham and A. Schmidt, Inhibition mode of a bisubstrate inhibitor of KDO8P synthase: a frequency-selective REDOR solid-state and solution NMR characterization, *J. Am. Chem. Soc.*, 2003, **125**, 4662–4669.
79. L. Kaustov, T. Baasov and A. Schmidt, Binding of the natural substrates and products to KDO8P synthase: ^{31}P and ^{13}C solution NMR characterization, *Bioorg. Chem.*, 2003, **31**, 306–321.
80. L. Kaustov, S. Kababya, S. C. Du, T. Baasov, S. Gropper, Y. Shoham and A. Schmidt, Direct identification of enzyme active site residues by solid-state REDOR NMR: application to KDO8P synthase, *J. Am. Chem. Soc.*, 2000, **122**, 2649–2650.
81. L. Kaustov, S. Kababya, S. C. Du, T. Baasov, S. Gropper, Y. Shoham and A. Schmidt, Structural and mechanistic investigation of 3-deoxy-D-manno-octulosonate-8-phosphate synthase by solid-state REDOR NMR, *Biochemistry*, 2000, **39**, 14865–14876.
82. A. K. Mehta, D. R. Studelska, M. Fischer, A. Giessauf, K. Kemter, A. Bacher, M. Cushman and J. Schaefer, Investigation of the binding of epimer A of the covalent hydrate of 6,7-bis(trifluoromethyl)-8-D-ribityllumazine to a recombinant F22W *Bacillus subtilis* lumazine synthase mutant by $^{15}N\{^{19}F\}$ REDOR NMR, *J. Org. Chem.*, 2002, **67**, 2087–2092.
83. L. M. McDowell, M. S. Lee, R. A. McKay, K. S. Anderson and J. Schaefer, Intersubunit communication in tryptophan synthase by carbon-13 and fluorine-19 REDOR NMR, *Biochemistry*, 1996, **35**, 3328–3334.
84. A. W. Hing, N. Tjandra, P. F. Cottam, J. Schaefer and C. Ho, An investigation of the ligand-binding site of the glutamine-binding protein of *Escherichia-coli* using rotational-echo double-resonance NMR, *Biochemistry*, 1994, **33**, 8651–8661.
85. C. A. Klug, K. Tasaki, N. Tjandra, C. Ho and J. Schaefer, Closed form of liganded glutamine-binding protein by rotational-echo double-resonance NMR, *Biochemistry*, 1997, **36**, 9405–9408.
86. L. M. McDowell, D. Barkan, G. E. Wilson and J. Schaefer, Structural constraints on the complex of elongation factor Tu with magnesium guanosine diphosphate from rotational-echo double-resonance NMR, *Solid State NMR*, 1996, **7**, 203–210.
87. J. X. Wang, Y. S. Balazs and L. K. Thompson, Solid-state REDOR NMR distance measurements at the ligand site of a bacterial chemotaxis membrane receptor, *Biochemistry*, 1997, **36**, 1699–1703.
88. C. G. Kim, Ph.D. Thesis, University of Oxford, Oxford, 2006.

89. T. Asakura, A. Aoki, M. Demura, J. M. Joers, R. C. Rosanske and T. Gullion, Structure of *Bombyx-mori* silk fibroin studied by REDOR NMR-spectroscopy, *Polym. J.*, 1994, **26**, 1405–1408.
90. T. Asakura, J. Ashida, T. Yamane, T. Kameda, Y. Nakazawa, K. Ohgo and K. Komatsu, *J. Mol. Biol.*, 2001, **306**, 291–305.
91. T. Asakura, T. Yamane, Y. Nakazawa, T. Kameda and K. Ando, *Biopolymers*, 2001, **58**, 521–525.
92. T. Asakura, J. Ashida and T. Yamane, *NMR Spectroscopy of Polymers in Solution and in the Solid State*, American Chemical Society, Symposium Series 834, Washington, DC, 2003, 71–82.
93. T. Asakura and Y. Nakazawa, *Macromol. Biosci.*, 2004, **4**, 175–185.
94. T. Asakura, K. Ohgo, K. Komatsu, M. Kanenari and K. Okuyama, *Macromolecules*, 2005, **38**, 7397–7403.
95. J. Ashida, K. Ohgo, K. Komatsu, A. Kubota and T. Asakura, *J. Biomol. NMR*, 2003, **25**, 91–103.
96. T. Kameda, Y. Nakazawa, J. Kazuhara, T. Yamane and T. Asakura, *Biopolymers*, 2002, **64**, 80–85.
97. T. Kameda, C. H. Zhao, J. Ashida and T. Asakura, *J. Magn. Reson.*, 2003, **160**, 91–96.
98. Y. Nakazawa and T. Asakura, *J. Am. Chem. Soc.*, 2003, **125**, 7230–7237.
99. J. M. Yao, Y. Nakazawa and T. Asakura, *Biomacromolecules*, 2004, **5**, 680–686.
100. C. A. Michal and L. W. Jelinski, *J. Biomol. NMR*, 1998, **12**, 231–241.
101. L. W. Jelinski, A. Blye, O. Liivak, C. Michal, G. LaVerde, A. Seidel, N. Shah and Z. Yang, *Intl. J. Biol. Macromol.*, 1999, **24**, 197–201.
102. J. J. Balbach, Y. Ishii, O. N. Antzutkin, R. D. Leapman, N. W. Rizzo, F. Dyda, J. Reed and R. Tycko, *Biochemistry*, 2000, **39**, 13748–13759.
103. D. J. Gordon, J. J. Balbach, R. Tycko and S. C. Meredith, *Biophys. J.*, 2004, **86**, 428–434.
104. C. P. Jaroniec, C. E. MacPhee, N. S. Astrof, C. M. Dobson and R. G. Griffin, *Proc. Natl. Acad. Sci. U.S.A.*, 2002, **99**, 16748–16753.
105. A. Naito, M. Kamihira, R. Inoue and H. Saito, *Magn. Reson. Chem.*, 2004, **42**, 247–257.
106. S. Toraya, K. Nishimura and A. Naito, *Biophys. J.*, 2004, **87**, 3323–3335.
107. F. Porcelli, B. Buck, D. K. Lee, K. J. Hallock, A. Ramamoorthy and G. Veglia, *J. Biol. Chem.*, 2004, **279**, 45815–45823.
108. M. L. Bodner, C. M. Gabrys, P. D. Parkanzky, J. Yang, C. A. Duskin and D. P. Weliky, *Magn. Reson. Chem.*, 2004, **42**, 187–194.
109. J. Yang and D. P. Weliky, *Biochemistry*, 2003, **42**, 11879–11890.
110. S. Kimura, A. Naito, S. Tuzi and H. Saito, *J. Mol. Struct.*, 2002, **602**, 125–131.
111. J. C. Lansing, J. G. G. Hu, M. Belenky, R. G. Griffin and J. Herzfeld, *Biochemistry*, 2003, **42**, 3586–3593.
112. S. O. Smith, T. Kawakami, W. Liu, M. Ziliox and S. Aimoto, *J. Mol. Biol.*, 2001, **313**, 1139–1148.
113. E. Hughes and D. A. Middleton, *J. Biol. Chem.*, 2003, **278**, 20835–20842.
114. K. Nishimura, S. G. Kim, L. Zhang and T. A. Cross, *Biochemistry*, 2002, **41**, 13170–13177.
115. S. O. Smith, M. Eilers, D. Song, E. Crocker, W. W. Ying, M. Groesbeek, G. Metz, M. Ziliox and S. Aimoto, *Biophys. J.*, 2002, **82**, 2476–2486.
116. T. M. Forrest, G. E. Wilson, Y. Pan and J. Schaefer, *J. Biol. Chem.*, 1991, **266**, 24485–24491.
117. Y. Pan, N. S. Shenouda, G. E. Wilson and J. Schaefer, *J. Biol. Chem.*, 1993, **268**, 18692–18695.
118. G. Tong, Y. Pan, H. Dong, R. Pryor, G. E. Wilson and J. Schaefer, *Biochemistry*, 1997, **36**, 9859–9866.
119. L. Cegelski, S. J. Kim, A. W. Hing, D. R. Studelska, R. D. O'Connor, A. K. Mehta and J. Schaefer, *Biochemistry*, 2002, **41**, 13053–13058.
120. A. M. Christensen, J. Schaefer, K. J. Kramer, T. D. Morgan and T. L. Hopkins, *J. Am. Chem. Soc.*, 1991, **113**, 6799–6802.
121. C. A. Klug, L. A. Burzio, J. H. Waite and J. Schaefer, *Arch. Biochem. Biophys.*, 1996, **333**, 221–224.
122. L. M. McDowell, L. A. Burzio, J. H. Waite and J. Schaefer, *J. Biol. Chem.*, 1999, **274**, 20293–20295.
123. Y. Pan, *Solid State NMR*, 1995, **5**, 263–268.
124. J. M. Gibson, V. Raghunathan, J. M. Popham, P. S. Stayton and G. P. Drobny, *J. Am. Chem. Soc.*, 2005, **127**, 9350–9351.
125. W. J. Shaw, J. R. Long, J. L. Dindot, A. A. Campbell, P. S. Stayton and G. P. Drobny, *J. Am. Chem. Soc.*, 2000, **122**, 1709–1716.

126. L. Cegelski and J. Schaefer, *J. Magn. Reson.*, 2006, **178**, 1–10.
127. D. D. Mueller, A. Schmidt, K. L. Pappan, R. A. McKay and J. Schaefer, *Biochemistry*, 1995, **34**, 5597–5603.
128. W. Humphrey, A. Dalke and K. Schulten, *J. Mol. Graphics*, 1996, **14**, 33–38.
129. U. Sternberg, R. Witter and A. S. Ulrich, *Advances in Solid State NMR Studies of Materials and Polymers*, I. Ando, ed., Academic Press, London, 2004, 53–104. (A special volume dedicated to I. Ando, ed.)
130. R. Witter, W. Priess and U. Sternberg, *J. Comput. Chem.*, 2002, **23**, 298–305.

Index